DETECTION AND MEASUREMENT OF PHASE TRANSFORMATION IN STEEL USING ELECTROMAGNETIC SENSORS

By

MAYORKINOS PH. PAPAELIAS

A thesis submitted to
The University of Birmingham
for the degree of
DOCTOR OF PHILOSOPHY

Department of Metallurgy and Materials
School of Engineering
The University of Birmingham
February 2004

SYNOPSIS

Modern strip steel production requires accurate control of the cooling process at the run out table in order to achieve the desired microstructure and hence mechanical properties. Optical pyrometers are currently used by the steel industry to monitor temperature, and hence infer microstructure, however, their performance is imperfect due to the harsh environment that exists within the run out table. Methods for measuring microstructure directly on a strip steel run-out table are the subject of investigation. The present thesis is concerned with the assessment of an electromagnetic (EM) sensor capable of detecting the formation of ferromagnetic ferrite from paramagnetic austenite below the Curie temperature. From the results obtained it was found that the EM sensor can successfully detect the formation of ferrite below the Curie temperature but that the signal (i.e. impedance) can be significantly affected by the formation of a decarburised ferrite layer around the samples. It was also revealed that the impedance value is monotonically (non-linear) related to the ferrite volume fraction and depends on the morphology / distribution of the ferromagnetic phase and hence is influenced by the prior austenite grain size. Results from finite element (FE) simulations designed to enable prediction of the impedance value from the microstructure are also presented showing that two dimensional FE simulations can be successfully used to model the experimental trends observed. The combination of modelling and measurement has shown that EM sensors can be used to directly monitor the ferrite transformation (below the Curie temperature) thus providing a measure of ferrite volume fraction and also a means of identifying ferrite distribution in the microstructure. Based on the conclusions drawn from the present thesis the development of an EM sensor that measures microstructure during transformation in an industrial hot rolling mill is a realistic possibility.

Dedicated to my parents

ACKNOWLEDGEMENTS

I take this opportunity to express my appreciation to those who have contributed to this project. I am greatly indebted to Dr Claire Davis for her enthusiastic support, constructive criticism and valuable suggestions. My appreciation to Dr Richard Binns for his help with the EM measurements and Dr Tony Peyton at Lancaster University for the provision of the technical means and assistance during the FE simulations. My sincere thanks to Dr Martin Strangwood for his help with the contiguity measurements and Thermo-Calc predictions, and Dr Peter Morris at Corus Group U.K. for his valuable remarks. Special thanks to Dr Michael Todinov for his many useful comments during the countless discussions we had. I am also deeply grateful to the very competent members of the technical and support staff of the Metallurgy and Materials Department at the University of Birmingham who gave their invaluable assistance whenever required.

I am pleased to acknowledge my indebtedness to EPSRC and Corus Group U.K. for supplying the needed funds. My most profound thanks to Dr Yago Masso Moreu and Dr Elias Nicolaides for their friendship, assistance and support during my stay in Birmingham. Thanks and apologies to others whose contributions I have overlooked.

Last, but certainly not least the continual encouragement and support of my family and friends is deeply and sincerely appreciated.

LIST OF PUBLICATIONS

1. Papaelias, M. Ph.; Davis, C. L.; Strangwood, M.; Binns, R. and Peyton, A. J.: In proc, of 16th National Conference in Solid State Physics, pp. 284-287, 17-20 September 2000, Nafplion, Greece.
2. Papaelias, M. Ph.; Davis, C. L.; Strangwood, M.; Binns, R. and Peyton, A. J.: In proc. of Materials Research Conference, Institute of Materials, London, 23 May 2001.
3. Papaelias, M. Ph.; Davis, C. L.; Strangwood, M.; Binns, R. and Peyton, A. J.: In proc. of Progress in innovative manufacturing engineering, pp. 123-128, 20-22 June 2001, Genoa, Italy.
4. Papaelias, M. Ph.; Davis, C. L.; Strangwood, M.; Binns, R. and Peyton, A. J.: In proc. of 17th National Conference in Solid State Physics, pp. 394-397, 6-9 September 2001, Xanthi, Greece.
5. Binns R.; Davis, C.; Dickinson, S.; Morris, P.; Peyton, A.; Papaelias, M. Ph.; Pritchard, W. and Strangwood, M.: In proc. of Instrumentation to innovation – Applications and developments in metal production and use, 27-28th February 2002.
6. Papaelias, M. Ph.; Davis, C. L.; Strangwood, M. and Peyton, A. J.: In proc. of 11th International Congress in Metallurgy and Materials, 5-8 June 2002, Istanbul, Turkey.
7. Davis, C. L.; Papaelias, M. Ph.; Strangwood, M. and Peyton, A. J.: J. Ironmaking and Steelmaking, pp. 469-476, No. 6, Vol. 29, 2002.

8. Papaelias, M. Ph.; Davis, C. L.; Strangwood, M. and Peyton, A. J.: In Proc. of Modelling the Performance of Engineering Structural Materials III, TMS Fall Meeting 2002, pp. 311-320, Columbus, OH, U.S., 6-10th October 2002.
9. Papaelias, M. Ph.; Strangwood M; Peyton, A. J. and Davis C. L.: J. of Metall. Trans. A, Accepted for publication.
10. Papaelias, M. Ph.; Davis, C. L.; Strangwood, M. and Peyton, A. J.: In proc. of 2nd Materials Research Conference, Institute of Materials, London, 17-18th February 2003.

TABLE OF CONTENTS

LIST OF FIGURES

Chapter 2

Chapter 3

Chapter 4

Chapter 6

LIST OF TABLES

CHAPTER 1: INTRODUCTION

1.1 Steel processing and products

For many decades steel has been one of the most commonplace engineering materials in use. Automobiles, tools, rails and buildings all rely on steel for their manufacture. The reasons for this extensive use of steel in a very large number of engineering applications are a) the abundance of iron in nature, b) its relatively low cost to process and c) its excellent mechanical properties.

Steel, although known to us for several centuries, used to contain large amounts of impurities making it hard and brittle and thus significantly reducing the range of its applications. This problem was overcome in the middle of the 19th century by introducing the Bessemer process, a process no longer in use, but the forerunner of the Basic Oxygen Steelmaking process (BOS), which is in wide use today [1].

The Basic Oxygen Steelmaking unit is basically a refractory-lined vessel that can tip to pour. It may be charged with molten pig iron and scrap and an oxygen lance (sometimes combined with argon) is brought in or ported from the bottom to reduce the carbon, sulphur and phosphorus in the melt. The BOS vessel may be "blown" either from the top or bottom or both [2].

The melt is poured into a ladle where usually the alloy additions are done rather than in the BOS unit. The ladle is then transported to the caster facility, and it is poured

into the caster tundish. The caster mould determines the shape of the semi-finished shape (semi) that the caster produces as shown in figure 1.1 [2].

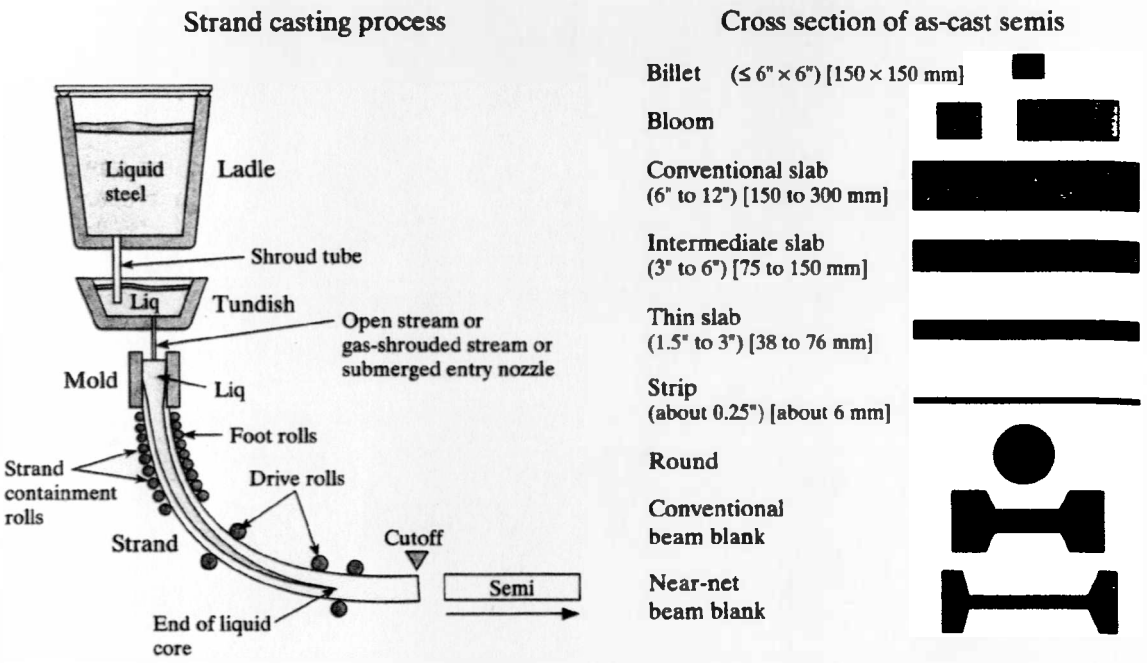

Figure 1.1: Schematic diagram of the strand casting process and semi-finished shapes produced. (Reproduced from Budinski and Budinski) [2]

The semis are categorised into billets, blooms or slabs. Literally thousands of different steel products are produced by further processing of the semis in steel rolling mills. The most common products rolled in a mill are bars, rods and tube rounds made from billets, structural shapes and rails made from blooms, and hot rolled strip, skelp and plates made from slabs (figure 1.2). This project is mainly concerned with the technology required to produce hot rolled multiphase steel strip, however, the findings reported in the following chapters can also be applied to other products.

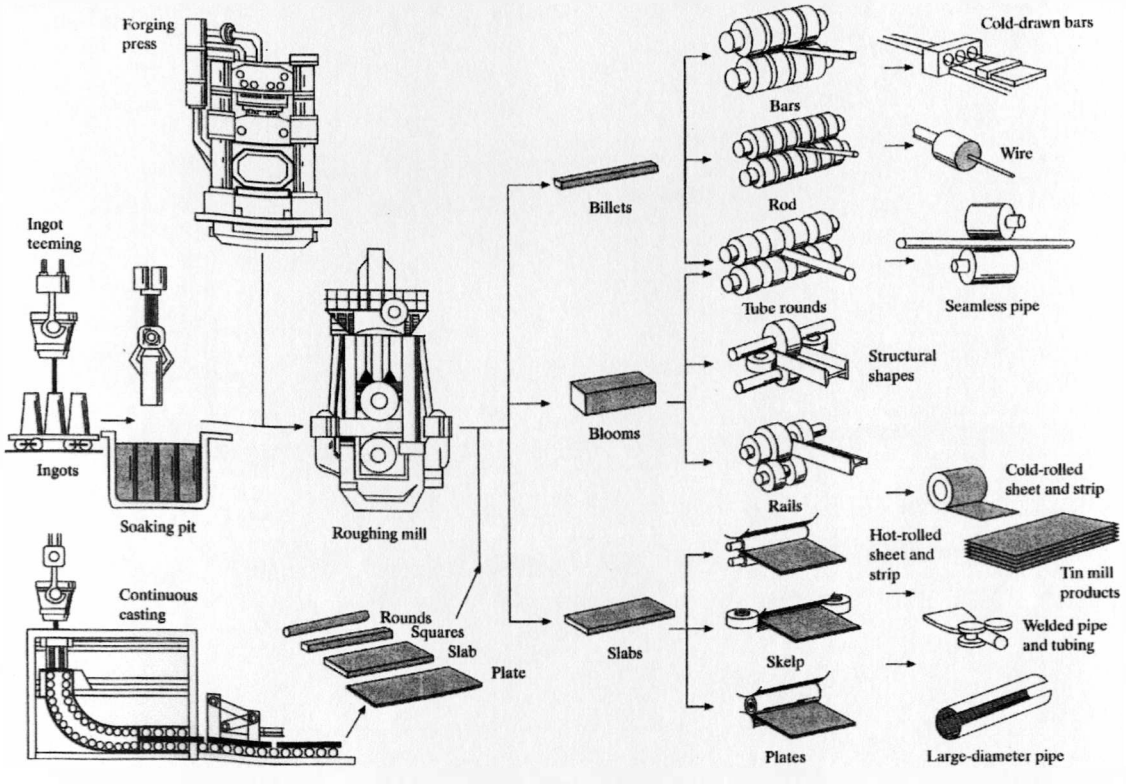

Figure 1.2: Processing of refined steel into products. (Reproduced from Budinski and Budinski) [2]

Within the area of strip products, the hot strip mill plays an important role in controlling the grain structure through the reheating practice and rolling schedule [3-4]. The factor that governs the type of microstructure formed is the controlled cooling of the strip on the run out table after hot rolling [5]. Heat is removed from the strip at the run out table by the application of cooling water. The cooling water is passed through laminar pipes which are located above and below the strip. For control purposes the pipes are grouped together to form cooling banks, where each bank can be controlled independently. This control can either take the form of simple on/off control, or

variable flow control. Figure 1.3 shows the general outline of the end part of a hot rolling mill.

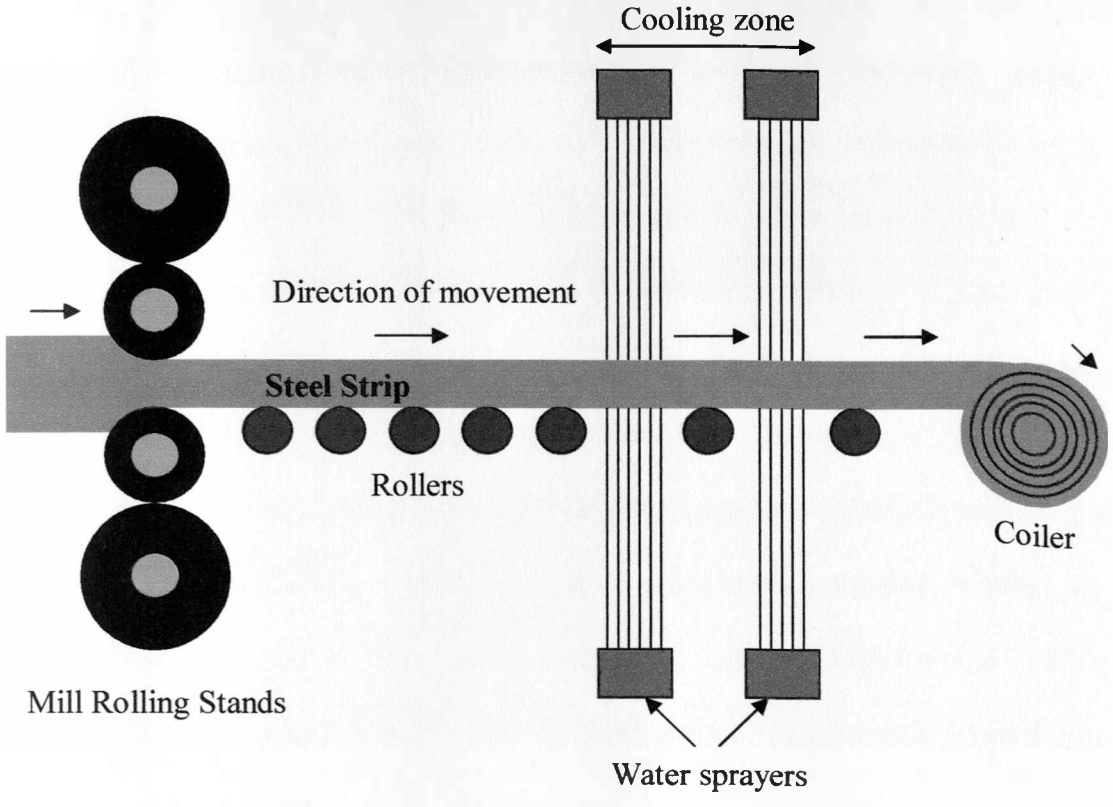

Figure 1.3: Schematic diagram of the end-part of a hot rolling mill.

Despite the fact that overall mill utilisation has been improved in the production of steel strip, in order to increase microstructural homogeneity, and hence improved mechanical properties, variations in temperature distribution and cooling rate must be avoided. Uncontrolled cooling of the strip at the run out table may result in undesired final microstructure and hence, poor mechanical properties [6]. Therefore, scatter of mechanical properties both from strip to strip and within the strip with regard to a

target specification needs to be minimised, if the steel rolling mills want to keep up with the growing demands of the customers.

As a result of increased customer demand for higher strength in steel strip, dual phase (ferrite - martensite and ferrite - bainite) and triple phase (ferrite - martensite - bainite) steels were developed in the late 1970s [7]. To increase the homogeneity of the mechanical properties in the steel strip, the correct cooling rate has to be achieved in order to obtain the desired microstructure. Furthermore, variations in temperature distribution and cooling rate need to be minimised. High strength multiphase strip steel is hot rolled as austenite, at temperatures exceeding 1000°C, water cooled on the run out table to give the majority of the ferrite transformation, usually around 80% of the total volume fraction, and then coiled at a prescribed temperature to allow any second phase to develop [8]. The coiling temperature can vary between 350°- 600°C (low coiling temperature) or 600° – 750°C (high coiling temperature) depending on what second phase is required [9]. Coiling temperatures of hot strip influence ferrite grain size and morphology, interlamellar spacings of pearlite, pearlite lamella thickness, grain boundary cementite morphology and thickness, and bainitic structure (upper or lower). To obtain fine equi-axed ferrite grains a low coiling temperature is needed [10]. However, some grades of low carbon steel requiring cold rolling and batch annealing need to be coiled at a high temperature. This permits good elongation to be exhibited by cold rolled and batch annealed steels [11]. Figure 1.4 shows grain shape during the hot rolling procedure and the effect of the coiling temperature.

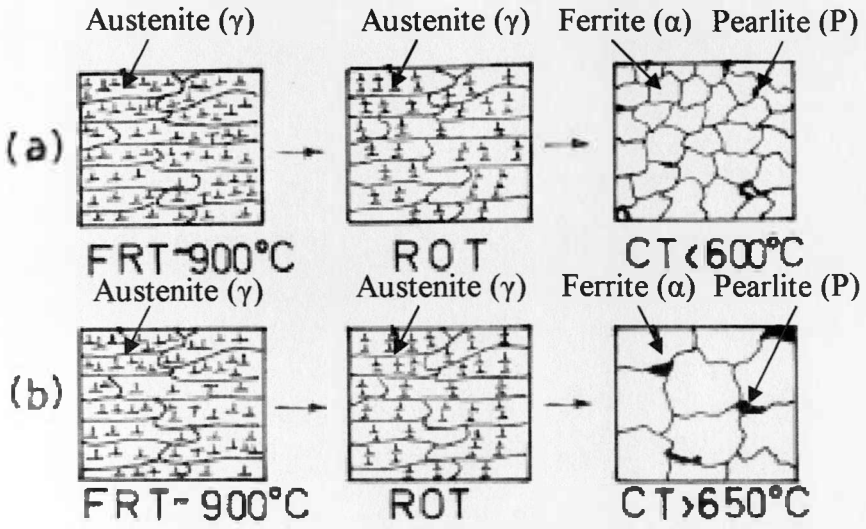

Figure 1.4: Decomposition of austenite to ferrite and pearlite during cooling of steel and influence of coiling temperature on final grain size. (FRT: Finishing rolling temperature, ROT: Run-out table, CT: Coiling temperature).

(Reproduced from Panigrahi) [9]

During steel production one of the directly measured quantities used for process control is temperature. Knowledge of the cooling rate enables the prediction of the microstructure formed in the final product. However, temperature is only an indicator that may contain inaccuracies and does not directly measure the final microstructure. Additionally, compositional variations may lead to phase transformation being affected, occurring at different temperatures than those expected [12]. Hence, by only monitoring temperature, inaccurate cooling schedules may result. Consequentially, destructive testing is required to verify the mechanical properties produced. Therefore, it is desirable for the steel manufacturers to develop better means of controlling and monitoring microstructure during the rolling and cooling processes.

1.2 Temperature monitoring in the finishing mill – Optical pyrometers

The use of optical pyrometers has been well established within the steel industry for implementing feedback control for cooling [13-15]. Pyrometers detect the emissivity of a material (heat radiation) and operate within the infrared band of the electromagnetic (EM) spectrum, typically between wavelengths of 0.4 and 30μm [16]. Figure 1.5 shows a schematic of a rolling mill with pyrometer positioning.

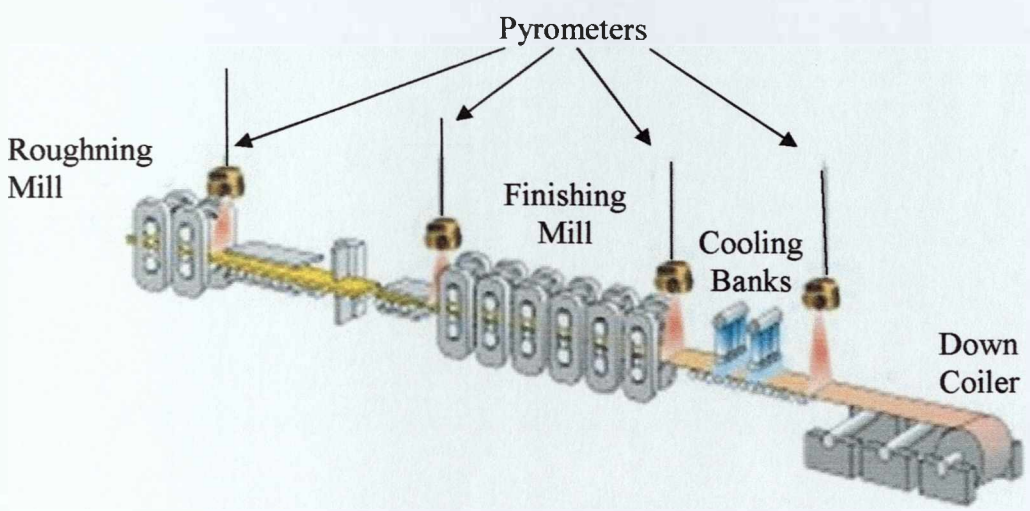

Figure 1.5: Schematic diagram of a rolling mill with pyrometer positioning.

(Reproduced from Brown) [21]

Above absolute zero, all bodies emit electromagnetic radiation due to the vibration of their electrons. Therefore, the distribution of wavelengths of the radiation emitted characterises their temperature. For a body that emits all wavelengths of energy, the spectral radiance is given by equation 1.1 [17].

$$L_\lambda = \varepsilon_\lambda \cdot L_{\lambda,b}(T_s) = \varepsilon_\lambda \cdot \frac{c_1}{\lambda^5}\left(e^{c_2/\lambda T} - 1\right)^{-1} \qquad \text{Equation 1.1}$$

Where L_λ is the spectral radiance of the body in W m^{-2} sr^{-1} nm^{-1} at temperature T_s, λ is the wavelength under consideration in μm, $L_{\lambda,b}$ is the spectral radiance of a dark body, c_1 is the first Planck radiation constant, 1.910.444 x 10^8 W μm^4 m^{-2} $seradian^{-1}$, T_s is the target temperature in Kelvin and ε_λ is the unitless spectral emissivity, i.e. the ratio of the energy emitted by the target relative to a dark body. In the case where emissivity is accurately known and no factors influence the levels of the detected infra-red radiation then temperature can be measured accurately.

Until recently measurement on hot strip mills had to rely largely on single point (spot) pyrometers. These pyrometers are limited by the fixed position to the strip, large spot size and slow response [18].

In ideal conditions the accuracy of optical pyrometers is satisfactory (error margin is smaller than ±1% of the actual temperature of the target) [16]. However, under the conditions prevailing in a hot rolling mill, reflected radiation and emissivity of the surroundings will cause some inaccuracy. Unfortunately, the atmosphere at a strip run-out table contains large quantities of steam, water droplets and dust that can be deposited on the pyrometer's window, adversely affecting its performance.

Optical pyrometers are therefore positioned between the cooling zones, in the strip run out table, and before the coiler. The cooling profiles obtained through the different stages provide some temperature information about the strip, which is then

used in mathematical models in order to produce cooling control algorithms. By using these algorithms, temperature can be inferred within the cooling zones and transformed fraction (i.e. percentage of austenite transformed to ferrite) can be predicted [19-20]. Unfortunately, these mathematical models must be continuously adapted to the changing mill parameters and composition of the steel. The fact that they are not self-adjustable results in further costs and loss of time.

Single wavelength pyrometers cannot reject external reflectance. Dual wavelength pyrometers, which have recently been developed, have the ability of rejecting external reflectance by superimposing two different wavelengths upon each other [16]. Integrated thermal profile systems take advantage of a rotating mirror in order to make measurements at various points across the surface of the plate or strip and are thus capable of acquiring more complete feedback from the processing line. The accuracy of these pyrometers is a function of both the optical and mechanical design of the system components. Many thermal profile systems use a similar principle of rotating mirror and a fixed detector. Most also use a conventional lens to focus the signal from the hot object onto the detector. Unfortunately the temperature of these optics has an influence on the temperature measured by the detector. Hence, most pyrometers suffer from drift and accuracy problems [21].

The optical design of some newly developed pyrometers overcomes the limitation by disposing with conventional design and use an accurately machined mirror to focus the signal onto the detector. As the signal does not have to be transmitted through any optical system there is a greater signal strength, less noise and better accuracy [21]. However, even these advanced devices cannot perform well in the run out table due to

the presence of steam, water droplets and dust which directly influence the signal strength and increase the noise levels in the pyrometer readings.

Due to the limitations of the optical pyrometers in the run out table environment other techniques for measuring the steel microstructure directly are currently being investigated and are discussed below.

1.2.1 Artificial Neural Networks (ANNs)

In an attempt to replace the empirical equations used in combination with pyrometers, the possibility of improving the accuracy of the cooling control system in the run out table by employing artificial neural networks (ANN) instead, has been investigated [22].

ANNs were developed as a means of artificially replicating the way in which a brain works, and were an attempt of implementing parallel processing functionality [23].

As a result of the method of implementation of ANNs, they are capable of learning the relationship between various input parameters and results. They are particularly suited to modelling non-linear systems where conventional approaches are traditionally weak [24]. The ANN, if trained correctly, will take into account any trends within the data. Once the ANNs have been trained, they are capable of processing data at a higher rate than conventional modelling techniques allow [25], which would increase the speed and accuracy of temperature control on the run-out table.

However, it is vital that the ANNs are trained correctly. If the training is not comprehensive, then it is possible that the network can produce erroneous results. The ANN requires a large dataset to be trained and tested on. In addition the dataset needs to be accurate and comprehensive (i.e. if any input parameters are missing the data cannot be used). Any errors in the dataset will be translated into inaccuracies in the ANN. Care is also required to ensure that the ANN is not "over-trained" i.e. it should not model statistical fluctuations in the data but the overall trends. The ANNs are dependent on empirical data and they make no reference to scientifically proved relationships that are modelled with proved mathematical formulae.

Although in general, the use of ANNs has been encouraging, only the first part of the run out table has been modelled to date and hence results were based on using a limited amount of data from the pyrometers placed outside the cooling zones and the final strip gauge. Therefore, a much larger number of inputs would be required in order to model the run out table in full [22]. ANNs have also been used to model the yield and tensile strengths of steel plates as a function of composition and rolling parameters [26]. Hence, as this approach is based on empirical data, ANNs could be used in the future in combination with any of the other techniques discussed in the following sections.

1.3 Techniques for phase transformation detection and measurement

In the past two decades, a large number of researchers around the world have been concerned with the accurate on-line detection of phase transformations that occur

during cooling of steel strip. The run out table of a hot-rolling mill is an extremely harsh environment for sensing equipment. Thus, any sensing device installed at the run out table should be able to withstand the extreme conditions that exist there. Such a sensing device would be then required to have better accuracy than optical pyrometers, be a non-contact technique i.e. work at a distance from the strip, be unaffected by electrical noise, have a relatively low cost, be intrinsically safe to humans and be of a relatively small size so that the general setup of the mill remains unmodified. As a result, a number of alternative solutions focusing on the problem of monitoring phase transformations at the run out table have been proposed. These techniques are examined individually in the following paragraphs.

1.3.1 X-ray diffraction

X-rays are a form of electromagnetic radiation that have high energies and short wavelength. When a beam of X-rays impinges on a solid material, a portion of this beam will be scattered in all directions by the electrons associated with each atom or ion that lies within the beam's path. Bragg's law states that if a monochromatic and coherent beam of X-rays is aimed at an angle on a solid the angle of the diffracted wave produced will be proportional to the initial wavelength and interatomic displacement within the targeted solid. Equation 1.2 quantifies Bragg's law [27].

$$n\lambda = 2\, d_{hkl} \sin\theta \qquad \textit{Equation 1.2}$$

where n is the number of wavelengths, λ is the wavelength, d_{hkl} is the interplanar spacing and θ is the angle of the incident beam with reference to the targeted solid.

The interatomic displacement will obviously depend upon the crystal lattice of the solid (i.e. Face-Centred Cubic or FCC, Body-Centred Cubic or BCC, Hexagonal-Close Packed or HCP, etc.). Hence, the presence of atoms in particular positions will result in a measurable characteristic diffraction pattern for each crystal lattice. Figure 1.6 shows the diffraction of X-rays by planes of atoms.

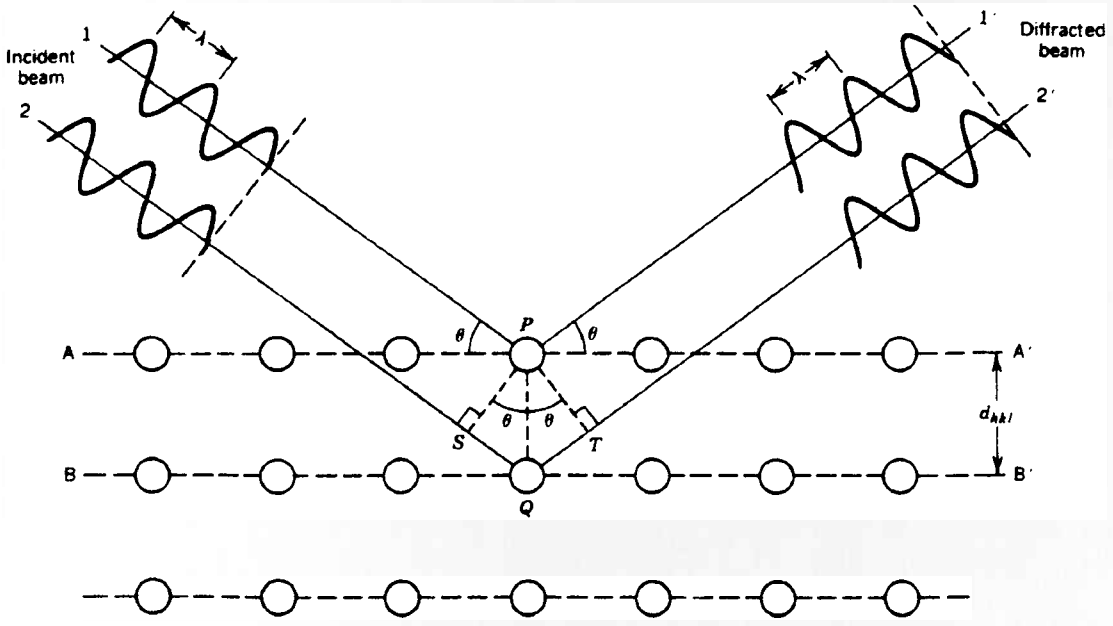

Figure 1.6: Diffraction of X-rays by planes of atoms (A-A' and B-B').

(Reproduced from Callister) [27]

As steel phases have different crystal structures, it is possible to differentiate the phases by use of X-rays diffraction. X-rays diffraction could therefore be applied in the run out table of a mill since the X-rays would remain largely unaffected by the water droplets, steam and dust.

Japanese patents Nos. 114518/74, 136442/76 and Japanese patent publication No. 25309/78 propose methods in which X-rays can be irradiated onto the surface of a steel. The fact that X-ray diffraction intensities are directly proportional to the phase volume fraction allows the transformation to be monitored [28]. In 1983, Kitagawa and Sohmura developed an X-ray diffraction method which was successfully employed in a production mill as a practical means of predicting inhomogeneities in the mechanical properties of strip steel by monitoring the relative amount of austenite and martensite present. Measurements were carried out by scanning a coil, cold rolled in a reversing mill, during the uncoiling operation in a sliting lane. Their detecting device involved a specially designed diffractometer for application in the mill, equipped with an X-ray source and three separate scintillation detectors. The most severe shortcoming with this method is the problem of calibration due to preferred orientation, since in reality all materials have a preferred orientation to some extent resulting to a number of intensities being obtained [29]. Thus, the obtained random intensities need to be averaged in order to acquire the desired result [30-31]. However, this method is also disadvantageous in that it is necessary to take safety protective measures in order to avoid X-ray injuries due to the high strength of the X-rays being irradiated. As a direct consequence, the detection system becomes large-sized, resulting in an increased installation cost, limitation to the maximum number of systems installed and several maintenance problems. Finally, the obtained information results from a surface depth no greater than 50μm, hence making it difficult to analyse bulk properties [28]. Transmission X-ray techniques capable of measuring bulk properties, also exist and are discussed next.

1.3.2 γ-ray or X-ray attenuation

An indirect method for detecting phase transformation has been proposed, involving the measurement of attenuation (absorption) of a gamma-ray or X-ray beam as a means of monitoring density changes. The number of X-ray or gamma-ray photons going without interaction through an object is related to the number of incident photons by an exponential law where the exponent is the product of the thickness, the apparent density and the mass absorption coefficient (equation 1.3) [32]. The latter depends only on the nature of the object and the energy of the radiation.

$$N = N_i \exp(-\chi \rho x) \qquad \text{Equation 1.3}$$

Where N is the number of photons exiting the targeted object, N_i is the number of incident photons, ρ is the object's density, x is the object's thickness and χ is the mass absorption coefficient.

This approach would allow phase detection based on the different crystal structures of austenite and ferrite and hence their different properties (density and mass absorption coefficient). Austenite is face-centred cubic and has a higher atomic packing factor than body-centered cubic ferrite and body-centred tetragonal martensite, making it more dense. Hence, detection of changes in the absorption of the beam leads to the conclusion that transformation has occurred. Figure 1.7 shows the outline of the proposed technique.

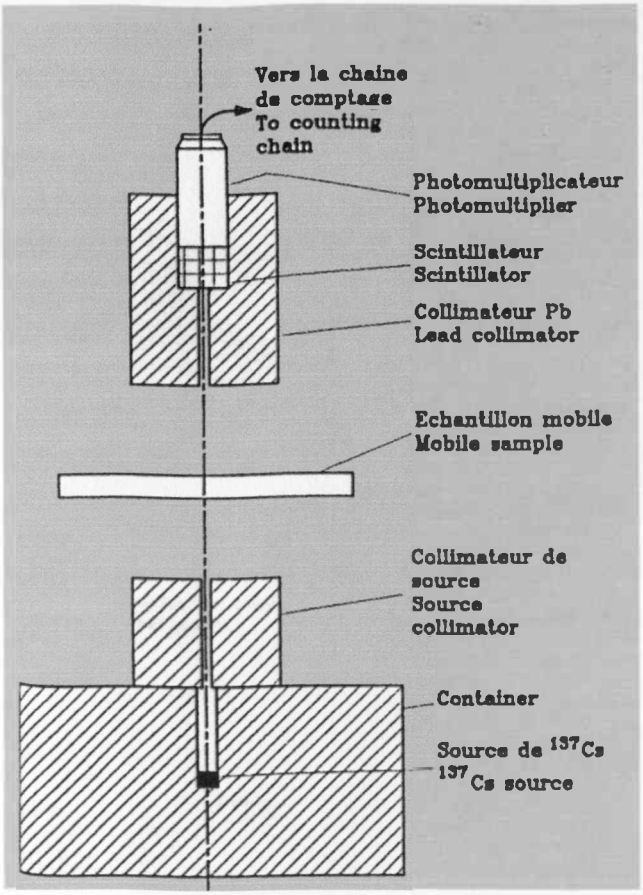

Figure 1.7: Schematic diagram of the X-ray attenuation setup for detecting phase transformation. (After Gaujé) [32]

This technique may also be used in other aspects of steel making such as the detection of the end of solidification in a casting machine, detection of contraction cavities in cast products or evaluation of the compactness of sintered parts [32]. It should be noted here that the use of radiographic techniques for examining steel castings for defects was originally proposed in the early 1950s [33].

Despite the fact that this method is relatively precise in measuring the transformed fraction and has possibilities of being used directly in the production line, safety is an

extremely important feature due to the very dangerous nature of X-ray and gamma-ray beams.

1.3.3 X-ray transmission

As an alternative to the X-ray-based on-line measurement methods previously discussed, X-ray transmission has been developed for the non-destructive determination of texture-dependent technological data of rolled strip [34]. Mechanical properties of steel strip can be derived through knowledge of the final crystallographic texture present in the rolled strip. In addition phase determination can be deduced from the change in texture associated with the change in type of the crystal lattice of the solid (face-centred cubic or FCC, body-centred cubic or BCC etc.)[35-36]. The Hoesch Stahl AG company in Germany has developed X-ray transmission systems for on-line measurement and study of crystallographic textures of rolled steel products. The aforementioned systems have been successfully installed in cold strip mills and tested over many years with excellent results according to published company reports [37-39]. It should be mentioned however that quantitative results in order to verify the efficiency of the system were not reported. Since the diffraction signal results from coherent scattering of the X-rays in the individual grains within the steel, the transmitted X-ray signal, contains direct evidence of the structure [40].

Koppineck et al. reported the development of an advanced X-ray transmission measuring procedure which can be used on-line for both hot and cold steel strip [34]. The measuring technique is based on the strip being irradiated by high-energy X-rays [energies between 60 and 100 keV are required] while energy-dispersive detectors

measure either the resulting X-ray energy spectrum or the intensity of the X-ray signal at point locations in the transmission direction.

The proposed technique allows the measurement of the entire thickness of the strip and not just of the near surface layer. However, the maximum thickness of the strip at which the technique can be applied is limited to 5 mm [34]. So far, the technique has been applied only outside the run-out table mainly as a means of verifying the quality of the rolled product after transformation has been completed. Thus, it is unknown if the instrumentation can function in the environment of the run-out table and how efficient it would be.

1.3.4 Laser Ultrasonics

Ultrasonic techniques have been used in the past in order to detect internal defects in semi-finished steel products at room temperature [41-42] and under laboratory and production conditions at high temperatures (up to 1200°C) [43-44]. Ultrasonics has also been a reliable method to characterise steel microstructure, i.e. grain size, phase contents and homogeneity [45].

However, ultrasonic measurements at the austenite-ferrite transformation temperatures are not easily obtained using conventional ultrasonic transducers due to the requirement for contact with the specimen. Laser-ultrasonics is a technique based on the generation of ultrasonic waves by a pulsed laser and on their detection by a laser interferometer and is a truly remote technique (working distances of over 1 m are possible) [46] and works relatively well at high temperatures [47-49].

Ultrasonic attenuation has been measured during the heating and cooling of carbon steel samples through the austenite-ferrite transformation using laser ultrasonics in the past [48]. However, the accuracy of the data obtained did not allow a reliable identification of the transformation temperatures, and no comparison with a conventional technique to monitor phase transformation was presented.

Many reports have been concerned with the ultrasonic absorption mechanisms in metals and explain the behaviour observed [50]. Ultrasonic attenuation, in hot-rolled carbon steels, is caused by a combination of microstructural parameters such as diffraction, grain scattering and absorption based on density [51]. However, ultrasonic attenuation is primarily related to grain scattering.

The development of laser ultrasonics in recent years has allowed new attenuation measurements with significantly improved accuracy at temperatures between 500°C and 1100°C. The sudden variations of ultrasonic attenuation observed in this temperature range are related to microstructural changes caused by the austenite-ferrite phase transformation [52-54].

A pilot study to assess the laser ultrasonic technique under real, albeit small scale, hot rolling conditions reported that the phase transformation was clearly detected at around 700°C. The same study reported results from a trial undertaken on a full commercial continuous annealing line. In this case the objective was to determine the degree of recrystallisation in thin strip product. The results obtained were encouraging, given the extreme heat and mechanical noise present within the

enclosure housing the experiment, however a laser ultrasonic system has not been installed in the run-out table yet [54].

More trials are needed however, to determine the impact of heat, noise, steam and scale build-up on the laser ultrasonic system [54]. Furthermore, the technique needs to be validated for grain sizes smaller than 100 μm using materials and thermal treatments showing a low tendency for abnormal grain growth and systematic tests should be carried out to delineate the sensitivity of the technique to steel chemistry. Finally, ultrasonic models need to be improved to include the effects of grain shape and grain size distribution in the calibration [53].

1.3.5 Ultrasonic velocity

Ultrasonic wave velocity measurement is another possible technique that can be used to assess the microstructure of a metal alloy. The technique is based on the transmission of ultrasonic waves from a longitudinal wave transducer at a pre-chosen frequency (i.e. 5, 10 and 20 MHz) into the specimen which is in contact with the transducer [55-56]. Then the echoes of the wave are detected by an oscilloscope and are stored in a computer. The stored data is then analysed in order to calculate the transit time. The transit times can be measured with an accuracy of ±0.2 ns and sample thickness with ±1 μm accuracy. The ultrasonic wave velocities are obtained with an accuracy of ±2 m/s [57]. Figure 1.8 shows an outline of the experimental setup.

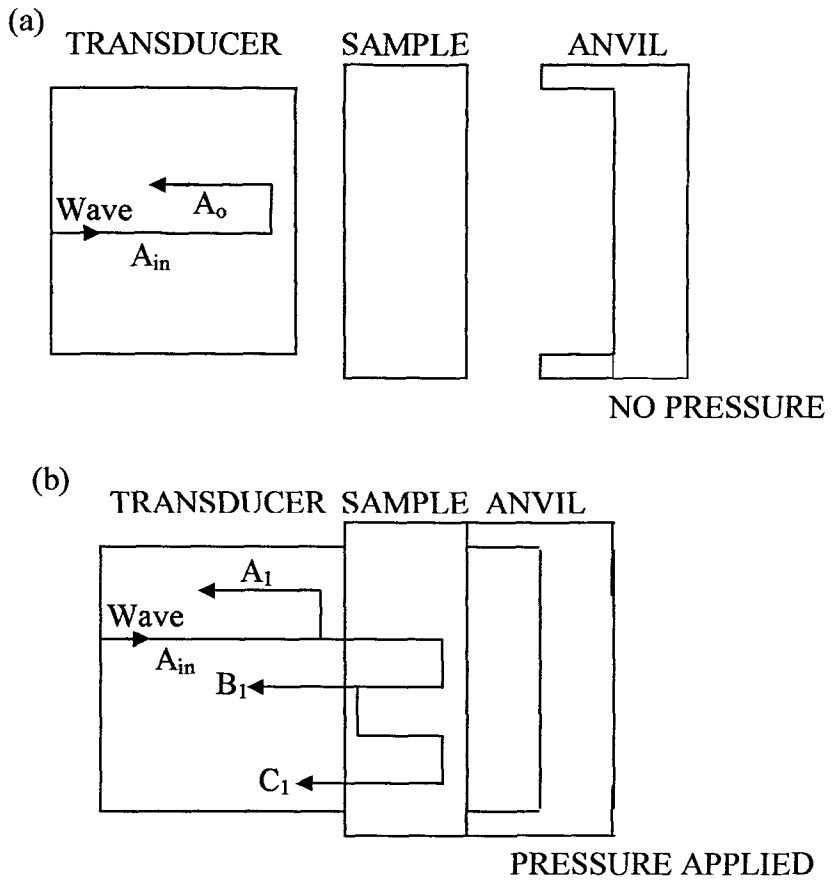

Figure 1.8: Echoes in the transducer before and during contact with the specimen. (Reproduced from Papadakis et al.) [44]

Palanichamy et al. used the aforementioned technique on alloy 625, a nickel-based alloy. The specimens were thermally aged at various temperatures in the range of 650° – 850°C to produce different microstructures. Microstructural variations in the previously heat treated samples were assessed by measuring ultrasonic wave velocity at room temperature. It was revealed that the ultrasonic wave velocity increased as the precipitation in the specimen increased [57]. Similarly, Orlowicz and Opickun used ultrasonic wave velocity measurements to determine the microstructure in cast iron. It was found that the ultrasonic wave velocity increased with increases in the graphite shape factor and pearlite volume fraction [58]. Figure 1.9 shows the propagation and

echo of ultrasonic waves depending on the average grain size present in the microstructure.

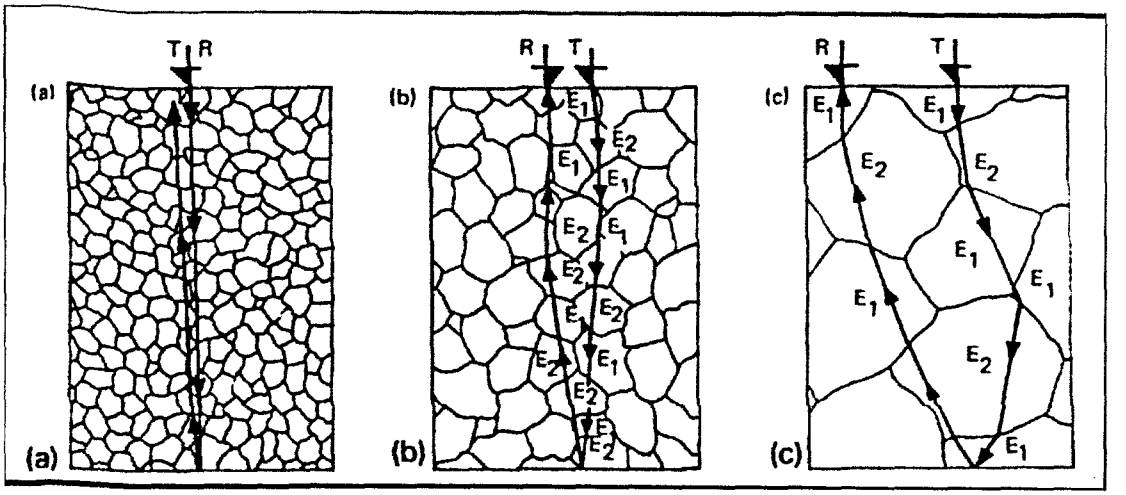

Figure 1.9: Schematics of ultrasonic wave path length in steel.

(a) Fine grain size. (b) Medium grain size . (c) Large grain size.

(Reproduced from Orlowicz and Opiekun) [58]

The main drawbacks of the contact ultrasonic velocity technique are the following: (a) the transducer needs to be in contact with the sample otherwise the ultrasonic wave will be reflected and (b) the piezoelectric materials employed for the manufacturing of transducers fail at temperatures above 600 K (323°C). Therefore, special designs need to be employed to keep operational temperatures of the transducer as low as possible for application at elevated temperatures. Non-contact ultrasonic sensors are in development, although are not currently used for phase determination during cooling following hot rolling of steel.

1.3.6 Through Transmission Ultrasonics

Recently Rajendran et al. employed a through transmission ultrasonic technique in order to characterise the microstructure of 8090 aluminium-lithium alloy by measuring ultrasonic velocity and attenuation [59]. Testing temperatures were limited however from ambient to 500 K (223°C).

The proposed experimental setup involves the use of recrystallised alumina rods that act as waveguides whilst the sample is positioned between them. The transducers are placed at the end of each rod and ultrasonic wave pulses are transmitted through the alumina rods and the sample. The whole setup is positioned in a tabular furnace in order to achieve the required temperatures. In figure 1.10 is shown an analytical schematic of the experimental setup used by Rajendran et al.

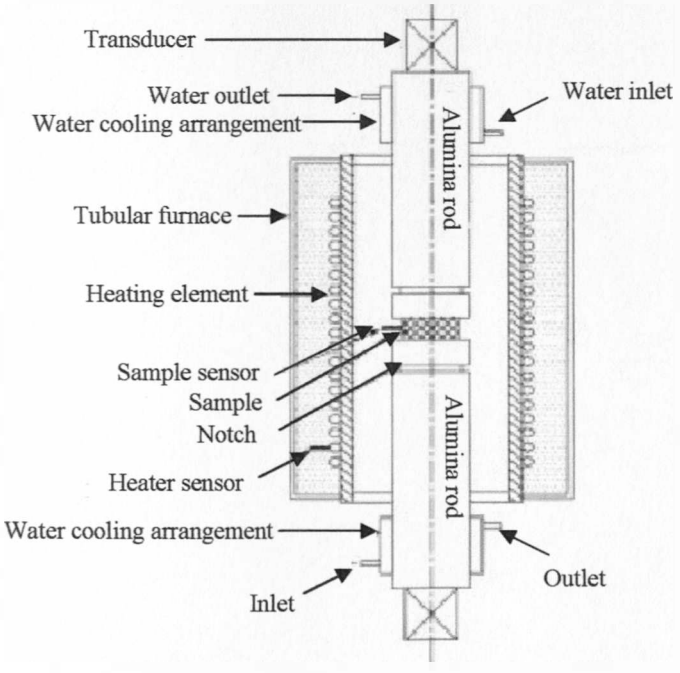

Figure 1.10: Cross-sectional view and mechanical arrangement of the specimen, waveguide and transducer in the high temperature experimental setup using through transmission technique. (Reproduced from Rajendran et al.) [59]

In the experimental setup, one transducer acts as a transmitter and the other as a receiver. In the absence of a sample, the transmitted ultrasonic waves travel through the alumina buffer rod and are received by the receiving transducer. Thus, the time, t_0, required for waves to travel through the buffer rods can be measured in nanosecond resolution. In a similar fashion, it is possible to measure the elapsed time, t_1, in the presence of a sample. The difference, Δt, between the transit times t_1 and t_0 gives the time needed for the waves to pass through the sample. The velocity of the ultrasonic waves in the sample can thus be calculated using equation 1.4.

$$v = \frac{d}{\Delta t} \qquad \text{Equation 1.4}$$

where v is the wave velocity in m/s, d is the thickness in m and Δt is the wave transit time through the sample. The overall accuracy of the measured velocity is ±5 m/s.

The attenuation, α, of the ultrasonic waves in the sample is measured using equation 1.5 [60, 61]

$$\alpha(f) = \frac{1}{d}\left(\ln T + \ln\left(\frac{A_w(f)}{A_s(f)}\right)\right) \qquad \text{Equation 1.5}$$

where A_w(f) refers to the amplitude of the signal with the waveguides and A_s(f) refers to the amplitude of the signal with the sample inserted between the waveguides and T is the combined transmission coefficient at the sample and waveguide interface. The magnitude of the attenuation is related to the different amplitudes of the ultrasonic

waves as they travel through the different mediums. As it was shown in figure 1.8 when the ultrasonic pulse reaches the interface between the transducer and the sample, only part of it is transmitted to the sample, which is known as the transmitted pulse. The rest of the pulse it reflected back to the source. The degree to which waves are reflected and transmitted at the boundary between different media can be analysed using a quantity called acoustic impedance. The acoustic impedance Z_A of a medium is a measure of the difficulty a wave has in distorting the medium and depends on the elasticity and density of the medium. Some absorption of a wave's energy also takes place when it reaches the boundary between two media. In fact absorption takes place at any part through which the wave travels. The coordinated vibrations of the atoms in the medium are turned into thermal energy. Whenever a wave passes between two media with different acoustic impedances, part of the wave is transmitted and part of the wave is reflected. By knowing the acoustic impedances of the two media, it is possible to calculate the amplitude of the transmitted and reflected waves relative to the amplitude of the incident wave.

In general, the through transmission ultrasonics technique is accurate for qualitatively characterising grain size and phase fraction. Nonetheless, the technique has yet to be applied within the harsh environment of the run-out table of a hot rolling mill and thus, it is unknown how efficient it will be.

1.3.7 Thermal analysis

At least one study has examined the possibility of thermal analysis as a means of detecting phase transformation in steel [62]. A number of conventional methods such

as dilatometry, differential scanning calorimetry (DSC), a laboratory rolling mill and a continuous annealing simulator (Casim) were used in conjunction with an in-situ thermal analysis (ISTA) mathematical model as a means of obtaining information about the phase transformation of steel during cooling. The ISTA mathematical model is applied on the experimental results (i.e. cooling curves) obtained by conventional experimental means (i.e. dilatometer, DSC, laboratory rolling mill and Casim). With ISTA it is possible to investigate transformation kinetics and resulting mechanical properties on a single test piece. The starting time and temperature of the transformation can be accurately determined; the transformation heat can be calculated within ±5 % of the real value and the mean transformation temperature within ±5°C. However, the applicability of the ISTA model relies on two conditions; a) no reheating other than due to natural causes during cooling of the specimen and b) the conduction of heat may not be a limiting factor in the transport of heat. Additionally, this study was restricted to laboratory setups and thus realistic cooling rates and conditions were not examined [62].

1.3.8 Electromagnetic sensing

Another possible approach to the problem of monitoring phase transformation during steel production is the use of electromagnetic detectors, capable of monitoring the electromagnetic properties of the strip during cooling. The electromagnetic method is based on the magnetic properties of austenite (paramagnetic) and ferrite, pearlite, bainite and martensite (ferromagnetic below the Curie temperature) [63]. The Curie temperature of steel and its variations with alloying elements and their content is discussed in chapters 2 and 3.

There are various types of electromagnetic sensors that can be employed to detect the ferromagnetic transformation such as AC, DC, Hall probes, and eddy current systems. An AC system uses an excitation coil to create a magnetic flux that is proportional to the induced voltage in the search coil(s). When transformation begins, changes occur in the magnetic flux due to variations to the permeability of steel as it transforms, which are followed by changes in the induced voltage in the search coil(s). By monitoring the changes in the induced voltage in the search coil(s) it is possible to determine when transformation occurs [64]. The schematic diagram in figure 1.11 shows the configuration of the proposed technique applied in the run out table of a hot rolling mill.

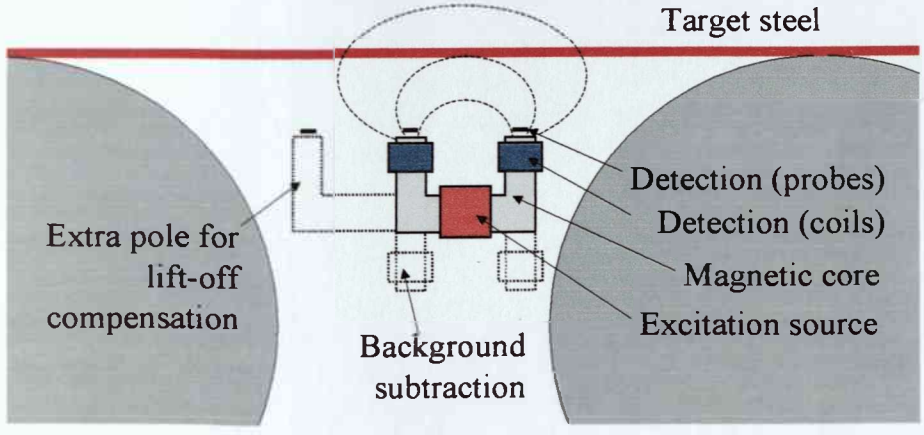

Figure 1.11: Schematic diagram of a U-shaped sensor design showing its intended position between two support rollers below the steel strip.

A DC sensor consists of a primary coil and a secondary (sensing) coil. However, in this case the primary coil alone produces a constant magnetic field. The flux density generated from the primary coil varies due to sample movement, phase transformation and paramagnetic to ferromagnetic transition of the microstructure of steel causing an

electromotive force to be induced within the sensing coil. The induced voltage at the sensing coil varies as the permeability of the steel changes. Hence by measuring the impedance a measure of permeability and hence transformed fraction can be deduced. In a similar manner, based on the Hall phenomenon, a Hall probe can be used to detect the transformed fraction. When a magnetic field is applied to a Hall probe an electromotive force is induced. Any variations in the electromagnetic field due to steel movement or steel permeability variation will result in changes of the recorded electromotive force. Finally, an eddy current probe consists of a coil which is fed with AC voltage and is located near the metallic sheet to be measured. This allows eddy currents to be induced in the near-surface region by the skin effect. The coil's impedance depends sensitively on the near-surface electrical conductivity and magnetic permeability and thus provides a method for measuring these properties.

The present study is concerned with the development of an AC electromagnetic sensor for monitoring phase transformation during cooling under laboratory conditions. Further discussion on the principles of the sensor and the relevant metallurgical parameters will be discussed in chapters 2 and 3.

1.4 Aims and objectives

The main objectives of the present study are accounted in the following paragraphs:

- To research and evaluate an on-line electromagnetic system capable of monitoring the transformation of the steel as it progresses in the run-out table through the cooling spray.

- To investigate the relationship between the dynamic electromagnetic properties of various steel compositions and the cooling path taken during transformation which dictates the resulting mechanical properties and microstructure of the steel.
- To determine the behaviour of the electromagnetic field during phase transformation of the steel and establish a relationship between developed microstructure, transformation kinetics and electromagnetic response.
- To investigate the effect of the operating frequency of the electromagnetic system in conjunction with the microstructure present on the electromagnetic signal.
- To model the effect of the ferromagnetic fraction present and its distribution in the microstructure on the behaviour of the electromagnetic field by means of Finite Element Analysis software.

CHAPTER 2: PHASE TRANSFORMATIONS IN STEELS

2.1 Introduction

Steels are iron-carbon (Fe-C) alloys that may contain appreciable concentrations of other alloying elements. Their mechanical properties may vary considerably, depending on the amount of the various alloying elements present such as carbon, manganese, silicon, titanium, niobium, vanadium, chromium, nickel etc. The effect of each alloying element alone and in combination with iron and other elements on the mechanical properties can be advantageous or deleterious. For example, iron when alloyed with carbon in sufficient amounts forms iron carbides that cause an increase in strength and hardness but a decrease in ductility of the steel. In contrast, sulphur has detrimental influences (i.e. alloy segregation at grain boundaries) on the performance of steel when the sulphur content is beyond the specification of the steel. The strength and most other properties of steel depend primarily on the changes in the microstructure (e.g. distribution of carbides, grain size , phase balance, etc.) which is affected by processing (i.e. temperature, strain, etc.) and composition.

A steel alloy can be heat treated to produce a great variety of microstructures and hence mechanical properties. Heat treatment of steel, in a broad sense, refers to any process involving heating and cooling of the solid metal by which the properties of the steel are altered without any intentional alteration of its chemical composition [65]. Modern steelmaking utilises accurate control of thermomechanical processing in order to adjust the microstructural parameters (i.e. grain size refinement, phase balance and precipitation / solid solution strengthening) which correspond to the

desired mechanical properties. In order to control the microstructural parameters it is necessary first to understand the phase transformations that occur in steel during heat treating and the influence of alloying elements [27]. However, control of phase transformation pre-requisites control of temperature during heat treatment and thus a means to accurately monitor temperature. The present study aims in establishing a link between electromagnetic (EM) data acquired through the EM sensor with microstructure. In order to achieve this, it is necessary to gain a better understanding of the processes involved during the heat treatment of steel, and describe its microstructural constituents and the phase transformations that occur as shown in detail in the following sections.

2.2 The Fe-C equilibrium phase diagram

A major contribution to the understanding of steel transformations is the application of the Fe-C equilibrium phase diagram (figure 2.1). Although the equilibrium diagram is insufficient to explain what happens in heat treatment involving higher pressures than one atmosphere and relatively high rates of heating or cooling, it provides a useful starting point. For the cases where very slow heating and cooling are used, equilibrium diagrams map out the fields of composition and temperature in which various phases are stable, and show the boundaries at which the phases transform. However, most steels will contain other alloying elements that modify the positions of these boundaries. In addition accelerated cooling and / or the presence of alloying elements can result in the formation of non-equilibrium phases (e.g. bainite, martensite) that are not included in the Fe-C equilibrium diagram. In a run-out table high cooling rates (of the order of several hundreds degrees Celsius per second) are

most likely to be experienced during cooling of strip. This is of high significance to this study since steels with carbon content below 0.6 in wt % during slow cooling (i.e. near equilibrium) start transforming above the Curie temperature (T_C), which for pure iron is 770°C [63].

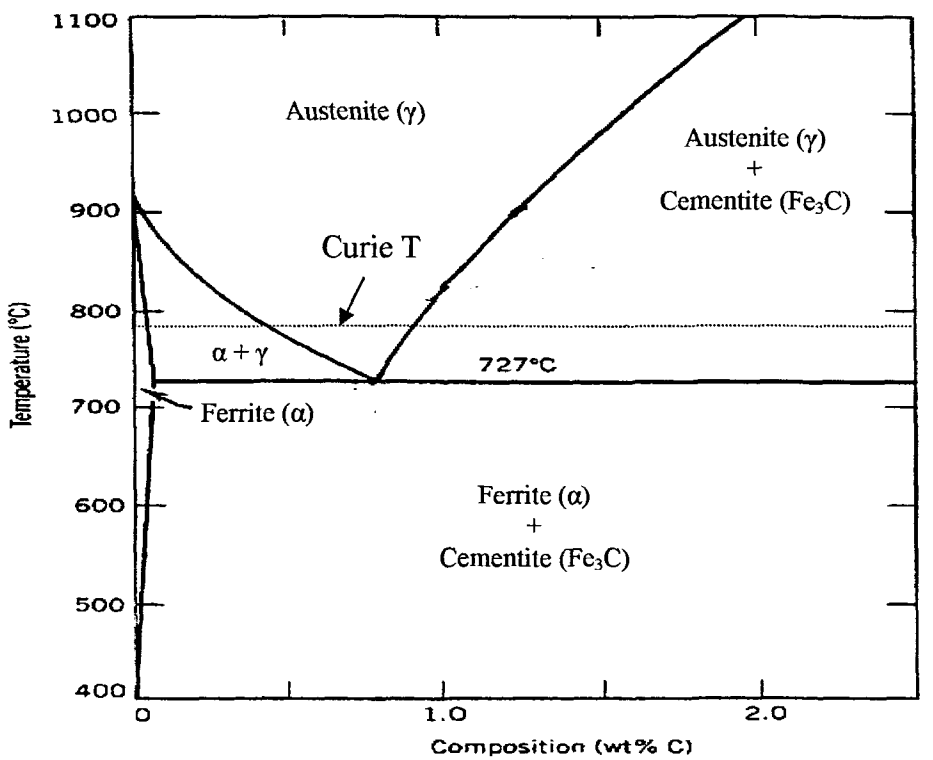

Figure 2.1: The Iron – Carbon (Fe-C) equilibrium phase diagram showing the temperature and compositional limits at which ferrite (α), austenite (γ) and cementite (Fe_3C) are stable under equilibrium conditions. The Curie temperature shown is an approximation and varies with the amount of carbon and other alloying elements present. (After Callister) [27]

The T_C of steel decreases slightly with increasing carbon content and increasing amounts of alloying elements. Exception to this general rule is vanadium and cobalt

as their content in steel rises, T_C increases slightly [63]. A more detailed analysis of the effect of alloying elements on the T_C of steel is given in chapter 3. For steels with very low carbon contents, i.e. <0.05 during near equilibrium cooling almost 100% of the transformation occurs above T_C and hence an EM sensor can only detect the paramagnetic to ferromagnetic transition of ferrite which has already formed earlier above T_C. However, in practice accelerated cooling systems on the run-out tables of strip mills reduce the austenite-to-ferrite transformation below the Curie point, hence allowing the use of electromagnetic sensors for steels containing carbon less than 0.6%. Despite the fact that the Fe-C equilibrium diagram can only be considered as a guide, knowledge of the changes that take place in a steel as equilibrium conditions are approached, provides the scientific basis for the heat treatment of steels.

As seen from the Fe-C equilibrium diagram, when pure iron is heated above 912°C, it exhibits a transformation in its crystal configuration. Up to that temperature, ferrite, a Body-Centred Cubic (BCC) crystal structure, also known as α iron, is stable. However, above 912°C, ferrite becomes unstable and transforms to austenite. Austenite, also termed γ iron, has a Face-Centred Cubic crystal structure and remains stable between 912°C and 1394°C. During hot strip processing in the cooling run-out table the temperatures experienced are typically between 400° - 1000°C, hence it is phase transformations in this range that will be considered.

2.3 Morphology of transformation products in steel

The microstructure of steels at room temperature may range from almost completely ferritic (hypoeutectoid), to all pearlite (eutectoid) and to pearlite plus cementite

(hypereutectoid). The microstructure of most air-cooled commercial steels is a combination of ferrite and pearlite. These are the structures that exist under equilibrium conditions. However, other non-equilibrium microstructures, martensite and bainite, may result in the cases where rapid cooling is involved. These two metastable phases will be discussed in more detail separately.

With regard to the electromagnetic sensing of phase transformation, morphology of steel is very important since permeability of steel varies with the phases present, i.e. ferrite has a slightly higher permeability than pearlite at any given temperature below the Curie point. Therefore, depending on the phase balance present the strength of the recorded electromagnetic signal will vary accordingly. Texture (grain size and distribution) is also very important and has a significant effect on the electromagnetic signal as it is shown in chapters 5 and 6.

2.3.1 Ferrite formation and kinetics

Most commercial steels are hypoeutectoid, i.e. they have a carbon content of less than 0.77 wt %. In these steels on cooling, austenite begins to transform into ferrite, well above the eutectoid temperature (727°C). Upon further cooling below the eutectoid temperature, the formation of the rest of ferrite and cementite as pearlite is allowed. However, this depends on the amount of carbon present. If carbon content is very low (<0.022 wt %) then ferrite formation continues below the eutectoid temperature otherwise transformation nominally occurs at the eutectoid point.

Additionally, the extent of undercooling below the eutectoid temperature before transformation depends on the cooling rate and full composition. Any ferrite forming above the eutectoid temperature is termed proeutectoid, while ferrite found in pearlite colonies is known as eutectoid ferrite. During slow cooling, proeutectoid ferrite may start forming at temperatures as high as 912°C in pure iron and continues growing until the eutectoid temperature is reached. If the effect of any alloying elements is ignored, the exact temperature at which proeutectoid ferrite starts forming, will depend on the steel's carbon content as seen in Fe-C equilibrium diagram.

As a result of an investigation on the behaviour of plain carbon steels, four well-defined morphologies of pro-eutectoid ferrite were recognised by Dubé et al. [66], which were later extended further by Aaronson (figure 2.2)[67].

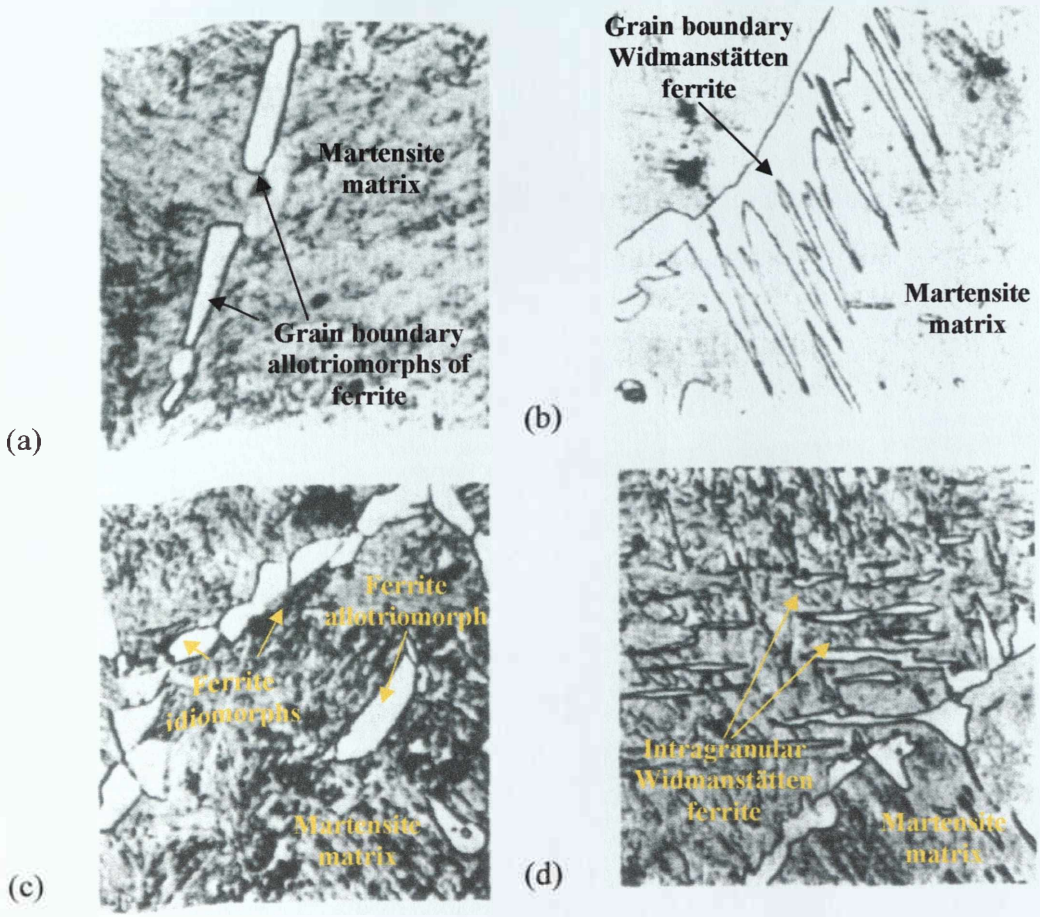

Figure 2.2: Growth of pro-eutectoid ferrite: (a) 0.34 C in wt % steel, 12 min at 790°C. Grain boundary allotriomorphs of ferrite. (b) 0.34 C in wt % steel, 15 min at 725°C. Widmanstätten ferrite growing from grain boundary ferrite. (c) 0.34 C in wt % steel, 12 min at 790°C. Grain boundary allotriomorphs and intragranular idiomorphs of ferrite. (d) 0.34 C in wt % steel, 15 min at 725°C. Intragranular Widmanstätten ferrite plates. (a)-(d) x500. (Reproduced from Honeycombe and Bhadeshia) [68]

During cooling conditions approaching equilibrium, ferrite crystals nucleate at the austenite grain boundaries and preferentially at double and triple points. Under these conditions there is ample time for diffusion but the thermodynamic driving force is relatively low and therefore relatively large nuclei form. Fully formed ferrite crystals

are usually equi-axed or lenticular in shape and are referred to as grain boundary allotriomorphs. As the temperature of transformation is lowered, these crystals develop facets on at least one side, but often on both sides of the boundary. Nucleation of allotriomorphs within an austenite grain is prohibitive because all the new parent-product interface would have to be created.

For low alloy steels, the transformation of ferrite can be suppressed to temperatures below the eutectoid temperature and as low as 600°C if the steel is undercooled or relatively higher cooling rates are used. Ferrite formation can be suppressed even further (as low as ~ 350°C) if the content of alloying elements present is high. In both cases, greater driving force is available for the formation of ferrite but the time for diffusion is limited. This leads to the formation of needle-like or plate-shaped grains that extend from the austenite grain boundaries, but grow along well defined-matrix planes. They grow either direct from the boundaries, or nucleate on pre-existing ferrite allotriomorphs. These plate-shaped crystals are referred to as Windmanstätten side plates or laths. The increased driving force apparently causes a shift to a mechanism that favours a closer crystallographic coupling between the austenite and the proeutectoid ferrite and some shear or cooperative movement of the iron atoms into the product crystal arrangement.

Ferrite crystals that nucleate within the austenitic grains in undercooled low alloy steel or at higher cooling rates are roughly equi-axed and possess either irregular curved boundaries, or boundaries with better-defined crystallographic characteristics. These crystals are referred to as intragranular idiomorphs and form due to deformation taking place during the transformation [69].

Any Widmanstätten plates or laths nucleating within the austenitic grains are called intragranular plates. Intragranular Widmanstätten ferrite is very similar to the form growing from the grain boundaries but it nucleates entirely within the austenitic grains.

The crystallographic relationship between a grain boundary allotriomorph nucleated on austenite grain boundaries and the two adjacent austenite grains is of significance in explaining the nature of growth of proeutectoid crystals. Grain boundary allotriomorphs at the highest temperatures will grow along the boundaries. However, as lower temperatures are approached they start growing into the austenite grains. The allotriomorphs nucleate having a Kurdjumov-Sachs (K-S) orientation relationship [70] with the austenite grain that they originate from.

$$\{111\}\gamma_1 \| \{110\}\alpha$$

$$<110>\gamma_1 \| <111>\alpha$$

The K-S relationship applies to Widmanstätten ferrite as well [71] although it has been shown that the habit plane of a plate is slightly scattered about the $\{111\}\gamma_1$ plane [72].

The crystallographic arrangement of the atoms between the growing grain boundary allotriomorph and the other austenite grain (γ_2) may not match as well, causing the formation of an incoherent interface allowing a high degree of diffusional mobility between the crystals. The incoherent interface responsible for this growth should migrate faster at higher temperatures and low undercooling [73]. However, there is

strong evidence that such boundaries readily develop growth facets, indicating that the growth rate of grain boundary allotriomorphs is anisotropic. The growth rate at which the allotriomorph forms is given by equation 2.1 [74]

$$a_1 = (D_C^{\gamma})^{1/2} \frac{(c^{\gamma\alpha} - \bar{c})}{[2(c^{\gamma\alpha} - c^{\alpha\gamma}) - (\bar{c} - c^{\alpha\gamma})]^{1/2}} \qquad \text{Equation 2.1}$$

where α_1 is the one-dimensional growth rate constant, D_C^{γ} is the diffusion coefficient of carbon in austenite, $c^{\gamma\alpha}$ is the molar fraction of carbon in austenite at the $\gamma/\alpha + \gamma$ phase boundary, $c^{\alpha\gamma}$ is the molar fraction of carbon in ferrite at the $\alpha/\alpha + \gamma$ phase boundary and $\bar{c}$ is the molar fraction of carbon in the steel.

If high degrees of undercooling are employed, the migration of the incoherent boundary by diffusion is restricted and the high driving force causes the ferrite with the coherent boundary in the other grain to propagate. This results in the formation of Widmanstätten plates [73]. It has been suggested that at low transformation temperatures shear displacements may be involved due to the increase in dislocation density of the ferrite with decreasing temperature. Under certain conditions, and in certain alloy compositions, both grain boundary allotriomorphs and Widmanstätten plates may form by motion of ledges parallel to coherent interfaces [68].

The growth kinetics of ferrite have been studied both along the austenite grain boundaries (lengthening) and into the austenite grains (thickening). Direct measurements of thickening kinetics of ferrite using a 0.11 wt % carbon steel alloy in

a thermionic emission microscope showed thickening to be a parabolic process [75]. This is quantified in equation 2.2.

$$S = a_1 t^{1/2} \qquad \text{Equation 2.2}$$

where S is the ferrite crystal half thickness, t is growth time and a_1 is the one-dimensional parabolic thickening rate constant. The thickening of a crystal as a function of time is graphically expressed in figure 2.3.

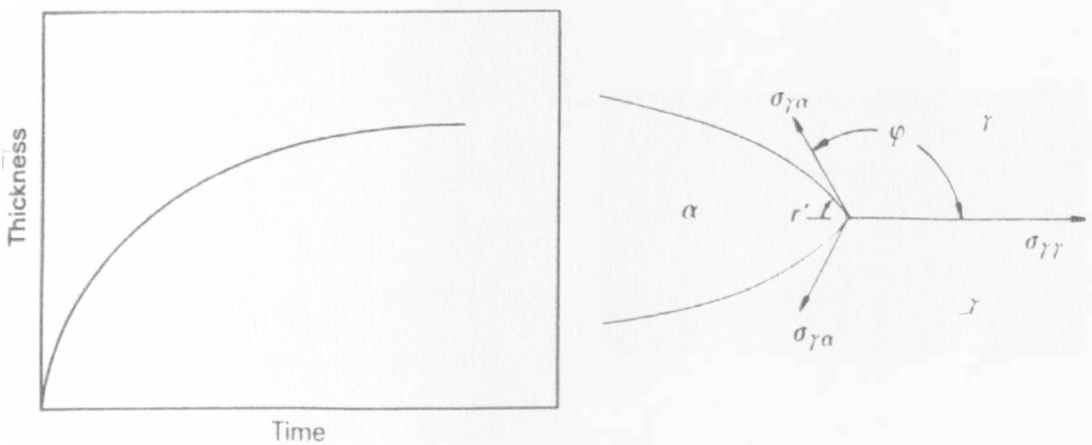

(a) (b)

Figure 2.3: (a) Plot of the parabolic thickening process described by equation 2.2. (b) Interfacial energies at the advantaging edge of a ferrite allotriomorph. (After Hillert) [76]

The parabolic increase of thickness results in a decrease of the growth rate as the crystal thickens. This can be explained by the attenuation of the driving force due to the increasing amounts of carbon being rejected into the residual austenite and hence making the diffusion of carbon more difficult.

Thickening kinetics of Widmanstätten ferrite plates using thermionic emission microscopy have shown that the process is irregular. The nature of this irregularity in the thickening of plates has been attributed to the repeated migration of steps along the coherent faces, the steps being short lengths of incoherent boundary (figure 2.4). The velocity, v, of these steps is given by equation 2.3 [77].

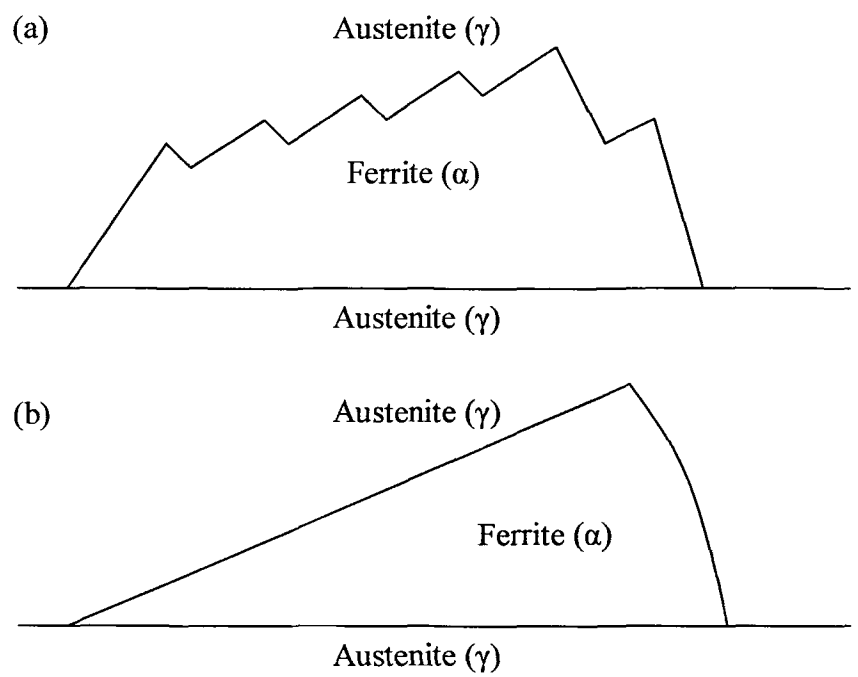

Figure 2.4: a) Schematic diagram of growth of ferrite from an austenite grain boundary by incoherent step movement. b) Schematic diagram of ferrite growth from an austenite grain boundary along a coherent face. (After Kinsman and Aaronson) [78]

$$v = \frac{D_C^{\gamma}(c^{\gamma\alpha} - \bar{c})}{\alpha\beta(\bar{c} - c^{\alpha\gamma})} \qquad \text{Equation 2.3}$$

where v is the velocity of the steps, D_C^{γ} is the diffusion coefficient of carbon in austenite, $c^{\gamma\alpha}$ is the molar fraction of carbon in austenite at the $\gamma/\alpha + \gamma$ phase boundary, $c^{\alpha\gamma}$ is the molar fraction of carbon in ferrite at the $\alpha/\alpha + \gamma$ phase boundary, $\bar{c}$ is the molar fraction of carbon in the steel, α is the step height and the constant β is a function of the velocity parameter $p = v\alpha/2\,D_C^{\gamma}$ [68].

The calculated velocities have been found to agree well with the velocities experimentally measured and hence it has been concluded that the rate of growth is governed by carbon diffusion in austenite.

The growth of a plate with curved ends has been theoretically investigated by assuming that the rate is controlled by the diffusion of carbon in austenite [76, 79]. The shape of the plate ensures that carbon rejected by the growing ferrite is distributed to the sides of the plates. Therefore, the carbon concentration profile ahead of the plate tip remains constant during the lengthening process. Consequently, the lengthening rate of the crystal will remain constant throughout the whole process, as shown from equation 2.4 [79].

$$G_L = D_C^{\gamma} \frac{(c^{\gamma\alpha} - \bar{c})}{4r'(\bar{c} - c^{\alpha\gamma})\sin\Phi} \qquad \text{Equation 2.4}$$

where G_L is the lengthening rate, r' is the radius of curvature of the allotriomorph adjacent to the grain junction and Φ is the equilibrium growth angle determined by the relative energies of the interphase and grain boundaries. Figure 2.5 shows the variation in the plate lengthening rate as a function of its tip radius [68].

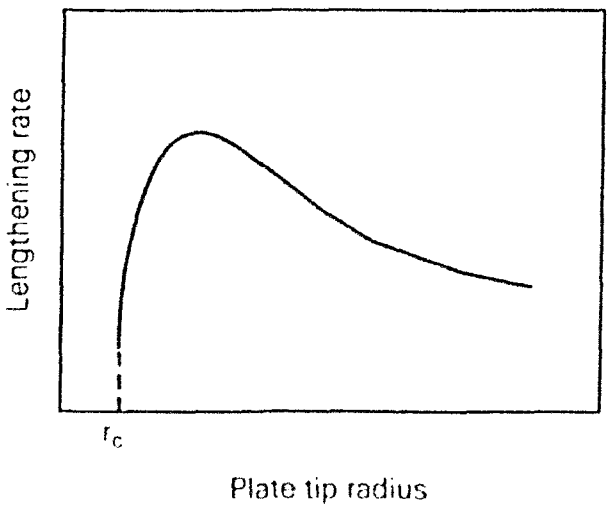

Figure 2.5: Variation in the plate lengthening rate as a function of its tip radius. r_c is the critical radius at which the lengthening rate becomes zero. (Reproduced from Honeycombe and Bhadeshia) [68]

Equation 2.3 can be applied to Widmanstätten ferrite by replacing the radius of curvature of the allotriomorph with the radius of curvature of the edge of the plate. For Widmanstätten ferrite, the lengthening rate reaches a maximum as the radius of curvature increases. Zener first introduced the theory that the plate assumes a radius consistent with the maximum growth rate [79].

The growth of proeutectoid ferrite has been experimentally determined in binary iron-carbon alloys by systematic measurement of both lengthening and thickening kinetics of grain boundary allotriomorphs at several temperatures [80]. Numerous experimental and theoretical studies have been concerned with the influence of alloying elements, such as Mn, V, Ni and others, on the velocity of the austenite-ferrite interface [81-92]. The interface mobility under various conditions, has also been modelled in order to reproduce the main characteristics of the austenite-ferrite transformation [93-95].

Finally, the effects of deformation and the application of stress on the austenite-ferrite transformation has been studied in numerous cases [96-99]. The significance of the aforementioned studies is paramount in understanding austenite decomposition and kinetics under various conditions.

2.3.2 Pearlite formation and kinetics

As mentioned earlier, pearlite consists of alternate lamellae of ferrite and cementite. The spacing of the lamellae in pearlite decreases as the degree of undercooling below the eutectoid temperature increases [100].

Pearlite is preferentially nucleated at austenite grain boundaries, but when these are already the sites for prior formation of proeutectoid ferrite or cementite (in hypereutectoid steels), the pearlite nodules grow from the interfaces of these two phases with austenite [100]. Growth of pearlite is shown in figure 2.6.

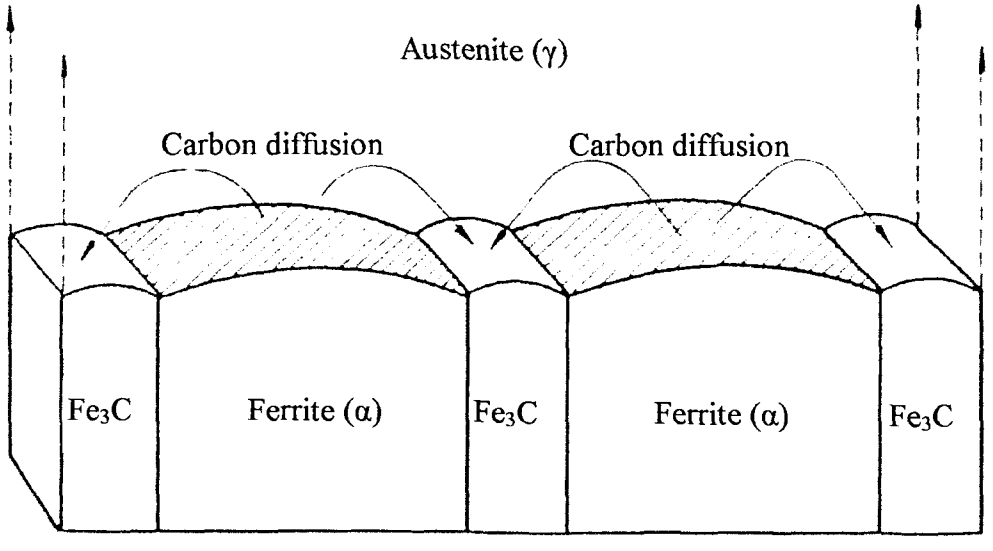

Figure 2.6: Schematic representation of pearlite. (After Hillert) [101]

It has been shown that the two main ferrite-cementite orientation relationships in pearlite depend on whether the crystal nucleates at an austenite grain boundary (Pitsch / Petch relationship) or on a proeutectoid phase (Bagaryatski relationship) [102].

Pitsch / Petch relationship

$(001)_c // (\bar{5}2\bar{1})_\alpha$

$(010)_c$ 2-3o from $[1\bar{1}\bar{3}]_\alpha$

$(100)_c$ 2-3o from $[131]_\alpha$

Bagarayatski relationship

$(100)_c // (0\bar{1}1)_\alpha$

$(010)_c // (1\bar{1}\bar{1})_\alpha$

$(001)_c // (211)_\alpha$

Alloying elements and particularly those that are strong carbide formers (i.e. Nb, V, Cr etc.) strongly influence the pearlite reaction [78, 103-105]. Although, cementite can take alloying elements into solid solution [106], it can also be entirely replaced by an alloy carbide as the alloy content is increased [107-109].

The growth of pearlite has been attributed to an incoherent high energy interface moving through an austenitic grain with which the pearlitic ferrite and cementite have no orientation relationship [73]. It has been experimentally demonstrated that the nodules which nucleate on grain boundaries of proeutectoid ferrite will grow into the

adjacent austenite due to the existence of an interface with higher energy as shown in figure 2.7 [100].

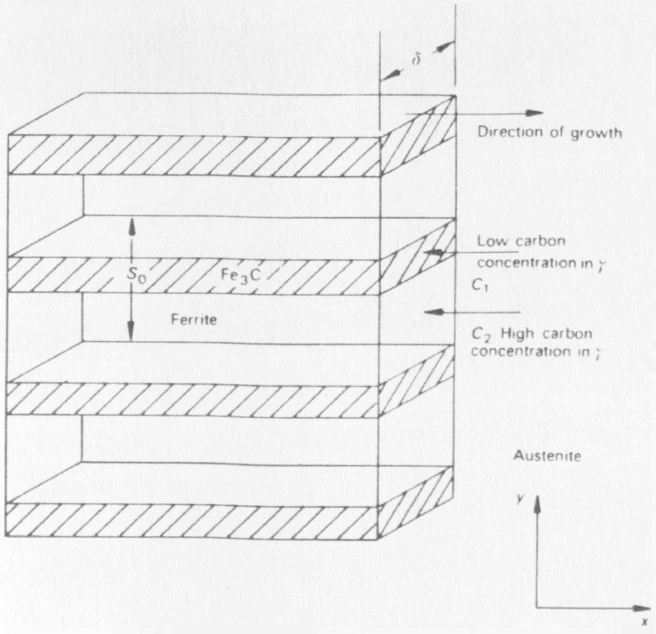

Figure 2.7: Pearlite growth model. (Reproduced from Honeycombe and Bhadeshia) [68]

Following the assumptions that pearlite colonies are spherical and randomly nucleated as a function of time, while the rate of nucleation and growth remain constant with time, the isothermal formation of pearlite is described mathematically by equation 2.5 [110]

$$f(t) = 1 - e^{-(\pi/3)NG^3t^4} \qquad \text{Equation 2.5}$$

where $f(t)$ is the volume fraction of pearlite formed at any time t at a given temperature, N is the nucleation rate of the colonies and G is the rate at which the colonies grow into the austenite.

This relationship gives a sigmoidal type of curve, when $f(t)$ is plotted. To elaborate, the initial transformation rate is quite low and is associated with what is referred to as an incubation period, the time when the first stable nuclei develop. As more and more nuclei develop and are in various stages of growth, the rate of transformation increases. Finally, the colonies impinge and the rate of transformation again slows as the microstructure gradually approaches complete transformation. However, in practice, the pearlitic reaction does not conform to the simple nucleation and growth model referred to above [111].

A new theoretical approach was therefore developed, which fully took into account the inhomogeneous nature of nucleation in the pearlite reaction. It was pointed out that not all grain boundary nucleation are equivalent. For example, grain corners are more effective sites for nucleation than edges, and edges better than grain surfaces. Assuming that in a normal situation, a high rate nucleation occurs at these special sites then consequently site-saturation occurs at an early stage of the reaction. Under these conditions the reaction is controlled by the radial growth velocity which has also been assumed to be constant in the Johnson-Mehl theory. This leads to the following modification of equation 2.5:

$$f(t) = 1 - e^{-(4/3)\pi\eta G^3 t^3} \qquad \text{Equation 2.6}$$

where η is the number of grain corners per unit volume. In practice, site saturation sets in before 20% of the transformation has been completed. Hence, the actual nucleation rate is unimportant and does not come into the equation [112].

The time, t_f, for the completion of the pearlitic reaction is simply defined as (equation 2.7):

$$t_f = 0.5d/G \qquad \text{Equation 2.7}$$

where d is the austenite grain diameter and d/G is the time taken for one nodule to absorb one grain.

Although experimental studies have found that the growth rates of pearlite are too large to be explained by a volume diffusion mechanism [112-115], it is strongly believed that the transformation proceeds mainly by diffusion along the advancing interface [116]. However, it is still not possible to predict absolute rates of transformation of pearlite.

2.3.3 Austenite formation and kinetics

In pure iron, on heating ferrite undergoes a polymorphic transformation to FCC austenite at 912°C. However, in hypoeutectoid steels the transformation temperature of ferrite to austenite transformation temperature is lower than in pure iron depending on the composition of the steel and heating rate.

Austenite grain size affects the transformation and deformation behaviour of heat treated steels. This is because austenitic grain boundaries are favourable sites for the nucleation of proeutectoid ferrite and pearlite. In the cases where austenite grains are coarse, the number of available nucleation sites is smaller and therefore transformation is retarded. Consequently, the size of ferrite and pearlite grains will

decrease with finer austenite grains causing an increase in the strength and impact toughness of steels. The mechanisms of these effects are not fully understood although it is believed that there is a relation with the segregation of impurity atoms to austenite grain boundaries during austenitising [117]. Austenite grain size also influences the starting temperature of transformation to martensite (M_s), with smaller austenite grains significantly lowering the M_s temperature. This effect is mainly attributed to the higher strength of fine-grained austenite which in turn increases the shear resistance of the austenite-martensite transformation [118].

Austenite grain size, depending on the alloying elements present, may be increased by increasing the austenitisation temperature. However, fine-grained steel alloys will show little grain growth unless a relatively high austenitising temperature (>1000°C) is employed [65]. In this case, once coarsening is initiated, it progresses very rapidly. Figure 2.8 displays a diagram of austenite grain size as a function of austenitising temperature for coarse and fine-grained steels [119].

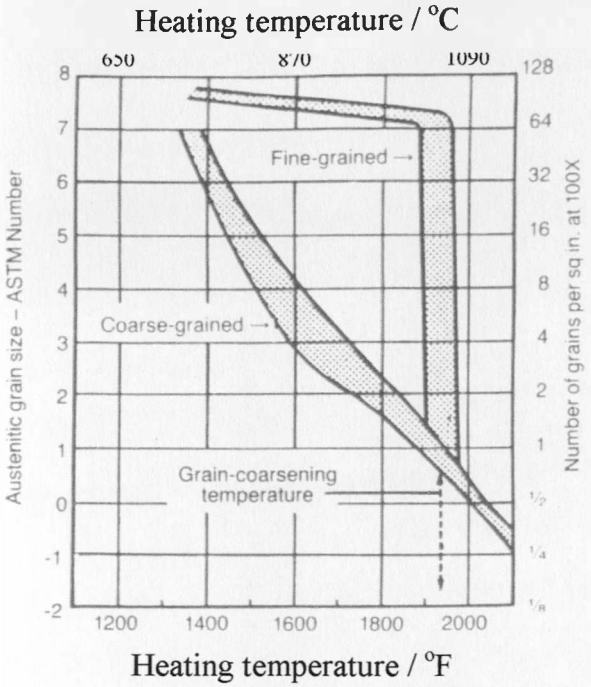

Figure 2.8: Diagram of austenite grain size as a function of austenitising temperature for coarse and fine-grained steels. (Reproduced from Melloy) [119]

The austenitisation behaviour of fine-grained steels is explained by the existence of fine particles such as microalloy (e.g. Al, Nb, V and or Ti) carbo-nitrides, distributed throughout the microstructure which pin the austenite grain boundaries and thus inhibit further growth. However, at higher temperatures this restraint mechanism is removed as particles dissolve allowing the austenite grain boundaries to become mobile. The superior mechanical properties of High Strength Low-Alloy (HSLA) steels is based on this pinning mechanism of austenite grain boundaries by fine particles [120-122].

The nature of austenite formation in steel relies heavily on the microstructure present prior to austenitisation. Austenite formation requires an incubation period before the

first nuclei are formed. After initial nucleation has taken place, the transformation accelerates as more nuclei develop and grow. The time dependence of the process is attributed to the carbon diffusion mechanism and the time required for the carbon atoms to be rejected from low-solubility ferrite to austenite. At higher temperatures the diffusion rate is higher and hence austenite forms more rapidly.

In a predominantly ferritic microstructure austenite will primarily nucleate at grain boundary faces and edges, whilst in pearlite, it will primarily nucleate at intersections of pearlite colonies but also at the interfaces of ferrite and cementite lamellae within a colony. In the case where the original microstructure is martensitic two different morphologies of austenite crystals are produced in carbon steels. The first austenite morphology is equiaxed and tends to form at prior austenite grain boundaries. Austenite formation in this case, is governed by the dissolution of fine carbide particles [123-124]. The other is acicular and forms by nucleation between the laths of martensite. This morphology is usually associated with a high nickel content in a carbon steel and accredited to a shear process [125].

2.4 Effects of alloying elements

Additions of other alloying elements in carbon steels gives rise to dramatic changes in the binary iron-carbon phase diagram and their mechanical properties. This is due to the ability of alloying elements to promote the formation of a certain phase or to stabilise it. The extent of the effect of an alloying element on the thermomechanical behaviour of steel is dependent on its concentration and the nature of the compounds it forms within the microstructure.

Alloying elements can be grouped as carbide-forming, ferrite-forming, austenite-forming and nitride-forming. Cr, W, Mo, V, Ti, Nb, Ta and Zr are primarily carbide formers. Some of the most common carbides formed by these alloys are Cr_7C_3, VC, Mo_2C and W_2C. Some carbide formers also promote ferrite formation. Cr, Si, Mo, W and Al are probably the most important ferrite-formers. Cr and Si are particularly good ferrite stabilizers, i.e. Fe-Cr alloys containing more than 13 in wt % Cr remain ferritic at all temperatures up to incipient melting. All carbide formers are also good nitride formers.

C, Ni and Mn are the most important austenite-forming elements. Sufficiently large amounts of Ni or Mn can render a steel austenitic even at room temperature. In a Hadfield steel, which contains 13% Mn, 1.2% Cr and 1% C (in weight), austenite remains stable at room temperature. In this case both Mn and C stabilize the austenite. For Ni-based steels the range of stability of austenite increases with increasing Ni content. A steel containing 10% Ni will become wholly austenitic at 700°C during heating, whilst upon cooling transformation from austenite to ferrite takes place at a temperature range between 700°-300°C [68, 111].

As a general rule, all alloying elements in solid solution within the microstructure affect the steel's hardness. Si and Mn have a particular effect on the hardness of steel while Cr gives the smallest hardness increase. In addition the formation of precipitates (e.g. carbides or nitrides) also affects hardness with a uniform distribution of fine precipitates giving greater strengthening than an equal volume fraction of coarse precipitates. The effect of Al, Nb, Ti and V on grain growth of steel is discussed further in section 2.9.

The eutectoid temperature of steel is lowered by the austenite-formers and raised by the ferrite-formers. For example a chromium based steel alloy will require a higher austenitising temperature than a nickel-based one. The dependence of eutectoid temperature on alloy concentration is shown in figure 2.9.

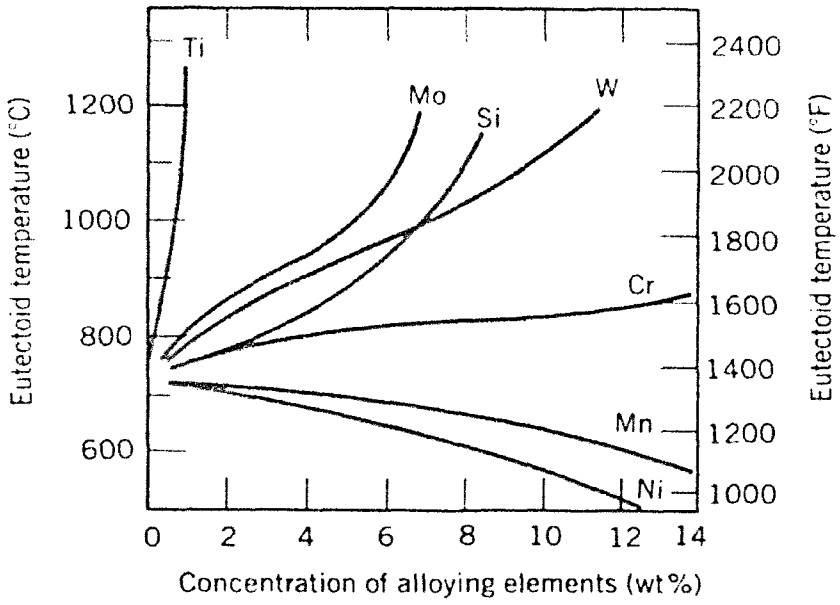

Figure 2.9: Effect of alloy concentration for several alloying elements in steel on the eutectoid temperature. (Reproduced from Bain) [126]

Additionally, all alloying elements, with the exception of cobalt lower the starting temperature of martensite formation (M_S) as well as the finish temperature (M_F). For most steels with carbon content above 0.5% in weight, M_F lies below the room temperature. Therefore, some austenite is retained at room temperature.

All alloying elements, with the exception of cobalt, delay the formation of ferrite and cementite during isothermal transformation. Some elements also delay the bainite reaction. However, certain elements will lead to acceleration of the transformations if

their concentrations exceed a certain limiting value. The most characteristic element of this case is Si.

In general, all alloying elements, with a small number of exceptions, enhance the ability of steel to withstand loss of hardness on tempering after hardening. This is due to their ability to decrease the rate of diffusional transformations of austenite and thus to increase hardenability [127]. However, there is no simple relationship between resistance to tempering and alloy content due to the large number of factors that affect the whole mechanism.

Kinsman and Aaronson showed that Si, Al and Co accelerate the kinetics of the austenite-ferrite transformation at least at the higher transformation temperatures. Si and Al appear to increase both the rates of nucleation and growth of ferrite, while Co only increases the rate of nucleation [78]. It has also been shown that these effects on the austenite-ferrite reaction are reflected in an increase in strength of the ferrite. This is assumed to be partly from increased dispersion hardening and partly from additional solution hardening [128].

2.5 Isothermal Transformation

Sometimes it is desired to determine the structure that corresponds to the transformation of austenite at a given temperature. It was shown earlier that transformation to ferrite and pearlite is based on a diffusion mechanism. However, diffusion in steel is temperature dependent and hence its rate will decrease with higher

degrees of undercooling. If undercooling is increased significantly martensite or bainite (based on diffusionless transformation) will result.

In order to investigate the resulting structure at a temperature of interest, a sample that has been austenitised is plunged into a molten lead or salt bath, and held at the required temperature. The austenitising treatment sets the austenite grain size and the extent of carbide dissolution. Both microstructural factors may influence the course of isothermal transformation of austenite and therefore it is necessary to record the austenitinising temperature employed.

After holding the sample at the temperature of interest for the required time, the specimen is quenched in order to transform to martensite any retained austenite. The specimen is then taken for metallographic examination to determine the phases, and their volume fraction, that have formed. Until the time at which the transformation starts at the temperature of interest, the quenched sample is completely martensitic. As holding time increases, part of the austenite transforms. If the sample is held even longer, austenite completely transforms to ferrite, pearlite, cementite and or bainite, and after quenching no martensite is observed. In cases where there are high degrees of undercooling then the sample transforms directly into martensite.

From these tests, Isothermal Transformation (IT) or Time-Temperature-Transformation (TTT) diagrams are produced. Time in this type of diagrams is plotted logarithmically. The different kinds of structure produced by transformation are indicated on the diagram, together with the holding times required for transformation to start and finish at each temperature. The result is a family of curves

representing the various stages of transformation as a function of temperature and time. Figure 2.10 shows a TTT diagram for steel of eutectoid composition (0.77 % in weight C).

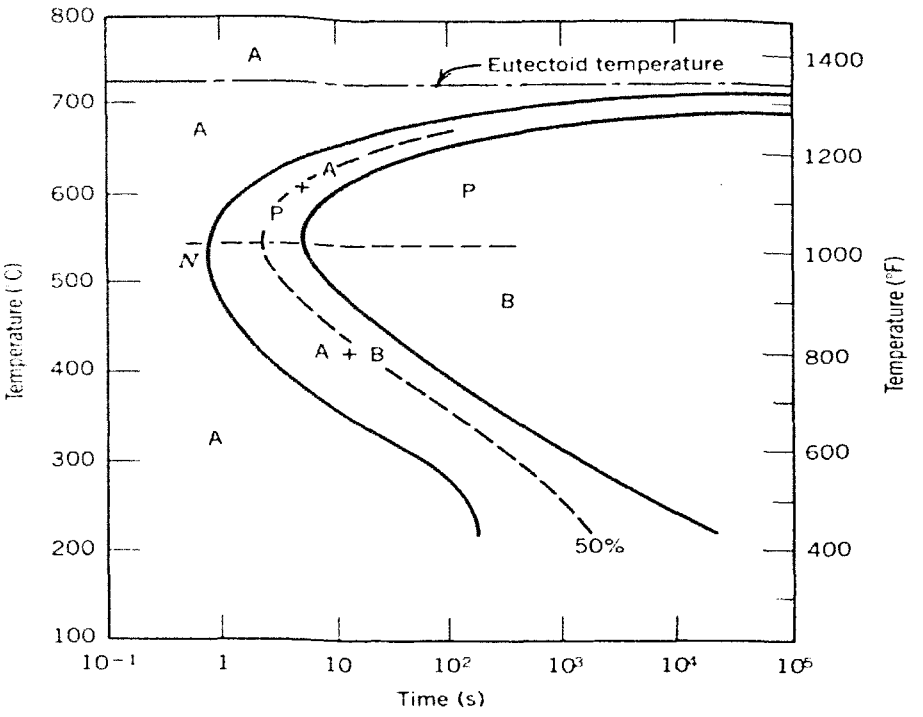

Figure 2.10: Isothermal transformation diagram for a steel alloy of eutectoid composition (0.77 % in wt C): A: Austenite; B: Bainite; M: Martensite; P: Pearlite. (Reproduced from Callister) [27]

2.6 Continuous Cooling Transformation

Few heat treatment processes involve isothermal transformation. In most cases, transformation is achieved by continuous cooling operations. For extremely slow cooling rates it is possible to relate the resulting phases to the upper regions of the

isothermal diagram. However, if faster cooling rates are used the starting temperature and progress of the transformation will be shifted considerably.

During continuous cooling, the time required for a reaction to begin and end is delayed. Thus the isothermal curves are shifted to longer times and lower temperatures. In order to determine the phases formed at various cooling rates a Jominy specimen can be used. This specimen is water quenched only at one end, and therefore the cooling rate is at maximum at that end and drops with increasing distance into the specimen. The cooling rates at various locations in the Jominy specimen are measured by attached thermocouples. With decreasing cooling rate or increasing distance from the quenched end of the Jominy specimen, the austenite transforms to microstructures containing increasingly greater quantities of ferrite and pearlite. The recorded temperature data and metallographic examination of the Jominy specimen are cross-referenced to produce the Continuous Cooling Transformation (CCT) diagrams.

A major difficulty in constructing CCT diagrams is the interpretation of transformation behaviour. Martensite and bainite are each affected by changes in composition of the parent austenite which may have resulted from any prior ferrite formation or carbide precipitation at higher temperatures. Undercooling and recalescence due to sudden liberation of latent heat can, in some cases, result in a reaction being completed at a temperature higher than that at which it began. The effects of such complicated behaviour are however included in the computation of these diagrams. A CCT diagram for a steel of eutectoid composition is presented in figure 2.11.

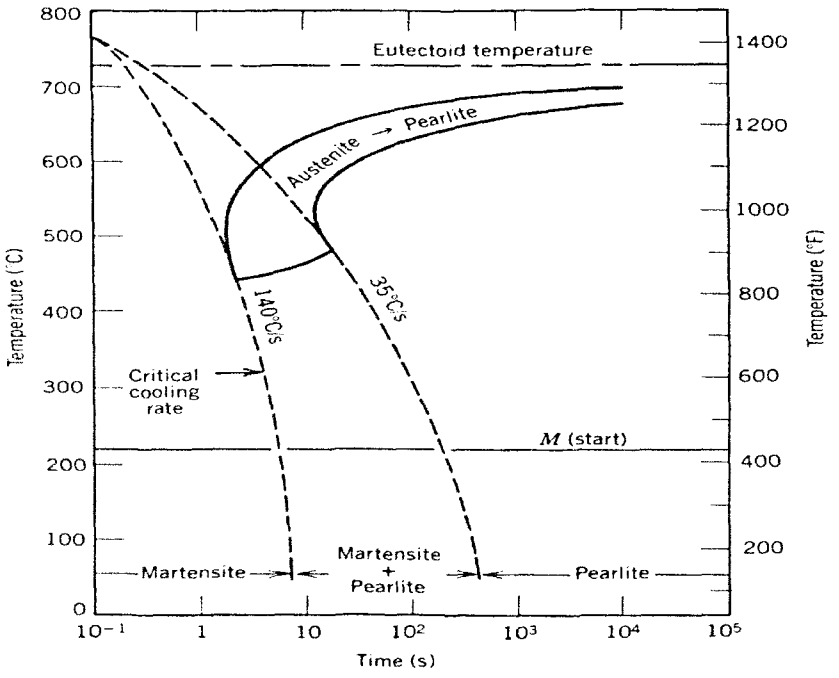

Figure 2.11: Continuous cooling transformation diagram for a eutectoid (0.77 % in wt C) steel and superimposed cooling curves demonstrating the dependence of the final microstructure on the transformations that occur during cooling. (Reproduced from Callister) [27]

In CCT diagrams it is possible to identify the approximate proportions of the major phases and also the hardness of the microstructure obtained by continuous cooling. The effect of tempering on these hardness levels is shown in many instances. The diagrams can be used to investigate continuous heat treatment cycles for thin sections, where particular microstructures are required to facilitate working or heat treatment.

CCT diagrams are suitable for the planning of appropriate heat treatment cycles for sections which need retarded cooling after hot working, to avoid low temperature transformation products. Additionally, prediction of machinability from expected microstructures and hardness levels is possible. Finally, CCT diagrams can be used to

determine the effect of mass and to help in the calculation of critical quenching rates for complicated shapes and varied sections, where an estimate of a predominant equivalent diameter is possible.

2.7 Quenching

In some cases during cooling of steel, it is desirable to obtain a harder microstructure than ferrite and pearlite. In order to achieve higher hardnesses, steel is commonly quenched into oil or water. The cooling rate achieved on a certain specimen depends on the rate of heat energy extraction, which is a function of the characteristics of the quenching medium in contact with the specimen surface, as well as the specimen size and geometry. Above certain cooling rates, a diffusionless, shear-type transformation takes place that results in martensitic microstructures. Under certain conditions bainite may form instead or co-coexist with martensite. The exact cooling conditions that will result in martensite in a certain steel are strongly dependent on carbon content, alloying and austenitic grain size.

If an austenitised sample is quenched at an adequate cooling rate, austenite remains stable until the martensite start temperature or M_S point is reached. At M_S austenite starts transforming into martensite, a hard and brittle microstructure. Upon further cooling down to the martensite finish temperature or M_F, the resulting microstructure is 100% martensitic. In the case where the cooling rate is lowered, or a certain temperature is held before M_F is reached, any retained austenite not transformed to martensite, either transforms to lower bainite or can decompose to carbides and ferrite or can be retained as austenite. Similarly, when an austenitic sample is undercooled at

a temperature above the M_S and is held there for enough time the resulting microstructure is bainite. Depending of the degree of undercooling, the resulting bainite is classified either as upper bainite for smaller degrees, or lower bainite for larger degrees of undercooling.

2.7.1 Martensite formation and kinetics

Martensite is the hardest and strongest phase found in a steel alloy and results after quenching of austenite. It has negligible ductility and its hardness is dependent on the carbon content. The maximum solubility of carbon in martensite is 0.6 % in weight. Austenite is slightly denser than martensite, and therefore, during phase transformation upon quenching, there is a net volume increase. Consequently, relatively large pieces that are rapidly quenched may crack as a result of internal stresses. Figure 2.12 shows an optical micrograph of a predominantly martensitic microstructure in a quenched medium carbon steel.

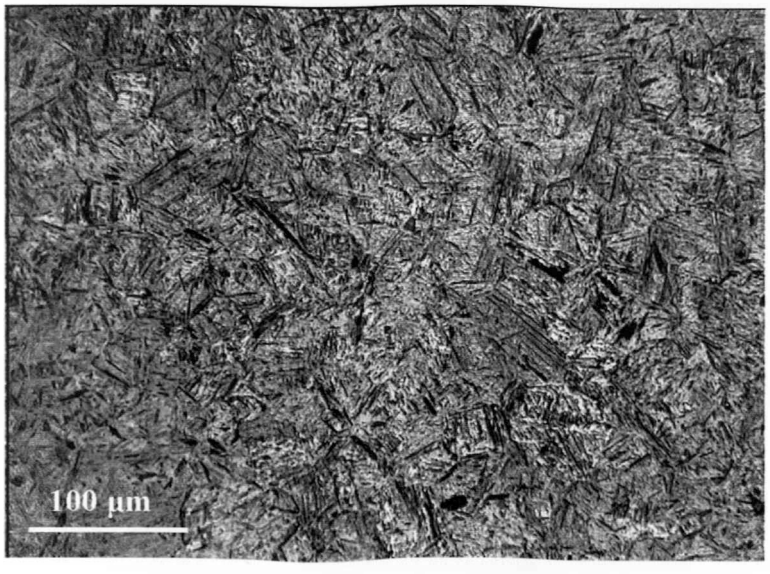

Figure 2.12: Optical micrograph of a martensitic microstructure in a medium carbon (0.4 wt %) steel.

As discussed earlier, fast cooling allows little time for any diffusion of carbon to occur. Therefore, since diffusion is suppressed, any carbon atoms are trapped in the octahedral sites of the BCC structure. Due to the higher solubility of carbon in austenite, martensite is supersaturated with carbon and therefore can no longer retain a BCC unit-cell and assumes a body-centred tetragonal (BCT) structure. The degree of tetragonality of martensite is dependent on the carbon content in a given steel.

Austenite to martensite start transformation temperature in a given steel alloy is designated as the M_S. The M_S reflects the amount of thermodynamic driving force required to initiate the shear transformation of austenite to martensite and is insensitive to cooling rates up to 50,000°C/s [129-131] and may vary from 500°C to well below room temperature, depending on the concentration of γ stabilisers. The M_S decreases significantly with increasing carbon content. Carbon in solid solution increases the strength or shear resistance of the austenite and, therefore, greater undercooling or driving force is required to initiate the shear for martensite formation in higher carbon alloys. The M_S can be calculated from the alloy composition and there are a number of formulas (equations 2.8 – 2.15) that have been proposed so far as shown below:

- Payson and Savage [132]:

$$M_S(°F) = 930 - 570C - 60Mn - 50Cr - 30Ni - 20Mo - 20W \quad \text{Equation 2.8}$$

- Carapella [133]:

$$M_S(°F) = 925 \times (1 - 0.620C)(1 - 0.092Mn)(1 - 0.029Mo)(1 - 0.045Ni)(1 - 0.070Cr)(1 - 0.029Mo)(1 - 0.018W)(1 + 0.120Co) \quad \text{Equation 2.9}$$

- Rowland and Lyle [134]:

$$M_S(°F) = 930 - 600C - 60Mn - 50Cr - 30Ni - 20Mo - 20W \quad \text{Equation 2.10}$$

- Grange and Stewart [135]:

$$M_S(^\circ F) = 1000 - 650C - 70Mn - 70Cr - 35Ni \quad \text{Equation 2.11}$$

- Nehrenberg [136]:

$$M_S(^\circ F) = 930 - 540C - 60Mn - 40Cr - 30N - 20Si - 20Mo \quad \text{Equation 2.12}$$

- Steven and Haynes [137]:

$$M_S(^\circ C) = 561 - 474C - 33Mn - 17Cr - 17Ni \quad \text{Equation 2.13}$$

- Andrews (linear) [138]:

$$M_S(^\circ C) = 539 - 423C - 30.4Mn - 12.1Cr - 7.5Mo \quad \text{Equation 2.14}$$

- Andrews (product) [138]:

$$M_S(^\circ C) = 512 - 453C - 16.9Ni + 15Cr - 9.5 + 217(C)^2 - 71.5(C)(Mn) - 67(C)(Ni) \quad \text{Equation 2.15}$$

All alloying elements, with the exception of Co, lower the M_S temperature. The equations developed by Andrews are based on measurements of M_S temperatures and compositions of a large number of steels of British, German, French and American manufacture with maximum carbon content 0.6 % in weight. Andrews showed that 92 and 95 % of measured M_S temperatures for the steels were within ±25°C of the M_S temperatures calculated from their compositions according to the linear and product equations, respectively. A test of Andrews' equations with M_S measurements and steel compositions published in the 1970s showed that Andrews' equations continue to give good agreement between measured and calculated M_S values within ±25°C [139]. A more recent evaluation of the M_S temperature equations recommends only slight changes in the Stevens and Haynes and Andrews linear equations, and incorporates the effects of cobalt and silicon [140].

Once the M_S of a steel is known, the extent of the athermal transformation of austenite to martensite is dependent only on the amount of undercooling below the M_S temperature. Equations 2.16 and 2.17 have been developed to describe the athermal transformation kinetics of martensite formation:

$$f = 1 - 6.96 \times 10^{-15}(455 - \Delta T)^{5.32} \qquad \text{Equation 2.16}$$

$$f = 1 - \exp - (1.10 \times 10^{-2}\Delta T) \qquad \text{Equation 2.17}$$

where f is the volume fraction of martensite and ΔT is the undercooling below M_S in degrees Centigrade. Equation 2.16 was developed by Harris and Cohen [141] for steels containing 1.1 % in weight carbon and equation 2.17 was developed by Koistinen and Marburger [142] for Fe-C alloys containing between 0.37 and 1.1 % in weight carbon.

Further transformation of austenite to martensite takes place until the M_F which is also a function of carbon content. At that point all austenite should have transformed into martensite, although in practice a small proportion of austenite is retained as the M_F drops below room temperature in alloys containing more than 0.3 % in weight carbon as shown in figure 2.13. Thus, each temperature between M_S and M_F corresponds to a definite proportion of martensite, but the amount actually formed depends on the grade of steel. No further martensite forms during isothermal holding at temperatures between M_S and M_F and bainite may be produced instead [129, 143].

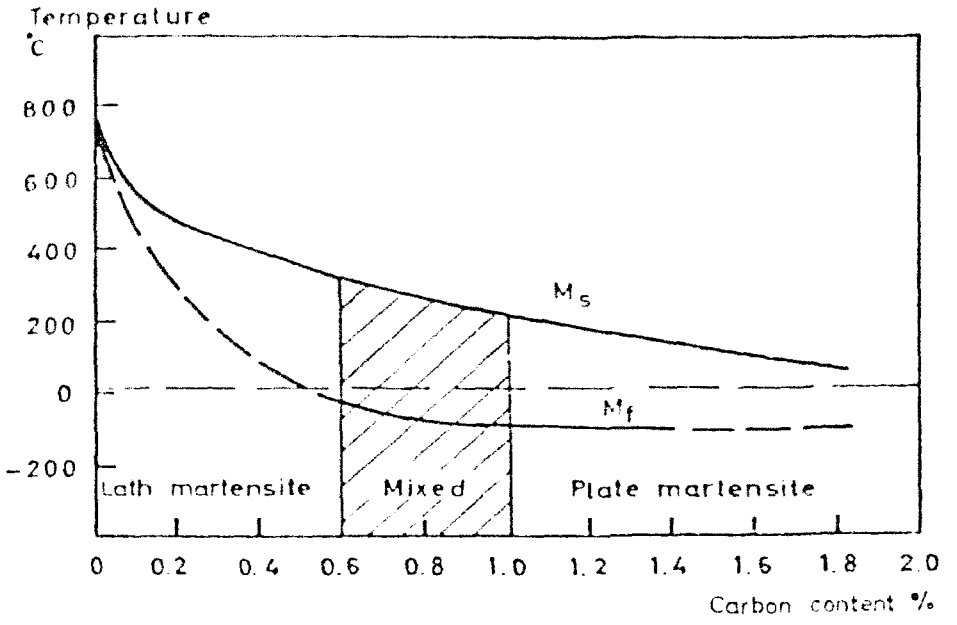

Figure 2.13: Diagram showing the effect of carbon content on M_S and M_F.

(Reproduced from Marder and Krauss) [144]

During austenite-martensite transformation, each austenite grain transforms by the sudden formation of thin plates or laths of martensite. The habit plane of martensite is not constant but changes as the overall carbon content in the steel is increased. In general for steels with overall carbon content 0.22-0.5 in wt % the plane is usually $\{111\}_\gamma$ (low carbon martensite), while for 0.5 to 1.4 in wt % C the usual plane observed is $\{225\}_\gamma$ (medium carbon martensite). The habit plane of martensite in steels containing higher amounts of carbon is $\{259\}_\gamma$. For the steel alloys with low carbon content the orientation relationship of the martensitic lattice with austenite is the one shown earlier to occur between austenite and ferrite. This orientation persists even when the habit plane changes to $\{225\}_\gamma$. Low carbon martensite has lath- or plate-like morphology, while medium and high carbon martensites are characterized by lenticular plates.

It has been suggested that the nucleation of martensite must take place heterogeneously on pre-existing embryos. The embryos are postulated to have a semicoherent dislocation interface with the austenite, envisaged as arrays of parallel dislocation loops. Growth then takes place by nucleation of new dislocations loops which join the interface and extend it [111]. Another theory of nucleation suggests that the first step is faulting on the closest packed planes derived from existing groups of dislocations. The most likely sites for such nuclei are grain boundaries, incoherent twin boundaries and inclusion particle interfaces [145]. The growth velocity of martensite plates has been found to be constant over a wide temperature range, an indication that the growth process is not strongly thermally activated. The growth is attributed to the movement of an array of parallel dislocations lying in the interface, all having the same Burgers vector.

A number of studies have shown that external applied stress, such as uniaxial tension, compression and hydrostatic pressure, affects martensitic transformation, i.e. M_S can be either raised or lowered [146-150].

2.7.2 Bainite formation and kinetics

Similar to pearlite, bainite is a mixture of ferrite and cementite. However, unlike the orderly structure of pearlite colonies, carbides in bainite are present either within laths that resemble the laths observed in martensite or on the lath boundaries. Therefore, the mechanism of formation of bainite involves shear as well as diffusion. Due to the nature of the bainitic reaction, bainite formation is accompanied by negligible internal stresses.

Bainite formation may take place over a range of temperatures starting at the bainite start temperature (B_S) and ending at the bainite finish temperature (B_F). These temperatures are given approximately by the following equations 2.18 and 2.19, where the symbols in brackets refer to weight percentages [151].

$$B_S(^{\circ}C) = 830 - 270[C] - 90[Mn] - 37[Ni] - 70[Cr] - 83[Mo] \quad \text{Equation 2.18}$$

and $$B_F(^{\circ}C) = B_S - 120[C] \quad \text{Equation 2.19}$$

Bainite can form under the following conditions:

a) Isothermally if undercooled at temperatures between pearlite formation and M_S or between M_S and M_F after the martensite transformation is complete.

b) By continuous cooling if appropriate cooling rates are employed so as neither pearlite nor martensite formation is possible.

Depending on the temperature of formation, bainite is distinguished into upper or lower bainite. Upper bainite forms at temperatures closer to pearlite formation whilst lower bainite forms at temperature ranges closer to M_S. Upper bainite is characterized by long ferrite laths free from internal carbide precipitation. Upper bainitic ferrite has a carbon concentration of less than 0.03% in weight. This means that large amounts of carbon are rejected to austenite. The transformation of bainite occurs by a displacive reaction accompanied by diffusion. Consequently precipitation does not occur in ferrite but in the austenite at the lath boundaries when a critical carbon concentration is reached. The morphology of the cementite formed at the lath boundaries is dependent on the carbon content of the steel. In low carbon steels, the

carbide will be present as discontinuous stringers and isolated particles along the lath boundaries, while in higher carbon steels the stringers may become continuous. Upper bainite nucleates from austenite grain boundaries and grows by movement of small ledges [152]. However, the shear involved cause a loss of coherency at the transformation interface and brings the growth process to a halt. Therefore, a large amount of nucleation occurs intragranulary, by secondary plates forming at the boundaries of primary plates away from the austenite grain boundaries [153].

Lower bainite is more acicular than upper bainite and is composed of ferrite plates that more resemble martensite plates. Cuckon first suggested a number of ways that may be used to differentiate lower bainite from martensite [154]. Carbides in lower bainite are in the form of very fine stringers, not resolved in the optical microscope, occurring within the plates. In some lower bainites the fine carbides have been identified as a transition carbide, called ε carbide, that forms prior to cementite at lower temperatures. ε carbide is especially stable in steel alloys containing aluminium and silicon. Normally, lower bainite forms from austenite grain boundaries although more shear is involved in the early stages of the reaction, prior to the growth of the plate by movement of small ledges. If lower bainite forms isothermally below M_S, then nucleation occurs at the martensite plate boundaries, which provide the necessary high energy interface that allow diffusion of carbon.

According to Enomoto, from the growth kinetics, incomplete transformation and the arrangement of carbides observed within bainitic plates, carbon atoms are likely to be partitioned at ferrite/austenite boundaries rather than by post-transformation redistribution. The diffusion of alloying elements within and near the boundaries

probably has a large influence on the transformation behaviour. Especially, whether or not solute drag operates may be an important clue for understanding the atomistic process in the substitutional lattice during the growth of bainite [155].

However, the complete mechanism of bainite reaction is not yet fullyunderstood and has been the issue of a large number of studies [152, 156-160]. According to Bhadeshia there are a large number of issues that are yet to be resolved [159]. The most important of these are:

a) The measured growth rate of individual plates of bainite is far greater than expected from the theory of diffusion-controlled growth [161-162]. It is clear that bainitic ferrite forms with a large supersaturation of carbon, but the possibility of some interstitial diffusion during growth cannot entirely be ruled out.
b) There are many features of transformation of plastically deformed austenite to bainite that are not fully understood.

Nevertheless, the theory of the bainitic reaction is at a sufficiently advanced stage to allow its use in the design of novel steels.

2.8 Heat Treatment of Steels

Normally, cold or hot-rolled steels do not have the desirable mechanical properties for use in engineering applications. For instance, carbon distribution throughout the steel may be inhomogeneous, hence resulting in anisotropy of the mechanical properties. In the case where martensite is the final microstructure residual stresses are usually

present potentially lowering the toughness and tensile strength. Furthermore, the average grain size of the steel may not be the required one or for low carbon steels, the hardness may be too low. Finally, the resultant microstructure may not be the desired one. Therefore, it is common to heat treat rolled products further, in order to obtain the mechanical properties and hence microstructure needed for a specific engineering application. Although there are several types of heat treatment, in this study full annealing and homogenization processes are of main interest.

2.8.1 Full annealing

The annealing heat-treating process consists of heating a steel above its austenitising temperature and then cooling it to room temperature at a slow enough rate to prevent the formation of a hardened structure. In most cases, the required slow cooling is achieved by simply switching off the furnace after soaking at the annealing temperature. Full annealing is often utilised in low and medium carbon steels that will be machined or will experience extensive plastic deformation. The resulting uniform microstructure consists of small grains of ferrite and pearlite. For cold rolled products, any residual stresses from the rolling operations are removed by full annealing. As steel is heated atomic mobility increases and dislocations previously accumulated during the rolling operation start to disappear leading to dissipation of any internal strains. The distorted grains recrystallise and new equiaxed grains appear.

2.8.2 Decarburisation

Steels with carbon contents above 0.2 in wt % C are quite readily decarburised during heating for rolling, forging, annealing or homogenizing [65]. Decarburisation occurs due to the loss of carbon to the atmosphere in the surface region of the steel (e.g. by the interaction of carbon with oxygen) resulting in the formation of a predominantly ferritic region around the steel as shown in figure 2.14.

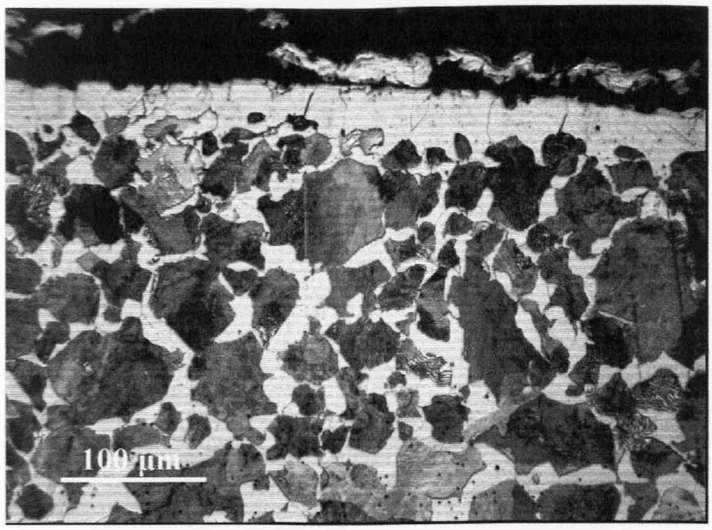

Figure 2.14: Optical micrograph of a 0.83 in wt % C steel rod sample showing the decarburised region after heat treatment above austenitisation temperature.

During heating in an air atmosphere above certain temperatures oxygen atoms diffuse at a much higher rate into steel than under ambient conditions and react with carbon atoms to form carbon monoxide or dioxide. The decarburisation rate is dependent on the temperature used and the alloying elements present in the steel. Certain alloying elements effectively prevent decarburisation from occurring as they are more reactive with carbon than oxygen and hence lock carbon in the solid. Decarburisation usually becomes a problem at temperatures above 600°C, where the mobility of carbon atoms

increases and thus reactivity is higher. Any decarburised region must be removed from the product if anisotropy in the mechanical properties is to be avoided.

Decarburisation may occur either through diffusion of oxygen in the steel leading to the formation of oxides and depletion of carbon from the outer regions or diffusion of carbon within the steel due to the presence of gradients in the carbon content throughout the volume of the steel (i.e. from richer to poorer in carbon content regions) or both. In any case, diffusion is the governing mechanism through which decarburisation takes place and is quantified by Fick's first and second laws of diffusion (equation 2.20) [163]:

$$J_B = -D_B \frac{\partial C_B}{\partial \chi} \qquad \text{Equation 2.20}$$

Equation 2.20 is usually known as Fick's first law of diffusion. J is the number of carbon atoms per m^2 that diffuse from plane 1 to plane 2 in 1s (atoms m^{-2} s^{-1}), D_B is the intrinsic diffusivity or the diffusion coefficient of carbon in m^2/s, C_B is the number of carbon atoms per m^3 (atoms / m^3) and $\frac{\partial C_B}{\partial \chi}$ is the concentration gradient of carbon varying with time. Equation 2.21 is referred to as Fick's second law [163]

$$\frac{\partial C_B}{\partial t} = D_B \frac{\partial^2 C_B}{\partial \chi^2} \qquad \text{Equation 2.21}$$

This equation relates the rate of change of composition with time to the concentration profile $C_B(\chi)$. Equation 2.21 has a simple graphical interpretation as $\frac{\partial^2 C_B}{\partial \chi^2}$ is the curvature of the C_B versus χ curve. If the concentration profile appears as shown in figure 2.15(a) it has a positive curvature everywhere and the concentration at all points on such a curve will increase with time ($\frac{\partial C_B}{\partial t}$ positive). When the curvature is negative as in figure 2.15(b) C_B decreases with time ($\frac{\partial C_B}{\partial t}$ negative).

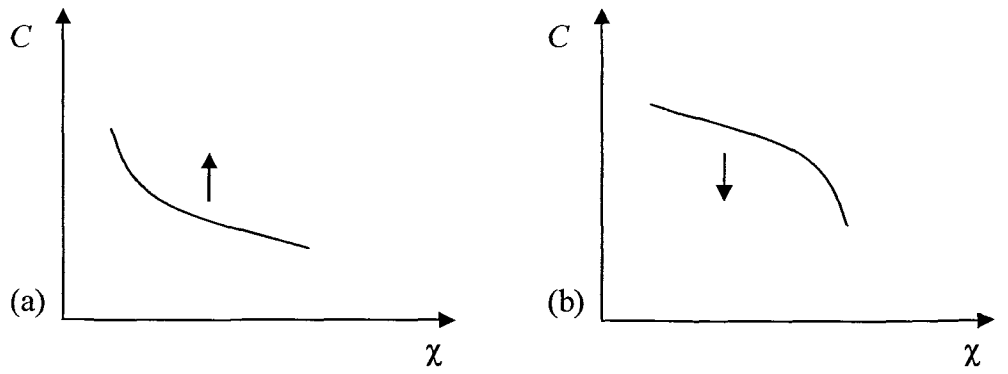

Figure 2.15: (a) $\frac{\partial^2 C_B}{\partial \chi^2} > 0$ all concentrations increase with time. (b) $\frac{\partial^2 C_B}{\partial \chi^2} < 0$ all concentrations decrease with time. (Reproduced from Porter and Easterling) [164]

Let us consider a homogenised steel sample that has been austenitised. By assuming constant concentration of oxygen in the atmosphere the concentration of carbon at the surface of the steel in equilibrium with oxygen can be maintained at a suitable constant value. At the same time oxygen continuously diffuses into the steel forming carbon monoxide and dioxide. Solving Fick's second law (equation 2.21) we have:

$$C = C_0 erf(\frac{x}{2\sqrt{(Dt)}})$$ Equation 2.22

C is the carbon concentration of the steel at time t and C_0 is the original carbon concentration, the thickness of the decarburized layer is χ. erf stands for error function which is an indefinite integral defined by the equation 2.23 [164].

$$erf(z) = \frac{2}{\pi}\int_0^z \exp(y^2)dy$$ Equation 2.23

The solution of equation 2.22 can be interpreted graphically in figure 2.16.

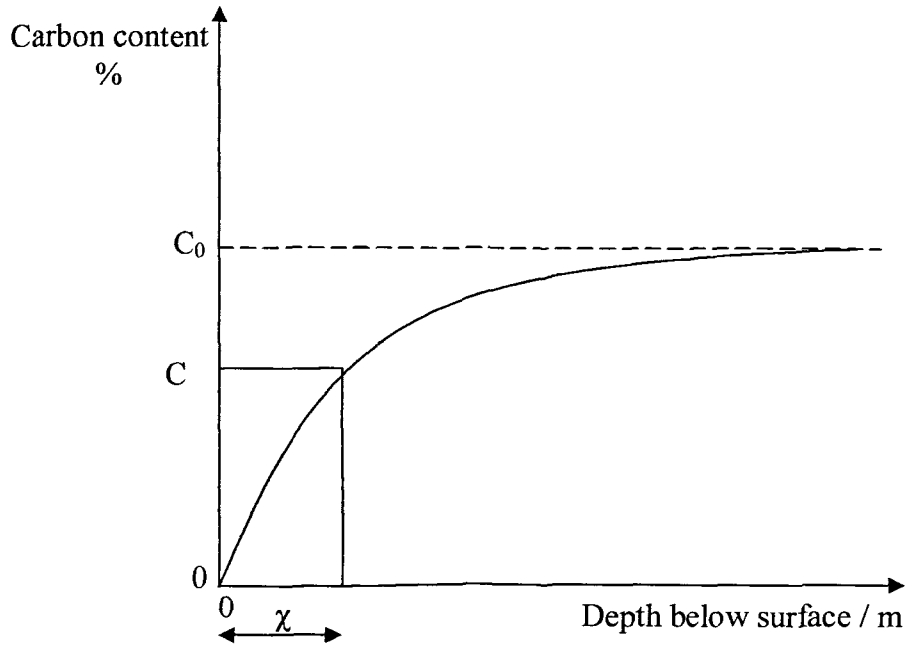

Figure 2.16: Decarburisation diagram. (Reproduced from Thelning) [165]

Decarburisation leads to the depletion of carbon at the outer regions of the steel thus causing the formation of gradients in carbon content between the core of the steel and the outer regions. Hence, in general decarburisation is a process that is followed by diffusion of carbon in an effort to maintain homogeneity of the steel, although both processes do not take place at the same speed. Decarburisation of steel becomes of significance at temperatures above 600°C and intensifies further as temperature increases. The carbon atom diffusion rate is a temperature dependent process and increases with increasing temperature [27]. Figure 2.17 shows a diagram of diffusion coefficient values variation for carbon and nitrogen with temperature.

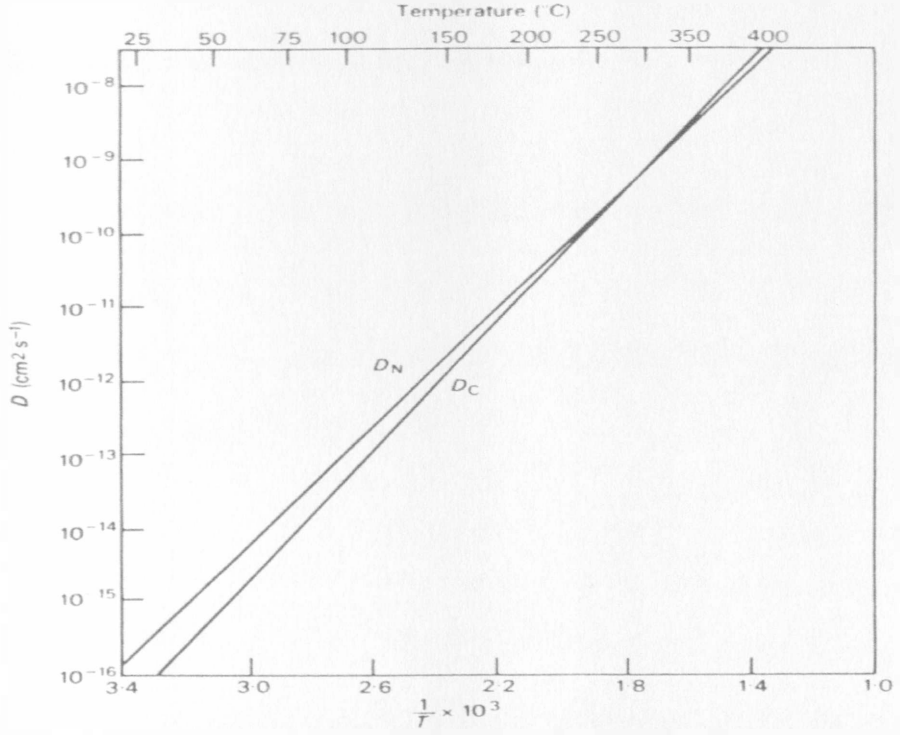

Figure 2.17: Temperature dependence of diffusion coefficients of nitrogen (D_N) and carbon (D_C) in α-iron. T is the absolute temperature. (Reproduced from Honeycombe and Bhadeshia) [68]

It should be noted here that diffusion of carbon in FCC austenite is also dependent on the carbon content of the alloy, i.e. at 1000°C the diffusion coefficient for a steel with 0.15 % in weight carbon content is 2.5 x 10^{-11} m^2 s^{-1}, while for a steel with 1.4 % in weight carbon it is 7.7 x 10^{-11} m^2 s^{-1}. The reason for the increase in the diffusion coefficient with carbon concentration is that the atoms strain the iron lattice thereby making diffusion easier as the amount of strain increases. The carbon loss rate at the steel-atmosphere interface is also a function of temperature and carbon content. Thus, for a steel alloy with carbon content 0.85 % in weight the diffusion coefficient of carbon at the steel-atmosphere interface at 900°C is 1.1 x 10^{-9} m^2 s^{-1} [165]. By comparing diffusion coefficients it is obvious that decarburisation takes place significantly faster than carbon migration and hence depletion of carbon from the decarburised regions is faster than its replenishment.

To avoid the deleterious effects of decarburisation in plain carbon steels, heat treatment must be performed either in salt baths or controlled atmosphere furnaces. Mild cases of decarburisation may sometimes be repaired, at least in part, by heating in a carburising controlled atmosphere [65].

2.8.3 Oxidation

Decarburisation can be accompanied by oxidation of the decarburised region and formation of scale. This is due to the further reaction of oxygen with iron once carbon has been depleted from a region. Steels have the disadvantage that other alloying elements present also participate in the scaling reaction, making interpretation difficult [166]. In early studies [167-170] the irregular behaviour of Fe-C

alloys was attributed to the development of appreciable pressures of CO and CO_2 beneath the scale when the carbon in the alloy is oxidised leading to the breakdown of otherwise protective scales by the formation of cracks and blisters. Others have suggested that the reaction takes place at the metal-scale interface proceeding in a parabolic rate. In general oxidation occurs much faster in pure iron than plain carbon steel alloys [171].

Oxidation of plain carbon steels commonly results in a scale consisting of three different oxides of iron. The outer scale layer consists of hematite, followed by magnetite, and the innermost layer being wustite. With pure iron, these three phases form three well-defined, parallel-sided layers, with magnetite and hematite accounting for approximately 5 % of the total scale thickness at temperatures of 700°C and above. However, this balance may be disturbed by the presence of carbon in the alloy, and indeed the scale layers are very much less regular in thickness and are often highly porous.

A fully decarburised region is virtually free of carbon and therefore in the initial stages of oxidation oxide scales typical of those of pure iron should be expected to form, until the decarburised layer has been completely oxidised. Indeed, in its initial stage oxidation takes place in a similar fashion as in pure iron. However, before the decarburised layer is completely consumed the oxidation rate decreases. This is because even though the decarburised layer has not been fully consumed, during oxidation carbon can diffuse through the decarburised surface layer to the alloy-scale interface and interact with the oxidation process. The oxidation process is of significance to the present work and is investigated thoroughly in chapter 5.

2.8.4 Homogenisation

During production of steel, a structure containing regions enriched with carbon and with reduced carbon level may result. This would give rise to an inhomogeneous microstructure and anisotropic mechanical properties. Furthermore, distorted grains may be observed in the microstructure in the rolling direction. These drawbacks can be overcome by homogenisation of the steel, a process that resembles full annealing. However, during homogenisation sufficient time must be allowed at a temperature well above the austenitisation start temperature for the carbon atoms to diffuse throughout the structure. The higher the temperature, the faster homogenisation will be completed as the energy provided through heat increases will cause the mobility of the atoms to increase. If we assume that carbon concentration in a steel sample is varying from region to region, then equation 2.24 can be applied in order to determine the time needed for complete homogenisation to occur [165]:

$$C = C_o \exp\left(-\frac{Dt\pi^2}{l^2}\right) \qquad \text{Equation 2.24}$$

where C is the concentration differential after annealing, Co is the concentration differential before annealing, D is the diffusion coefficient at a given temperature, t is the homogenization time and l is the diffusion path length.

Steel is then slowly cooled in order to avoid any hardening of the microstructure. Homogenisation at temperatures above 1000°C can lead to grain growth, resulting in

prior-austenite grain diameters of up to several hundred microns if adequate time is given, i.e. of the order of several tens of hours.

2.9 Grain growth and control

Grain size is a major contributing factor to the strength and toughness of a steel. Fine grain size allows very high strength in conjunction with good toughness and ductility while coarse grain size diminishes the strength and toughness. The importance of grain size on the mechanical properties of steel is illustrated by the Hall – Petch equation (2.25) [172]:

$$\sigma_y = \sigma_i + k_y d^{-1/2} \qquad \text{Equation 2.25}$$

where σ_y is the yield stress in MPa, σ_i is the friction stress opposing dislocation movement in MPa, k_y is the dislocation locking constant in MPa $mm^{1/2}$ and d is the grain size in mm. Fine ferrite grain sizes in the finished steel are greatly expedited by the addition of small concentrations (<0.1 % in weight) of grain refining elements such as niobium, titanium and vanadium and also aluminium. These elements are strong carbide and nitride formers.

Dynamic recrystallisation of austenite is the primary grain refinement mechanism in controlled rolling. The process of dynamic recrystallisation is significantly influenced by the temperature and degree of deformation which takes place during each pass through the rolls. In the absence of second phase particles the high temperatures

involved during hot rolling of steel lead to grain growth resulting in coarse grain sizes.

Grain growth can be avoided or limited if fine particles (i.e. AlN, Ti(C, N), Nb(C, N), and V(C, N) are introduced into the austenitic matrix. These precipitates may not be completely dissolved in the austenite until temperatures in excess of 1300°C are reached. It is equally essential that there is sufficient solid solubility at the highest austenitising temperatures to allow fine precipitation to occur during controlled rolling at temperatures which decrease rolling proceeds. All the aforementioned carbo-nitrides have a small but increasing solubility in the critical temperature range (900 - 1300°C). Equations 2.26–2.29 for solubilities expressed in weight % as a function of absolute temperature have been introduced by Irvine et al. [173]:

$$\log_{10}[A][N] = -6770/T + 1.03 \qquad \text{Equation 2.26}$$

$$\log_{10}[V][N] = -8330/T + 3.46 \qquad \text{Equation 2.27}$$

$$\log_{10}[Nb][C] = -6770/T + 2.26 \qquad \text{Equation 2.28}$$

$$\log_{10}[Ti][N] = -7000/T + 2.75 \qquad \text{Equation 2.29}$$

Figure 2.18 shows the solubility curve for NbC in a steel with carbon content 0.15 % in weight.

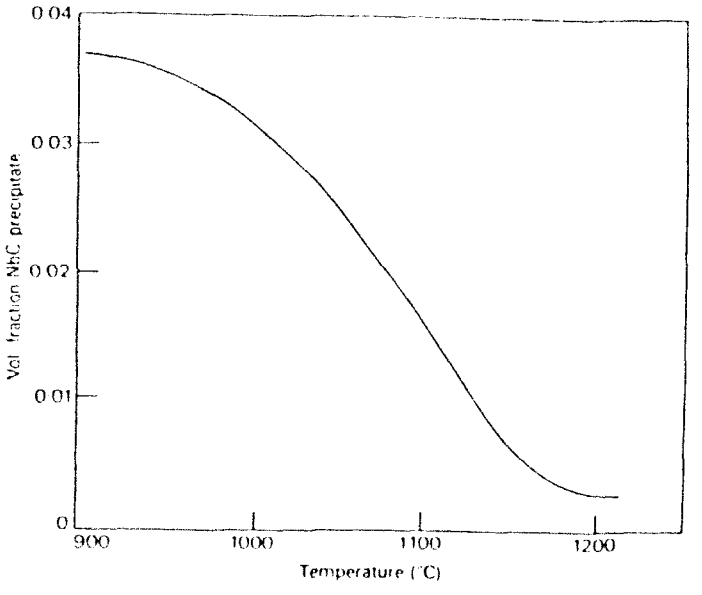

Figure 2.18: Solubility of niobium carbide (NbC) with increasing temperature. (Reproduced from Honeycombe and Bhadeshia) [68]

The particles are usually found on grain boundaries, because an interaction takes place between the particle and the boundary. A short length of boundary is replaced by the particle and the interfacial energy ensures a stable configuration. Upon high temperature heat treatment the migration mechanism of the boundary is severely restricted by the presence of the particles which exert a drag on the boundary. The effectiveness of the boundary pinning by particles however, is a function of both their total volume fraction and size. In the absence of an adequate number of fine precipitates the boundary pinning effectiveness reduces. Similarly, coarse precipitates which are not dissolved at the slab reheating stage are ineffective as strengthening agents.

It is obvious, that during full annealing the temperatures involved are lower than those needed for the precipitates to completely dissolve and thus grain growth is restrained.

In the case of homogenisation however, temperatures may well exceed 1300°C and thus the precipitates will dissolve. In this case the boundary pinning mechanism disappears and the boundary interface is free to migrate during the time allowed for homogenisation.

2.10 Thermally activated migration of grain boundaries

In metallurgical specimens there are always boundaries with a net curvature in one direction and thus the surface tensions are not balanced over all the boundary faces. Consequently, a random grain structure is inherently unstable and on annealing at high temperatures the unbalanced forces will cause the boundaries to migrate.

During annealing certain grains shrink and disappear as others grow and occupy the area of those that shrink. Assuming that all boundaries have the same energy independent of orientation metastable equilibrium at the grain boundary junctions is dependent on the angular conditions, i.e. the resulting angles at each boundary junction. This is verified by equation 2.30 for boundary tensions [164]:

$$\frac{\gamma_{23}}{\sin\theta_1} = \frac{\gamma_{13}}{\sin\vartheta_2} = \frac{\gamma_{12}}{\sin\theta_3} \qquad \text{Equation 2.30}$$

where γ_{23}, γ_{13}, γ_{12} are the grain boundary tension in N and θ_1, θ_2, θ_3 are the angles formed at the grain boundary junctions as shown in figure 2.19.

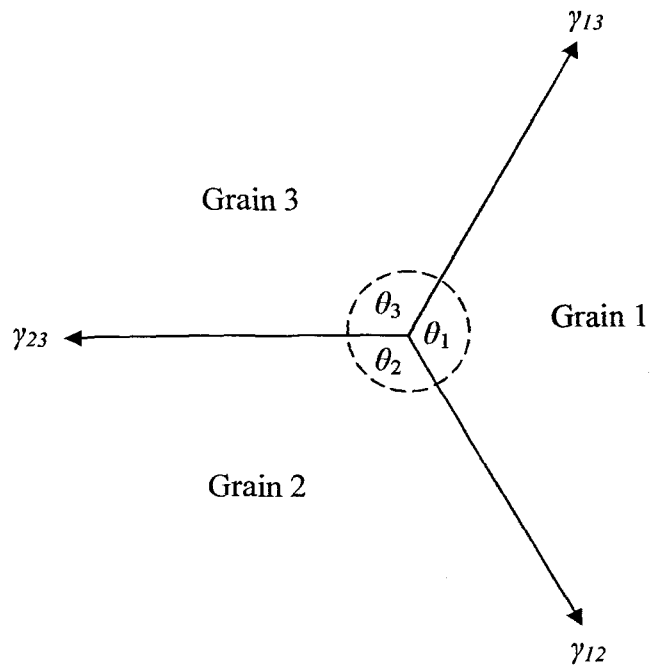

Figure 2.19: The balance of grain boundary tensions for a grain boundary intersection (junction) in metastable equilibrium. (Reproduced from Porter and Easterling) [164]

Taking into account the aforementioned assumption in conjunction with figure then equation 2.30 results in $\theta_1 = \theta_2 = \theta_3 = 120^\circ$. If a second assumption is made according to which equilibrium at each boundary junction results in angles of 120° then the number of boundaries that a grain consists of determines whether a grain will grow or shrink. Therefore, if a grain has six boundaries they will be planar and the structure is metastable. However, if the total number of boundaries around a grain is less than six each boundary must be concave inwards. These grains will shrink and eventually disappear during annealing. Larger grains on the other hand will have more than six boundaries and will grow. The overall result of such boundary migration is a reduction in the number of grains and hence an increase in the mean grain size or in other words grain growth or coarsening.

As a grain grows, the atoms from the surrounding shrinking grains detach themselves from the lattice on the high pressure side of the boundary and relocate themselves on the lattice site of the growing grain. The effect of the pressure difference caused by a curved boundary is to create a difference in free energy (ΔG) or chemical potential ($\Delta\mu$) that drives the atoms across the boundary. In a pure metal ΔG and $\Delta\mu$ are identical and are given by equation 2.31:

$$\Delta G = \frac{2\gamma V_m}{r} = \Delta\mu \qquad \text{Equation 2.31}$$

where ΔG and $\Delta\mu$ are in J, γ is the grain tension which is temperature dependent, V_m is the molar volume in m^3 and r is the radius of curvature of the grain boundary in m. This free energy can be thought of as a force pulling the grain boundary towards the grain with the higher free energy. As shown in figure 2.20, if unit area of grain boundary advances a distance $\delta\chi$ the amount of moles of a material that enter the growing grain is given by equation 2.32:

$$n = \frac{\delta\chi}{V_m} \qquad \text{Equation 2.32}$$

where n is the number of moles $\delta\chi$ is the distance that the grain boundary has covered.

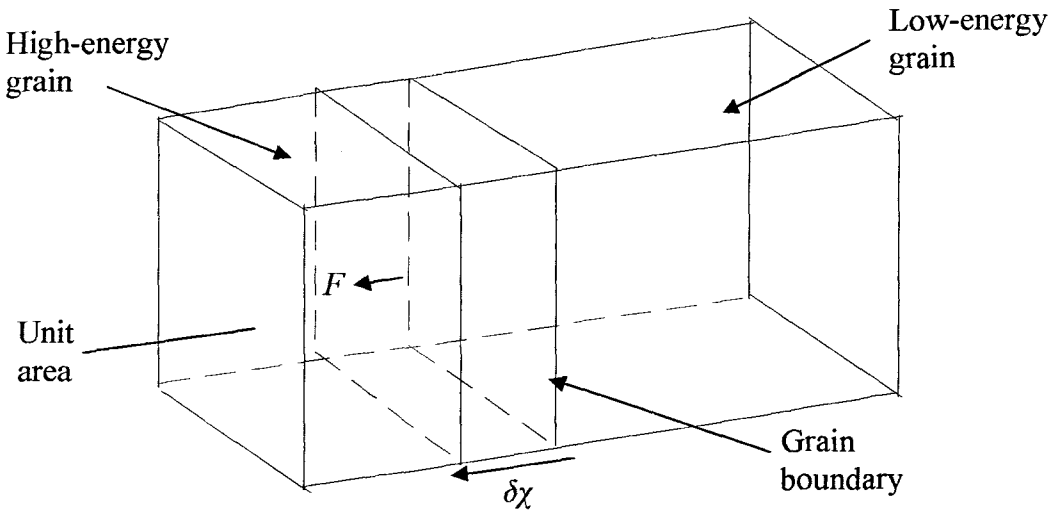

Figure 2.20: A boundary separating grains with different free energies is subjected to a pulling force F. (Reproduced from Porter and Easterling) [164]

The free energy released during the boundary movement can be equated to the work done by the pulling force $F\delta\chi$ as shown in equation 2.33:

$$W = F\delta\chi = \Delta G\frac{\delta\chi}{V_m} = G \qquad \text{Equation 2.33}$$

where W is the work done by the pulling force in J, F is the pulling force in N and G is the free energy released in J. Equation 2.33 can be modified to calculate the pulling force by dividing both sides with $\delta\chi$, then (equation 2.34):

$$F = \frac{\Delta G}{V_m} \qquad \text{Equation 2.34}$$

The velocity, v, at which a grain boundary moves is given by equation 2.35

$$v = M \cdot \frac{\Delta G}{V_m} \qquad \text{Equation 2.35}$$

where v is in ms^{-1}, M is the mobility of the grain boundary in $m^3N^{-1}s^{-1}$ and increases exponentially with temperature. If v is constant the distance covered by the boundary is given by equation 2.36

$$\delta\chi = vt \qquad \text{Equation 2.36}$$

where t is the period of time for which the boundary movement lasted in s.

2.11 Microstructural segregation

Steel strip products are subject to chemical inhomogenieties during solidification after casting. As the steel solidifies dendrites tend to form and the final solidified structure can be comprised of dendrites, columnar grains and / or equiaxed grains (figure 2.21).

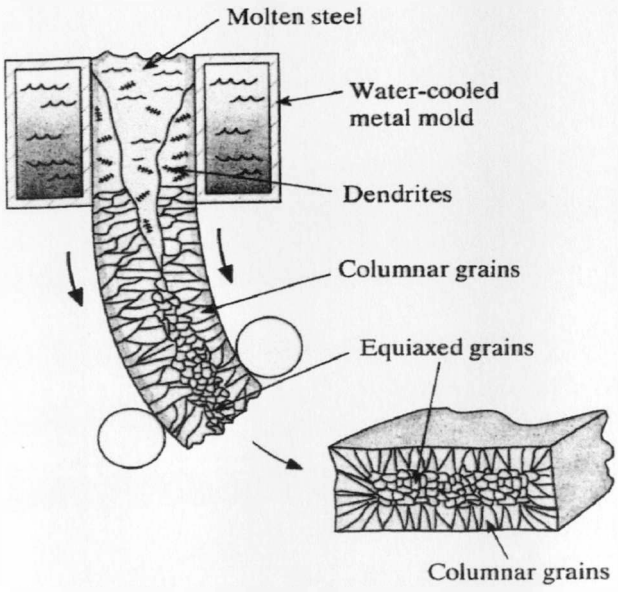

Figure 2.21: Grain size in a strand cast semi. (Reproduced from Budinski and Budinski) [2]

Alloys can segregate to either the dendrite core or the interdendritic regions. The first liquid to solidify will be alloy rich if the alloy addition raises the melting temperature, whereas the alloy will be segregated to the interdendritic regions if the alloy addition lowers the melting temperature. In steel strip the microstructure is further altered by plastic deformation due to the hot rolling process causing banding parallel to the rolling direction. This creates banded microstructures of ferrite and pearlite resulting from the segregation of manganese during solidification.

Greater rolling reduction produces a finer spacing between the bands. The segregated manganese also produces a partitioning of carbon because manganese is an austenite stabiliser. Thus, as the steel is cooled through the transformation temperatures to form ferrite and pearlite, it is the manganese rich regions are the last austenite to

transform. During quenching segregation can be manifested as banded microstructures of martensite and bainite [174].

Phosphorus is normally considered an impurity in steel and exists exclusively as a solid solution in ferrite. If phosphorus concentration exceeds a limit, the grain size is coarsened and massive undesirable segregates are produced. This is due to the tendency of phosphorus to segregate into interdendritic regions and subsequently form low temperature melting phosphates. Similarly, sulphur in excessive concentrations in steel also causes segregation [175]. Alloying elements that are strong carbonitrides formers and have a high solution temperature, such as Al, Nb, Ti and V, also promote segregation effects.

The existence of banded ferrite grains in segregated microstructures that form a continuous path through the steel as shown in figure are of primary significance to this study. Banded ferrite grains constitute a favourable ferromagnetic path through which flux can go through thus giving a higher electromagnetic signal. The effect of ferrite banding on the electromagnetic signal is discussed in detail in chapter 5.

2.12 Conductivity of steel

All materials inherently resist the flow of an electric current through them. The resistance of a metal to the flow of an applied electric current is directly related to its geometrical dimensions (i.e. length and cross-section) and resistivity as defined by Ohm's law (equation 2.37).

$$R = \rho \frac{L}{A}$$ Equation 2.37

where R is the resistance of an object in ohm, ρ is the resistivity of the material, a proportionality constant that depends on the type of the material and varies with temperature and is measured in ohm m, L is the length of the object in m and A is its cross-sectional area in m^2.

The resistivity, ρ, of a material depends on the intrinsic properties of the material, such as the number of electrons per unit volume that are able to move and the hindrance these electrons experience as they travel through the material. Impurities in a metal cause an increase in the resistivity as the field in the vicinity of the impurities is in general different from that near the host atoms. The impurities thus produce deviations from the periodicity of the potential and act as scattering centres for electrons. Resistivity tends to increase with temperature due to the increasing vibration of the atoms that comprise the crystal lattice of a metal hence impeding the movement of electrons towards the direction of the electric current flow.

Therefore, the resistivity of a metal is a function of temperature and its alloying elements. This is mathematically expressed by equation 2.38

$$\rho_T = \rho_0 (1 + \alpha \Delta T)$$ Equation 2.38

where ρ_T is the resistivity at temperature T, ρ_0 is the resistivity at a reference temperature (usually 0°C), α is the temperature coefficient of resistance (sensitive to alloying elements and impurities) and is measured in $°C^{-1}$ and ΔT is the temperature

interval between the reference temperature and the current temperature of the metal. Representative values of α are given in table 2.1 [176].

Table 2.1: Temperature coefficients of resistance for various elements. (Values reproduced from Van Heuvelen) [176]

Material	α ($^{o}C^{-1}$)
Iron	0.0050
Carbon	-0.0005
Aluminium	0.0039
Copper	0.00393

Detection of steel transformation by means of electromagnetic means relies on the detection of the changes exhibited in conductivity and permeability of steel during phase transformation. Thus, the measured electromagnetic signal is inextricably linked to the microstructure of steel, and hence to temperature. The conductivity, σ, of a material is inversely related to its resistivity as shown in equations 2.39 and 2.40

$$\sigma = \frac{1}{\rho} \qquad \text{Equation 2.39}$$

or

$$\sigma = \frac{1}{\rho_0(1+\alpha\Delta T)} = \frac{\sigma_0}{1+\alpha\Delta T} \qquad \text{Equation 2.40}$$

where σ is the conductivity of a material in Siemen. Conductivity of pure iron at room temperature (20°C) has been measured to be 1.044 x 10^{-7} Siemen [176, 177]. However, as carbon content and temperature increases the value of conductivity varies accordingly. In table 2.2 is shown the variation of resistivity and conductivity

values for a steel with 0.06 % in weight carbon content with increasing temperature [178].

Table 2.2: Variation of resistivity and conductivity values for a 0.06 % in weight carbon steel. (Reproduced from ASM Handbook, Properties and Selection: Iron and Steel) [178]

Temperature (°C)	Resistivity (μ· Ω·m)	Conductivity (Siemen)
20	0.13	7.69×10^{-6}
100	0.178	5.62×10^{-6}
200	0.252	3.97×10^{-6}
400	0.448	2.23×10^{-6}
600	0.725	1.38×10^{-6}
700	0.898	1.11×10^{-6}
800	1.073	9.32×10^{-6}
900	1.124	8.90×10^{-6}
1000	1.16	8.62×10^{-6}
1100	1.189	8.41×10^{-6}

The graphical representation of the variation of conductivity values with increasing temperature is shown in figure 2.22.

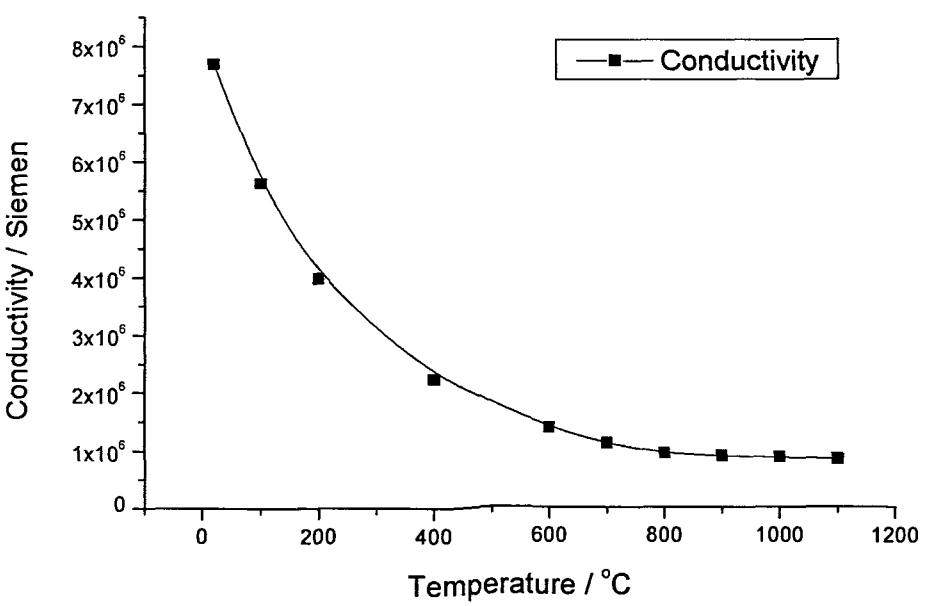

Figure 2.22: Graph of conductivity values versus temperature for a steel with carbon content 0.06 % in weight.

Table 2.3 shows the variation of resistivity and conductivity values with increasing carbon content in steel at room temperature.

Table 2.3: Variation of resistivity and conductivity values with increasing carbon content in steel at room temperature. (Reproduced from ASM Handbook, Properties and Selection: Iron and Steel) [178]

C content in wt %	Resistivity (μ· Ω·m)	Conductivity (Siemen)
0.06	0.130	7.69×10^{-6}
0.42	0.171	5.84×10^{-6}
0.80	0.180	5.55×10^{-6}
1.22	0.196	5.10×10^{-6}

Figure 2.23 displays the graphical representation of the variation of conductivity values with increasing carbon content at a room temperature.

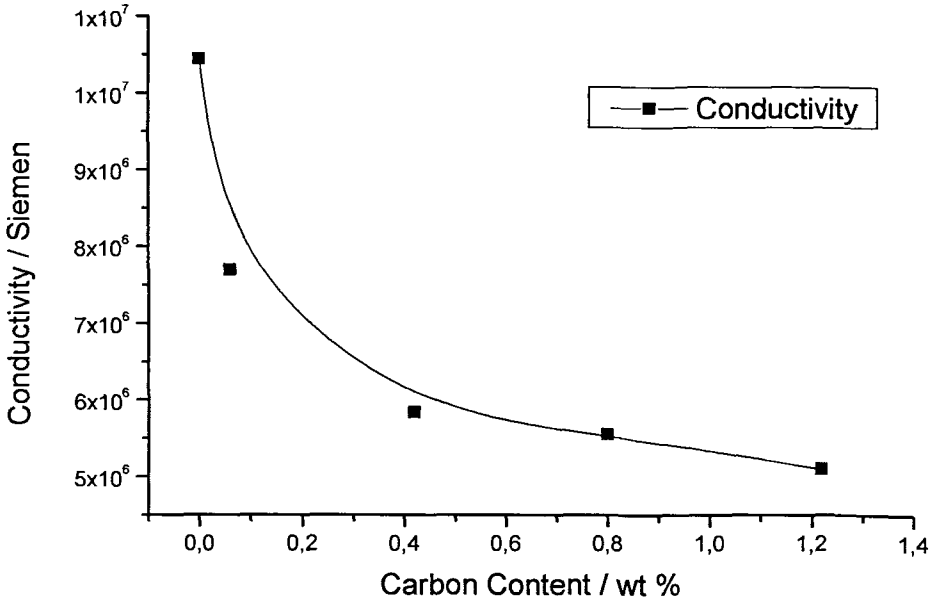

Figure 2.23: Graph of conductivity values versus increasing carbon content at room temperature.

Taking into account the variation of conductivity with carbon content in steel at room temperature as displayed in table 2.3, ferrite exhibits a slightly higher conductivity than pearlite, i.e. 7.69×10^{-6} and 5.55×10^{-6} siemen respectively. Similarly ferrite and austenite at the temperature range of 770°C exhibit effectively the same conductivity , i.e. 1.11×10^{-6} siemen.

As induced eddy currents within an object due to the application of an electromagnetic field can be directly related to conductivity, such electrical characteristics can be accurately measured. This relationship has been exploited in both oxide [179-180] and coating detection [181]. As conductivity varies with temperature, variance in detected eddy currents provides an indication of the temperature of the sample.

2.13 Permeability of steel

The relationship between magnetic permeability and phase transformation is complex and depends on many factors such as steel composition and thermal treatment. This relationship is not well documented in the literature and is subject of on-going research. The electromagnetic method for measuring phase transformation is based on the detection of changes that occur in both conductivity and relative permeability, μ_R (unitless), of steel during phase transformation of austenite to ferrite below T_C. Permeability of steel is strongly affected by temperature variation. Above T_C any transformed ferrite is paramagnetic and therefore permeability is equal to 1. However, as temperature drops below T_C ferrite becomes ferromagnetic signalling an

abrupt increase in the permeability value. Nonetheless, the permeability value of steel is not only a function of temperature but of composition as well.

The permeability of steel varies with alloying elements content. For example, 99.95 % in weight pure iron has a permeability value of 1.5×10^{-4} while for 99.8 % in weight pure iron the permeability value falls to 3.5×10^{-3} [178]. Figure 2.24 presents the effect of carbon content in steel on permeability value at room temperature.

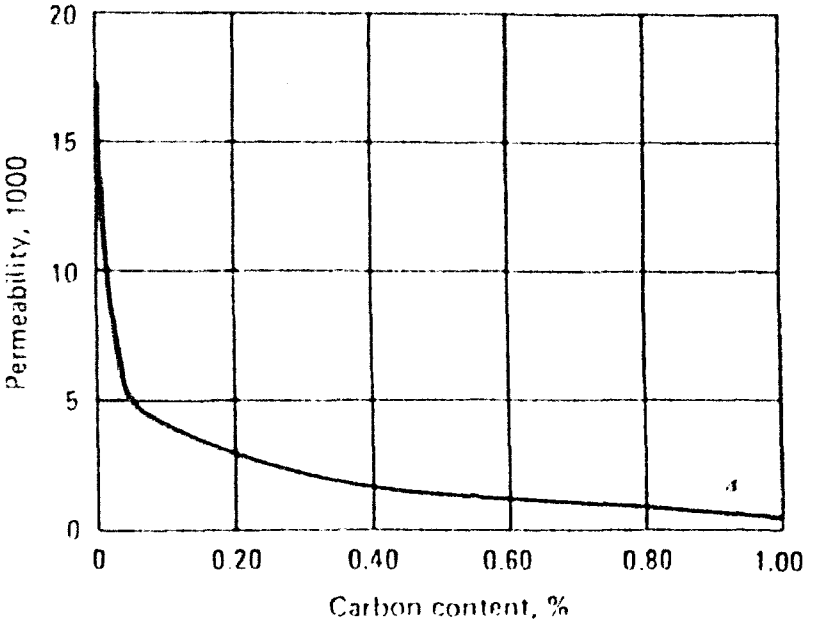

Figure 2.24: Variations in permeability of steel with carbon content at room temperature. (Reproduced from ASM Handbook, Properties and Selection: Iron and Steel) [178]

As is clearly seen from figure 2.24, the permeability value diminishes rapidly as carbon content increases. Ferrite in steel contains a maximum of 0.022 % in weight C and therefore its permeability is significantly higher than that of pearlite which contains 0.77 % in weight C. The effect of permeability value will be reflected in the

impedance value recorded by an electromagnetic sensor, i.e. the higher the permeability the stronger the electromagnetic signal. Thus, the transformation of ferrite will result in a stronger electromagnetic signal than pearlite due to the difference in permeability. Other alloying elements also have a detrimental effect on the permeability of steel with the exception of cobalt [63].

Permeability of a material can be measured using SQUIDS [182] in a process that involves constant temperatures and permeability. As the present investigation concerns the analysis of hot steel in respect to its permeability, such processes are therefore unsuitable. Furthermore, so far there is no known relationship between permeability and temperature during phase transformation of steel and therefore it is only possible to speculate the actual permeability value of the steel alloy through the trans-impedance value recorded. In order to create a relationship between permeability and temperature, the influence of conductivity upon impedance has to be rejected. Permeability value variations with temperature are discussed in more detail in chapter 5.

2.14 Summary

This chapter has reviewed the main microstructures that can form in carbon steels including the morphology and distribution of these phases. The effects of heat treatment and the nature of cooling on the produced microstructure have been presented. The significance of alloying elements on the transformation of austenite to ferrite and pearlite has been analysed and the transformation kinetics have been discussed. Furthermore, heat treatment of steel has been related to decarburisation

and oxidation. The thermodynamics of decarburisation have been explained while the process of diffusion has been carefully analysed.

Additionally, the reasons for homogenisation have been presented whilst the effect of temperature on grain growth and the thermodynamics involved have been discussed. Finally, the nature of segregation in steel and the resulting microstructures have been presented. The electromagnetic theory, the effect of alloying elements on the Curie temperature and previous research on the electromagnetic sensing technique are discussed in chapter 3.

CHAPTER 3: FUNDAMENTALS OF ELECTROMAGNETIC SENSOR DESIGN

3.1 Introduction

Steel does not display the same magnetic properties at all temperatures. Changes in the magnetic properties of steel may arise on heating either due to phase transformation of ferromagnetic ferrite to paramagnetic austenite, or due to its heating above the Curie temperature, (T_C), causing steel to become paramagnetic regardless of the phases present in the microstructure.

The application of an electromagnetic sensor capable of detecting phase transformation in steel during cooling relies in principle on the changes that occur on the magnetic properties of steel during austenite transformation below the T_C. More specifically, the decomposition of austenite, when this occurs below the T_C, is associated with changes in the conductivity and permeability of steel which can be accurately measured by an electromagnetic-based detector. Electromagnetic detectors are adversely affected by electromagnetic noise created by high magnitude electrical currents which exist in a hot-rolling mill. Nevertheless, by filtering the recorded signal it is possible to compensate for any abnormalities hence minimising the effect of electromagnetic noise on the recorded signal.

This chapter is mainly concerned with the background theory on which the electromagnetic technique is based. Additionally, a brief review of past research on

the electromagnetic technique is presented along with a description of the proposed electromagnetic detectors used for this study.

3.2 The electromagnetic field

A magnetic field may be produced by a current of electricity as well as by a magnetised solid (i.e. a magnet) and the unit of field strength can also be defined in terms of current. Albeit this study is concerned with the magnetic field produced by an electric current and how this field interacts with a steel sample during cooling from austenitisation temperatures above T_C, however it is worth briefly discussing the nature of magnetic materials as well.

3.2.1 Magnetic materials

A bar magnet, like all magnetic materials, derives its properties from the magnetic fields created by atoms and the magnetic forces acting on the atoms. An atom consists of a very small nucleus surrounded by clouds of electrons, which can be thought of as circling the nucleus in elliptical orbits. The motion of each electron is equivalent to a loop wire carrying one electron. The magnetic field produced by this electron current loop is identical to that produced by a bar magnet of atomic size. The electron also produces a magnetic field because it has an intrinsic magnetic dipole moment with a north and south pole and acts like a bar magnet itself. Thus, an electron in an atom creates a magnetic field because of its orbital motion and because of its intrinsic magnetic moment [176].

In atoms with more than one electron, the fields created by different electrons often cancel each other. The electrons pair off so that the intrinsic magnetic moment of one electron points in an opposite direction to that of the other electron, and hence their magnetic fields cancel. The fields caused by the orbital motion of electrons also cancel since some electron currents move opposite to others. In the case where the cancellation is incomplete, the atom is said to have a net magnetic dipole moment and produces a magnetic field. Atoms with non-zero magnetic dipole moments are known as paramagnetic atoms. In a normal case, the paramagnetic atoms in a material are oriented randomly and therefore, the magnetic field produced by one atom is cancelled by the field of another atom that is oriented in the opposite direction. However, if a material that consists of paramagnetic atoms is placed in an externally generated field, the magnetic dipole moments of the atoms have a tendency to align with the external field producing their own field.

In certain materials such as iron, the alignment of the atoms is not random. In these materials, known as ferromagnetic materials, the magnetic dipoles are locked together and orientated in the same direction by a complicated electromagnetic force. The alignment of neighboring atoms in these materials is uniform in small regions which are known as domains and these are responsible for the magnetic properties exhibited by a bar magnet [176].

3.2.2 Electromagnetic field produced by a current loop

A magnetic field has direction as well as strength. The direction is determined by the effect of the field on a compass needle. Faraday showed that some of the properties

of magnetism may be likened to a flow and suggested that it could be represented by endless lines of magnetic field, B, that represent the direction and, by their concentration, the flow at any point: the total number of lines crossing a given area at right angles is the flux in that area. The flux per unit area is the flux density, or magnetic induction. The magnetic induction is defined by the relation (equation 3.1) [63].

$$B = \mu_o (H + M) \qquad \text{Equation 3.1}$$

where B is the magnetic flux density in Tesla, μ_o is the magnetic permeability of free space in henry/m, H is magnetic field strength in A/m, and M is the magnetisation in A/m. It is helpful at this point to explain the difference between B and H. In the magnetic field the primary vector is the magnetic induction (or magnetic flux density) B, defined in terms of the mechanical force on a loop. With the establishment of the magnetic circuit law, it becomes convenient to introduce a secondary vector H, directly associated with the current linked with a closed imaginary circuit. H is therefore associated with the currents which cause the field and B is associated with the effect of the electromagnetic field, making itself felt by forces on the circuit [183].

The simplest way of producing a magnetic field of known strength and direction is by the use of a long coil or solenoid of wire. The field is parallel to the axis of the coil, and when a current of I amperes flows in the windings (having n turns per m) the field strength, H, within the coil is (equation 3.2) [176]

$$H = nI$$ Equation 3.2

When an electric circuit encloses a changing magnetic flux, φ, an electromotive force, E, is generated in the circuit proportional to the time rate of change of flux, $d\varphi/dt$, and to the number of times, N, the circuit threads the flux. Thus, if N turns of wire are wrapped around a piece of iron of cross-sectional area, A, and a change in the magnetic induction, B, is produced in the iron, a voltage is produced at the ends of the wires equal to 10^{-8}NA times the rate of change of induction in Tesla per second (equation 3.3) [183].

$$E = 10^{-8} NA \frac{dB}{dt}$$ Equation 3.3

In the present study, the proposed electromagnetic sensor consists of one exciting and one sensing coil. The exciting coil is driven at a certain voltage; as the electromagnetic flux density, B, created by the exciting coil, varies, an electromotive force is induced into the sensing coil. Equation 3.3 describes the mathematical relationship between the variations in the magnitude of the electromagnetic field and the resulting induced electromotive force.

3.2.3 Fundamental electromagnetic relationships

The Maxwell's fundamental equations that govern the relationship between the electromagnetic field, the permeability of a material and its magnetisation are

presented next. The derivation of these equations can be found in the literature [184] and is not presented here.

A relationship exists between magnetic flux density ($\overline{B}$) and electric field intensity, $\overline{E}$; these are most succinctly presented within the four Maxwell equations, expressed in their derivative form, in equations 3.4 - 3.7. Within these equations, ρ is the free charge density, $\overline{J}$ represents current density and $\overline{D}$ is the electric field displacement and $\overline{H}$ is the magnetic field intensity [183].

$$\nabla \times \overline{E} = \frac{-\partial \overline{B}}{\partial t} \qquad \text{Equation 3.4}$$

$$\nabla \times \overline{H} = \overline{J} + \frac{\partial \overline{D}}{\partial t} \qquad \text{Equation 3.5}$$

$$\nabla \cdot \overline{D} = \rho \qquad \text{Equation 3.6}$$

$$\nabla \cdot \overline{B} = 0 \qquad \text{Equation 3.7}$$

Relationships between constants, such as permittivity, ε, in $C^2\ m^{-2}\ N$, conductivity, σ, in Siemen and permeability, μ, in $T\ m\ A^{-1}$ and electromagnetic fields, are referred to as constitutive equations; these are shown in equations 3.8 - 3.10 [183].

$$\overline{B} = \mu_0 \mu_r \overline{H} \qquad \text{Equation 3.8}$$

$$\bar{J} = \sigma \bar{E}$$ Equation 3.9

$$\bar{D} = \varepsilon \bar{E}$$ Equation 3.10

where μ_0 is the relative permeability of free space and μ_r is the relative permeability of the magnetised solid. Permeability and permittivity have been represented as vectors in the above equations, which is a generally applicable approximation, although strictly they are tensor quantities. The Maxwell Finite Element software package (Ansoft Corporation) used in this study to simulate the behaviour of the electromagnetic field during ferrite formation and the resulting signal discussed in chapter 6 calls upon the equations presented so far.

3.2.4 Electromagnetic field induced by a coil

The electromagnetic sensor used in this study consists of an excitation coil (which produces the electromagnetic field) and a sensing coil (in which an electromotive force is induced due to magnetic induction).

The electromagnetic field or induction B produced in a coil which is fed by an electric current is directly related to the number of turns that the coil consists of. This is mathematically analysed as (equation 3.11) [63]:

$$B = \mu_0 nI$$ Equation 3.11

where B is the electromagnetic induction produced by the coil in Tesla, n is the number of turns per meter and I is the electrical current with which the coil is fed in Amps. The strength of the electromagnetic field, B, at a random point P outside the coil is rather more complex and is given by equation 3.12 [63]

$$\vec{B}(P) = \frac{\mu_0 I}{4\pi} \int_0^{2\pi} \frac{\vec{dl} \times \vec{r}}{r^2} \qquad \text{Equation 3.12}$$

where $\vec{B}$ is the vector of magnetic induction at point P in Tesla, μ_0 is the permeability of vacuum in Henry/m, I is the electrical current flowing through the coil in Amp, $\vec{dl}$ a length of the coil in m, $\vec{r}$ is the unit vector of the distance between the coil and point P somewhere outside the coil in m and r the distance between the coil and point P in m.

The occurring magnetic flux through a coil with a single turn or current loop depends on the orientation of the coil. If the coil is parallel to the magnetic field, the field lines pass along the sides of the coil but not through it and the flux is zero. If the coil's surface is at an angle, θ, to the field direction then the flux through the coils is given by equation 3.13 [176]

$$\Phi = BA\cos\theta \qquad \text{Equation 3.13}$$

where Φ is the magnetic flux in Weber and B is the magnetic field in Tesla, A is the area of the coil or loop and θ is the angle of the coil to the magnetic flux lines. If θ is 0° then equation 3.13 becomes

$$\Phi = BA \qquad \text{Equation 3.14}$$

Any change that takes place in the flux through a current loop will be counter acted by an induced voltage in the current loop. Nonetheless, the induced voltage also generates itself a voltage in the current loop. This is called the self-inductance L of the coil and is given by equation 3.14 [63]

$$L = \frac{N\Phi}{I} \qquad \text{Equation 3.15}$$

where L is the self-induction of a single current loop in Wb/Amp, N is the number of loops that the coil consists of, Φ the magnetic flux in Wb and I the electric current flowing through the loop in Amp. Taking into account equations 3.11 and 3.14 then the self-induction of a coil can be calculated by equation 3.15 [63]

$$L = \frac{\mu_0 N^2 A}{l} \qquad \text{Equation 3.16}$$

where L is the self-induction of the coil in Henry, μ_0 is the permeability of vacuum in Henry/m, N is the total number of turns in the coil, A is the area of the coil in m^2 and l is the length of the coil in m. The self-inductance of a coil depends on the size and shape of the coil, on the number of turns in it, and also the magnetic permeability of material inside it.

3.3 Paramagnetism

If a paramagnetic material is placed in a strong magnetic field, it becomes a magnet, and as long as the strong magnetic field is present, it will attract and repel other magnets in the usual way. But when the strong magnetic field is removed the magnetisation is lost. Paramagnetic materials are considered to be non-magnetic because they exhibit magnetisation only when in the presence of an external electromagnetic field. Also, the flux density within paramagnetic materials is almost the same as it would be in a vacuum.

For paramagnetic materials, each atom possesses a permanent dipole moment by virtue of the incomplete cancellation of electron spin and/or orbital magnetic moments. In the absence of an external magnetic field, the orientation of these atomic magnetic moments are random, such that a piece of material possesses no net macroscopic magnetisation, M. These atomic dipoles are free to rotate, and paramagnetism results when they preferentially align, by rotation, with an external field. However, the dipole moments are prevented from becoming perfectly aligned by their random thermal motion. These magnetic dipoles are acted on individually with no mutual interaction between adjacent dipoles. Inasmuch as the dipoles align with the external field, they enhance it, giving rise to a relative permeability that is slightly greater than unity, and hence the material has a relatively small but positive magnetic susceptibility, χ. The susceptibilities of paramagnetic materials range from about 10^{-5} to 10^{-2} (unitless) [63].

Above a critical temperature, T_C, the spontaneous magnetisation of ferromagnetic materials vanishes and they become paramagnetic. Well above the T_C the susceptibility follows the Curie-Weiss law,

$$\chi = \frac{C}{(T - T_\theta)} \qquad \text{Equation 3.17}$$

where χ is the susceptibility (unitless), C is a constant (different for each material), T is the temperature in Kelvin, and T_θ is the paramagnetic Curie temperature [185].

3.4 Ferromagnetism

Of all the elements found in the periodic table only iron (Fe), nickel (Ni), cobalt (Co), gadolinium (Gd) and dysprocium (Dy) are ferromagnetic. However, there is a relatively large number of ferromagnetic alloys and oxides, including most steel alloys and some iron-based oxides. These materials can possess a permanent magnetic moment in the absence of an external magnetic field and can show very large and permanent magnetisations. Their permeability values are higher than those of the paramagnetic materials, often of the order of several hundreds. Magnetic susceptibilities as high as 10^6 are possible for ferromagnetic materials [63].

Above the critical temperature of the ferromagnetic Curie point, the magnetisation vanishes and the material becomes paramagnetic hence the Curie temperature, T_C, is defined as the temperature above which a ferromagnetic material becomes

paramagnetic [185]. Temperature effects on magnetism have been also investigated by Bethe [186]. Extensive calculations revealed that the atomic displacement of atoms is directly related to the materials magnetic characteristics. Therefore, depending on the distance between the atoms a specific magnetic behaviour is exhibited by the material. For iron, when the microstructure has a BCC crystallography, below the T_C, it is ferromagnetic. If iron is austenitised, the microstructure obtains an FCC crystallography and it becomes paramagnetic. As iron undergoes a phase change between FCC and BCC, it can be shown that interatomic displacement is such that under an FCC orientation, paramagnetism occurs, whereas a BCC structure results in ferromagnetism below T_C [63].

Further experiments on ferromagnetic materials have shown that the permanent magnetic moments and hence the spontaneous magnetisation result from atomic magnetic moments due to electron spin and more specifically from uncancelled electron spins as a consequence of the electron structure [187 - 189]. There is also an orbital contribution to the spontaneous magnetization of a ferromagnetic material resulting from the movement of the electrons in the solid, which is small in comparison to the spin moment. In a ferromagnetic material coupling interactions cause net spin magnetic moments of adjacent atoms to align with one another, even in the absence of an external magnetic field. The origin of these coupling forces is well understood, and has been found to arise from the electronic structure of the metal. This mutual spin alignment exists over relatively large volume regions of the crystal called domains [63].

3.5 Domain magnetism

Experimental studies on paramagnetism have concluded that the application of a small magnetic field has a negligible effect on the magnetisation of a system of free and independent elementary magnetic moments. This can be rationalized by assuming that each domain is intrinsically fully magnetised under the influence of exchange interactions described by a magnetic field. Changes in overall magnetisation are almost all due to rearrangements of domains and the boundaries between them [63, 185]. The reason for the formation of the domain structure is that the potential energy associated with the magnetised sample is thereby minimised. This is inspite of the cost in energy of forming the domain boundaries. Studies of domain properties in ferromagnets tend to be on the properties of either soft or hard magnetic materials. The technological aim of such work is to improve soft materials, such as iron and steel, by making it possible for domain boundaries to sweep through the solid with the minimum constraint, while in hard materials the usual aim is to lock the magnetised state into position as permanently as possible [185]. Figure 3.1 shows the domain orientation in ferromagnetic materials. The favourable domain orientation for soft ferromagnetic materials is shown in figure 3.1c). In producing a domain wall there is a certain amount of energy involved. Equilibrium condition is achieved with a number of domains such that the energy required to produce one or more domain boundaries is equal to the resulting reduction of the field energy. A domain structure such as in figure 3.1c) has zero magnetic field energy. This is achieved by introducing the triangular prism domains at top and bottom of the crystal.

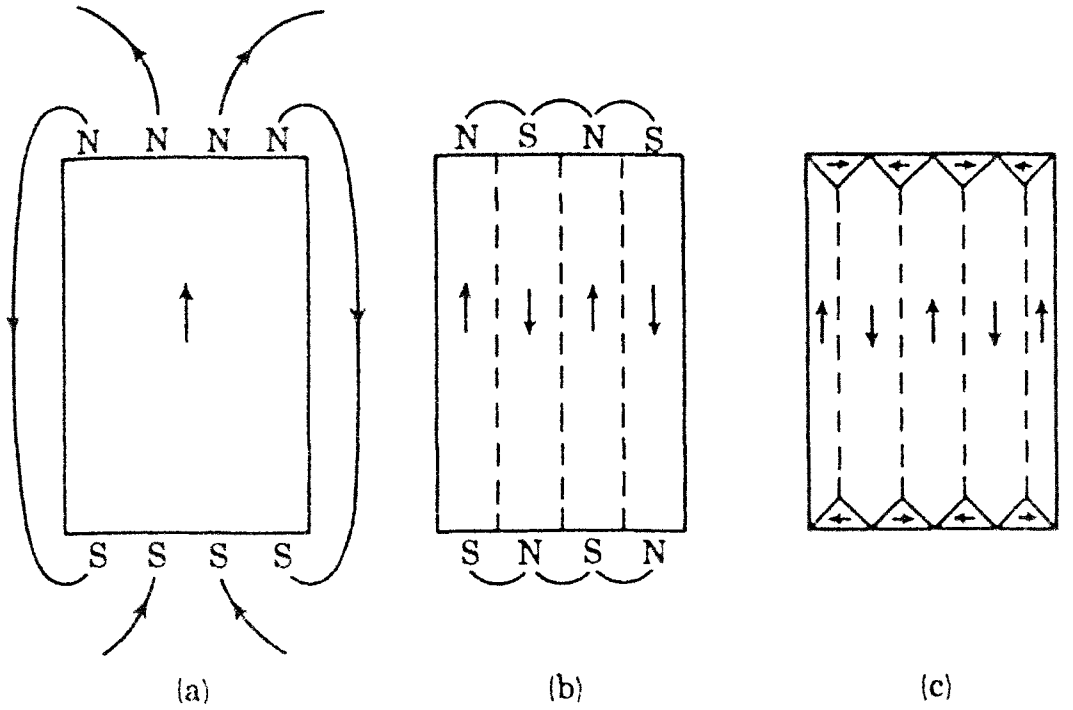

Figure 3.1: Possible orientation of domains in ferromagnetic materials. (Reproduced from Dekker) [185]

Crystal orientation is important when domain properties are considered. Due to magnetocrystalline anisotropy differing energies are involved in magnetising a specimen in different crystallographic directions. The potential energy of a single crystal sample of a ferromagnet depends on the direction with respect to the crystal axes in which it is magnetised. The energy is lowest in an easy direction and a higher field must be applied to make the magnetisation lie in a harder direction. The effect of this energy on the domain structure is that it imposes a constraint on the direction that the magnetisation takes up in a given crystal when no external field is applied. Another significant effect is that it contributes to the intrinsic energy of domain boundary walls and controls their thickness [63].

A domain boundary wall or Bloch wall, consists of the transition layer which separates adjacent domains magnetised in different directions. The total angular displacement across a wall is commonly 180 or 90 degrees. The whole change in spin direction does not usually occur in one discontinuous jump at a single atomic plane but takes place gradually over many planes [63]. The thickness or width of the wall is determined by the opposing influences of exchange energy and magnetocrystalline anisotropy energy. Figure 3.2 shows a schematic representation of a 180° Block wall.

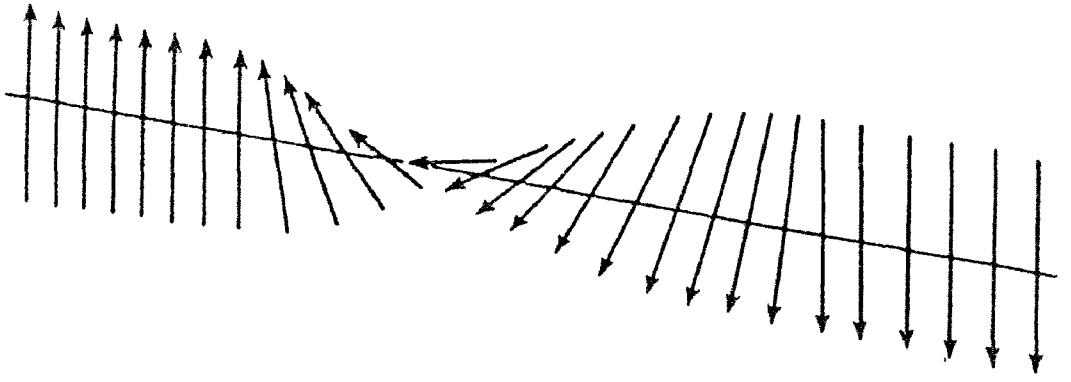

Figure 3.2: Schematic representation of a 180° Block wall. (Reproduced from Dekker) [185]

The shape and size of the domains present at equilibrium in a specimen are given by the condition that the total energy shall be a minimum. They depend considerably on the actual configuration of the specimen. In a long thin single crystal of iron cut with its surface accurately parallel to a (100) crystal face the domain boundaries are parallel lines and the domains which they separate are alternately oppositely magnetised in the direction of the lines. At the end surfaces domains of closure are formed. These minimise the formation of free poles and reduce the magnetostatic energy [185].

The theory of ferromagnetism is centred about the two following hypotheses put forward by Weiss [190]:

a) A ferromagnetic specimen of macroscopic dimensions contains, in general, a number of small regions (domains) which are spontaneously magnetised. The magnitude of the spontaneous magnetisation of the specimen is determined by the vector sum of the magnetic moments of the individual domains.
b) Within each domain the spontaneous magnetisation is due to the existence of a "molecular field" which tends to produce a parallel alignment of the atomic dipoles.

Spontaneous magnetisation implies cooperation between the atomic dipoles within a single domain, i.e. there must be some kind of interaction between the atoms which produces the tendency for parallel alignment of the atomic magnetic dipoles.

The maximum possible magnetisation or saturation magnetisation, (M_S), of a ferromagnetic material at a certain temperature, corresponds to the magnetisation that results when all the magnetic dipoles in a solid piece are mutually aligned with the external field. The saturation magnetisation is equal to the product of the net magnetic moment for each atom and the number of atoms present. The maximum spontaneous magnetisation in ferromagnetic materials occurs at very low temperatures close to absolute zero (0 K). As the temperature rises, increasing thermal vibrations of the atoms causes rotation of the magnetic moments causing a decrease in spontaneous magnetisation [185].

The magnetisation of a soft material such as steel can significantly be affected by pining, i.e. the presence of precipitates in a ferrite or pearlite grain and in the microstructure in general tend to impede the rotation of the magnetic moments causing a reduction in the total magnetisation of the sample. However, in the present thesis the steel types used were largely free of precipitates and thus, the pining factor did not receive further consideration.

3.6 External electromagnetic fields and ferromagnetic materials

When a magnetic field is applied to a demagnetised ferromagnetic sample below its T_C, the domains start to align to the direction of the applied field. The extent of the magnetisation of the material is directly related to the strength of the electromagnetic field. Hence, as the strength of the magnetic field is increased magnetisation also increases, although the relationship is not linear [63].

Flux density is related to H via both the permeability of free space and the materials magnetisation, M, which is in turn dependant upon the material susceptibility to magnetic alignment. The relationship between B, H and M is given in equation 3.18 [63]. However, magnetisation is a function of H, thus B can be directly related to H via two parameters (μ_0 and μ_r) that describe the magnetic properties of the material (equations 3.18 and 3.19).

$$B = \mu_0 H + \mu_0 M = \mu_0 H + \mu_0(\chi \bullet H) \qquad \text{Equation 3.18}$$

$$B = \mu_0 H \bullet (1 + \chi) = \mu_0 \mu_r H \qquad \text{Equation 3.19}$$

where B is the magnetic induction in Tesla, μ_0 is the permeability of vacuum in Henry/m μ_r is the relative permeability (unitless). Initially un-magnetised ferromagnets consist of saturated domains that are randomly arranged. If a magnetic field is applied, the existing magnetic dipoles within each domain will start to align with the field and magnetic moment rotation will occur. Domain rotation is not an irreversible process. If the magnetic field strength is relatively low, removal of the field, depending on the material, may result in the materials magnetic characteristics reverting to those prior to field application. Increasing the field strength above a critical point will result in domain growth, as the Bloch walls are removed through forcible domain alignment. The resulting domain arrangement is irreversible and new magnetic characteristics are obtained. If an even stronger magnetic field is applied, a critical point will be reached where no domain growth and rotation will occur with further field increases. As a direct effect further increase in magnetisation of the material is impossible and the body is then referred to as saturated [63].

3.7 Effect of alloying elements on Curie Temperature and ferromagnetism

Localised magnetic moments are a consequence of non-equilibrium electron shell arrangement, however, thermal agitation affects the atomic equilibrium position. Consequentially, at the Curie temperature, which is related to atomic quantum parameters, the strongly aligned magnetic moments that occur, for example in iron, are destroyed. The relationship between magnetisation and temperature for iron is shown in figure 3.3. As it is seen in figure 3.3 below the T_C iron is ferromagnetic, however, as temperature increases to T_C magnetisation disappears [63].

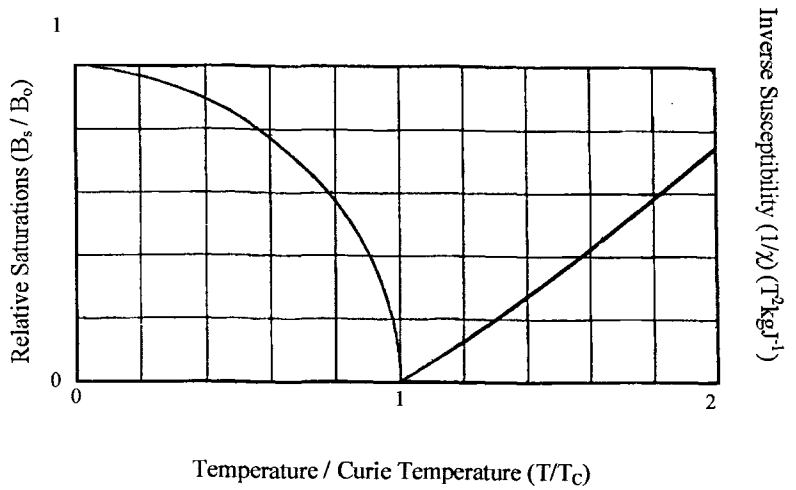

Figure 3.3: Relationship of magnetisation to temperatures relative to the T_C for iron. (Reproduced from Bozorth) [63]

As a connsequence of the interactions between electrons of different atoms, and the affects of atoms upon a crystal lattice, addition of solute atoms, changes a materials magnetic properties [63, 191]. In general alloying elements with increasing content in steel have a lowering effect on the T_C of the steel as shown in figure 3.4. This is a consequence of the interactions between electrons of different atoms, and the affects of atoms upon the iron crystal lattice [63, 191]. The only exception to this general rule is vanadium (V). For up to 6 in wt % V content in steel, the T_C tends to increase. However, above this concentration the T_C starts decreasing again down to 750°C for V contents of up to 40 in wt %. For the level of alloying elements seen in commercial carbon steels used as strip the T_C will be affected greatly.

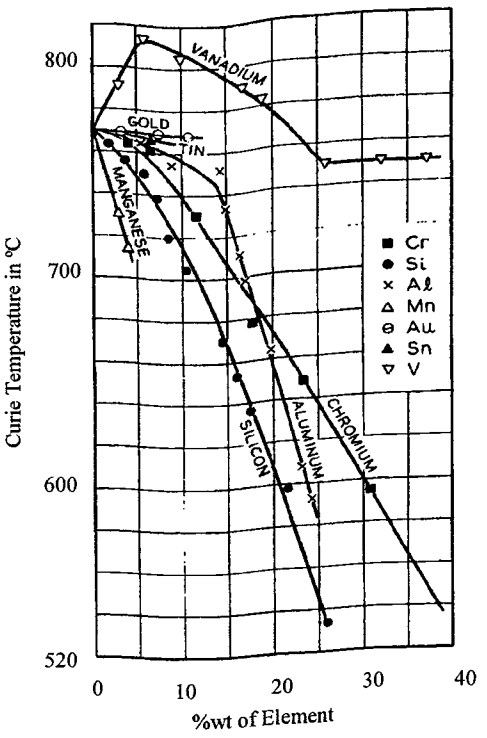

Figure 3.4: Relationship between the Tc and some alloying elements.

(Reproduced from Bozorth) [63]

Precipitation of a finely dispersed, non-ferromagnetic phase in a ferromagnetic matrix is usually accompanied by a decrease in permeability, known as magnetic aging. The basic cause of the magnetic aging effect is believed to be well understood. The precipitated particles interact with the Bloch walls present in the matrix for a number of reasons [192-195]. Because of this interaction they form obstacles which hinder the free movement of these walls and macroscopically this is reflected in the observed increase in magnetic hardness. Magnetic aging is a rather complex phenomenon, the main reason being that the changes in the bulk magnetic properties not only depend on the amount and intrinsic magnetisation of the precipitated phase but also on numerous other parameters which define the form of the precipitate on a micro scale such as particle size, size distribution, degree of randomness of the particle

distribution in the matrix, particle shape, particle orientations for nonspherical shapes, and on the degree of coherency with the matrix [196].

3.8 Eddy currents

Faraday's early studies showed that an electric current is induced in a closed circuit when a nearby magnet is moved. Later observations showed that the induced current could be produced in a variety of ways. Thus, instead of a magnet being moved in the neighbourhood of a stationary coil, by moving the coil itself the same result is produced. Similarly, the effect will be observed in the circuit of a wire loop situated in a magnetic field, if the loop is distorted so that its area is changed. Again, induction can take place if the intensity of the magnetic field in a coil were changed, for example by altering the current in a neighbouring coil. The induced voltage or induced electromotive force (EMF) induced in a loop of wire is equal to the time rate of change of the magnetic flux through the loop. If N loops are wound in a coil, the induced EMF is N times that for one loop. This is called the Faraday law and is quantified by equation 3.20 [176].

$$\varepsilon = -N\frac{\Delta\Phi}{\Delta t} = -N\frac{\Phi - \Phi_0}{t - t_0} \qquad \text{Equation 3.20}$$

where ε is the EMF in volts, N is the number of turns in the coil and Δt is the time in seconds. Lenz stated that the direction of the induced EMF is such that any current it produces tends to oppose the change of flux (Lenz's law) [183]. The significance of Lenz's law may be explained with reference to figure 3.5.

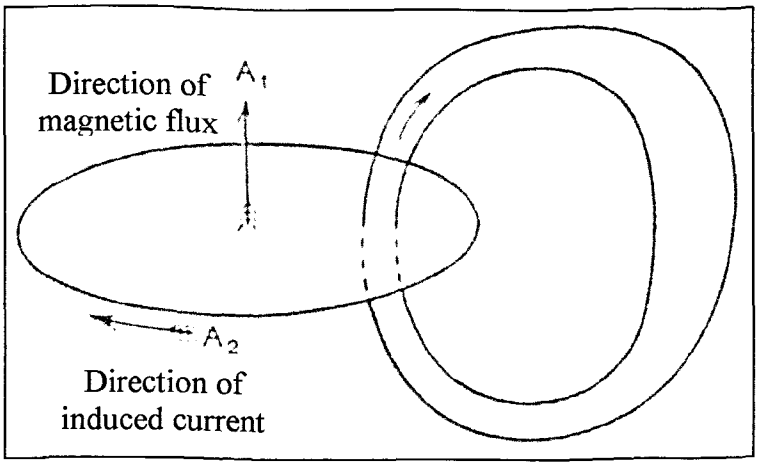

Figure 3.5: The resultant electromagnetic flux and its direction A_1 due to the presence of an electric current with direction A_2. (Reproduced from Carter) [183]

If the resultant flux through the circuit has the direction A_1 and is increasing, the induced current will tend to set up a flux in the direction opposite to A_1. The direction of the current must therefore be as indicated by the arrow A_2.

When an alternating current flows in a coil the resulting electromagnetic field has a varying direction. In the case where the coil is placed in close proximity to, or around, a conducting surface an EMF is induced in the material. Following the laws put forward by Faraday and Lenz, the changes in the electromagnetic field of the coil will be resisted by currents setting up an electromagnetic field of opposite direction to that of the coil. These induced circulating currents are known as eddy currents [183].

Eddy currents always resist the penetration of flux in a ferromagnetic material when this derives from an a.c. electromagnet. Eddy currents cease to exist if a d.c. electromagnet is used. Their density and magnitude varies with the frequency of the

a.c. flowing in the coil, i.e. the higher the frequency of the a.c., the faster the changes on the electromagnetic field. Therefore, a rapidly changing electromagnetic field would cause a higher electromotive force which in turn would give rise to an increased density of flowing eddy currents and with higher magnitude. The result of this would be that the flux penetration reduces as the frequency becomes higher. For the case of a very good conductor and an a.c. electromagnetic field operating at a relatively high frequency (of the order of a few kHz) the flux penetration can be limited to a few tens of micrometers from the surface of the sample. The magnitude and phase of the eddy currents will also affect the induced voltage on the coil and thus its impedance which will increase [183].

Eddy current sensors have been used for a number of years as a means of detecting defects under the surface of a solid [197-202]. As an example, assume that there is a deep crack in the surface immediately underneath the coil. This will interrupt or reduce the eddy current flow, thus decreasing the loading on the coil and increasing its effective impedance.

This is the basis of eddy current testing, by monitoring the voltage across the coil in such an arrangement it is possible to detect changes in the material of interest. Note that cracks must interrupt the surface eddy current flow to be detected. Cracks lying parallel to the current path will not cause any significant interruption and may not be detected. A number of factors, apart from flaws, will affect the eddy current response from a probe. Successful assessment of flaws or any of these factors relies on holding the other factors constant, or somehow eliminating their effect on the results. It is the

elimination of undesired response that forms the basis of much of the technology of eddy current inspection. The main factors are:

a) material electrical conductivity. The conductivity of a material has a very direct effect on the eddy current flow: the greater the conductivity of a material the greater the flow of eddy currents on the surface. Conductivity is often measured by an eddy current technique, and inferences can then be drawn about the different factors affecting conductivity, such as material composition, heat treatment, work hardening etc.

b) permeability. This may be described as the ease with which a material can be magnetised. For non-ferrous metals such as copper, brass, aluminium etc., and for austenitic stainless steels the permeability is the same as that of 'free space', i.e. the relative permeability (μ_R) is one. For ferrous metals however the value of μ_R of may be several hundred, and this has a very significant influence on the eddy current response, in addition it is not uncommon for the permeability to vary greatly within a metal part due to localized stresses, heating effects etc.

c) frequency. Eddy current response is greatly affected by the current (i.e. a.c.) frequency being used, i.e. as the a.c. frequency increases the eddy current effect increases as discussed earlier.

d) geometry. In an engineering component, for example one which is not flat or of infinite size, geometrical features such as curvature, edges, grooves etc.

will exist and will effect the eddy current response. Test techniques must recognise this, for example in testing an edge for cracks the probe will normally be moved along parallel to the edge so that small changes may be easily seen. Where the material thickness is less than the effective depth of penetration (see equation 3.20) this will also affect the eddy current response.

e) proximity or lift-off. The closer a probe coil is to the surface the greater will be the effect on that coil in terms of the magnitude of the induced voltage. This is due to the fact that more magnetic flux goes through the product thus causing a stronger induction effect and hence giving rise to a higher induced electromotive force in the sensing coil.

f) depth of penetration. The eddy current density, and thus the strength of the response from a flaw, is greatest on the surface of the metal being tested and declines with depth. It is mathematically convenient to define the "standard depth of penetration" where the eddy current is 1/e (37%) of its surface value. The standard depth, δ, of penetration in m is given by the formula [203]:

$$\delta = \sqrt{\frac{2}{\omega\sigma\mu}} = \frac{\sqrt{2}}{\sqrt{2\pi\mu_0}} \cdot \sqrt{\frac{\rho}{\mu_R}} = 503\sqrt{\rho / \nu * \mu_R} \qquad \text{Equation 3.21}$$

where ω is the angular frequency of the applied magnetic field in rad/s, σ is the conductivity in Siemen, μ is the permeability of the material in Henry/m, μ_0 is the permeability of vacuum in Henry/m, ρ is resistivity of the material at

temperature T in ohms, v is frequency in Hz and μ_R is relative permeability at temperature T.

From equation 3.21, it can be concluded that depth of flux penetration decreases with an increase in frequency, decreases with an increase in conductivity and decreases with an increase in permeability. This is very significant as penetration into ferromagnetic materials at high frequencies is very small and hence the sampling depth is minimised. In the case where deeper sampling is needed for a ferromagnetic material such as steel a possible method is to magnetically saturate the sample so as to create a situation in which all the randomly orientated magnetic dipoles in the ferromagnetic material are aligned in the same direction i.e. parallel to the applied magnetic field. Under this situation, the slope of the flux density vs. field intensity curve (B-H curve) becomes constant and the material behaves as if a non-ferromagnetic material and hence, allows higher sampling depth. However, in the present project no testing was conducted towards this direction due to the difficulties involved in the hot electromagnetic tests and the limited experimental time available.

It should be also noted that high magnitude eddy currents cause very high values of impedance to be recorded by an electromagnetic sensor due to the strong effect of their electromagnetic field which adds to the induction effect hence creating a much higher electromotive force within the sensing coil [183]. Therefore, although eddy currents cause a reduction in the sampling depth, the effect of the electromagnetic noise becomes negligible due to the much stronger electromagnetic signal recorded as it is shown in chapter 5.

3.9 The electromagnetic sensing technique for microstructural determination

The electromagnetic method is based on the magnetic properties of austenite (paramagnetic) and ferrite, pearlite, bainite and martensite (steel is considered to be ferromagnetic below the Curie temperature ~ for steels with low carbon and alloy content the T_C is approximately 770°C [63]). The Curie temperature of a steel alloy depends on its chemical composition as discussed in section 3.7.

Based on the magnetic properties exhibited by steel at T_C an electromagnetic sensor should be able to distinguish the paramagnetic to ferromagnetic transition and hence the phase transformation of austenite to ferrite, pearlite, bainite and/or martensite when this occurs below the Curie point. For most carbon steels with carbon contents higher than 0.6 % C in weight, the initiation of phase transformation, under equilibrium conditions, lies below 770°C [64] (it is noted that the exact temperature at which phase transformation starts is affected by the presence of other alloying elements as discussed in chapter 2). However, the temperature at which phase transformation begins can be suppressed by using relatively high cooling rates, i.e. of the order of several hundred degrees Celsius per second. In this case, most or complete phase transformation in steel alloys with carbon contents lower than 0.83 % C in weight and depending on the content of other alloying elements present, can be achieved at temperatures below the Curie point and hence be detectable by an electromagnetic-based sensor. In practice, accelerated cooling systems on the run-out tables of strip mills can suppress the austenite to ferrite transformation temperatures to below the T_C [64].

There are various types of electromagnetic sensors that can be employed to detect the ferromagnetic transformation such as a.c., d.c. and eddy current systems [204]. An a.c. system uses an excitation coil to create a magnetic flux that is proportional to the induced voltage in the search coil(s). As it was shown earlier, when an a.c. current passes through the loops of the excitation coil a magnetic field is produced. Since the loops of the sensing coil are concentric with those of the excitation coil the magnetic-field lines caused by the current in the excitation coil will pass through the sensing coil. Due to the a.c. current, changes will occur in the magnetic field and hence magnetic flux produced by the excitation coil resulting in a voltage being induced in the sensing coil. This process is called mutual inductance and is the basic principle of the sensor design discussed in the present thesis.

An a.c. current i_1 passing through the excitation coil, which has N_1 turns. Produces a magnetic field. The magnetic-field lines produced by the excitation coil pass through the sensing coil with N_2 turns. The magnetic flux through each loop of the sensing coil is designated by the symbol Φ_{21} (the subscript 21 refers to the flux through the loops of the sensing coil that are caused by the current in the excitation coil). The total flux through all N_2 turns of the sensing coil is $N_2\Phi_{21}$. Therefore, the mutual inductance M_L of the coils is defined in equation 3.22 as [176]:

$$M_L = \frac{N_2\Phi_{21}}{i_1} \qquad \text{Equation 3.22}$$

where M_L is the mutual inductance in volts, N_2 is the number of turns of the sensing coil, Φ_{21} is the magnetic flux that passes through the loops of the sensing coil and i_1 is

the operating current of the excitation coil. M_L depends on the size, orientation and separation of the coils as well as on the magnetic permeability of the material within the two coils. If the current in the excitation coil varies with time from equations it is found that the induced EMF in the sensing coil is equal to [176]:

$$\varepsilon_2 = -M_L \frac{\Delta i_1}{\Delta t} \qquad \text{Equation 3.23}$$

In the proposed sensor design, the operating alternating current i_1 in the excitation coil produces a magnetic field whose magnitude at each instant of time is given by equation 3.24 [176]:

$$B = \frac{N_1 \mu_R i_1}{2r} \qquad \text{Equation 3.24}$$

where N_1 is the number of loops in the excitation coil, μ_R is the relative permeability of the steel sample inside the coil, and r is the radius of the coil. Since the sensing coil is concentric with the excitation coil the magnetic field through each of its N_2 loops is the approximately the same as that through the loops of the excitation coil. Thus the flux in the sensing coil caused by the current in the excitation coil is approximately given by equation 3.25 [176]:

$$N_2 \Phi_{21} = N_2 BA = N_2 \left(\frac{N_1 \mu_R i_1}{2r} \right) A \qquad \text{Equation 3.25}$$

where A is the area inside the sensing coil. By combining equation 3.22 with equation 3.25 it is found that the mutual inductance between the coils is equal to [176]

$$M_L = \frac{N_2 N_1 \mu_R A}{2r} \qquad \text{Equation 3.26}$$

The variation of the ε_2 caused by the varying relative permeability of the steel sample and the a.c current passing through the excitation coil will result in a self-induced EMF, ε_L, to occur in the sensing coil due to the phenomenon of self-inductance given by equation 3.27 [176]:

$$\varepsilon_L = -\Delta L \frac{\Delta i_1}{\Delta t} \qquad \text{Equation 3.27}$$

where, ε_L is the self-induced EMF in volts, ΔL is the variation of self inductance due to variations in the magnetic flux in Henry Δi_1 is the variation of the current in Amps over time Δt in seconds.

The current through a resistor caused by an alternating voltage is calculated using Ohm's law (I = V/R). A more complex expression is needed to determine the resistance in a coil due to the phenomenon of self-inductance. It is noted that the term impedance rather than resistance is commonly used to describe the opposition to current flow through an a.c. circuit. The impedance of a coil is given by the equation 3.28 [176]

$$Z = R + j\varpi L - j\frac{1}{\varpi C} = R + j(\omega L - \frac{1}{\omega C}) \quad \text{Equation 3.28}$$

where Z is the total impedance of the circuit, R is the resistance of the coil in ohms, ωL is the inductive reactance of the coil in ohms and $1/\omega C$ is the capacitance. ω is the angular frequency and is equal to the $2\pi v$ where v is the frequency of the operating a.c. current in the excitation coil. If capacitance is equal to zero equation 3.28 is re-written in the form

$$Z^2 = z'^2 + z''^2 = R^2 + (\omega L - \frac{1}{\varpi C})^2 = R^2 + (\omega L - 0)^2 \quad \text{Equation 3.29}$$

or

$$|Z| = \sqrt{R^2 + (\varpi L)^2} \quad \text{Equation 3.30}$$

where z' is the real impedance in ohms and is equal to R and z'' is the imaginary impedance and is equal to the inductive reactance and capacitance of the circuit in ohms. Imaginary impedance is defined as the impedance 90° out of phase with the driving current. In electromagnetic circuits, imaginary impedance relates the induced voltage in a secondary or sensing coil to the source, i.e. the primary or excitation coil. As real impedance, is defined the impedance which is in phase with the source.

By monitoring the changes of the induced EMF in the sensing coil it is possible to measure the impedance which can then be related to the transformed fraction [207]. Thus, taking into account Ohm's law imaginary impedance at any given moment will be given by equations 3.31 and 3.32 [176]:

$$z'' = 2\pi\nu L = \varpi L = \frac{\varepsilon_L}{i_1} \qquad \text{Equation 3.31}$$

or

$$z'' = \frac{\varepsilon_L}{i_1} \qquad \text{Equation 3.32}$$

where z'' is the imaginary impedance of the sensing coil in ohms, ε_L is the self-induced voltage in Volts and i_1 is the exciting current in Amps. For the needs of the present project a Solartron SI 1260 impedance analyser was employed in order to record directly the real and imaginary impedance values.

The self-induced EMF at the sensing coil varies as the permeability of steel changes. Hence by measuring the imaginary impedance a measure of the transformed fraction can be deduced. The present study is concerned with the development of an a.c. electromagnetic sensor for monitoring phase transformation during cooling under laboratory conditions.

3.10 Past research and results

Lacroix et al. [64] are known to have been the first to develop a phase transformation detector that measures the magnetic response due to induced eddy currents. The proposed sensor consisted of one excitation and one sensing coil (flat shape) and was used for the detection of phase transformation in steel strip and plate in the run-out tables of a strip and a plate rolling mill. The measured quantity related to the phase transformation of steel was the impedance of the sensing coil. The detecting system employed in the run-out table was composed by eight sensors placed along the length

of the run-out table and at a distance of 10 mm from the steel sampled. The sampling frequency used was rather high, 10 kHz, and thus the penetration depth in austenite was a few millimetres whilst in ferrite, due to its higher permeability it would not exceed a few tenths of a millimetre. The experiments were conducted for two different strip thickness, 2.5 mm and 4.75 mm. It was found that the detecting system was capable of detecting the paramagnetic to ferromagnetic transition and the end of phase transformation. However, the exact position of the run-out table where the paramagnetic to ferromagnetic transition occurred is not known since the probes were fixed and picked up the ferromagnetic phase as the strip passed over them. Furthermore, the volume fraction that had transformed before the paramagnetic to ferromagnetic transition was picked-up by the sensor is unknown. The exact point where the phase transformation was found to be completed is also unknown for the same reasons. However, it is highly doubtful that the end of the phase transformation was accurately detected since the sampling depth achieved by the detection system is only a fraction of the thickness of the steel strips tested. It is likely that the centre would have transformed a little bit later than the outer part of the steel without causing any variation to the recorded electromagnetic signal due to the low sampling depth. For the steel plate, experimental results were limited only to the detection of the paramagnetic to ferromagnetic transition due to the fact that there were temperature gradients over the width of the plate. Although the work conducted by Lacroix et al. has prompted further research there are a number of issues in their report that need further clarification, in particular any direct link between impedance and transformed volume fraction.

Early work by Morita et al. (1985, 1986) [205, 206], in Kawasaki Steel Corporation, reported the development of an experimental on-line transformation detector consisting of an alternating current (a.c.) exciting coil and two search (sensing) coils (with the capability of adding more if required) positioned along the rolling axis of the steel strip. Figure 3.6 shows the EM sensor design proposed by Morita et al.

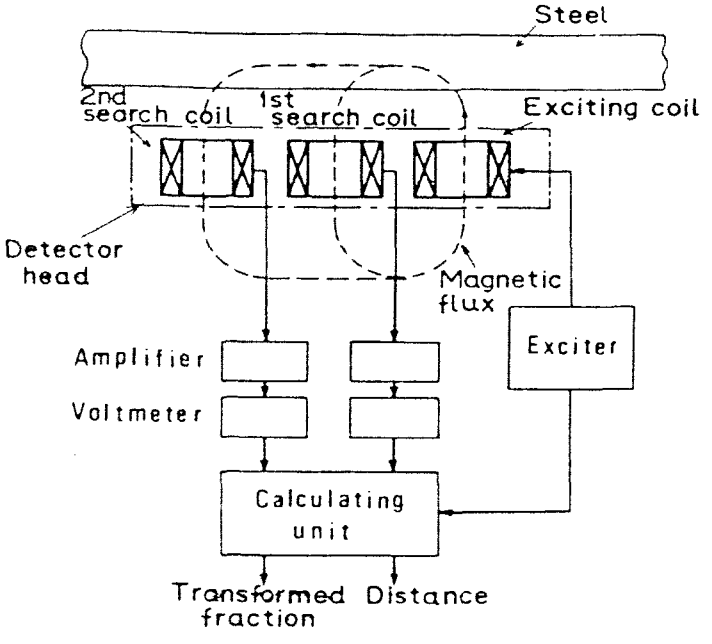

Figure 3.6: The EM sensor design proposed by Morita et al. (Reproduced from Morita et al.)[205]

The operational range of frequencies possible with the specific detector was between 5 Hz – 10 kHz. According to the results reported by Morita et al. the proposed detecting system was capable of detecting phase transformation of steel as it progressed along the run out table of a hot rolling mill. The feedback from the sensor was used as input data to a computing unit connected with the detecting unit in order to calculate the transformed fraction in the steel. The system also measured the flatness of the strip. Unfortunately, in this report Morita et al. focus on the technical

design of the sensor and do not provide results in order to verify the accuracy of the proposed system.

In another report (1985) Morita et al. [207] produce more details regarding the accuracy of their proposed detector design. The technical details of the detecting system remain identical as those presented earlier. According to this report quantitative and accurate measurement of the fraction transformed is possible even under the condition of rapid change in distance between hot rolled steel and the detector due to simultaneous distance correction. Additionally, the transformation rate of austenite into ferrite can be evaluated through the calculating unit with data fed to it by the detector. The distance from the steel at which the detector is effective is given to be in the range of 20-120 mm. The samples used in the experimental work were carbon steel strips with carbon content ranging from 0.07 - 0.47 in wt %. The fraction transformed at the simulated cooling and coiling temperatures and the transformation rate measured by the transformation detector for a steel strip with 0.35 in wt % carbon content was found to have a very good correlation with the mechanical properties of hot rolled steel. Figure 3.7 shows the cooling curve and transformed fraction measured by optical thermometer and transformation detector, respectively on coiling of sheet sample for various cooling patterns.

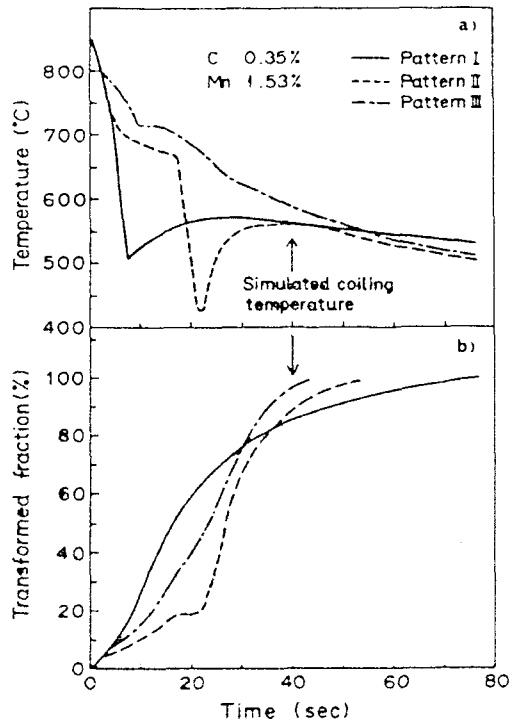

Figure 3.7: Cooling curve and transformed fraction measured by optical thermometer and transformation detector, respectively on colling of sheet sample for various cooling patterns. (After Morita et al.) [207]

Further experimental work conducted by the research group in Kawasakin Steel Corp. (Ishibashi, Morita et al., 1987) [208], based on the aforementioned detector design aimed at establishing a relationship between electromagnetic measurement, induced electromotive force and steel strip temperature. In this report the Kawasaki-based research group investigated the effect of strip temperature on the induced electromotive force in the sensor by performing experimental tests in the continuous annealing line. It was shown that the induced electromotive force increased monotonically (i.e. linearly related with temperature) up to the T_C; just above the T_C the induced electromotive force became zero as shown in figure 3.8.

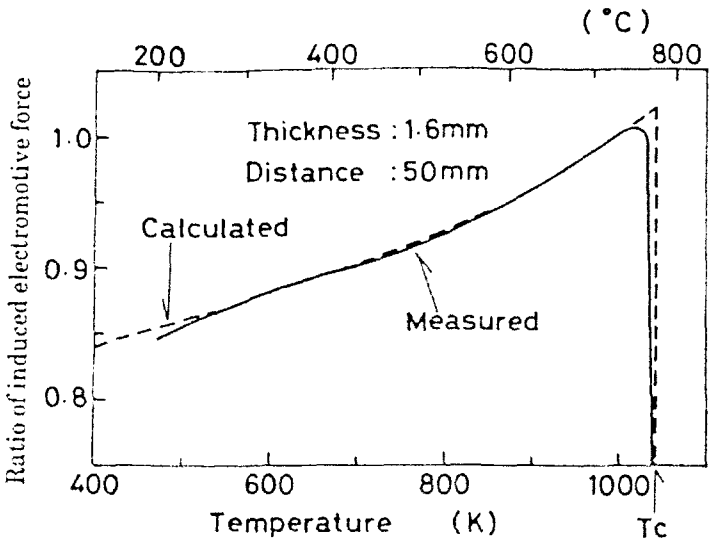

Figure 3.8: Temperature dependence of the induced electromotive force measured with the EM sensor (Laboratory data). (After Ishibashi et al.) [208]

Comparison of the ratios of calculated and measured induced electromotive forces were found to agree quite well with temperature (±2 % difference between the calculated and the measured values). Hence, through the measured induced electromotive force it is possible to obtain the strip temperature. However, the relationship between the ratio of induced electromotive force and the transformed fraction with temperature was not presented in the report. It is not known whether the system requires calibration for each steel type or whether a fundamental relationship was developed to allow accurate modelling.

A more recent article (1991) [209] obtained from the Kawasaki-based research group reported the installation of the electromagnetic detecting system in the run out table of the finishing mill at the Mizushima Works hot strip mill. A newly developed mathematical transformation progress model was introduced in the cooling control system in 1991 as a means of improving product quality uniformity. The

mathematical transformation progress model is tuned by the electromagnetic transformation detector and a precise temperature model in which consideration is given to the dependence of the heat transfer coefficient on temperature and temperature distribution in the depth direction. According to the report, the two models make possible the exact prediction of changes in surface and mean temperatures, and of the transformed fraction in the cooling process, resulting in improved coiling temperature accuracy. Figure 3.9 displays an example of the process model calculation of cooling zone.

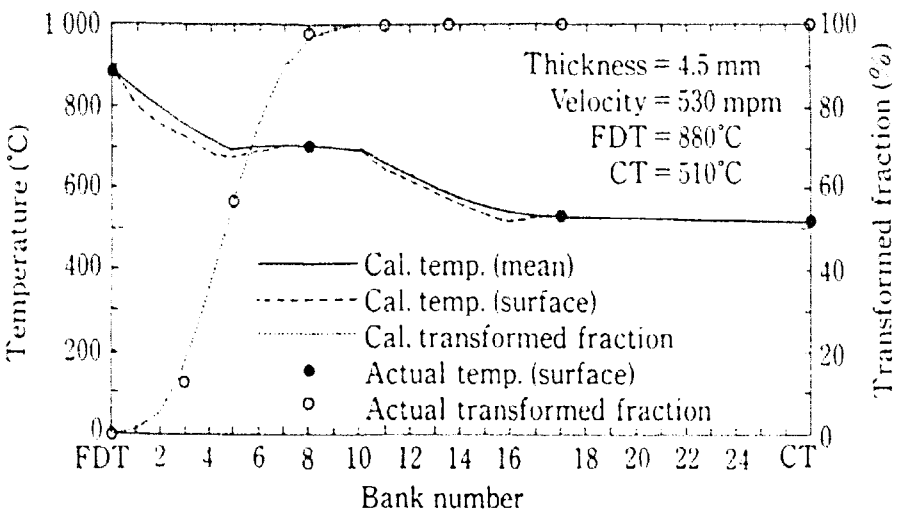

Figure 3.9: Example of process model calculation of cooling zone.

(After Yahiro et al.) [209]

The results produced for a strip with thickness 2.5 mm regarding temperature coiling control displayed an accuracy ±10.9°C with reference to the coiling temperature as shown in figure 3.10.

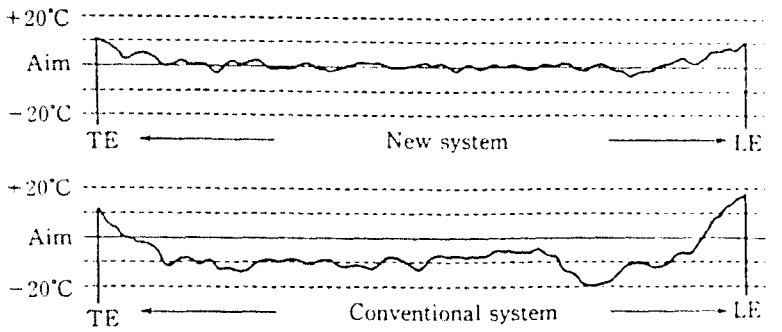

Figure 3.10: Example of coiling temperature control for strip steels with thickness of 2.5 mm. (Yahiro et al.) [209]

Unfortunately, the article does not include information regarding the compositions of the steel used during the experimental testing.

Duijn (1999) [203] at Corus Group developed an electromagnetic detector following the electromagnetic detector design proposed by Morita et al. Initial measurements were performed at room temperature in order to determine the capability of the electromagnetic detector to distinguish paramagnetism (Al), diamagnetism (Cu and Cu-Zn) and ferromagnetism (Ni and Steel). It was found that the detector could successfully distinguish the different magnetic properties of materials whilst the effective operating distance was determined to be 1-6 cm. The frequency employed during measurements was 1000 Hz. Hot tests were performed in the Continuous Annealing Simulator (CASIM). CASIM is capable of resistance-heating a strip or plate by the application of an a.c. current. After heating, cooling can be accelerated in different ways, i.e. compressed air and/or with water droplets. During the experimental procedure the temperature is registered and controlled by thermocouples. However, temperature uniformity of the samples during tests was found not to be very good; unfortunately exact details were not included in the report.

Hot tests on steel plates at a distance of 2.3 cm from the detector succeeded in determining the paramagnetic to ferromagnetic transition during cooling as shown in figure 3.11.

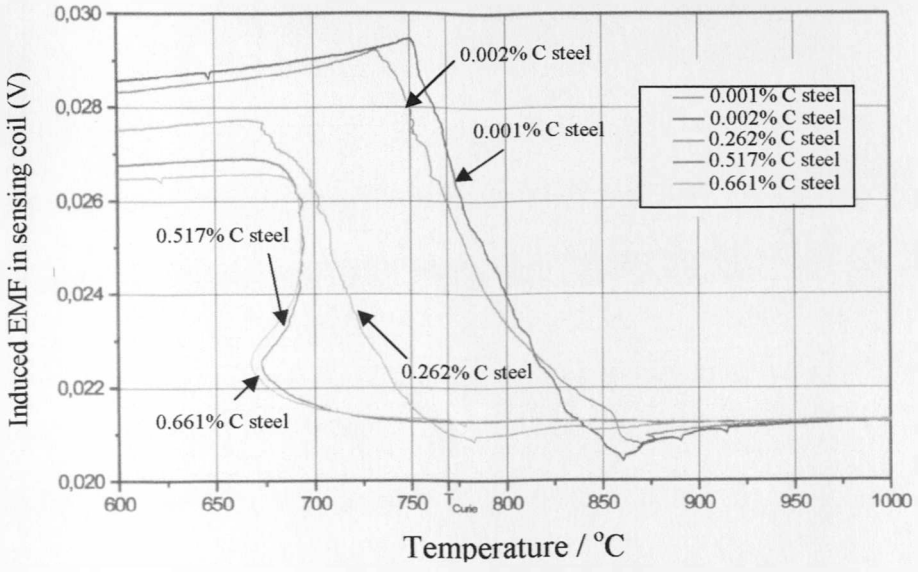

Figure 3.11: Induced voltage – temperature traces showing the electromagnetic response for steel plate samples of various compositions during cooling. (Reproduced from Duijn) [203]

The carbon content of the steel plates used in the experimental procedure ranged from 0.004 - 0.661 in wt %. Due to thermal gradients over the samples and the high frequency used during the tests, the detection and measurement of phase transformation during cooling was only possible for the high carbon steel compositions, i.e. for the 0.517 and 0.661 in wt % C as seen in figure 3.11, where the transformation occurs at approximately 660 – 690°C. For the low carbon steels (0.001 and 0.002 in wt%) transformation would be expected to be complete by the Curie temperature, the change in induced EMF registered above the Curie temperature in figure 3.11 is not explained but may be due to the inaccuracies in temperature measurement. The main reason for the poor results obtained, and this was recognised

in part by Duijn in his report, was the very small sampling depth achieved during tests due to the high frequency employed. It is also apparent that the experimental setup was not the most appropriate one and uniformity of temperature during cooling of the samples was not achieved adding further to the drawbacks of the experimental procedure.

Recent work at Corus investigated the possible sensor designs that could be employed for the detection of phase transformation during steel cooling. Johnstone et al. (2001) [204] reported results for U-shaped d.c. and a.c.-based detectors. It was revealed that the d.c. type sensor had the potential of measuring the average percentage phase transformation for thin strip (thickness 2-5 mm) while a.c. type sensors could measure the transformation at varying depths of the steel as determined by frequency and thus could be employed for measurements in thicker plates. Tests were conducted on a low carbon steel block (composition was not reported) on a pilot scale industrial mill. Temperature during testing was measured through the use of pyrometers. The frequencies employed for the a.c. detector were 1 kHz and 10 kHz. Lift-off effects (i.e. distance between the detector and the steel sample) were also investigated and revealed that the signal output of the detector decreased parabolically with distance. The results obtained with the a.c. detector for the specific frequencies are shown in figure 3.12.

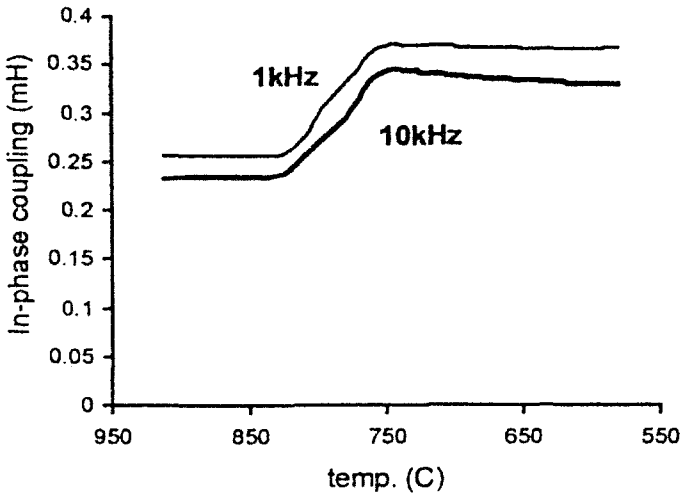

Figure 3.12: Self-induction - temperature diagram showing the response of a two-coil eddy current sensor at frequencies 1 and 10 kHz. (After Johnstone) [204]

Sharif et al. [210] used an array of electromagnetic sensors to image the progression of transformation along a sample steel block, 2.5 mm thick (carbon content 0.077 in wt %) on a pilot scale industrial mill. The sensor array employed consisted three U-shaped d.c. sensors placed along the width axis of the plate and five temperature sensors (pyrometers) placed along the rolling axis. The sample block was heated to above 1100°C in a gas-fired furnace. Then the sample was removed from the furnace and during the experiment one end was quenched in a water bath to induce a thermal gradient along the length of the sample to simulate the conditions in a run-out table. The sample was then passed repeatedly back and forth over the sensor array while transforming. The temperature sensors were used to image the temperature profile of the steel block during cooling. The data obtained through the temperature sensors were then correlated to the data obtained through the electromagnetic sensors. Figure 3.13 shows the experimental setup used by Sharif et al.

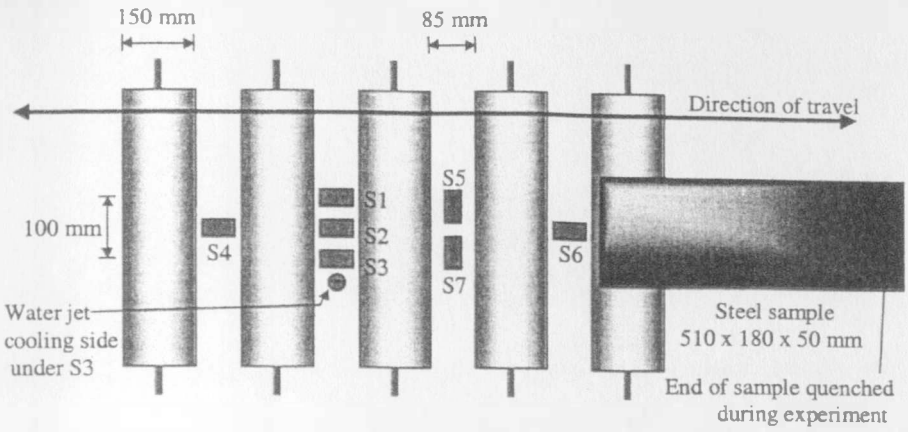

Figure 3.13: Deployment of the array for the hot tests. S1-S3 are EM sensors while S4-S7 are temperature sensors (pyrometers). (After Sharif) [210]

The electromagnetic sensors were capable of detecting the paramagnetic to ferromagnetic transition of the ferrite which had formed already above the Curie temperature whilst the temperature sensors successfully imaged the temperature profile of the steel block during cooling. Figure 3.14 shows the signal obtained from the electromagnetic sensors.

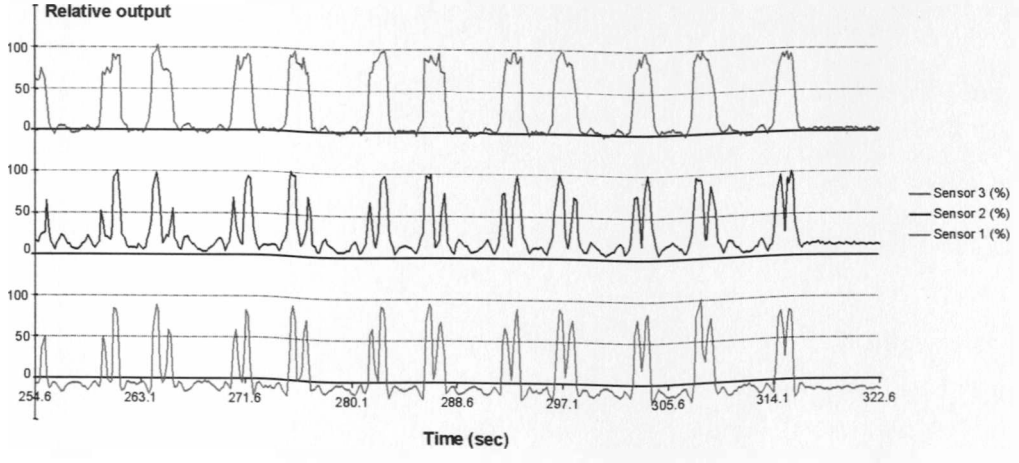

Figure 3.14: Output of sensor channels S1 (lower trace)-S3 (upper trace) from 255-325 s. (After Sharif et al.) [210]

The progress of phase transformation could not be detected by the electromagnetic sensors due to the fact that the steel type used in the experiments transforms from austenite to ferrite above T_C.

Further work by Binns et al. (2001) [211] involved the use of a Multi-Frequency Impedance Analyser (MFIA) node to monitor steel strip transformation. The purpose of the MFIA is to simultaneously measure the relative impedance of the sensing head at eight frequencies. Impedances are recorded relative to a datum, i.e. the values when no sample is present. The MFIA sensing head consisted of a primary excitation coil and four sensing coils wound on a H-shaped ferrite core. To investigate the applicability of the proposed design to on-line monitoring the sensor was placed in proximity to a 2 mm thick steel strip sample as it cooled from 830°C to 200°C. The frequencies used varied from 781 Hz to 100 kHz. Investigation of the lift-off effect by varying distance between the sensor and the sample between 40-70 mm showed that the signal reduced significantly as the distance increased. In the report three different steel compositions have been considered (0.3, 0.4 and 0.76 in wt % C). It was found that the sensor was capable of detecting the paramagnetic to ferromagnetic transition for all the samples and in addition to measure the phase transformation as it progressed below the T_C for the 0.4 and 0.76 in wt % samples as shown in figure 3.15.

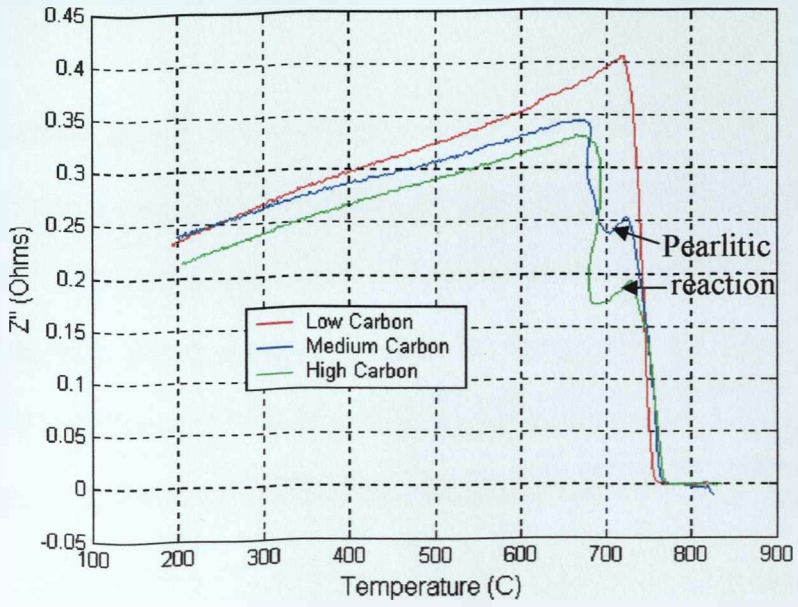

Figure 3.15: Comparison of impedance – temperature traces obtained for 0.3, 0.4 and 0.76 in wt % C steels. (After Binns et al.) [211]

No correlation of the obtained signals and electromagnetic response with microstructure development is offered in the particular report.

Related work conducted by the present research group at the University of Birmingham in co-operation with researchers from the University of Lancaster and Corus Group has succeeded in correlating microstructural development and variations with the electromagnetic response. The results produced from the present partnership have been reported in a number of published articles [212-221] which are not presented in this section. The experimental procedure employed and the results obtained are the subject of the rest of the present thesis.

3.11 Sensor design principles

The a.c. electromagnetic sensor design used in the present study consisted of a ceramic cylinder around which the primary (exciting) and secondary (sensing) coil were wrapped. The exciting coil was operated at a pre-chosen voltage at a frequency range of 1 Hz to 5 kHz in order to generate the required electromagnetic field. Low frequencies (1 - 10 Hz) are of most interest, because at these frequencies the effects of eddy currents are minimised and maximum depth penetration of the magnetic flux is possible. At low frequencies the magnitude and density of the eddy currents flowing within the material is low and therefore the electromagnetic field generated by the exciting coil is capable of penetrating deeper in the sample. However, if the operating frequency of the excitation coil increases this gives rise to eddy currents with higher magnitudes that resist the penetration of the electromagnetic field produced from the excitation coil and reduce the sampling depth. Any changes that occur in the electromagnetic properties (permeability and conductivity) of the sample cause a change in the magnetic flux density followed by a change in the magnitude of the induced voltage in the sensing coil. Variations in the magnitude of the recorded self-induced voltage in the sensing coil cause a change in the recorded impedance as it was shown earlier. Impedance value increases when phase transformation takes place from paramagnetic to ferromagnetic phase, i.e. in the case of steel during cooling below the Curie temperature. The opposite would occur during the phase transformation (or transition) from ferromagnetic to paramagnetic phase, i.e. the magnitude of the induced voltage would decrease giving a minimum impedance value.

3.12 Summary

During heating of steel, the magnitude of thermal vibrations of atoms increases. This causes the directions of any magnetic moments that may be aligned to tend to become random. For ferromagnetic materials, the atomic thermal motions counteract the coupling forces between the adjacent atomic dipole moments, causing some dipole misalignment, regardless of whether an external electromagnetic field is present. With increasing temperature the saturation magnetisation diminishes gradually and then abruptly drops to zero at the Curie temperature. At T_C the mutual spin coupling forces are completely destroyed, such that for temperatures above T_C ferromagnetic materials are paramagnetic. Therefore, during cooling below T_C the paramagnetic to ferromagnetic transition and the ferromagnetic phase formation can be detected with the use of an EM sensor.

In the present chapter, the principles and fundamental mechanisms that govern the relationship between ferromagnetism, paramagnetism, T_C, eddy currents and the electromagnetic field were presented. Techniques from past research works on detection of phase transformation by electromagnetic techniques were discussed and the results produced were analysed. Whilst existing sensors are capable of detecting the paramagnetic to ferromagnetic transition no direct relationship that links sensor output with transformed volume fraction and variations in the microstructure has been reported so far.

CHAPTER 4: MATERIALS AND EXPERIMENTAL PROCEDURE

4.1 Introduction

This chapter presents a comprehensive analysis of the experimental procedure employed during the present study. A number of steel grades and two different shapes of samples (rod and strip) were used to investigate the capabilities of the two experimental electromagnetic (EM) sensors designed by Lancaster University. Three steel rod compositions, for testing with the cylindrical sensor, were chosen to represent conditions where transformation occurs either below the T_C or above it. An as-rolled low carbon strip steel was used with the flat MFIA sensor. This chapter also describes the results obtained from the work carried out to optimize the experimental setup.

4.2 Materials and Heat Treatment

Three grades of carbon-manganese (C-Mn) steel rods (10mm diameter) were selected for the test programme conducted with the cylindrical EM sensor. These were assigned as low, medium and high carbon steel in accordance with the carbon percentage present. The compositions for each steel grade, and their source are given in table 4.1.

Table 4.1: Compositions and providers for the steels used for the experimental work.

Steel Grade	Provider	Type	C	Si	Mn	P	S
Low Carbon	Corus	Rod	0.03	0.05	0.23	0.009	0.013
Medium Carbon	McReady's	Rod	0.45	0.21	0.85	0.013	0.026
High Carbon	Corus	Rod	0.83	0.24	0.64	0.012	0.01

Figure 1.1 shows SEM micrographs for the three steel rod compositions. The reason for choosing these steel grades was because equilibrium phase transformation for the low carbon steels is predicted to occur above T_C, for the medium carbon steel close to T_C and for the high carbon steel well below T_C. From the Fe-C equilibrium phase diagram, for the low carbon steel, transformation of austenite during cooling is predicted to start at approximately 905°C and be completed at 727°C. Similarly, for the medium carbon steel, austenite transformation is predicted to start at approximately 780°C and finish at 727°C. Finally, for the high carbon steel, austenite is expected to start transforming just above the eutectoid point (727°C) and end just below it.

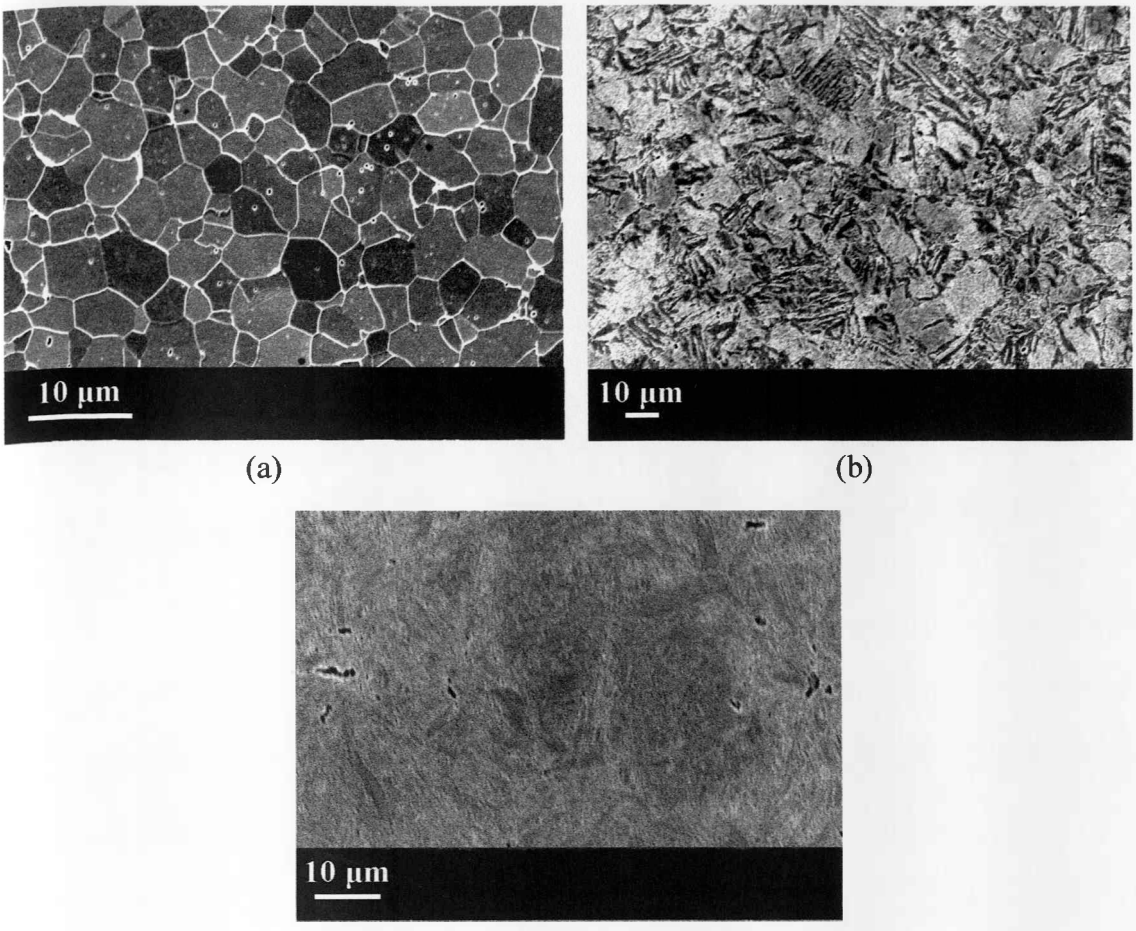

(a) (b)

(c)

Figure 4.1: SEM micrographs of a) low carbon steel, b) medium carbon steel and c) high carbon steel in the as received condition.

The low and high carbon steel rods provided by Corus were received in coiled form. The coils were cut into smaller pieces, approximately 30 cm long, then put into a hot furnace at 750°C. As soon as the curved rods reached 750°C, they were removed from the furnace and straightened by placing them against a metallic fixed wall and gently pressing them at the centre of the piece with a hammer until they became straight. Samples of the as-rolled and straightened material were examined using optical and scanning electron microscopy to make sure that the straightening process did not

result to decarburisation or variation of the microstructure. The medium carbon steel was received as straight rods.

A number of low carbon rod steel samples were heated in a vacuum furnace at 1000°C for 72 hours to increase the average grain size. Similarly medium carbon steel samples were heated in a vacuum furnace at 1000°C and at 1200°C for 72 hours to increase the average prior austenite grain size. Heat treatment at 1200°C resulted in significantly larger grain sizes than at 1000°C. High carbon steel samples were heat treated in a vacuum furnace at 1000°C for 72 hours and at 1200°C for 60 hours in an argon gas atmosphere. The argon gas atmosphere was preferred over simple vacuum at this elevated temperature to reduce the decarburisation effect since the vacuum was not completely perfect.

4.3 Gleeble testing

Early EM trials were conducted on the Gleeble 3500 thermomechanical simulator (figure 4.2) on the basis that accurate control of the heating and cooling stages of the trials could be achieved within the Gleeble aluminium chamber. The aluminium-made chamber ensured that the magnetic interference from the surroundings of the experimental setup was kept to a minimum during EM testing.

Figure 4.2: The Gleeble 3500 thermomechanical simulator.

The Gleeble 3500 uses a digitally controlled resistance-heating system to heat a sample. A high magnitude d.c. current that ranges from a few tens to a few thousands Amps flows through the sample. Depending on the size and material of the sample, heating rates of up to 20000°C/s and temperatures above 3500°C are possible with the Gleeble. Cooling rates of up to 10000°C/s are possible by water quenching. The temperature is accurately controlled by pairs of K-type thermocouples (other types can also be used if required) that are welded on the skin of the sample. Up to four pairs can be used at any one time – one controlling and three monitoring pairs – while temperature accuracy is within ±1°C at 900°C. A layout of the Gleeble configuration is shown in figure 4.3.

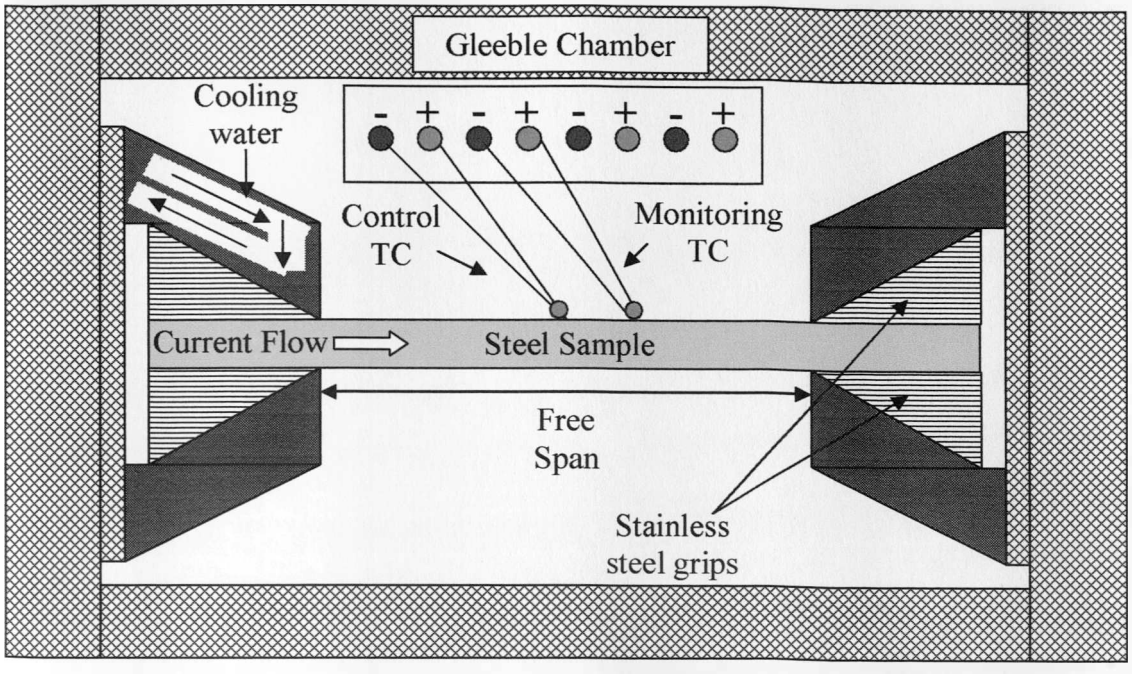

Figure 4.3: Gleeble chamber and experimental configuration for thermal trials.

Unfortunately, uniform temperature over the whole length of a sample is not achieved in the Gleeble because of the cooling effect of the grips. The use of monitoring pairs of thermocouples allows the measurement of thermal gradients occurring over the length of the sample.

Thermal gradients across the sample would produce inaccurate EM results, especially if temperature variations occurred at, or around, the Curie temperature. A large number of heating trials were conducted on 10mm diameter rod specimens of varying lengths made of commercial low carbon steel to determine the maximum uniform temperature region possible within the Gleeble. The heating trials were conducted using the following method: three pairs of thermocouples; one for controlling and two for monitoring temperature were employed. The controlling thermocouple pair was

welded exactly in the middle of the sample while the monitoring pairs were placed at different positions away from the controlling pair.

4.3.1 Initial EM trials

Early EM trials were aimed in determining the validity of the experimental technique. During these tests, the Gleeble controlled and recorded the sample temperature, the sensor consisted of one exciting and two sensing coils and was connected to a Solartron SI 1260 [146] impedance analyser. Test coils, consisted of an exciting-sensing coil arrangement of 50 and 80 turns respectively, which were wound directly upon a steel specimen. To provide access to the centre of the sample, for temperature measurement, the secondary coil consisted of two individual 40-turn sections, as shown in figure 4.4.

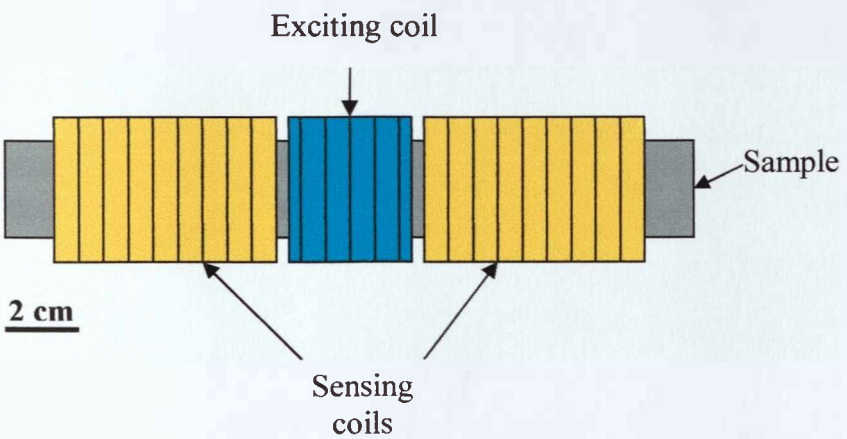

Figure 4.4: Initial sensor – sample arrangement.

To maintain temperature, current flows into the sample, the magnitude of the current is related to the required temperature. The consequences to impedance response stability of holding the sample at a constant temperature were compared to that of free

cooling over a range of temperatures; these temperature ranges were 300°C-450°C and 500°C-750°C. Several excitation frequencies were investigated in conjunction with each region, the data from which are presented in figures 4.5. Within these figures, dashed lines represent a constant temperature with the heating current switched on, whereas solid lines represent the response of the sensor to the sample freely cooling with the heating current switched off.

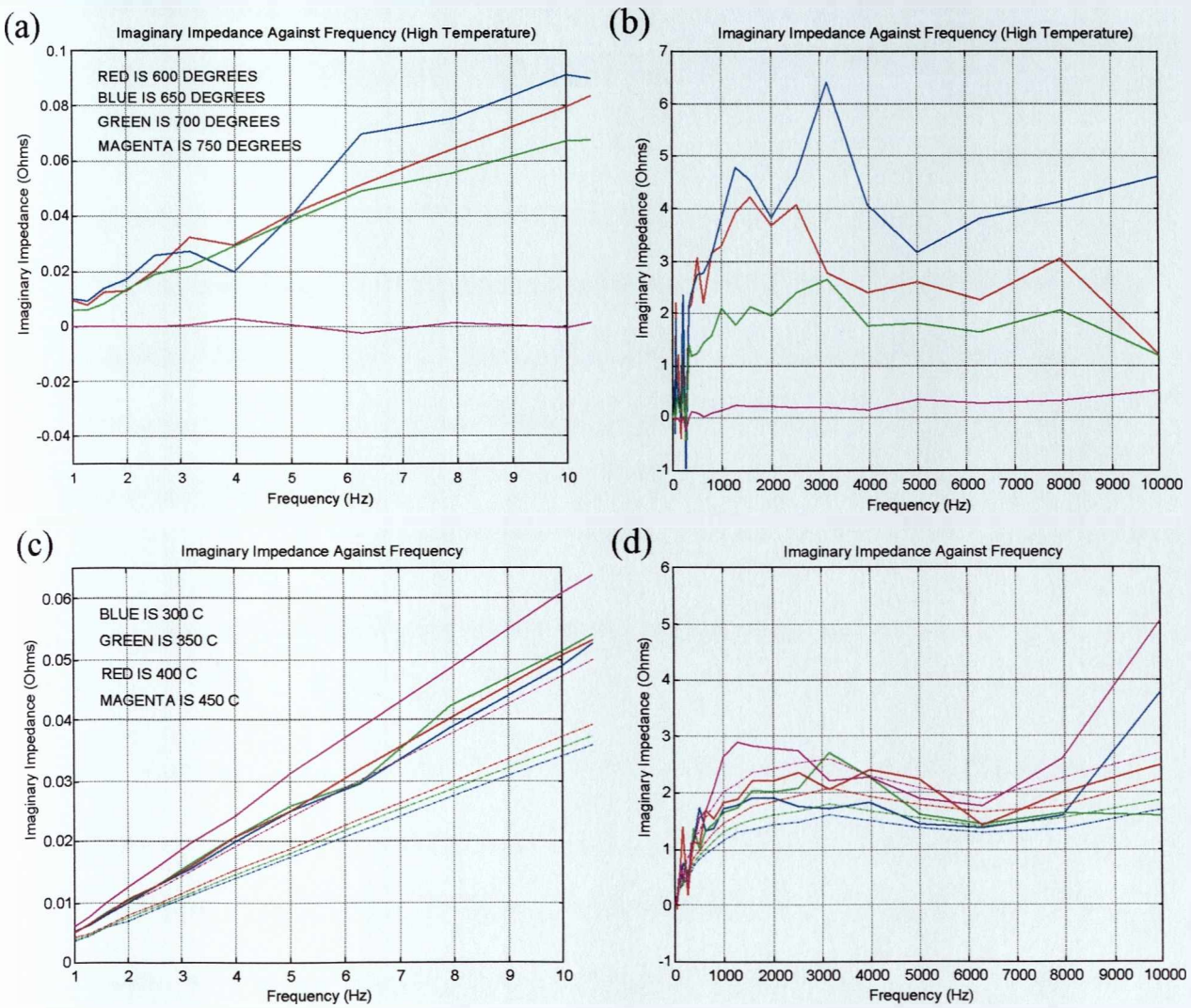

Figure 4.5: EM sensor outputs for various frequencies over different temperature ranges.

From figure 4.5 (a) and (b) it can be seen that at the highest temperature range (750°C) the sensor output (impedance) has zero magnitude. This implies that the sample is paramagnetic, as the steel used was a low carbon grade (0.11 in wt %) and therefore this is due to the sample temperature being above the Curie point and hence paramagnetic ferrite is present. For the initial EM trials the Gleeble temperature control had not been calibrated suggesting error in the thermocouple outputs. As the initial trials were designed to determine experimental procedure they were not repeated, however, temperature calibration was carried out. For the other test temperature ranges (600 – 700°C) the impedance increases with frequency for frequencies 1-10 Hz (figure 4.5 (a)). From figure 4.5 (d) it can also be seen that during the maintenance of temperature, EM noise is much greater than that recorded during free cooling, which is a consequence of the electromagnetic field created by the heating current. Subsequent Gleeble testing was therefore undertaken during dynamically cooling steel.

4.3.2 Determination of maximum region of uniform temperature

Early trials were conducted on 220 mm long, 10 mm diameter specimens, free span 160 mm, at maximum temperatures between 500°C and 900°C and at a heating rate of 1.5°C/s using copper grips. The maximum temperature was held for a period of five minutes. A heat affected zone (HAZ) could be observed on the sample (from discolouration due to oxide formation) and was approximately 125 mm long with a uniform temperature region (±2°C), determined from the thermocouple readings, of 5 mm long. It is apparent that the good thermal conductivity of the copper grips resulted in a significant cooling effect on the hot sample causing a 300°C difference between

the temperature observed at the middle and the ends of the HAZ at the hold temperature. For that reason, stainless steel, which is much less thermally conductive than copper, was used to replace the copper grips. The trials were repeated with the use of the stainless steel grips. The length of the HAZ increased to 160mm (i.e. the length of the free span) at 900°C while the maximum region of uniform temperature increased to 15 mm. Nevertheless, temperature variations due to the cooling effect of the grips remained significant.

Further trials, involving shortened samples (130mm long) machined down to a 7mm diameter near their ends to act as heat raisers and a reduced contact area with the grips of 0.5mm on each side gave better results with a maximum temperature of uniform temperature 70 mm.

The main drawbacks of this technique was that the machined sections acting as heat raisers were much hotter than the centre and machining of a large number of samples was inherently time consuming. It was decided to replace the area of the sample in contact with the grips with special 35mm long stainless steel spacers that could both hold the sample in place and allow the current to flow. The sample was held in place by applying a small compressive constant load on it during the heating trial. To avoid thermal losses from the sample, a hole, 3mm deep and 7mm diameter, was drilled in the spacer end in contact with the sample. Hence the sample was in contact only with a very small area of the spacers, minimizing the cooling effect. This method resulted in absolute temperature uniformity being achieved (± 1°C) over a 100mm long sample when held at 800°C as shown in figure 4.6. Although temperature differences during heating and cooling were observed these are not critical as EM sensor readings would

be taken during a hold at constant temperature. However, for dynamic cooling tests more uniform temperature profiles would be needed.

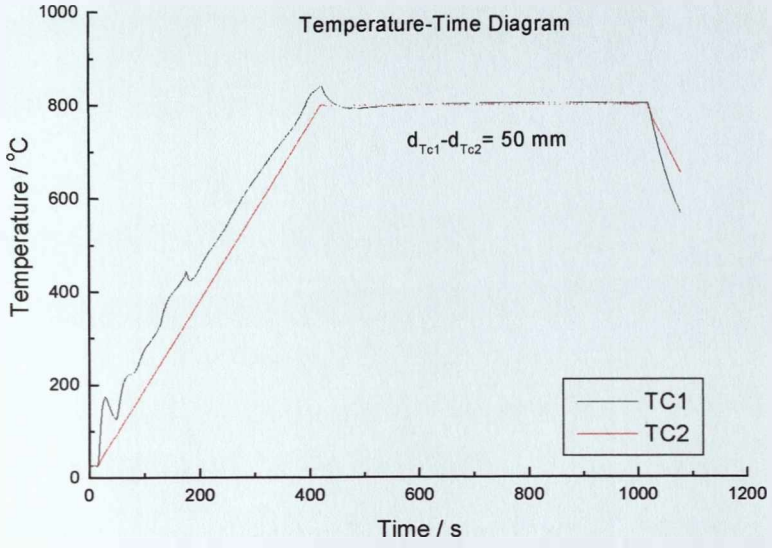

Figure 4.6: Thermal profile obtained for a 100mm long, 10mm diameter rod. Thermocouple TC2 is the controlling thermocouple, placed in the middle of the sample while thermocouple TC1 is monitoring the temperature at the right edge of the HAZ (distance between TC1 and TC2 is approximately 50mm).

4.3.3 Gleeble EM sensor design

The a.c.sensor design employed for the Gleeble tests needed to fulfill a number of operational criteria, listed below:

- The sensor should be capable of operating at several excitation frequencies in order to allow variable sampling depths of steel specimens.
- It should be reusable.
- It should be capable of withstanding temperatures in excess of 900°C without significant degradation.

- It should have stable coil geometry to permit repeatable impedance measurements.
- It should allow the attachment of thermocouples on the sample.
- Any components associated with the sensor should be made of non-magnetic and non-conductive material.

A number of types of wire are capable of sustaining temperatures above 900°C but few of them are also non-magnetic. For the sensor in this work, chromel wire, the positive leg of a K-type thermocouple [222], was used in conjunction with Nextel [222], an insulating high temperature ceramic braid, which provided increased thermal protection to the wire.

Thermocouple attachment on the sample was made possible by using a former made of a split alumina tube [222] 80mm long and with an 11.25mm internal diameter. To facilitate thermocouple attachment, while providing coil stability and reusability, both the coils and former were constructed as two 40mm lengths. Each half of the primary and secondary coils was connected in series, a technique known as summation. The primary or exciting coil consisted of 90 (2 x 45) turns and the secondary or sensing coil of 65 (33 + 32) turns. For simplicity, the sensing coil was wound over the exciting coil. The sensor geometry is shown schematically in figure 4.7 and in the Gleeble unit in figure 4.8.

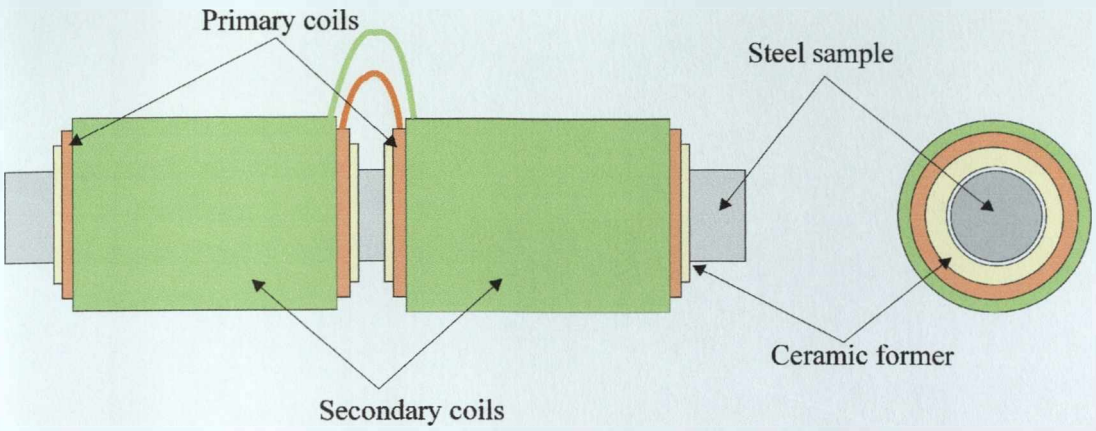

Figure 4.7: Sensor geometry for Gleeble testing.

4.3.4 Gleeble EM Technique

Although complete temperature uniformity was achieved over the sample, as shown in figure 4.6, the problem of achieving slow and uniform cooling without using heat input remained unsolved. To allow slow and uniform cooling a simple mechanism was designed to allow the removal of the sample from the jaws during cooling. Stainless steel spacers, 60 mm long were placed in the grips to avoid any part of the sample being in contact with the colder grips. The samples used were 80mm long and 10mm diameter; two steel grades were used; low carbon steel (0.03% in weight carbon) and eutectoid carbon steel (0.83% in weight carbon steel). The sample was placed between the stainless steel spacers and was held in place by applying a small load.

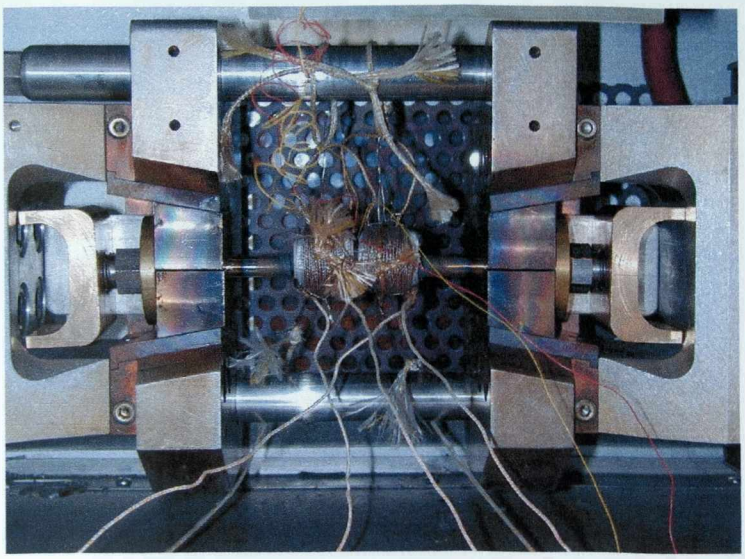

Figure 4.8: The experimental configuration. The EM sensor coils are seen in the middle of the photograph.

The sample was then heated at a heating rate of approximately 70°C/min to the required temperature (900°C) and held there for a period of five minutes to allow complete austenitisation. The temperature during heating and cooling was measured with four pairs of K-type thermocouples two of which were attached to the centre and two to the ends of the sample. The reason for using two pairs at each position was because two of them were connected to the Gleeble and the other two to a Tracker 224 panel meter that was employed to amplify the thermocouples d.c. voltage for input into a PC DAC acquisition card (DAS 802-16). The reason for doing this was to ensure confidence in the temperature measurements. It was found that the recorded temperature when compared to that of the Gleeble showed a difference of 2°C at 800°C.

At the end of the holding period the jaws were retracted and the sample was released. Upon release, the sample was held in the cooling position by two Nextel braids

attached to the ends of the sample. As soon as the sample was released the ends quickly cooled down to maintain a temperature slightly below that of the centre of the sample for the duration of the test. A frequency range of 0.5, 1, 5, 10 and 20Hz was used to provide full material information, and the influence of eddy currents upon the sample.

4.4 Furnace Testing

A high temperature furnace (capable of heating up to 1300°C) was used to provide a more uniform hot zone for the sample. A different design of sensor was required which had the following properties:

- The sensor should be capable of withstanding temperatures up to 950°C.
- The structure associated with the sensor should be made to withstand the same temperature as the sensor and be relatively robust to sustain manual handling.
- Sample should remain stationary and in a repeatable position relative to the sensor coils during cooling.
- Sample temperature should be uniform during heating and cooling.
- The experimental setup should allow easy access for thermocouple attachment.
- The experimental setup should be magnetically inert.
- The coils should be protected so as not to come in contact with the sample to avoid short circuiting of the sensor.
- High signal to noise ratios (SNR) should be achievable.
- The sensor should be able to operate at various frequencies.

- The operational lifetime of the sensor should be long enough to allow the performance of a relatively large number of EM trials.

The a.c. sensor employed in the furnace experimental setup consisted of one primary (100mm long, 132 turns) and one secondary coil (90mm long, 95 turns). The sample - 80mm long and 10mm diameter- was placed in a 120mm long, 13mm internal diameter alumina tube. Both coils were wound around the tube to ensure constant temperature and coil protection. The maximum coil length was limited, by sample size and available space. Due to the difficulty in winding Nextel braided K-type wire, interwinding secondary and primary coils was avoided, the secondary was therefore wound directly upon the primary, each coil having 2 layers.

The insulating properties of the alumina tube resulted in a more uniform sample temperature. To fully insulate the sample and create a uniform test environment, two end caps were made of Duratec 750 (magnesium silicate). Holes were drilled in each cap to permit thermocouple attachment on the sample. In addition, an insulation board, also made of Duratec 750, was manufactured to support the sensor during testing as shown in figure 4.9.

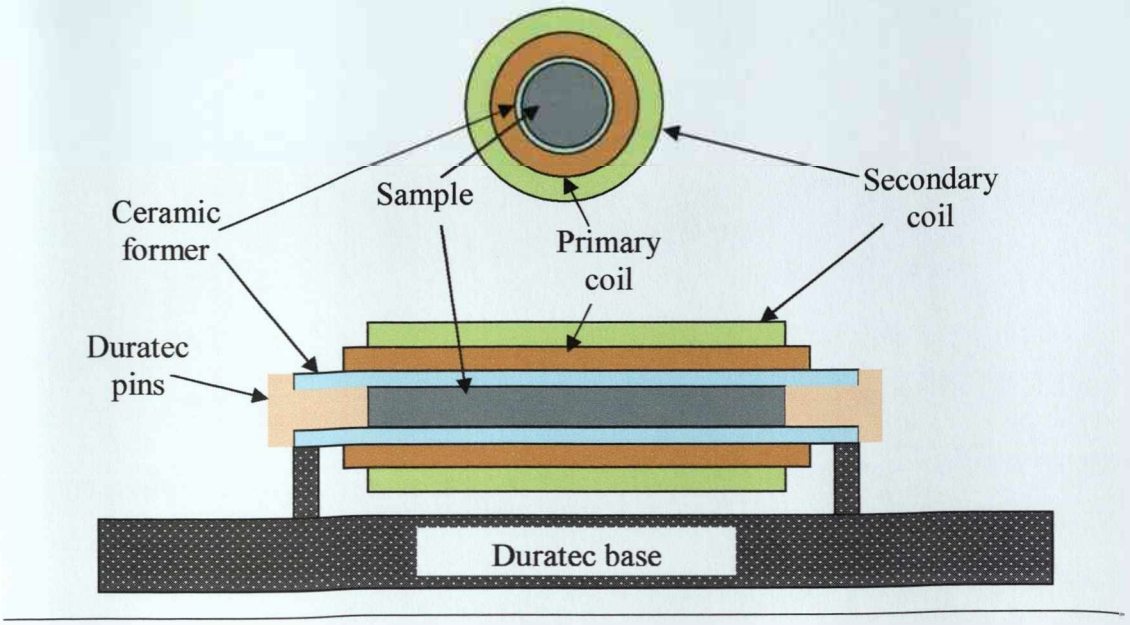

Figure 4.9: EM sensor configuration used in the furnace tests. The entire setup was placed inside the furnace during EM testing.

Initial trials aimed to determine the temperature uniformity during testing. A low carbon sample (0.03 wt % carbon) enclosed in the experimental setup was placed in the furnace with its length orientation perpendicular to the furnaces heating elements. The experimental arrangement was then heated up to 832°C at a heating rate of 15°C/min. The temperature was monitored by two pairs of K-type thermocouples, one attached to the centre and one 4mm away from the end of the sample, connected with a PC DAC acquisition card (DAS 802-16) via a Tracker 224. The sample was held for 20 minutes between 800°C and 832°C to allow the ferromagnetic to paramagnetic transition of the sample. The experimental arrangement was then removed from the furnace and allowed to cool naturally. This process resulted in unacceptable temperature variations as the centre cooled slower than the ends of the sample as observed in figure 4.10.

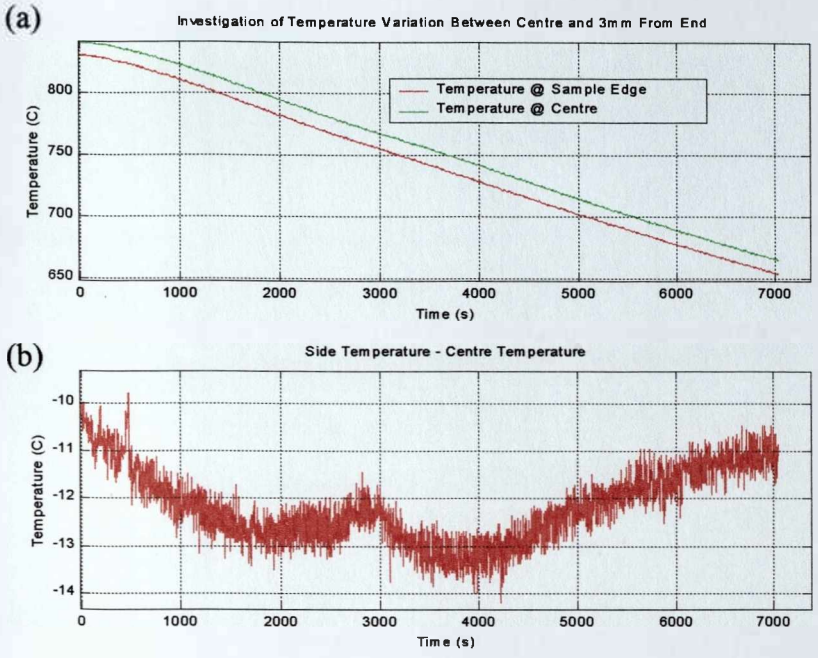

Figure 4.10: a) Cooling profile and b) temperature variations across the sample (i.e. between the centre and the end) during cooling out of the furnace.

Improvement of cooling uniformity was achieved by furnace cooling the sample. Following the same heating procedure as before the furnace was switched off at 832°C to allow cooling of the sample. Figure 4.11 shows the cooling profile of the sample; the maximum temperature variation observed at the temperature range where the magnetic response (approximately 770°C) took place was found to be no more than 2°C. The sample was removed from the furnace at 650°C to minimise test duration. The slow cooling rate, approximately 3°C /min, achieved during the furnace cooling allowed the use of smaller excitation frequencies due to increased integration periods, minising the eddy current effects and increasing sensitivity of the sensor.

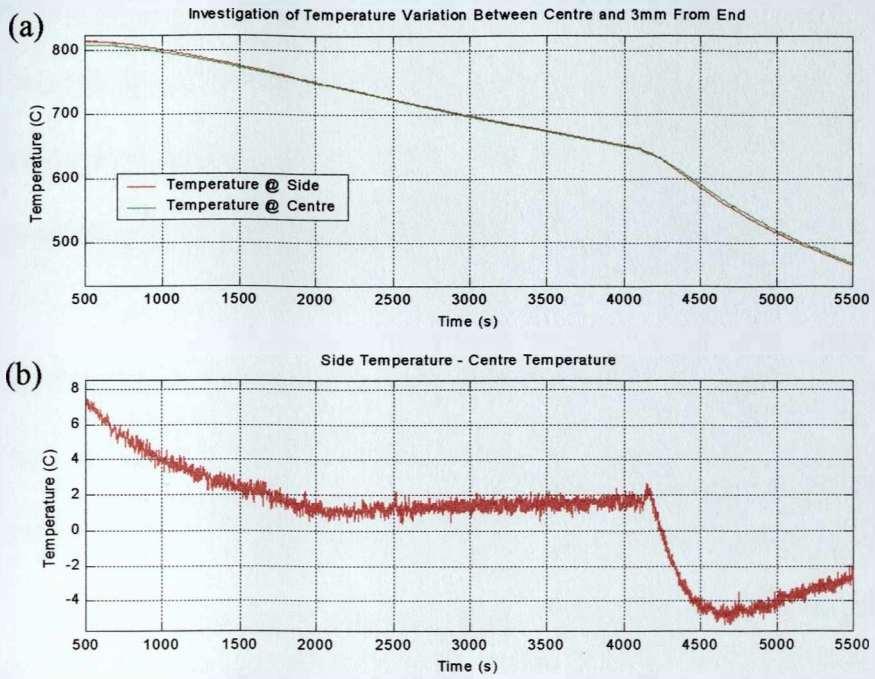

Figure 4.11: a) Cooling profile and b) temperature variations across the sample during cooling within the furnace.

4.4.1 Minimisation of Decarburisation and Oxidation Effects

Decarburisation and oxidation of the steel samples was a factor that could not be ignored since the EM tests were conducted in an uncontrolled atmosphere. Additionally, the high temperatures used and the relatively long soaking periods enhanced their effect. In order to minimise decarburisation effects samples were coated. The requirements of the protective layer are:

- allow the attachment of thermocouples.
- be capable of withstanding temperatures up to 950°C.
- bond with the sample.
- be non-porous.

- be capable of sustaining the dilation of the sample.
- not crack during heating or cooling at slow cooling rates.
- be magnetically inert.
- allow repeatability of the test.

Achesion CG501, a ceramic-based coating that fulfilled the above specifications was used. The coating was applied in liquid form by dipping the sample and then the coating was allowed to dry for a minimum of 24 hours before testing.

4.5 Microscopy and Image analysis

Samples from available rod and strip material were mounted in conductive bakelite, ground to 1200 grit, diamond polished to 1μm and etched in 2% nital (nitric acid in alcohol) to reveal the microstructure. The samples were observed using both optical and scanning electron microscopy (SEM).

Quantitative image analysis was performed using a KS400 system on transverse metallographic samples polished then etched in 2% nital. Ferrite area fraction measurements were taken from a minimum of 1 mm^2 of microstructure. Average prior austenite grain sizes (measured as equivalent circle diameters) were determined from a minimum of 500 grains. In addition, average ferrite grain sizes and decarburisation depths were measured.

Primarily, the shading of the micrograph was corrected to avoid variation in the grey levels that would have resulted in false measurements. Then the threshold was set to

maximise the contrast between the phase or the feature to be measured and the rest of the microstructure. If manual measurement is to be avoided, processing of the micrograph to be examined with an image processor can be performed to increase the contrast between the features to be measured and the rest of the microstructure.

4.6 Contiguity measurements

The purpose of contiguity measurements is to describe the degree of particle contact of one phase in a two phase microstructure. Contiguity measurements were performed on interrupted quenched test samples in order to determine the connectivity of the ferrite phase at different temperatures (and hence area fractions). Contiguity values were obtained from intercept measurements on a random plane of polish as shown in figure 4.12 and by employing equation 4.1 [223]:

$$C_\alpha = \frac{2N_L^{\alpha\alpha}}{2N_L^{\alpha\alpha} + N_L^{\alpha\beta}} \qquad \text{Equation 4.1}$$

where C_α is contiguity of the phase in question (unitless) and $N^{\alpha\alpha}$, $N^{\alpha\beta}$ are the number of intercepts of the α / α and α / β interfaces respectively within a random line of unit length on a plane of polish. For these measurements phase α is ferrite and phase β is martensite.

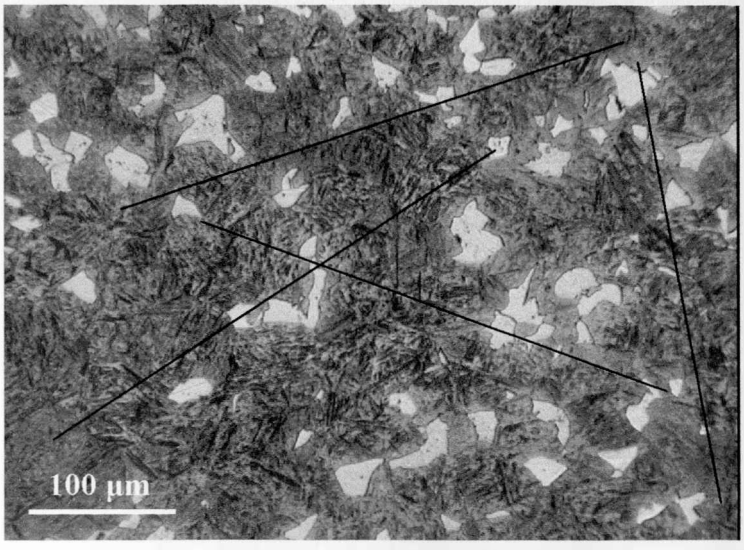

Figure 4.12: Random intercepts on an optical micrograph obtained from a quenched medium carbon steel sample. White areas are ferrite and dark areas are martensite.

4.7 Transformation temperature range prediction using Thermo-Calc

Thermodynamic calculations were carried out utilizing the Thermo-Calc software (by ThermoCalc AB) as a means of predicting the trends of phase transformation under equilibrium conditions for each of the steels used during EM trials. Despite the fact that experimental work was not conducted under equilibrium conditions, the relatively slow cooling rates used in the experiments, allowed the solution obtained with Thermo-Calc to be used as a good indication of the phase transformation temperature range. A phase transformation prediction is achieved by using the available model parameters, data and information on the alloy system of interest in the solution databank provided by ThermoCalc AB. By making use of the available data Thermo-Calc solves a thermodynamic problem by calculating the Gibbs free energy of the defined alloy system; in this case Fe-C-Mn. The available databases of relevance for

the present work in Thermo-Calc are the following: Fe-C, Fe-C-Mn, Fe-Si, Fe-Mn-Si, Fe-Si-C, Fe-P and Fe-C-P [224-233].

The diagrams (number of molecules, np* - temperature) in figures 4.13 - 4.15 show the predicted austenite decomposition into ferrite and cementite under equilibrium conditions. The np* - temperature diagrams indicate the fraction of weight, not the volume, of austenite transformed into ferrite and cementite against temperature. Figure 4.13 shows that for the low carbon steel and for equilibrium conditions, austenite begins transforming mainly into ferrite well above 900°C. Ferrite formation is seen to be completed at approximately 765°C. However, over 90% of the total phase transformation has already taken place above 800°C. The amount of cementite, found in the microstructure, which forms during austenite decomposition is almost negligible for the low carbon steel.

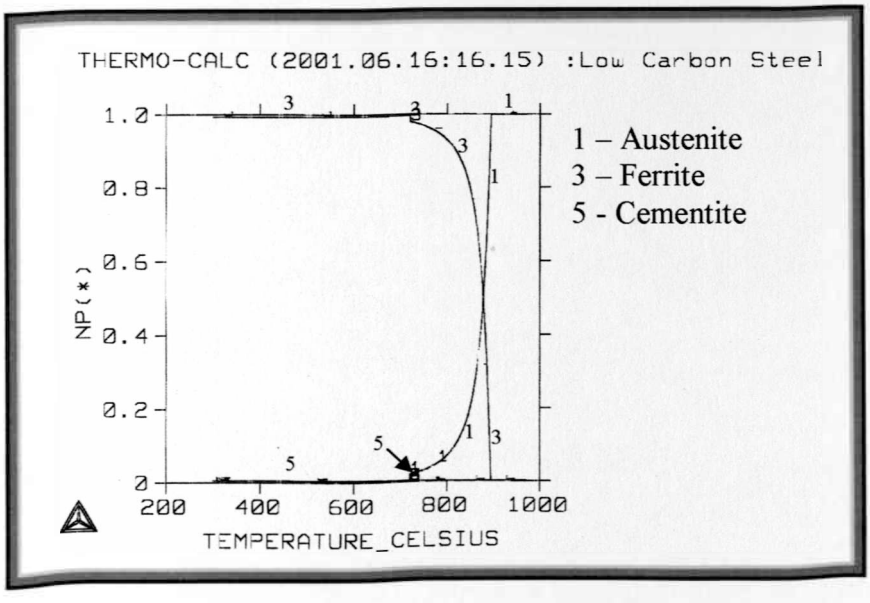

Figure 4.13: Thermo-Calc prediction for low carbon steel. Line 1 indicates austenite %, line 3 indicates ferrite % and line 5 indicates cementite %.

Figure 4.14 indicates that for the medium carbon steel, austenite to ferrite transformation starts at 770°C and finishes at 715°C under equilibrium conditions. Cementite starts forming at 723°C and terminates at 715°C.

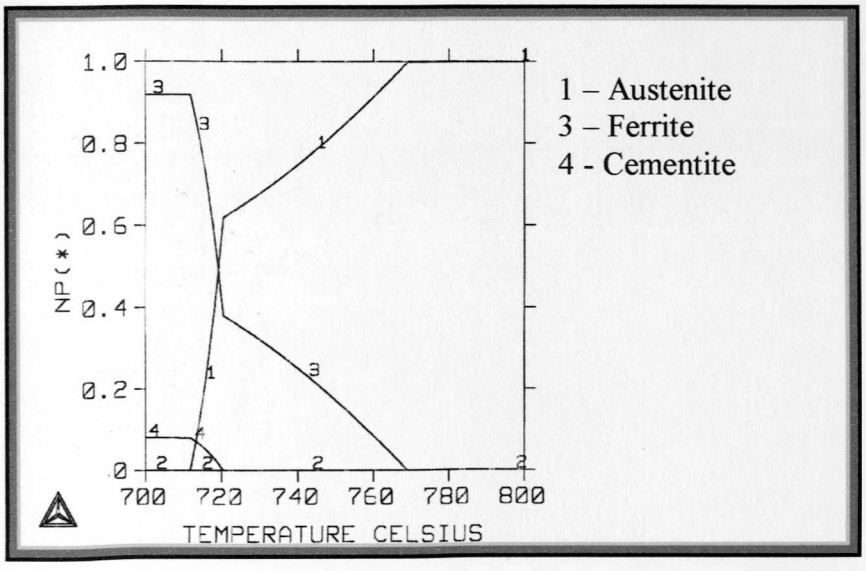

Figure 4.14: Thermo-Calc prediction for medium carbon steel. Line 1 indicates austenite %, line 3 indicates ferrite % and line 4 indicates cementite %.

For the high carbon steel, figure 4.15, austenite starts transforming into ferrite and cementite at 728°C and finishes at approximately 718°C.

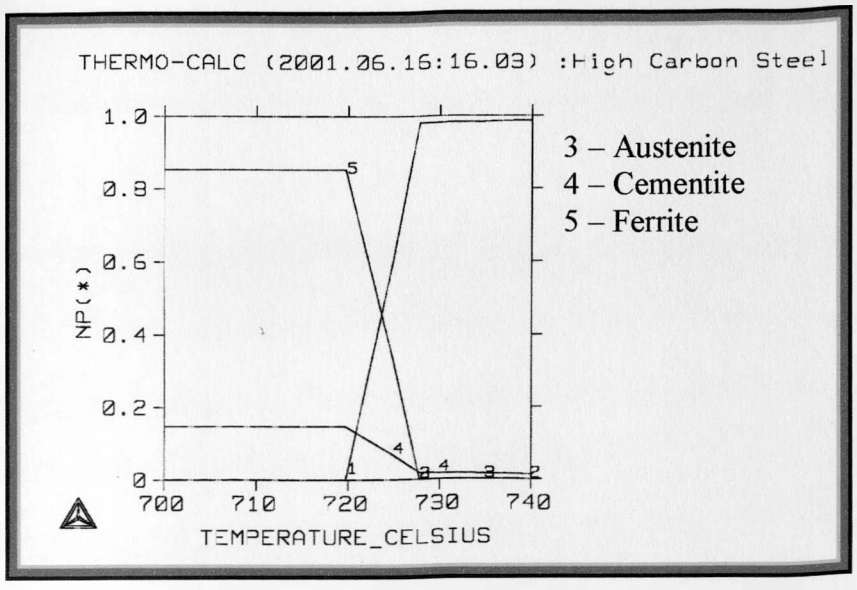

Figure 4.15: Thermo-Calc prediction for high carbon steel. Line 3 indicates austenite %, line 4 indicates cementite % and line 5 indicated ferrite %.

4.8 Finite Element (FE) simulations

Finite Element (FE) simulations using the commercial software package 2-D Maxwell from Ansoft Corporation were conducted in order to determine the influence of microstructure upon the measured impedance. In this package, the problem space is user-defined through a Computer Assisted Design (CAD) orientated drawing interface. Material parameters, such as permeability and conductivity, and coil dimensions, number of turns and excitation frequencies are also specified by the user. Mesh creation can be accomplished either manually, i.e. the user specifies mesh seeding over which the solver will operate, or the FE solver automatically creates a mesh, which describes the problem region. Mesh refinement, in both cases, will continue until the error between the FE estimate and the calculated Laplacian solution of the problem calculated by the computer, are within a level of error assigned by the

user, in this case no more than 5 %. Maxwell software solves the problem by calculation of fields using the Helmotz, Poisson and Laplace equations [183, 184].

The methodology employed by Maxwell FE package is that of a Laplacian problem. Similar methodologies are employed to solve diffusional problems such as phase transformation of carbon steel. The pillar concept of FE analysis is the creation of a solution that approximates the actual solution of the problem, however, a direct solution to the time-space equation is unnecessary, as imposed boundaries restrict the problem to a spatial domain.

Finite element analysis accomplishes this through:

- Problem domain segmentation into discrete areas.
- Assigning boundary conditions to each area.
- Application of the rule of energy minimisation.
- Simultaneous solution of individual area equations.
- Summation of element potentials for solution to the complete problem region.

All geometries can be described by triangular elements of varying dimensions. In FE analysis this process takes place automatically and the element size is determined through error minimisation. Each element must be solved such that the imposed boundary conditions are fulfilled. Minimisation of the error between the Laplacian solution and the estimation from the FE method, dictates solver accuracy. Therefore, large-sized elements involve larger errors while smaller-sized elements minimise the

error in the solution but involves longer processing times due to the larger number of elements (figure 4.16).

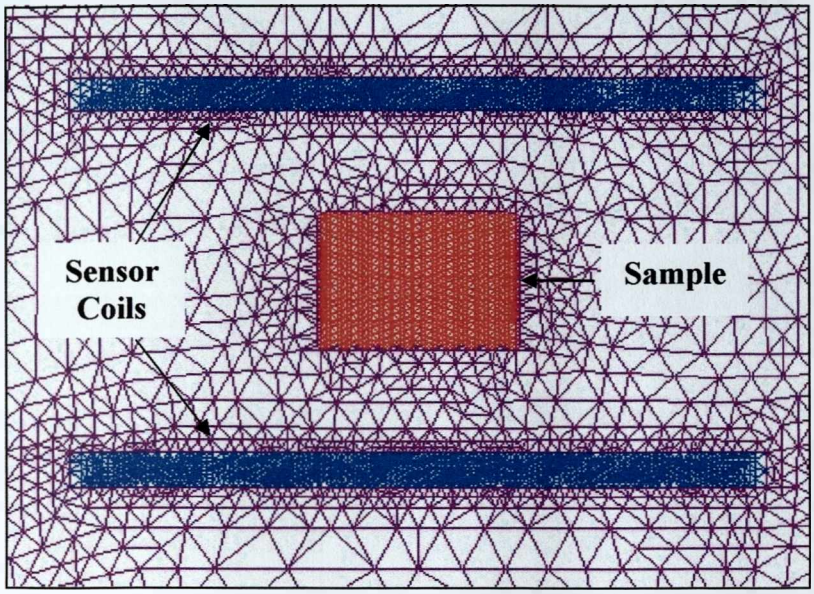

Figure 4.16: 2-D mesh of the sample and coils representing the sensor. The problem needs to be solved for each of the triangular elements shown in order to obtain an average solution for the complete setup.

The configuration employed for the FE simulations, although two-dimensional, follows the same principles as the experimental setup. The simulated EM sensor, following the experimental design of the cylindrical EM sensor, consisted of two coils; one primary or exciting and one secondary or sensing coil. The sample was represented by a 20x20 grid of equilateral hexagonal cells (as shown in figure 4.17) that were defined either as paramagnetic (i.e. representing austenite with a relative permeability of 1) or ferromagnetic (i.e. representing ferrite with a relative permeability of 1000). Each cell was defined to have a side of 20 μm and hence the total length of the sample was 400 μm. The length of the coils was defined to be 1200

μm and each had one turn only. The background of the simulated setup was taken to be a vacuum with a relative permeability of one and conductivity of zero.

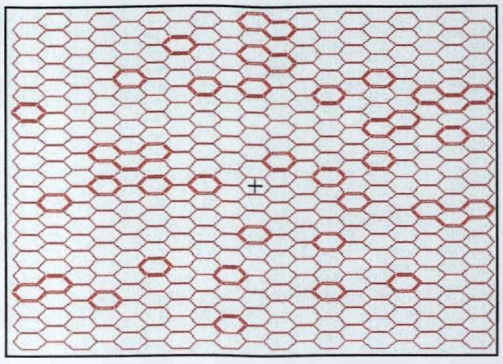

Figure 4.17: 2-D array of cells representing the steel sample.

The conductivity of all cells was defined to be 1.1 x 10^6 Sm^{-1} and held constant at all times. Although, the simulations seem not to take into account temperature and thus conductivity variations, this is not the case. This was done because previous trials that used varying conductivity values within the transformation range of temperatures (720°C – 680°C) for the sample showed that the effect on the impedance values was negligible; the conductivity variation at this temperature range was less than 0.185 x 10^6 Sm^{-1} [234].

The frequency used for the electromagnetic tests was 2Hz. However, for the FE trials a higher frequency of 50 Hz was chosen in order to provide a large range of impedance values during simulation between the fully paramagnetic and fully ferromagnetic conditions. Due to the very small size of the sample used in the simulations, full penetration of the magnetic lines of flux through the sample is permitted even at high frequency, ensuring that the impedance values are comparable

with the experimental results. The frequency chosen is still relatively low which ensures that the eddy current effects within a sample of this size can be ignored.

A second set of simulations was carried out using a 60 x 60 grid of equilateral hexagonal cells where the total length of the sample was increased to 1200 μm. The length of the coils was also tripled in order to maintain the proportions of the previous simulations and to have a reference with the previous impedance values. The background was set to be a vacuum and the same frequency was employed as before.

The problem of representing actual microstructure in the simulation was overcome by overlaying the computer monitor with transparencies of optical micrographs of the microstructures of interest in front of the FE grid. Then, the cells behind the areas of the micrographs showing ferrite were marked as ferromagnetic, while the remaining cells were assigned as paramagnetic, hence austenite. The optical micrographs used in these FE simulations were obtained from samples quenched at pre-chosen temperatures determined by the experimental EM tests that aimed to determine phase transformation, ferrite fraction and microstructure evolution during cooling.

To avoid prolonged solution times due to the large number of hexagons involved, all cells that represented the austenitic matrix were grouped as one object to cut down the number of variables. The same was done for any groups of cells that represented ferrite. By using this method, it was possible to maintain solution times in the order of minutes instead of several hours.

4.9 Summary:

This chapter was concerned with the experimental processes and techniques used in this study. One steel strip composition and three steel rod compositions were used in the experiments. Thermo-calc calculations were performed in order to determine the range of phase transformation temperature for each steel rod composition. A number of thermal trials were conducted on the Gleeble 3500 to determine the maximum region of temperature uniformity on the samples. Initial EM tests found that impedance response was adversely affected by the heating current of the Gleeble and measurements were only possible with the current switched off. The limitations of the Gleeble experimental setup were overcome by using a high temperature furnace as an alternative means of conducting EM trials. The experimental setup allowed excellent temperature uniformity over the length of the sample. Microscopy and image analysis and contiguity measurements were performed on pre-tested and post-tested EM samples in order to correlate microstructural development with EM response. Finally, FE simulations were conducted in order to determine the behaviour of the EM response with microstructural variations and confirm the experimental results. Chapter 5 presents the experimental results obtained with the EM sensor.

CHAPTER 5: ELECTROMAGNETIC DETECTION OF FERROUS PHASE TRANSFORMATION – RESULTS AND ANALYSIS

5.1 Introduction

Following optimization of the test procedures to ensure uniform temperature profiles for the samples EM tests were carried out to characterise the relationship between impedance and microstructure development during transformation. Thermo-Calc predictions presented in the previous chapter were used to predict the phase transformation for each steel grade in order to compare these values with those determined from the EM tests.

In this chapter, EM measurements performed in the Gleeble and furnace are presented for each steel grade. Decarburisation and oxidation influences in the experimental results are analysed and the effect of connectivity of the ferrite phase on the magnetic response is shown. Furthermore, a qualitative relationship between microstructure and magnetic response is established. Finally, the significance of other factors (i.e. frequency, grain size, length of the ferromagnetic path, etc.) that need to be taken into account in an effort to quantitatively represent the relationship between microstructure and impedance value are discussed.

5.2 Gleeble EM results

Low and high carbon steel samples were tested in the Gleeble using the EM sensor. The aim of the tests were to establish if the phase transformation and/or the Curie

temperature could be detected during slow cooling from 900°C through the transformation temperature range. The effect of testing at different frequencies was also investigated.

5.2.1 Low Carbon Steel EM Response

The phase transformation of the low carbon steel samples is expected to be almost complete above the Curie temperature at slow cooling rates. Thus, the purpose of the EM tests on low carbon steel samples was to identify the point where the paramagnetic to ferromagnetic transition occurs and hence pinpoint the Curie temperature. Figure 5.1 shows the EM response and the cooling profile for a low carbon steel sample tested at a frequency of 1 Hz.

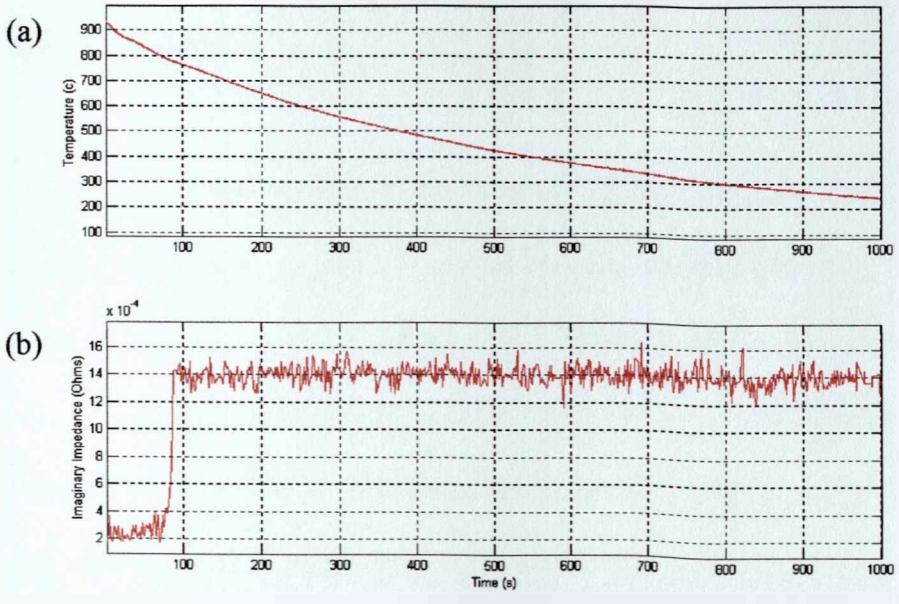

Figure 5.1: a) Temperature – time and b) impedance-time diagrams for a low carbon steel sample tested at a frequency of 1 Hz.

From figure 5.1(a) it can be seen that the samples cool slowly from 900°C, with a cooling rate of approximately 1.3°C/s between 900°C and 600°C. From figure 5.1(b) it is apparent that the impedance values show the effect of noise in the signal caused by the voltage variations in the power supply to which the sensing apparatus is connected and from nearby electronic equipment. The operation of the Gleeble itself is a source of electromagnetic noise in this case. The low frequency used in this test increases the sensitivity of the electromagnetic sensor to the effect of noise as the recorded electromagnetic response is very low due to small electromotive force induced in the sensing coil. Despite the noise in the recorded electromagnetic signal an abrupt change in the impedance value (from ~2 x 10^{-4} Ohms to ~14 x 10^{-4} Ohms) at approximately 80 seconds, which corresponds to approximately 770°C. This corresponds to the Curie temperature for pure iron and most steels with low alloying concentration [63], hence demonstrating that the sensor can detect the paramagnetic to ferromagnetic transition at T_C.

Figure 5.2 shows the measured impedance at a frequency of 20 Hz. At such a high frequency the impedance measurement can be seen to be virtually unaffected by noise. This is due to the much higher signal obtained due to the use of a higher frequency. Electromagnetic induction is affected by the frequency levels used (rate of change) during testing. Higher frequency causes a more rapid change in the direction of current flowing in the excitation coil giving rise to a higher electromagnetic induction and hence a higher induced electromotive force in the sensing coil. This leads to a significantly stronger electromagnetic signal being recorded during testing. As the noise levels remain the same regardless of the frequency being used, noise tends to be ignored in a much stronger signal; i.e. at 1 Hz the recorded impedance

value was of the order of 10^{-4} whilst at 20 Hz the impedance value is of the order of 10^{-2}, hence the obtained signal is 100 times stronger. Despite the fact that higher frequencies reduce the effect of electromagnetic noise and provide a much stronger signal the sampling depth is reduced significantly during testing due to the eddy current effect. The magnitude of the recorded impedance is also dependent, although considerably less than with frequency, on the size of the sample used, i.e. the smaller the sample the smaller the impedance response recorded. The effect of eddy currents can be avoided by magnetically saturating the sample. However, in our case the magnitude of the electromagnetic field produced by the proposed sensor is very small, i.e. 12 Oersted which is inadequate to saturate the sample.

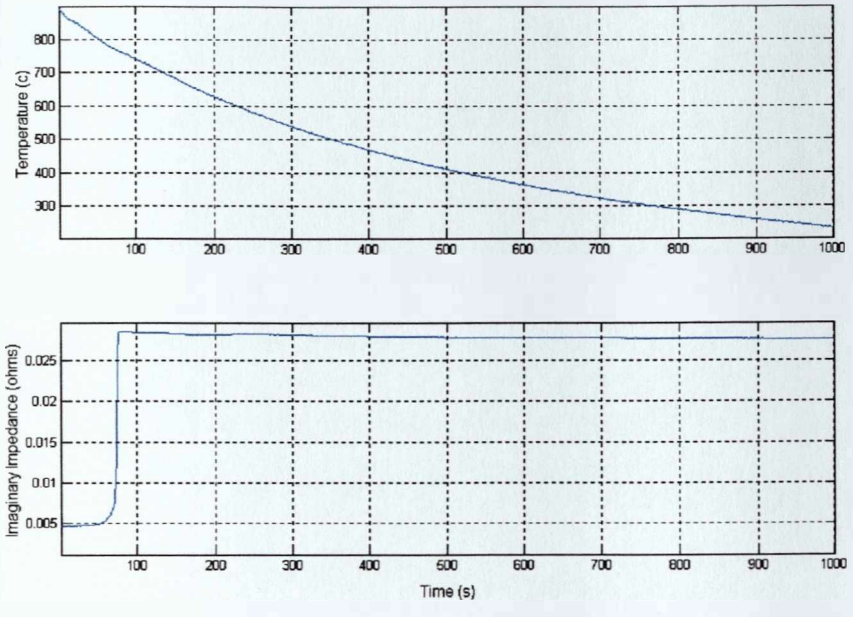

Figure 5.2: a) Temperature - time and b) impedance-time diagrams for a low carbon steel sample tested at a frequency of 20 Hz.

Figure 5.2(b) shows clearly the abrupt change in impedance value at approximately 80 seconds corresponding to the Curie temperature of 770°C reflecting the transition from paramagnetic to ferromagnetic ferrite. Note that at the Curie temperature the

austenite to ferrite transformation will be complete. It would be expected that the impedance change at T_C should be characterised by a vertical trace, however, it can be seen that the impedance value starts increasing slightly above 770°C and continues increasing over a small temperature range which does not meet with the expected behaviour. Careful examination of the impedance - temperature diagram in conjunction with the cooling profiles of the centre and ends of the sample led to the conclusion that the measurement is affected by thermal gradients which are associated with the cooling procedure in the Gleeble.

In general, the results in figure 5.2 agree well with previously reported impedance – time responses in terms of the large increase of impedance value at the T_C and slightly decreasing impedance between 770°C and 200°C, due to the increasing eddy current effect associated with the increasing conductivity value [204, 211, 235]. As conductivity of the sample increases the magnitude of the eddy currents flowing in the sample will increase as well. This produces a stronger electromagnetic field which opposes the electromagnetic field generated by the sensor. As a direct result the sampled area is reduced resulting in a lower impedance response. The decrease in the impedance value during cooling is more obvious at higher frequencies where the eddy current effect increases.

5.2.2 High Carbon Steel

High carbon steel rod specimens were cooled at the same cooling rate as the low carbon samples. Therefore, due to the relatively slow cooling rate employed during electromagnetic testing, the phase transformation for high carbon steel samples was

expected to take place at a temperature close to, but below, the eutectoid point (723°C). The occurrence of a slight suppression to the start and end of phase transformation in the high carbon steel samples is due to the non-equilibrium cooling during EM testing. Since the composition of the high carbon steel specimens is near eutectoid almost 100% of the phase transformation is due to the pearlitic reaction. The pearlite reaction is exothermic and occurs, normally, at a single temperature (for equilibrium conditions) hence during slow cooling the temperature - time profile of the steel shows a change in gradient at the transformation temperature due to the release of latent heat of transformation.

The effect of electromagnetic noise on the impedance signal is not critical on low carbon steel specimens as phase transformation occurs above T_C and hence only a large change in impedance is expected at T_C due to the paramagnetic to ferromagnetic transition of ferrite. However, in the case of high carbon steel samples, the impedance signal needs to indicate the phase transformation (austenite to pearlite) as it progresses and hence improved accuracy is desired. Thus, it was decided to carry out further testing at frequencies above 2 Hz. The sample re-heat temperature was also lowered from 950°C to 900°C to avoid the ends getting too hot (over 1000°C) and allow longer operational lifetime of the experimental setup.

5.2.3 EM response for High Carbon Steels

The phase transformation for the high carbon steel samples is dominated by the pearlitic formation. Quantitative image analysis on the as received material showed

that the ferrite content represented less than 1% of the total volume as seen in figure 5.3.

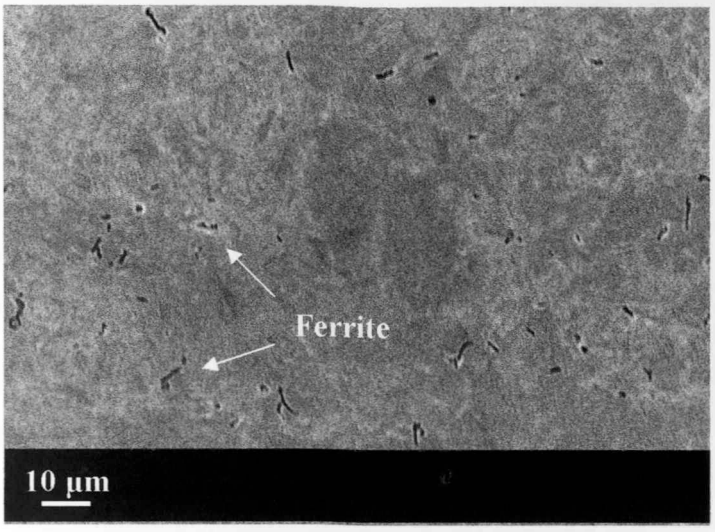

Figure 5.3: SEM micrograph showing pro-eutectoid ferrite in high carbon steel.

The release of large amounts of energy during pearlite formation leads to the re-heating of the sample and hence the impedance-temperature diagram is expected to show an increase in temperature indicating the start and end of the phase transformation as shown in figure 5.4.

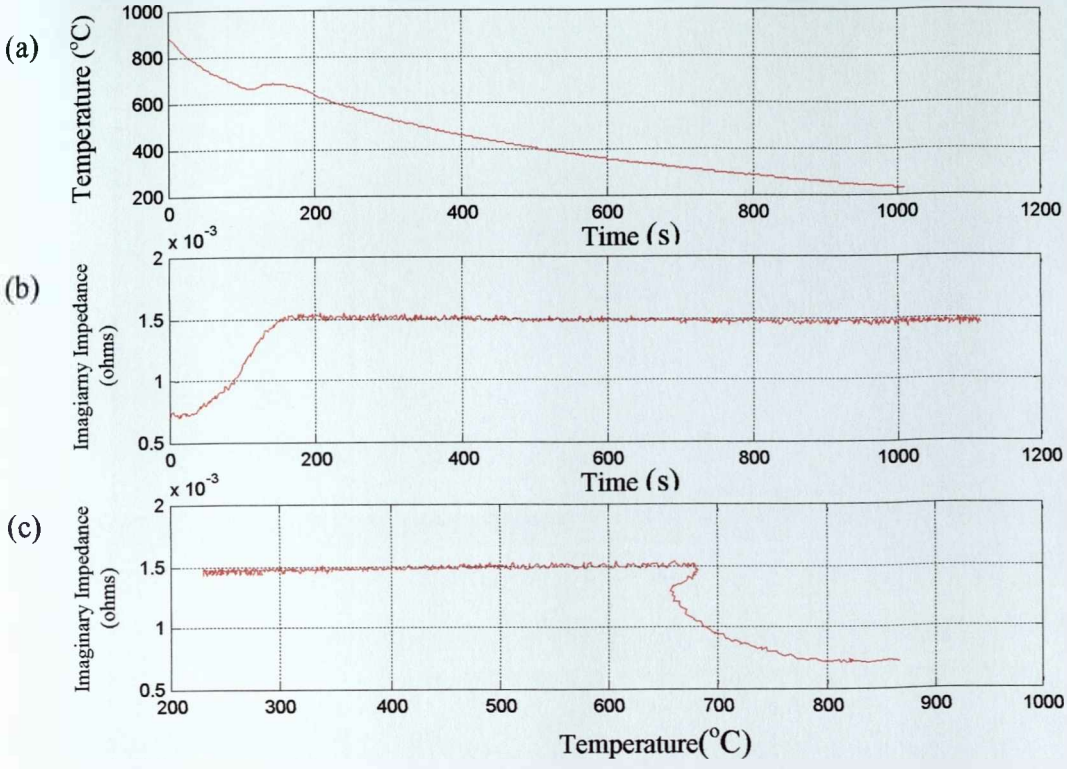

Figure 5.4: a) Temperature - time b) impedance - time and c) impedance – temperature diagrams for a high carbon steel sample tested at a frequency of 5 Hz.

Figure 5.5 shows the EM response (impedance – temperature) for a high carbon steel sample compared with the response measured for a low carbon steel sample. Comparison of the impedance values at temperatures less than 650°C confirms the variation of permeability value with carbon content, as discussed in chapter 2, causes a difference in impedance value, i.e. the impedance difference seen e.g. at 300°C between the two samples is attributed to the degrading effect of carbon reducing permeability and hence impedance [63].

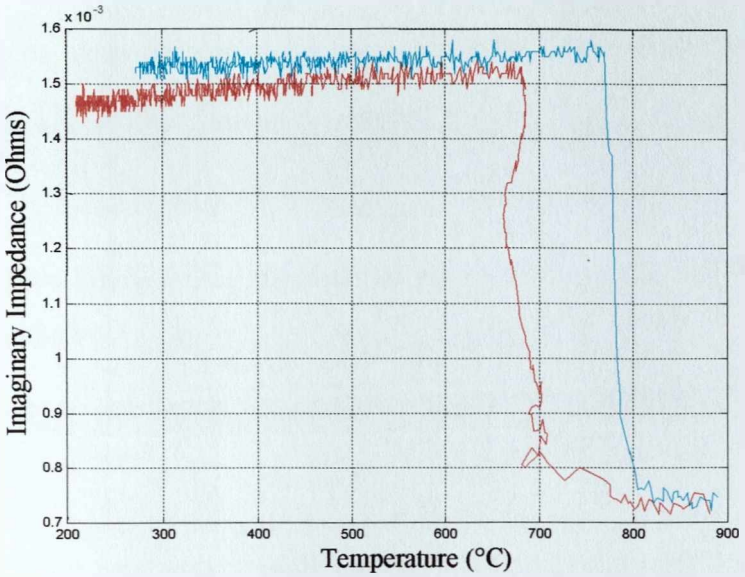

Figure 5.5: Comparison of high (red line) and low carbon (blue line) steels EM measurements at 5 Hz.

From figure 5.5, it is evident that for the high carbon steel the impedance starts increasing earlier than expected for a eutectoid transformation at 680°C, i.e. a small increase can be seen (~0.74 x 10^{-3} to 0.8 x 10^{-3} Ohms) just below the T_C. The temperature difference between the expected and the observed change in impedance values is such that it cannot be attributed to the existence of thermal gradients only. The reasons for this initial change in impedance, before the expected transformation will be discussed in section 5.3.2. The eutectoid temperature observed (680°C) is lower than that predicted by Thermo-Calc (720°C) due to non-equilibrium cooling,

5.2.4 Repeatability

For the low carbon steel samples the phase transformation occurred above the T_C resulting in large and easily defined impedance change, hence it was decided that further testing on this steel was not necessary. However, for the high carbon steel samples phase transformation takes place below the T_C, hence further EM tests where carried out in order to ensure the consistency of the recorded EM response and validate the experimental technique used. High carbon rod samples were repeat tested by cycling the same sample through a temperature range of 900° to 500°C. The number of repeat tests and the frequency the EM sensor was operated at is given in table 5.1.

Table 5.1: Number of heating cycles and frequency used for the tests.

		Frequency	
Cycle	**Sample 1**	**Sample 2**	**Sample 3**
1	5 Hz	10 Hz	2 Hz
2	5 Hz	10 Hz	2 Hz
3	5 Hz	10 Hz	
4	5 Hz	10 Hz	
5	5 Hz	10 Hz	

EM tests involving reheating of high carbon steel specimens produced unexpected EM responses. For a high carbon steel sample tested for two consecutive thermal cycles at frequency 2 Hz the impedances measured are shown in figure 5.6.

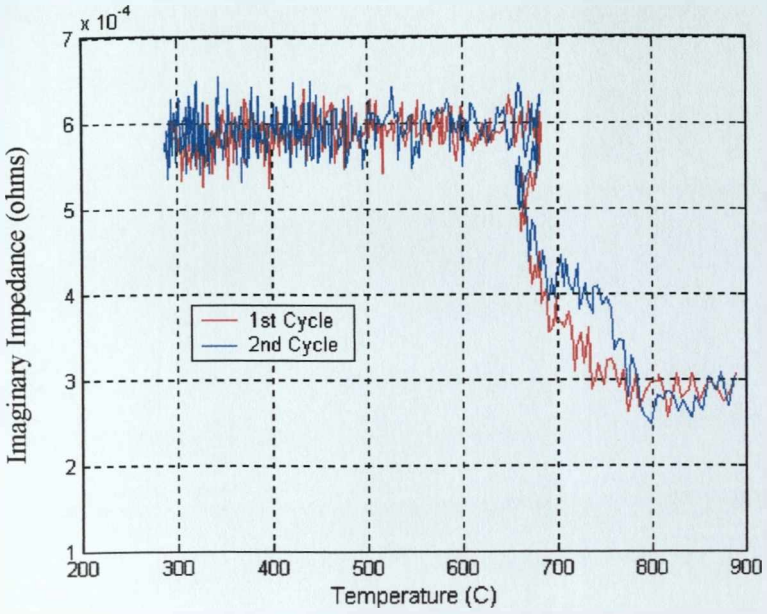

Figure 5.6: Comparison of the first and second heating cycles for high carbon steel at a frequency of 2 Hz.

The impedance – temperature traces shown in figure 5.6 are strongly affected by electromagnetic noise in a similar fashion with the low carbon steel measurement at a frequency of 1 Hz. In both traces the impedance begins to increase just below the T_C (approximately 770°C) and pearlite formation is seen to start approximately at 680°C. For the second thermal cycle however, the impedance value increases more rapidly at 770°C. The initial abrupt increase of impedance at 770°C is followed by a slower increase between 770°C and 680°C. At 680°C the impedance value increases rapidly again, and as the impedance value increases there a small increase in temperature which is related to the latent heat of transformation due to pearlite formation increasing the overall temperature of the sample.

Further tests involving a larger number of consecutive thermal cycles showed a more complex migration pattern of the impedance response. Figure 5.7 shows the response

of a high carbon steel sample following five consecutive thermal cycles at an EM sensor frequency of 5 Hz.

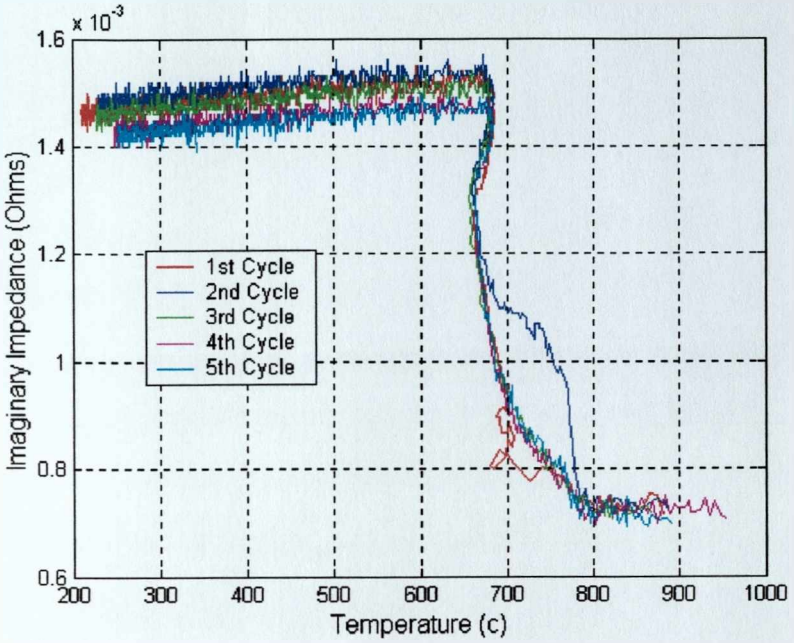

Figure 5.7: Comparison of impedance response for a high carbon steel sample during five consecutive heating cycles at an EM sensor frequency of 5 Hz.

In a similar manner as before, the impedance values increases more rapidly at T_C in the second thermal cycle. However this is not the case for the third, fourth and fifth thermal cycles for which the impedance response is nearer to the first cycle. EM tests at a higher frequency agreed relatively well with the previous diagrams. The results shown in figure 5.8 were produced after testing on a high carbon steel sample for five thermal trials at 10 Hz.

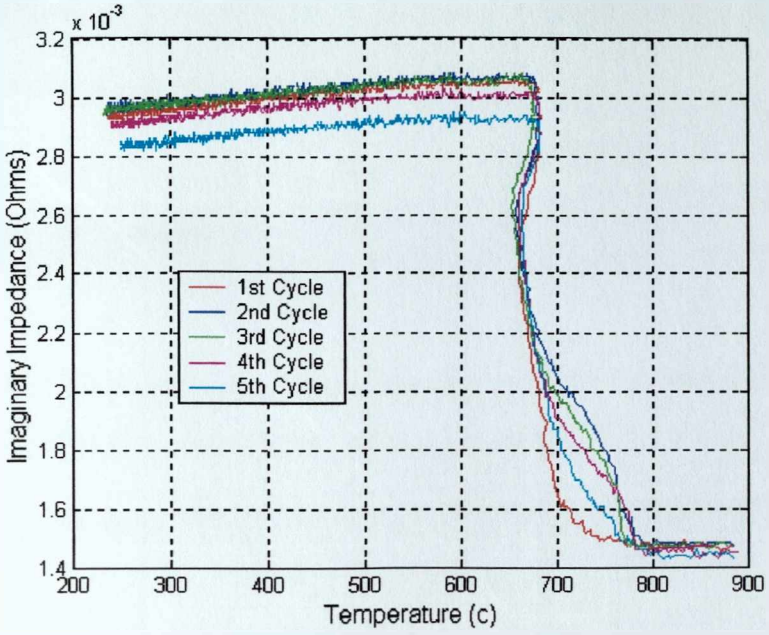

Figure 5.8: Comparison of impedance response for a high carbon steel sample during five consecutive heating cycles at frequency 10 Hz.

The difference in the impedance value increase between the first and second (and subsequent) thermal cycles appears to be a consistent trend due to its observation for different samples and EM testing at different frequencies. The increase in impedance cannot be explained by a phase transformation in the bulk of the steel sample as the steels are of eutectoid composition and no transformation is predicted. However, the samples must be displaying a change in conductivity and/or permeability in order to cause a change in the impedance value. Initial microstructural characterisation of the tested samples showed the presence of the decarburised area is affecting the impedance values. This effect will be discussed in more detail in section 5.3.2. The variation of maximum impedance value between the fifth and the rest of the cycles is likely to have occurred due to a slight buckling of the sample caused by the pressure applied by the Gleeble jaws in order to keep the sample in place. Slight buckling of

the sample is likely to have affected the flow of the electromagnetic flux resulting to lower impedance value been recorded.

5.3 Furnace EM results

The Gleeble EM trials yielded promising results regarding the validity and advantages of the EM technique in detecting and measuring phase transformation in steels. Nonetheless, the technical limitations of the experimental setup associated with the Gleeble 3500 thermomechanical simulator were a significant problem and thus a new methodology was required if thermal gradient effects along the length of the sample were to be minimised and the influence of decarburisation, grain size, material composition, oxidation and repeated heating cycles upon impedance response to be determined.

EM sensor tests using samples that could be thermally cycled in a furnace were therefore carried out. Temperature gradients during testing were found to be significantly lower in comparison with those linked to the Gleeble trials as discussed in chapter 4.

5.3.1 Calibration

In order to calibrate and reject the incidence of coil dimensional changes upon the temperature – impedance response, a hot test, with the sample omitted, was undertaken prior to each sample test. Such a calibration procedure ensured that data

recorded during each sample test was only due to steel transformation. Figure 5.9 shows the calibration curves recorded.

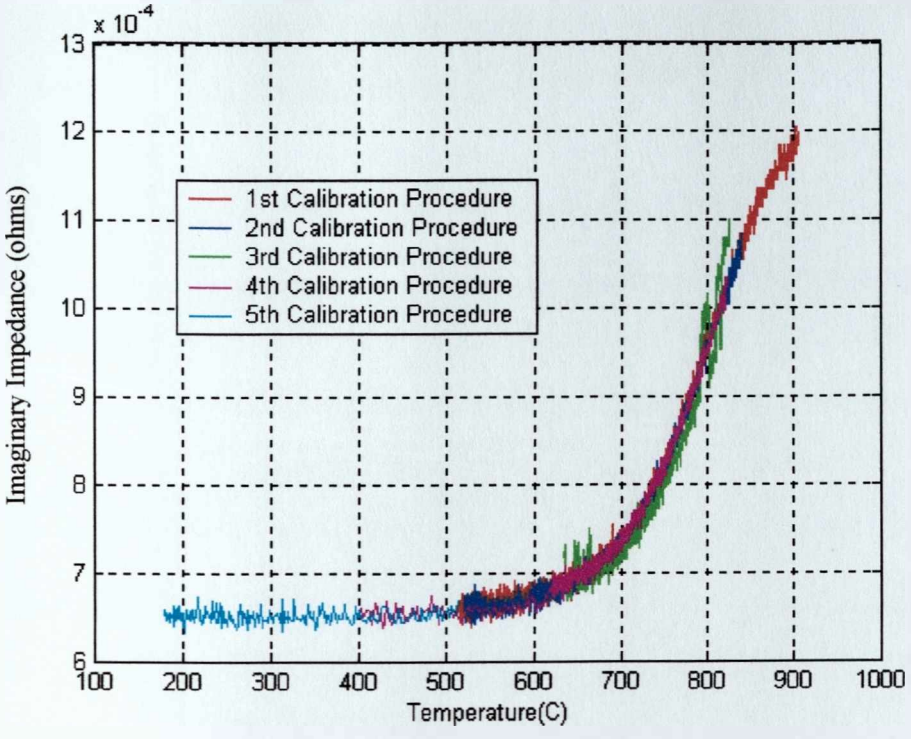

Figure 5.9: Repeatable coil response to temperature without the presence of a steel sample for a frequency of 2Hz.

5.3.2 Low Carbon Steel

A low carbon steel sample was heated to 830°C and held there for 20 minutes. Then the furnace was switched of and the sample was allowed to cool inside the furnace. At that temperature and hold time low carbon steel is not expected to have transformed fully to austenite. However, since any austenite that does form will transform back to ferrite on cooling the sample fully transforms above the Curie temperature means that the paramagnetic to ferromagnetic transition of ferrite at the

Curie temperature can be investigated. The EM sensor operated at frequencies 0.5 Hz and 2 Hz. The recorded impedance response is shown in figure 5.10.

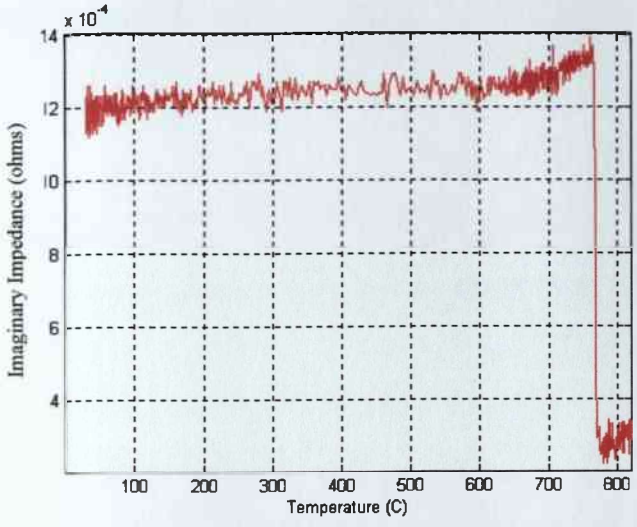

(a)

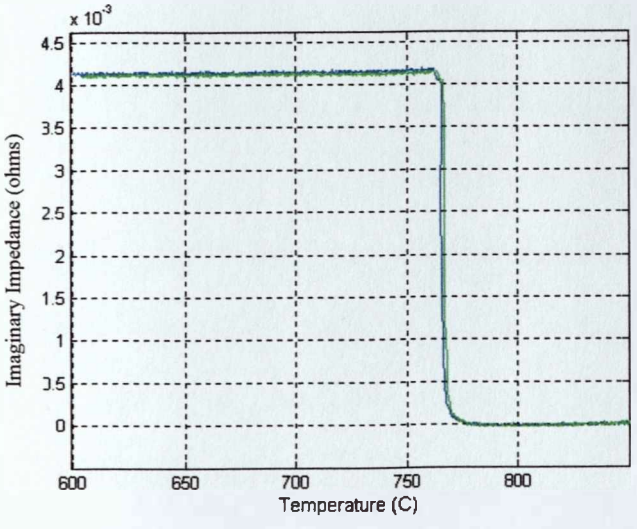

(b)

Figure 5.10: Impedance - temperature response for low carbon steel at (a) 0.5Hz and (b) 2Hz.

As it can be seen from figure 5.10 there is an abrupt increase recorded in the impedance value at 770°C. Comparison of the above results with previously reported

data proved to be in good accordance ensuring the validity of the experimental technique [204, 211, 235]. The anomalous decrease of the impedance value seen in the trace for the frequency of 0.5 Hz at temperatures just above T_C is likely to have been caused due to the excessive effect of the electromagnetic noise at such low frequencies.

5.3.3 High Carbon Steel

High carbon steel samples were tested with the EM sensor using the same experimental procedure as for the low carbon steel. The samples were heated to 870°C for 15 minutes to ensure phase transformation to austenite and then cooled inside the furnace down to 600°C. Since phase transformation finishes well above this temperature, the sensor-sample arrangement was then removed from the furnace and air-cooled to 200°C to reduce test time. The heating-cooling process was repeated for a number of times for each sample to examine the repeatability and validity of the experiment. Tests were also conducted on homogenised samples to investigate the effects of larger prior-austenite grains on impedance response. In figure 5.11 are shown the EM recordings for an unhomogenised high carbon steel specimen tested for two heating cycles at a frequency of 2 Hz.

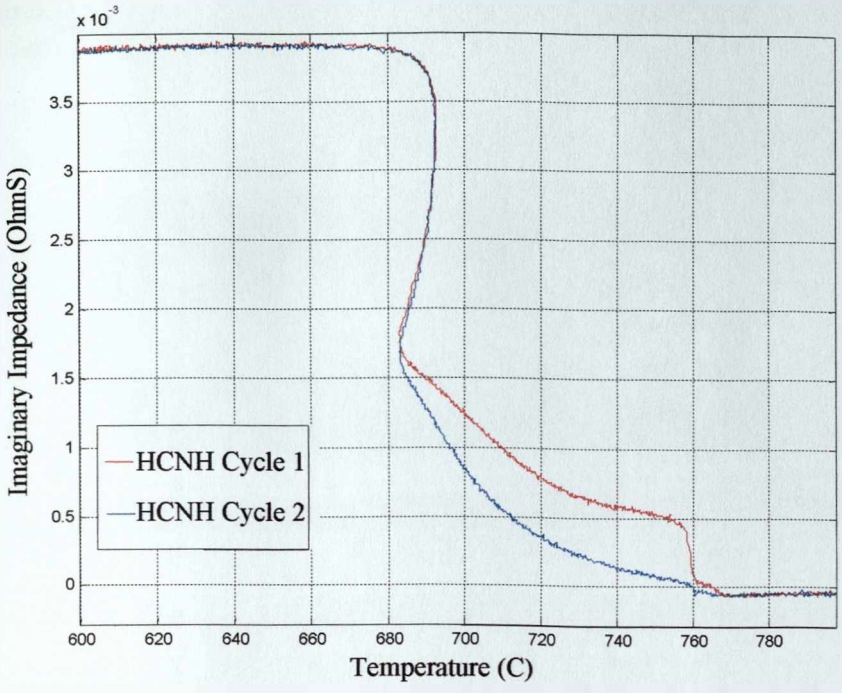

Figure 5.11: Impedance - temperature traces for an unhomogenised high carbon (HCNH) steel at an EM sensor frequency of 2Hz.

It can be seen in figure 5.11 that the impedance values start increasing considerably earlier than expected, at 760°C. Image analysis on high carbon steel samples before the EM tests revealed that the volume fraction of pro-eutectoid ferrite represented significantly less than 1% of the total volume. This small amount of pro-eutectoid ferrite would form immediately before the pearlite reaction, i.e. over a narrow temperature range just about between 690° - 685°C, hence the bulk pro-eutectoid ferrite in the sample cannot account for the impedance change at 760°C. Microscopy analysis of the sub-surface area of the samples (figure 5.12) revealed the existence of a decarburised region which could have transformed to ferrite at temperatures above 690°C and thus could be responsible for the otherwise unexplained impedance response observed in the particular EM measurement.

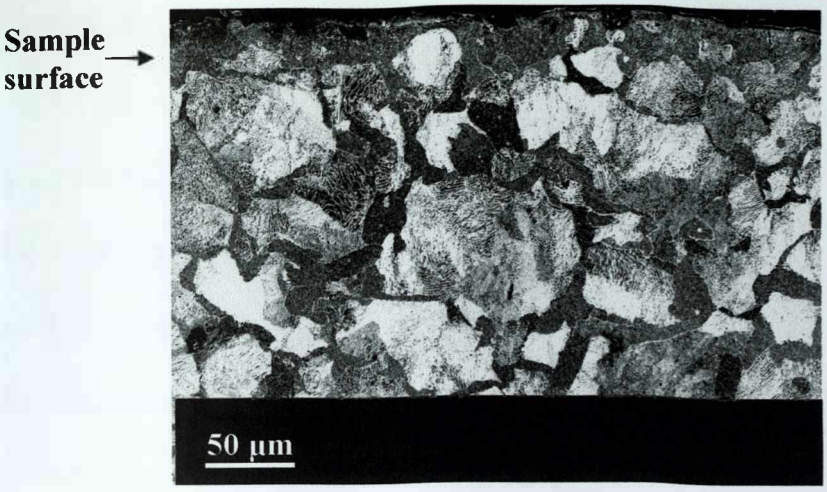

Figure 5.12: SEM micrograph showing the decarburised region at the surface of unhomogenised high carbon steel after two heating cycles.

Further EM tests conducted on high carbon steel samples homogenised in vacuum for 72 hours exhibited stronger impedance responses before pearlite formation started. Figure 5.13 shows impedance traces for a sample tested four times after reheating to a maximum temperature of 830°C at a frequency of 2 Hz. A lower re-heat temperature was employed in this case to prevent coil degradation.

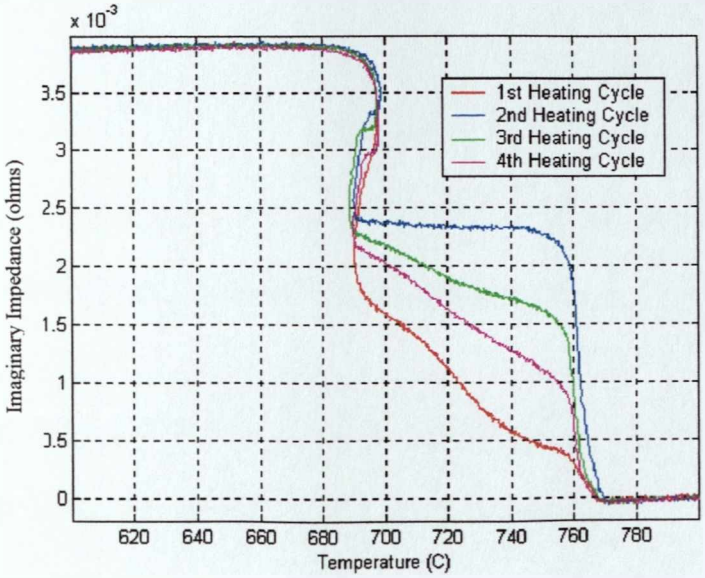

Figure 5.13: Electromagnetic response for a 1000°C vacuum homogenised high carbon steel sample at an EM sensor frequency of 2Hz reheated to 830°C.

The EM response in figure 5.13 follows the same pattern as for the Gleeble tests (shown in figures 5.6 – 5.8), with the second thermal cycle showing the largest impedance change at the Curie temperature followed by the third, fourth than the first thermal cycle. In an attempt to investigate the effect of higher reheat temperatures, a homogenised sample was heated for two cycles to 870°C. Figure 5.14 shows the recorded impedance – temperature traces after two thermal cycles at 2 Hz. The small differences observed in the T_C temperature in figures 5.10 – 5.13 (between 760 – 770°C) are discussed in detail later in the present chapter.

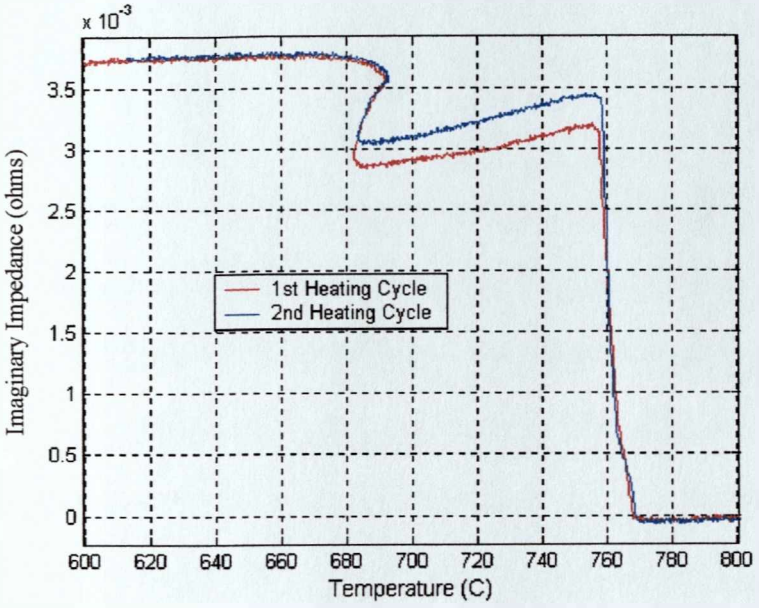

Figure 5.14: Recorded EM response during phase transformation of a vacuum homogenised high carbon steel at an EM sensor frequency of 2 Hz reheated to 870°C.

At higher reheat temperatures decarburisation increases causing the formation of more ferrite at the surface of the sample as shown in figure 5.15.

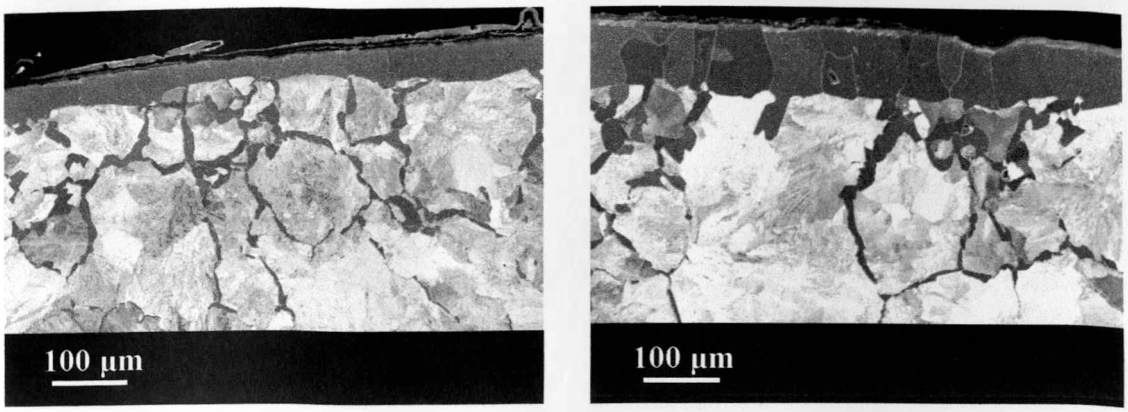

(a) (b)

Figure 5.15: SEM micrographs showing decarburisation depths for a) vacuum homogenised steel tested for two thermal cycles at a test temperature of 830°C and b) vacuum homogenised steel tested for two thermal cycles at a test temperature of 870°C.

Figure 5.15 shows the effect of the reheat temperature upon depth of decarburisation on vacuum homogenised high carbon steel. In figure 5.15(a) for a reheat temperature of 830°C the average depth of the ferrite layer present at the surface of the sample is approximately 50 µm, whilst for a reheat temperature of 870°C the average depth of the ferrite layer present is seen to be approximately 90 µm. The size of the ferrite layer at the surface of the sample is a crucial factor which directly affects the impedance value below the T_C. Apparently, the increasing amount of ferrite causes a stronger initial EM response just below the Curie point, similar to the one exhibited in low carbon steel tests. As it will be shown later this impedance response is dominated by the amount of ferrite formed from decarburisation. A comparison between low carbon and high carbon (homogenised and reheated to 870°C) steel response at a frequency of 2 Hz is shown in figure 5.16.

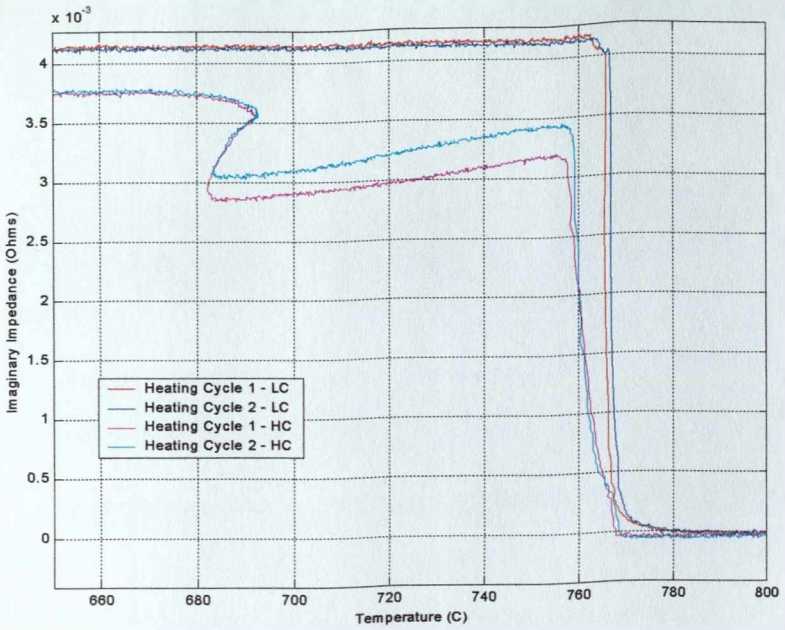

Figure 5.16: Comparison of impedance – temperature traces for the first two thermal cycles for the low and vacuum homogenised high carbon steels at a frequency of 2 Hz.

From figure 5.16 a slight difference in the Curie temperature for each steel grade is observed. This slight difference in the T_C between low and high carbon steel results from the differences in the alloying elements (especially carbon) present in the steel and their concentration as discussed in chapters 2 and 3. Also evident is the effect of carbon content upon permeability, i.e. low carbon steel has higher impedance, thus permeability, than high carbon steel when fully transformed (e.g. at 660°C).

5.3.4 Argon Homogenisation (1200°C)

To minimise any decarburisation during homogenisation high carbon steel samples were homogenised at 1200°C in an argon atmosphere for 72 hours and were examined over two heating cycles. Each test had a reheat temperature and time, of 870°C and

16 minutes respectively. In figure 5.17 are shown the impedance responses for the vacuum and argon homogenised samples.

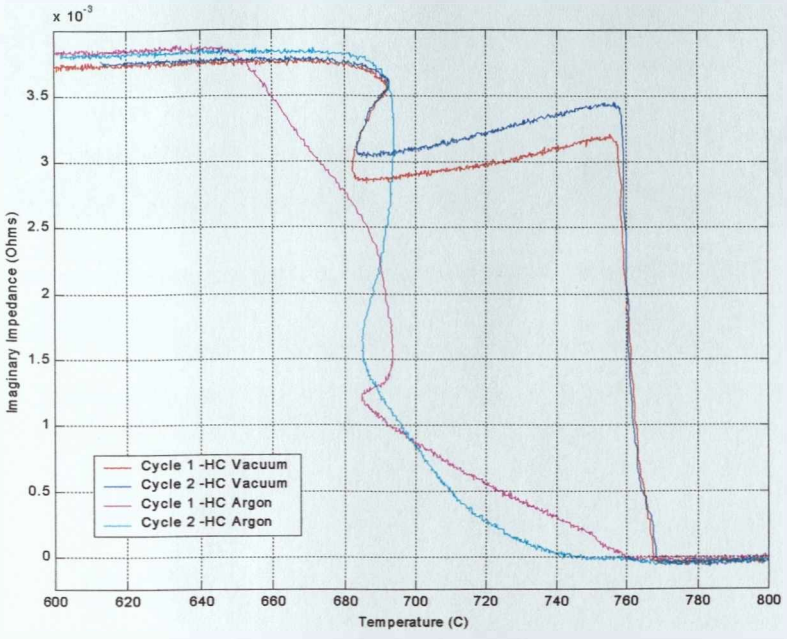

Figure 5.17: Comparison of impedance – temperature traces for vacuum and argon homogenised high carbon steel samples tested for two thermal cycles at 2 Hz.

In figure 5.17 an abrupt increase in the impedance response is seen at 770°C for the vacuum homogenised high carbon steel sample, which is followed at 685°C by a further increase in the impedance value due to the pearlite formation. For the argon homogenised high carbon steel the impedance value is shown to increase steadily between 760° and 685°C. At 685°C the impedance response corresponds to the pearlite formation. The impedance responses prior to any pearlite formation is related to the amount of ferrite present in the decarburised region. In figure 5.18(a)-(b) it is shown that the amount of ferrite formed in the argon homogenised sample is significantly lower than in the vacuum homogenised sample even though identical thermal cycles were employed.

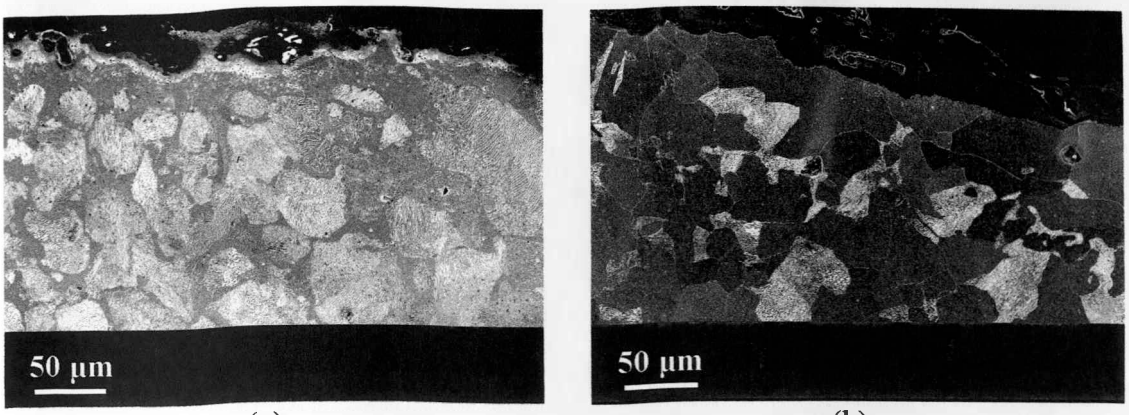

(a) (b)

Figure 5.18: SEM micrographs showing decarburisation levels after two thermal cycles for a) argon homogenised and b) vacuum homogenised high carbon steel at 870°C.

The ferrite layer forming in the vacuum homogenised high carbon steel is free of carbon and hence it is likely to have a higher T_C, close to the one observed for low carbon steel, than the bulk of the sample. Thus, the shift observed in the T_C temperature is due to extensive decarburisation which has taken place at the surface of the sample resulting in the formation of complete ferrite layer. For the argon homogenised sample the initial impedance increase on cooling starts at a slightly lower temperature and increases more slowly showing that less ferrite has formed due to decarburisation as seen in figure 5.18(a). The EM response observed in the second test on the argon homogenised specimen shows that the decarburisation effect on impedance is lower. This could be attributed to oxidation up to a certain degree of the ferrite layer forming at the surface of the sample as seen in figure 5.19.

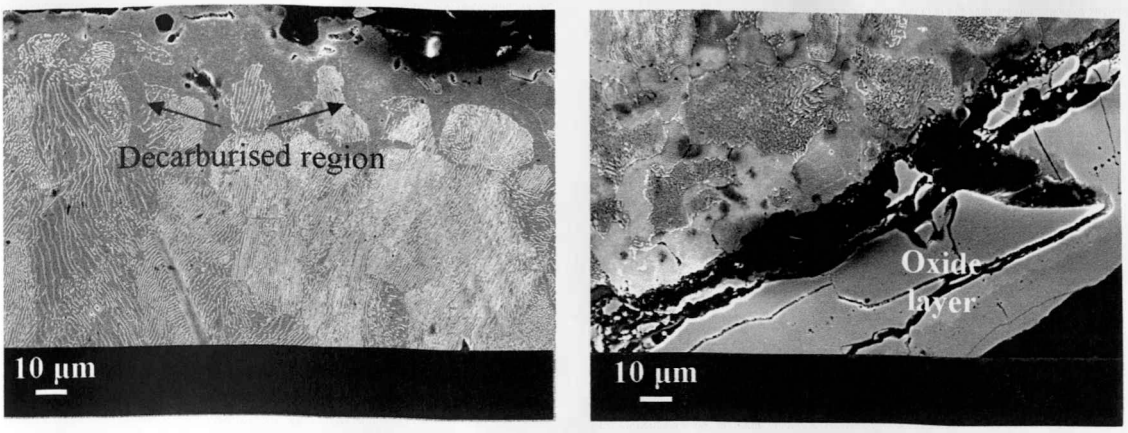

(a) (b)

Figure 5.19: SEM micrographs showing decarburisation and oxidation levels in an a) argon homogenised high carbon steel sample before testing and b) argon homogenised high carbon after two thermal cycles.

Microscopy analysis of the tested samples revealed the existence of a decarburised region at the surface of the samples. The amount of ferrite formed due to carbon depletion at the surface is not identical in every sample and is related to the carbon content and heat treatment conditions. The decarburisation effect is more severe if through the homogenisation process some carbon depletion already takes place as seen in the micrographs in figure 5.20. As no vacuum is perfect some decarburisation occurred during the homogenisation of the high carbon steel. However, this is not the case for the samples homogenised under argon atmosphere where oxygen presence is minimised and hence decarburisation is kept to the lowest level possible [2, 65, 166].

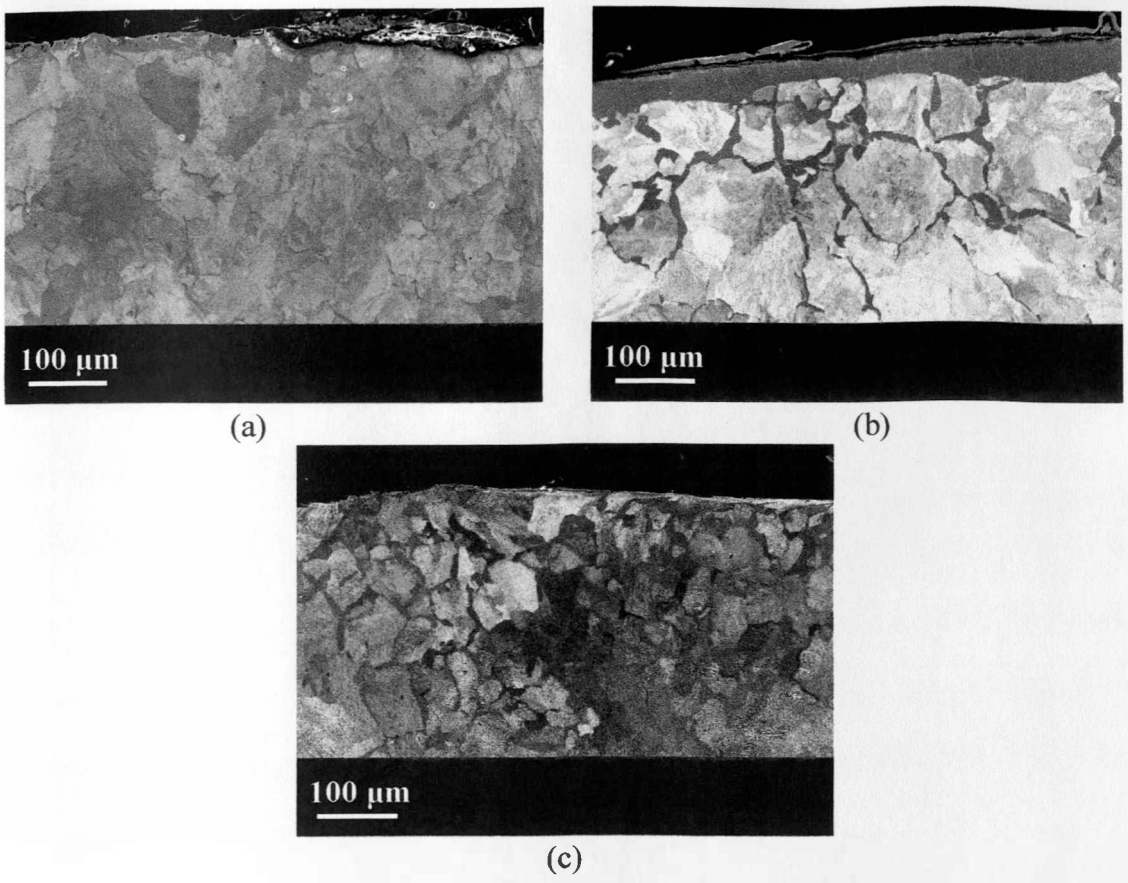

Figure 5.20: SEM micrographs showing levels of decarburisation before testing for a) unhomogenised, b) homogenised in vacuum at 1000°C and c) homogenised in argon at 1200°C high carbon steel.

Image analysis of the micrographs of the high carbon steel samples showed that the decarburisation effect is localised at the surface of the sample and up to a certain depth from the surface. The area affected from decarburisation should increase in depth with each thermal cycle. However, the ferrite formed in the outer decarburised area from the first thermal cycle contains very small amounts of carbon. Hence, at the steel – atmosphere interface in the absence of carbon, iron atoms react with oxygen atoms to form the oxide scale which consists of three iron oxides - wustite (FeO), hematite (Fe_2O_3) and magnetite (Fe_3O_4) [166]. The oxide scale produced, although it is extremely brittle and tends to break off from the main body of the sample easily

giving way for new layers to form, has the capability of protecting up to a certain degree the rest of the sample by preventing oxygen atoms from reaching the steel interface. Both the scale and decarburised area tend to increase in depth with each thermal cycle. Nonetheless, the rate at which the sample decarburises is lower than the rate at which it oxidises [166]. As a result a large part of the ferrite formed from the decarburisation process is replaced by scale. This leads to less ferrite being present in the decarburised zone and hence a smaller magnetic response is detected by the sensor. Despite the fact that Fe_3O_4 is ferromagnetic and makes up the top part of the scale, it does not affect the recorded impedance response because its Curie temperature lies at 580°C [63], significantly lower than the temperature range of interest for the present study. FeO and Fe_2O_3 are paramagnetic and thus their presence does not affect the EM signal at any temperature.

Figure 5.21 presents a comparison of the recorded impedance traces for unhomogenised and homogenised samples during the first two heating cycles.

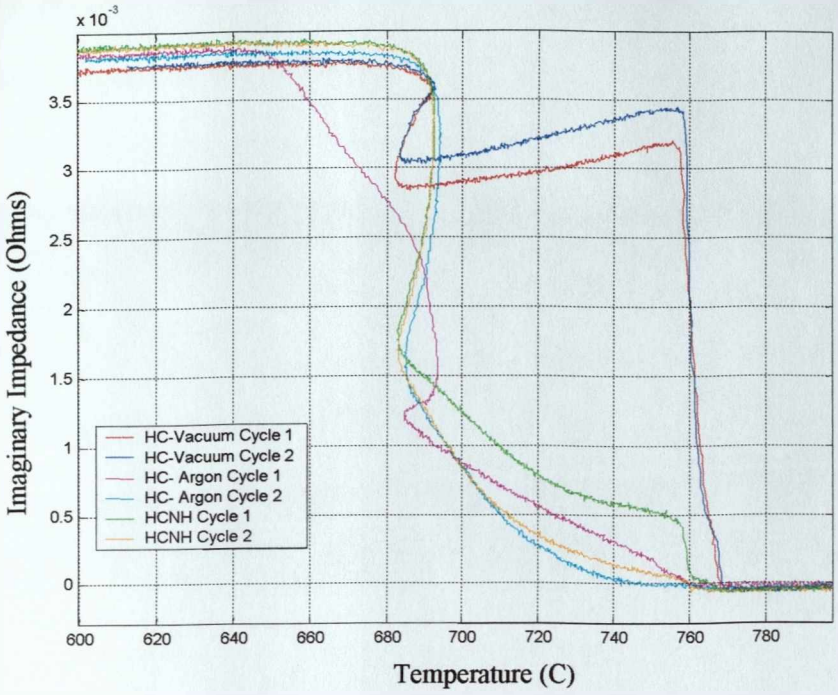

Figure 5.21: Impedance – temperature traces for unhomogenised high carbon steel (assigned as HCNH), argon homogenised high carbon steel (assigned as HC – Argon) and vacuum homogenised high carbon steel (assigned as HC – Vacuum) for two thermal cycles at a frequency of 2 Hz.

In figure 5.21 there is a clear similarity between the unhomogenised and argon homogenised responses to sample reheating. This is due to the similar amount of decarburisation observed in the unhomogenised and argon homogenised sample after two thermal cycles as shown in figure 5.20. For the vacuum homogenised sample an abrupt increase in impedance at 770°C is observed indicating the presence of a large fully decarburised region at the surface of the sample. It is noted that the T_C for the unhomogenised and argon homogenised sample lies at 760°C as shown in figure 5.21. Although some decarburisation has taken place in both unhomogenised and argon homogenised samples as shown in figure 5.22, there is not a fully decarburised region present at the surface of the samples. Hence the surface of the samples is not

completely free of carbon as for the vacuum homogenised carbon resulting in a lower T_C as expected from the theory [63].

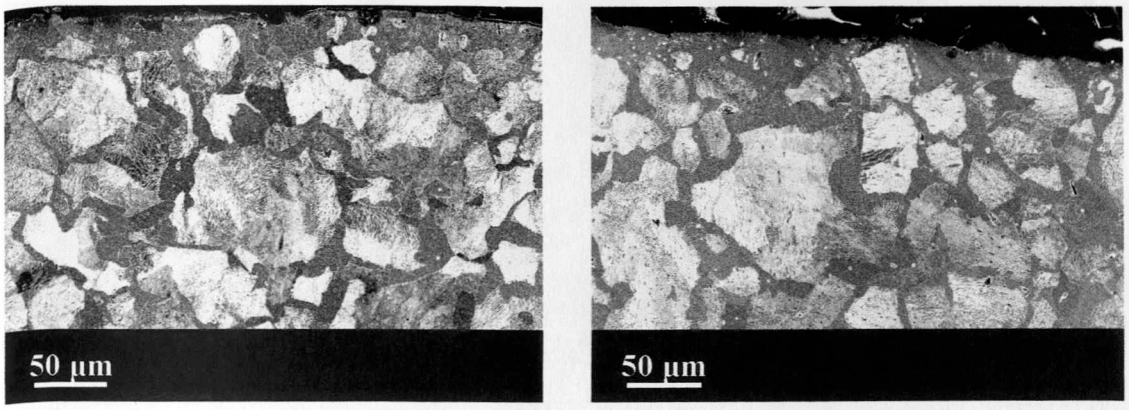

(a) (b)

Figure 5.22: SEM micrographs showing decarburisation levels after two thermal trials for a) unhomogenised and b) argon homogenised high carbon steel.

5.3.5 Medium carbon steel

Unhomogenised medium carbon steel was tested over two heating cycles to investigate the influence of pro-eutectoid ferrite formation over a range of temperatures below the Curie point. From results obtained with Thermo-Calc ferrite formation in the medium carbon steel is predicted to occur at temperatures just below the Curie temperature under equilibrium conditions. However, due to dynamic cooling of the sample during tests the start of austenite decomposition is suppressed to lower temperatures as seen for the high carbon steel samples. The conductivity of steel also decreases as carbon content increases, however, the difference between a steel with carbon content 0.45 in wt % and a steel with carbon content 0.80 in wt % is very small (i.e. at room temperature the measured conductivity is 5.84 x 10^6 and 5.88

x 10^6 Siemen respectively) [178]. Therefore, although the conductivity value is of importance, in this case the variation observed between the impedance response recorded for the medium and high carbon steels is primarily due to the difference in permeability. Figure 5.23 shows the impedance response on cooling for the non-homogenised medium carbon steel compared to results from the non-homogenised high carbon steel. Due to decarburisation effects, an abrupt impedance increase occurs for the medium carbon steel at approximately 760°C with an increase in impedance from 0 to approximately 1.5 x 10^{-3} Ohms. This is then followed by a reduced rate of impedance increase (1.5 x 10^{-3} to approximately 2 x 10^{-3} Ohms) over the temperature range 760° to 720°C. This is then followed with an increased rate of impedance rise between 720°C and the eutectoid temperature of ~680°C. The final permeability is greater in medium carbon steel, than for high carbon, due to the reduce content of paramagnetic cementite (which diminishes the steels permeability) [63, 178].

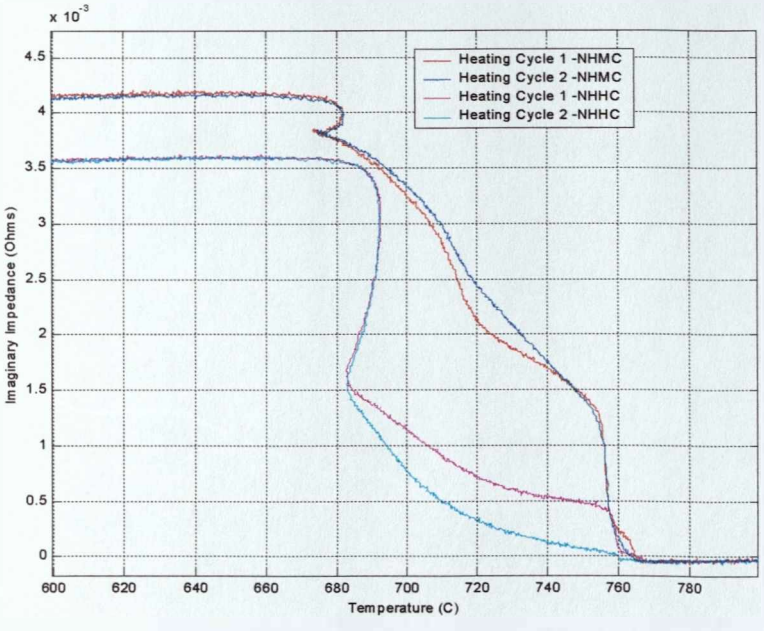

Figure 5.23: Impedance – temperature traces for unhomogenised medium carbon steel (assigned NHMC) and unhomogenised high carbon steel (assigned NCHC) at a frequency of 2Hz.

So far it is apparent that the EM response for medium and high carbon steel samples is largely affected by the presence of ferrite occurring due to decarburisation at the surface of the samples during testing as seen in figure 5.24.

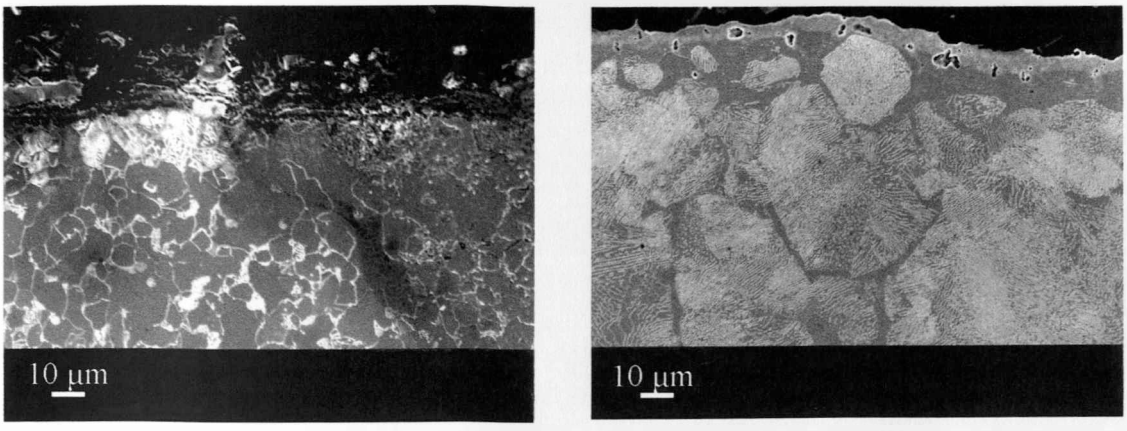

(a) (b)

Figure 5.24: SEM micrographs showing decarburization depth after two thermal trials for a) unhomogenised medium carbon steel and b) unhomogenised high carbon steel.

Micrographs of the tested samples have shown that the decarburised area is much smaller in comparison with the total area of the sample. The impedance response that corresponds to the ferrite presence at the skin of the sample is disproportionate to its volume. Quantitative image analysis on medium carbon steel samples before testing showed that pearlite occupies 72 % of the total volume and the other 28 % is ferrite. The part of the impedance trace corresponding to the pearlite formation is significantly smaller than the part originating from the ferrite present in the decarburised area or in the bulk. This indicates that the impedance response is not proportional to ferrite formation and is affected by other microstructural factors, this will be discussed later.

5.4 Decarburisation Growth Investigation

EM tests were conducted to determine the relationship between the decarburised layer, EM test temperature and impedance response. As a consequence the maximum test temperature was raised to 925°C to enhance the decarburisation of the samples. Three frequencies were employed during these tests; 2 Hz, 50 Hz and 5000 Hz. Table 5.2 shows the frequency details for the tests. At high frequencies the magnetic flux created from the sensor's exciting coil is constrained at the outer area of the sample due to the existence of strong eddy currents that flow in the sample. Therefore, the resulting magnetic response at high frequencies should be dominated by the presence of ferrite at the decarburised layer.

Table 5.2: Test details for the decarburisation growth investigation.

Composition	Frequency / Hz	Heating Cycles
Low carbon	2	2 cycles
	50	2 cycles
	5000	2 cycles
Medium Carbon (Homogenised)	2	1 cycle
		2 cycles
		3 cycles
	50	2 cycles
High carbon (Homogenised)	2	1 cycle
		2 cycles
		3 cycles
	50	2 cycles
	5000	2 cycles
High carbon (Unhomogenised)	2	1 cycle

The exact sampling depth during testing could not be determined because the exact permeability of the varying carbon content surface region is not known. However, using equation 3.20, a relative permeability of 2000 (for a medium carbon steel) and 10,000 (for a low carbon steel), see figure 2.24, and a conductivity of 1.11×10^6 siemens (for 770°C, see figure 2.22) then the skin depths for the different frequencies can be determined as presented in Table 5.3.

Table 5.3: Relative permeability – frequency relationship with sampled depth.

Relative Permeability / μ_R	Frequency / Hz	Sampled depth / mm
2000	1	10.6
	5	4.77
	10	3.33
	50	1.5
	5000	0.15
10000	1	4.77
	5	2.13
	10	1.5
	50	0.67
	5000	0.067

5.4.1 Low Carbon Steel

Tests were performed on low carbon steel samples to determine the effects of the various frequencies on the impedance response. Figure 5.25 shows the results obtained for three low carbon steel samples at different frequencies.

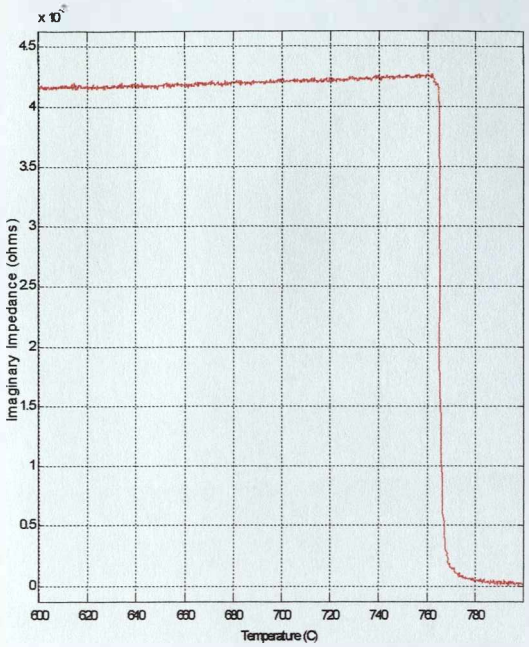
x 10^3
4.5
4
3.5
3
2.5
2
1.5
1
0.5
0
Imaginary Impedance (ohms)
600
620
640
660
680
700
720
740
760
780
Temperature (C)

(a)

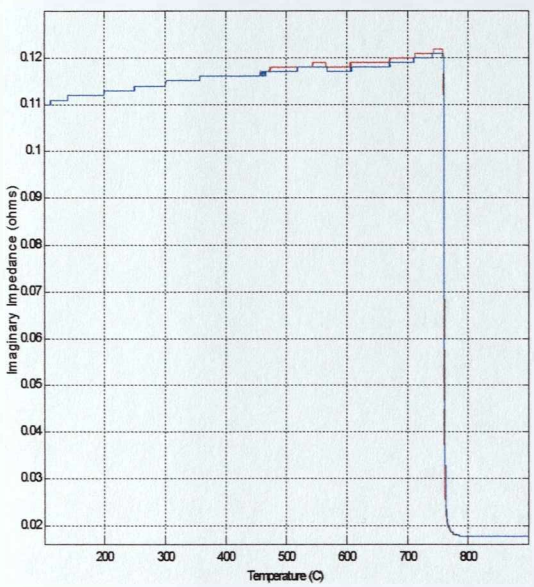
0.12
0.11
0.1
0.09
0.08
0.07
0.06
0.05
0.04
0.03
0.02
Imaginary Impedance (ohms)
200
300
400
500
600
700
800
Temperature (C)

(b)

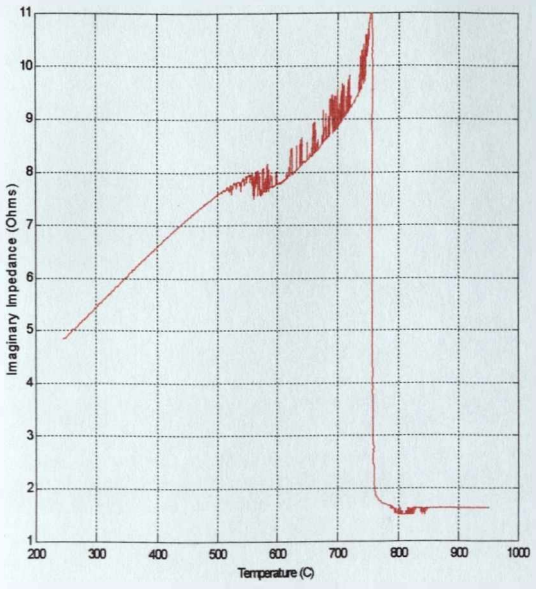

(c)

Figure 5.25: Impedance – temperature traces showing the eddy current effect with increasing frequency at a) 2 Hz, b) 50 Hz and c) 5 kHz.

The paramagnetic to ferromagnetic transition is successfully detected at 770°C in all trials. The rate of decrease of the impedance value with temperature below the Curie point is a direct result of the attenuation caused by eddy currents. The eddy current effect is stronger in figure 5.25(c) where the frequency is highest.

5.4.2 High Carbon Steel

The impedance - temperature trace for a vacuum homogenised high carbon steel sample tested at frequency 2 Hz is presented in figure 5.26.

Figure 5.26: Impedance – temperature response for vacuum homogenised high carbon steel after one heating cycle at a frequency of 2Hz.

It can be seen that impedance abruptly increases at 770°C from 0 to ~ 2.5 x 10^{-3} Ohms and then reduces slightly until pearlite formation begins. As soon as pearlite formation commences the impedance value increases up to a maximum value that corresponds to the end of the phase transformation. Figure 5.27 shows an SEM micrograph of the sample after the first thermal cycle. A fully decarburised ferrite layer of approximately 150 μm can be seen at the surface of the sample with a partially decarburised layer of approximately 400 μm below it. The decarburised ferrite layer will transform above the Curie temperature thus the large impedance change observed at 770°C appears to be due to the relatively thin ferrite layer.

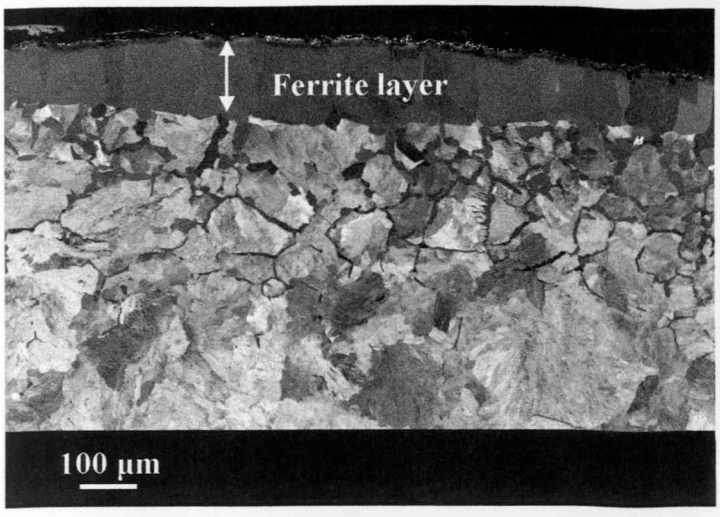

Figure 5.27: SEM micrograph showing the decarburised zone of a vacuum homogenised high carbon steel after EM testing for one heating cycle at a frequency of 2Hz.

The formation of the ferrite along prior austenite grain boundaries, below the fully decarburised layer, is expected to have taken place between the T_C and the eutectoid temperature. However, in figure 5.26 it is seen that the impedance value reduces slightly between T_C and the eutectoid temperature, when it should increase as a consequence of the formation of extra pro-eutectoid ferrite. This anomaly is of significance for the present study and is discussed later in this chapter.

If it is assumed that the median conductivity and permeability values of the specimen were 3.5×10^6 Sm^{-1} and 1000 respectively at T_C, for frequency 2 Hz solving equation results to a sampling depth of 6 mm, i.e. the full volume of the specimen. The pro-eutectoid ferrite layer is expected to have higher conductivity and permeability values than the bulk of the sample and hence a reduction in the sampling depth should occur. In figure 5.28 it is seen that the pro-eutectoid ferrite layer attracts the magnetic flux between T_C and eutectoid temperature at which pearlite formation begins. Obviously,

a contiguous high permeability layer has a dominant effect on the recorded impedance value while isolated pro-eutectoid ferrite regions forming dispersed in the lower parts of the decarburised region are not detected.

The impedance - temperature trace obtained for the second thermal cycle (figure 5.28) agrees well with the conclusions drawn regarding the effects of decarburisation and oxidation on the impedance value.

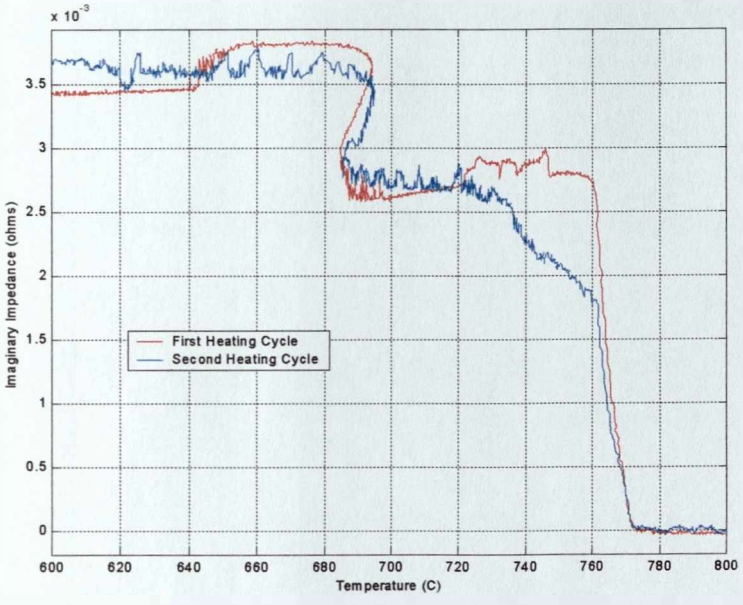

Figure 5.28: Impedance – temperature response to two heating cycles for a vacuum homogenised high carbon steel at frequency of 2 Hz.

Impedance increase at 770°C is smaller in the second thermal cycle, which signifies some oxidation of the decarburised layer. Figure 5.29 shows two SEM micrographs at different magnifications obtained from the sample after two heating cycles.

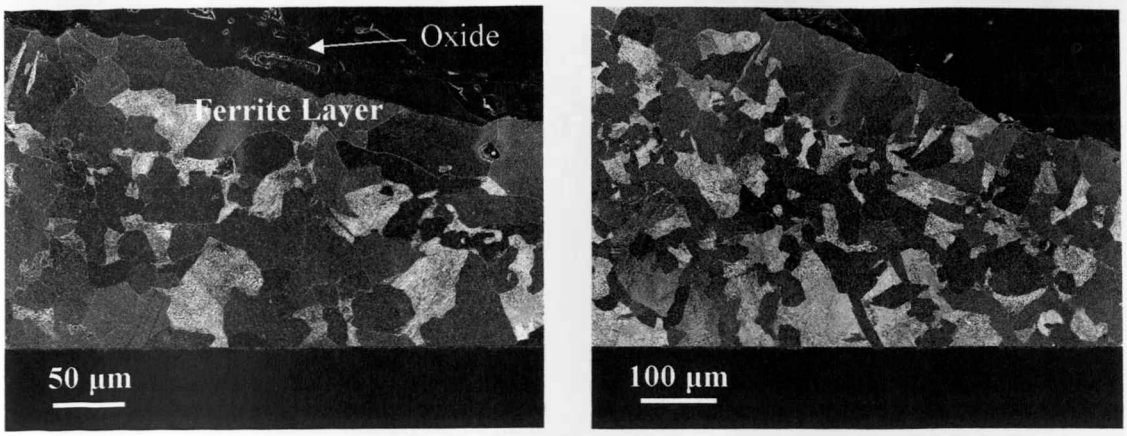

(a) (b)

Figure 5.29: SEM micrographs showing the decarburised region of the vacuum homogenised high carbon steel after two heating cycles at two different magnifications: a) x350 and b) x200.

As seen in figure 5.29(a) the thickness of the fully ferrite decarburised layer has decreased to approximately 15 – 20 μm due to oxidation and the depth of the partially decarburised region has increased to above 500 μm, figure 5.29(b). Examination of the impedance – temperature trace for the second cycle shows that after the initial response, the impedance continues to increase slowly between T_C and eutectoid temperature as a result of the pro-eutectoid ferrite forming in the deeper parts of the decarburisation affected area. Hence, the thickness of the decarburised layer is an important factor that influences the EM response observed.

The resulting response for the third heating cycle tends towards that of the first cycle as shown in figure 5.30. Micrographs of the sample obtained with SEM (figure 5.31) showed an increase in the decarburised layer's thickness resulting in an increase of the impedance value.

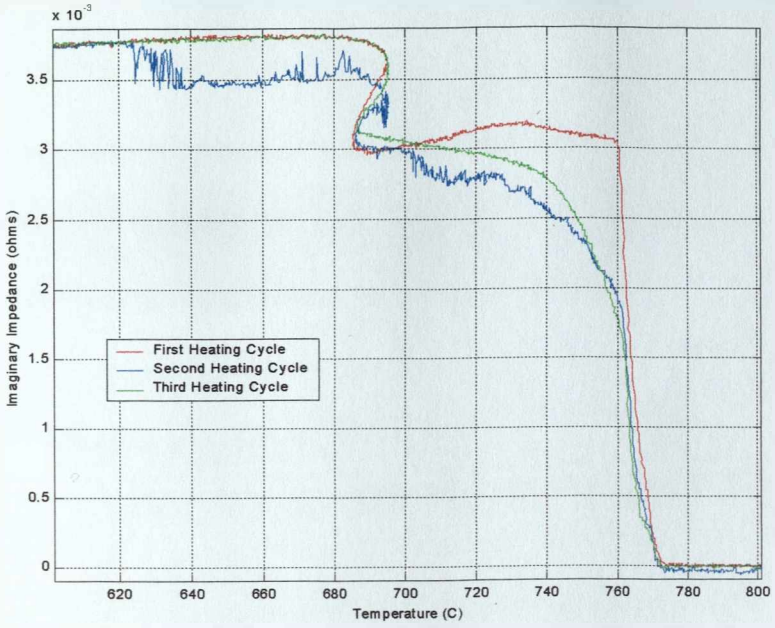

Figure 5.30: Impedance – temperature traces for a vacuum homogenised high carbon steel tested at 2 Hz for three thermal cycles.

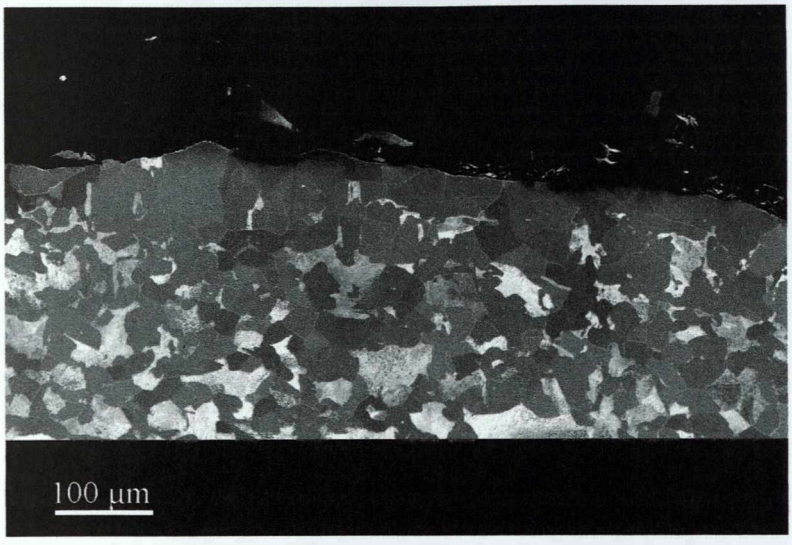

Figure 5.31: SEM micrograph showing decarburisation in a vacuum homogenised high carbon after three heating cycles.

Studying the impedance trace for the third cycle in conjuction with the SEM micrograph obtained from the sample, it is clear that the pro-eutectoid ferrite forming

in the decarburised region between T_C and eutectoid point is detected by the sensor for testing at 2 Hz. The electromagnetic noise observed in the impedance – temperature trace for the second heating cycle is likely to have occurred due to the operation of nearby equipment during the particular test or progressive degradation of the sensor due to the high temperatures involved in the tests.

5.4.3 50 Hz Excitation Frequency

EM tests on a vacuum homogenized high carbon sample at a frequency of 50 Hz produced similar responses with the tests at 2 Hz. At 50 Hz the sampling depth should be significantly smaller, approximately 1.2 mm at 770°C. In figure 5.32 are displayed the recorded impedance responses for each cycle.

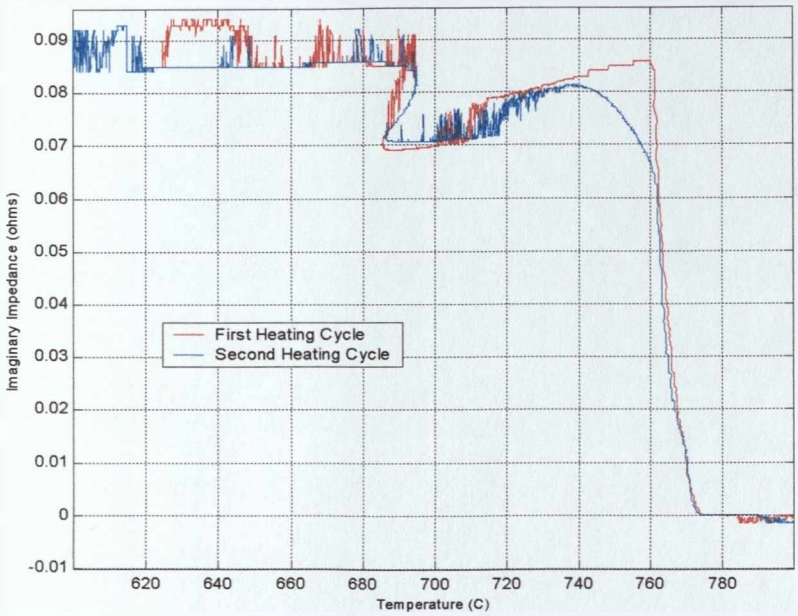

Figure 5.32: Impedance – temperature response of two thermal cycles at a frequency of 50Hz for vacuum homogenised high carbon steel.

Comparison of the recorded traces at 2 Hz and 50 Hz shows that in both cases the impedance response results from the fully pro-eutectoid ferrite layer forming at the outer skin of the samples. The anomaly seen in the second cycle in figure 5.32, where impedance increases between 770°C and 740°C and then decreases between 740°C and the eutectoid point, is owed to the concentration of the flux at the outer parts of the decarburised area. The concentration of the flux in the outer parts of the decarburised area is caused by the presence of strong eddy currents due to the higher frequency employed. The electromagnetic noise observed in both traces is probably due to the operation of nearby equipment or sensor degradation. However, due to the relatively high frequency used it is concluded that the observed noise in the signal is due to sensor degradation rather than due to operation of nearby electrical equipment.

5.4.4 5 kHz Excitation Frequency

Assuming the same conductivity and permeability values as before, the sampling depth is limited to 0.12 mm at T_C, 770°C, for a frequency of 5 kHz and hence the magnetic flux should be constrained at the surface of the sample regardless of the existence of a pro-eutectoid ferrite layer. As expected, both responses shown in figure 5.33 are approximately identical with those obtained at 50 Hz.

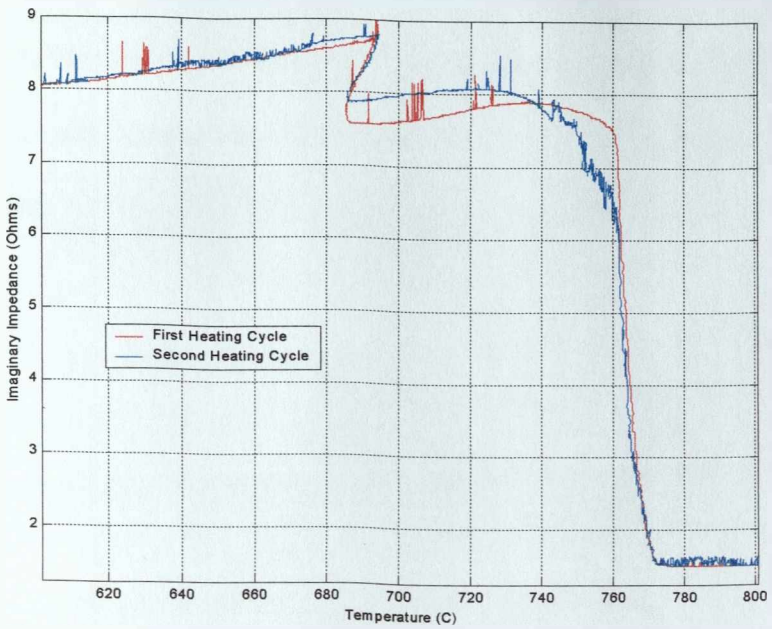

Figure 5.33: Impedance – temperature responses for vacuum homogenised high carbon steel after two heating cycles at 5kHz.

The increase in impedance at the eutectoid point is a direct result of pearlite formation and the existence of pro-eutectoid ferrite islets formed earlier in the decarburised region. The formation of pearlite in the decarburised area creates a contiguous high permeability path which attracts some of the magnetic flux to flow under the pro-eutectoid ferrite layer. As a result, the impedance value rapidly increases up to the point where pearlite formation is concluded.

5.4.5 Non-Homogenised High Carbon Steel

EM testing of a non-homogenised high carbon sample at a frequency of 2 Hz was carried out to confirm the findings, i.e. this was expected to produce a relatively small impedance response at T_C, 760°C (due to the small amount of decarburisation present), increasing slowly between the T_C (due to ferrite formation in the partially

decarburised region) and another sudden increase in impedance at the eutectoid point. Figure 5.34 shows a comparison of the impedance traces obtained for the unhomogenised and vacuum homogenised samples, which agrees well with the predictions made.

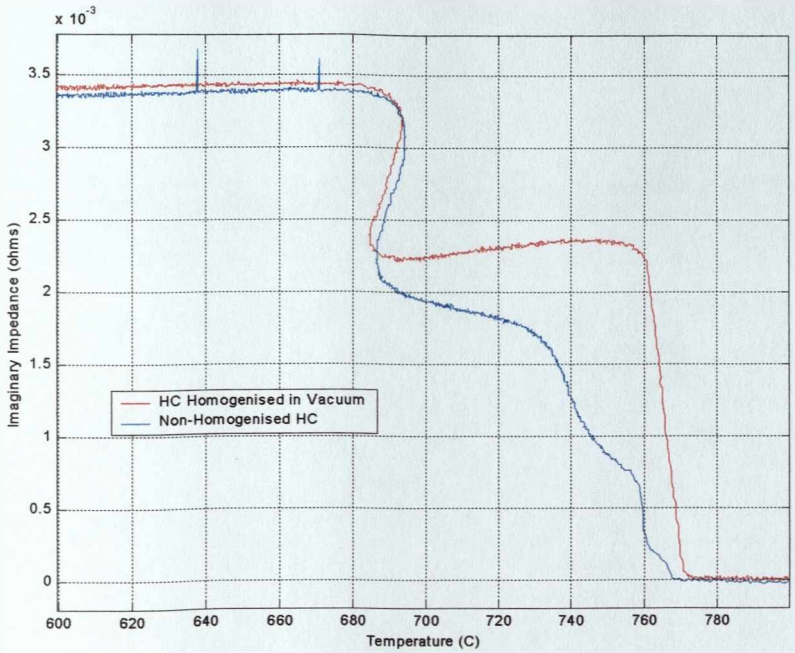

Figure 5.34: Comparison of the impedance – temperature traces for the vacuum homogenised and unhomogenised high carbon steel at 2Hz.

The difference in the T_C value observed for the unhomogenised and vacuum homogenised samples in figure 5.34 is due to the variation of the decarburised region in each sample as seen in previous micrographs.

5.4.6 Medium Carbon Steel

A medium carbon steel was selected for testing as it was predicted to start transforming below the T_C and transform over a range of temperatures. These tests

were performed to investigate the link between impedance change and microstructure (e.g. phase fraction and distribution). The heating and cooling procedure for the specimen was the same as for the high carbon steel samples and the frequency used was 2 Hz. In figure 5.35 are shown the impedance – temperature responses over three thermal cycles.

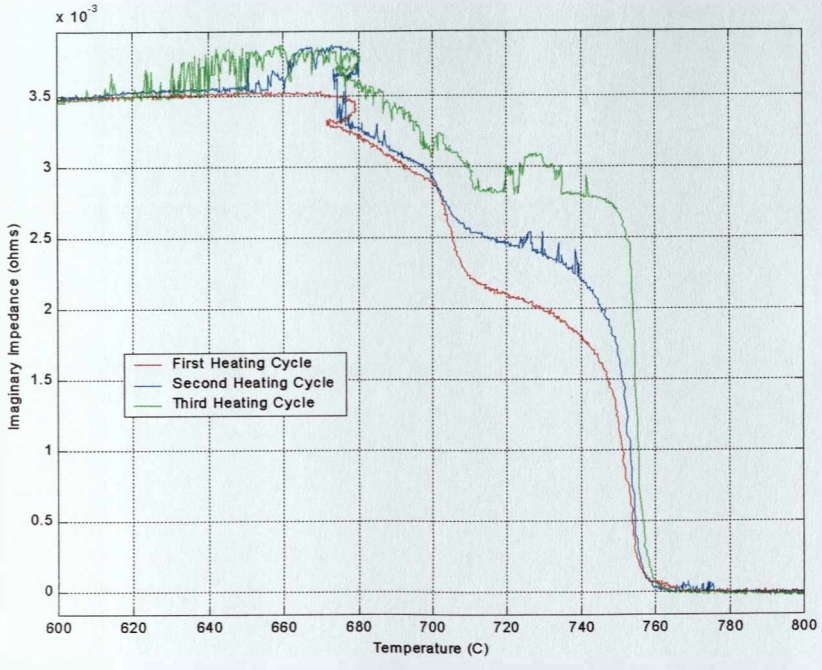

Figure 5.35: Impedance - temperature response for unhomogenised medium carbon steel during three heating cycles at 2Hz.

The gradual increase of impedance to higher values at T_C, 760°C, signifies increasing levels of decarburisation with each cycle. Microstructural examination of the sample after the first and third cycle revealed the existence of a decarburised region. The decarburised region was found to be greater in the third cycle. The electromagnetic noise observed in the impedance – temperature traces for the second and third heating cycles is either due to the operation of nearby electrical equipment or sensor

degradation. The SEM micrographs in figure 5.36 display the decarburised region at the surface of unhomogenised medium carbon steel after one and three thermal cycles.

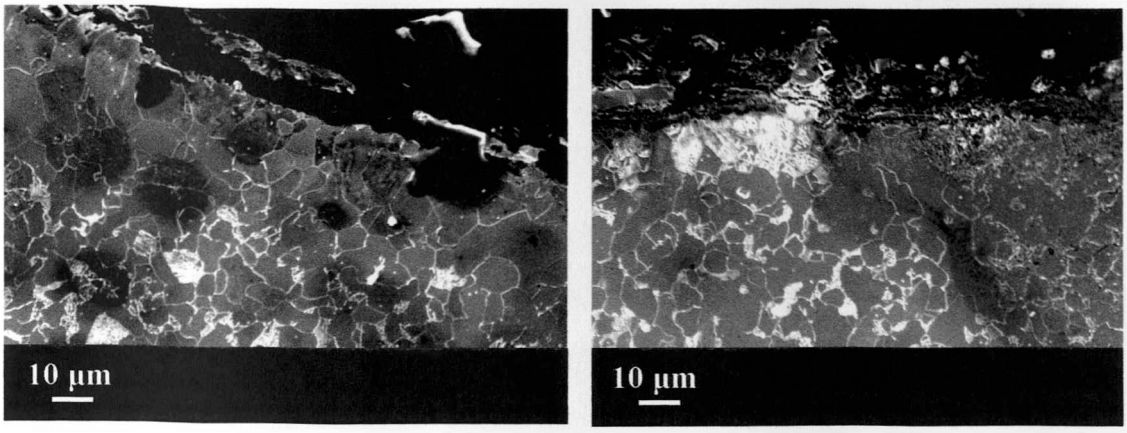

(a) (b)

Figure 5.36: SEM micrographs for the unhomogenised medium carbon steels showing decarburised layer a) after one and b) after three thermal cycles.

Despite the presence of a slightly discontinuous ferrite layer in the third cycle of 10 – 20 µm thickness, ferrite formation occurring in the lower parts of the decarburised area and in the bulk of the sample causes a small increase in impedance over the temperature range 710° – 680°C, hence it is detected. The reason for this is not only that the pro-eutectoid ferrite layer at the surface is slightly discontinuous but also the large quantities that ferrite forms in the rest of the decarburised region and bulk of the sample.

5.5 Summary of impedance response due to decarburisation

The relationship of decarburisation, thickness of the decarburised area, oxidation, carbon content, test temperature and repeated heating at elevated temperatures with impedance values has never been examined before. Nonetheless, there are various reports which are concerned with the processes of decarburisation and oxidation with respect to the carbon content of steel [166, 236-238].

Decarburisation and oxidation has been proved to be closely related to the impedance response recorded during EM tests. It has been shown that the presence of a fully pro-eutectoid ferrite layer, depending on its thickness, has a dominant effect on the level of impedance response regardless of the test frequency employed. This causes a reduction in the sampling depth due to the higher permeability, limiting the magnetic flux near the decarburised area. The effect of decarburisation is smaller when oxidation of the pro-eutectoid ferrite occurs. The level of decarburisation varies depending on the previous heat treatment (i.e. homogenisation), carbon content and test temperature. In a similar fashion, the oxidation process is directly related to carbon content and test temperature.

Since medium carbon steel contains less carbon the carbon dioxide produced is considerably less. Hence, the scale formed contains less cracks or voids limiting oxygen diffusion to the steel interface to a minimum. Due to the relative rates at which oxygen reacts with carbon in these steels, a larger decarburised region forms in high carbon steel. In order to link the impedance values to the bulk microstructural changes the effects of decarburisation need to be minimised.

5.6 Prevention of Decarburised Layer Growth

Due to the formation of the decarburisation layer the impedance response cannot be accurately related to the bulk phase transformation in the medium and high carbon steel. Thus, it was necessary to minimise decarburisation to the maximum degree possible if detection of the bulk phase transformation was to take place, in particular the pro-eutectoid ferrite transformation.

A number of medium and high carbon steel samples were coated with 3 layers of Acheson CG501, a ceramic based coating, in order to minimise decarburisation during heat treatment. Thermal trials were conducted to determine the effectiveness of Acheson CG501 as a protective means against decarburisation. It was found that the use of the coating minimised decarburisation of the samples. However, during dynamic cooling some degradation of the coating occurred, producing cracks and voids that allowed oxygen to diffuse in the skin of the sample during subsequent heating cycles. Nonetheless, the resulting decarburisation was not as high as in previous tests and hence detection of the actual phase transformation could be accomplished satisfactorily. To ensure a repeatable test procedure, each sample was raised to 930°C for 30 minutes before cooling.

5.6.1 Vacuum homogenised at 1000°C high carbon steel

As discussed earlier in this chapter, vacuum homogenised high carbon steel samples exhibited some decarburisation during the homogenisation process. Figure 5.37 shows the impedance versus temperature response for the coated vacuum

homogenised (i.e. large grain sized) high carbon steel sample. It can be seen that the impedance value starts to increase at approximately 735°C, considerably lower than the T_C. Then the impedance value slowly increases between 735°C and the eutectoid temperature. The increase in impedance over the temperature range, 735° – 680°C is attributed to a very small, partial decarburised region which formed during the homogenisation process as shown in the SEM micrographs in figure 5.38.

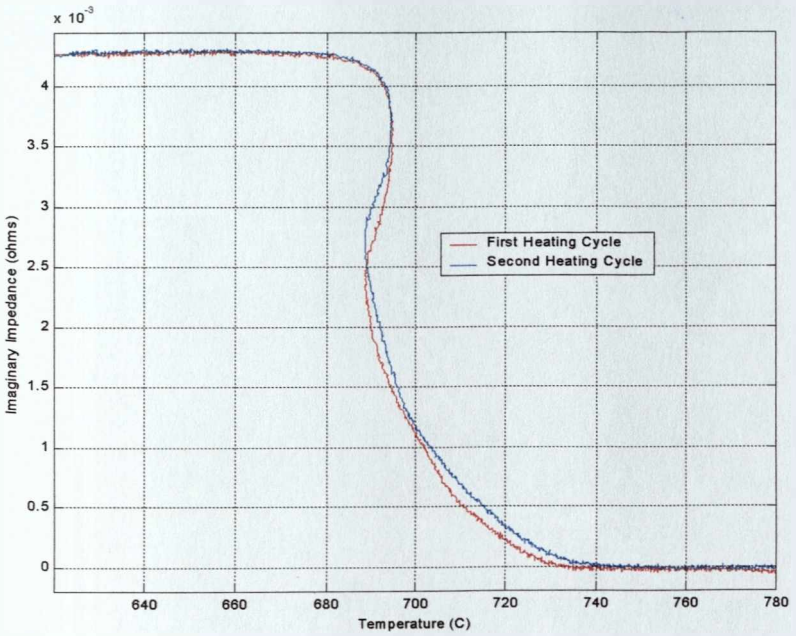

Figure 5.37: Impedance – temperature traces for coated vacuum homogenised high carbon steel during two thermal cycles at 2 Hz.

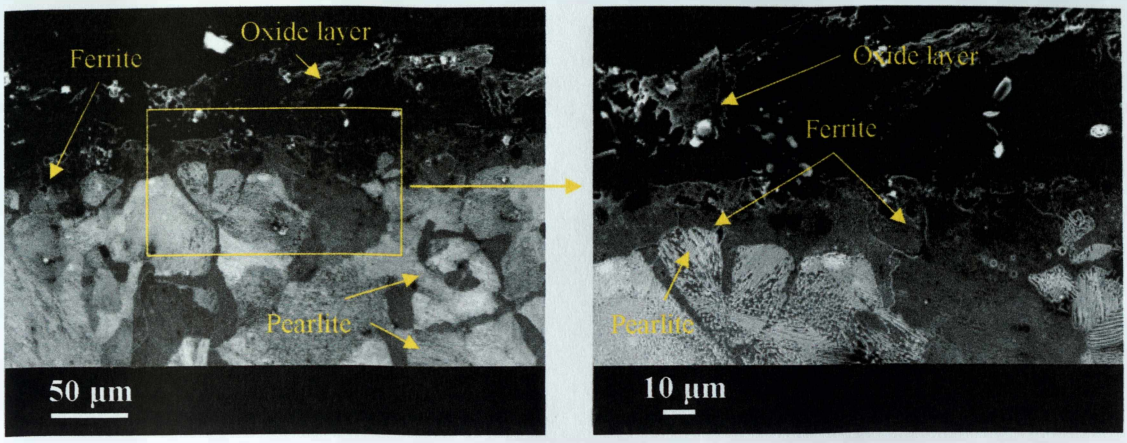

(a) (b)

Figure 5.38: SEM micrograph showing decarburisation in vacuum homogenised high carbon steel after two thermal cycles. The yellow box in micrograph a) indicates the area shown at a higher magnification in micrograph b).

5.6.2 Argon homogenised high carbon steel

In contrast to vacuum homogenisation, for samples homogenised under an argon atmosphere the presence of decarburised regions before testing is negligible. However, some further decarburisation is expected to take place due to the partial protection achieved with the ceramic coating. Figure 5.39 shows the differences that exist between the impedance responses of vacuum and argon homogenised high carbon samples. Although the initial impedance increase occurs at approximately 740°C for all the homogenised samples, the rate of increase of impedance between 740°C and the eutectoid point is smaller for the argon, rather than the vacuum, homogenised sample. This indicates that the total amount of pro-eutectoid ferrite forming in the decarburised region is slightly smaller for the argon homogenised sample than in the vacuum homogenised sample.

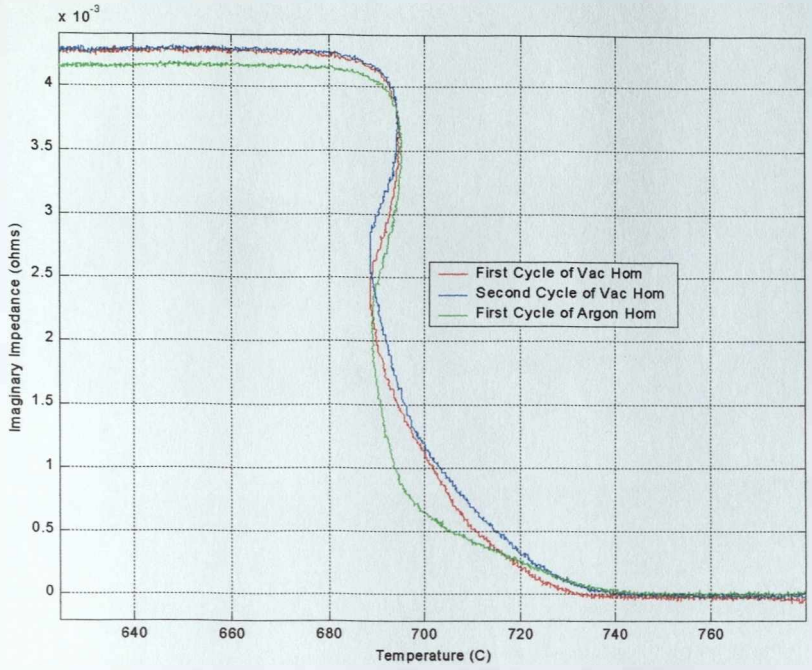

Figure 5.39: Impedance – temperature traces for vacuum and argon homogenised high carbon steel at 2 Hz.

SEM analysis revealed the existence of a thin and discontinuous pro-eutectoid ferrite layer very similar to that of the vacuum homogenised high carbon steel sample as shown in figure 5.40. The similar nature of the pro-eutectoid ferrite layers is thus responsible for the similar initial impedance response in both cases.

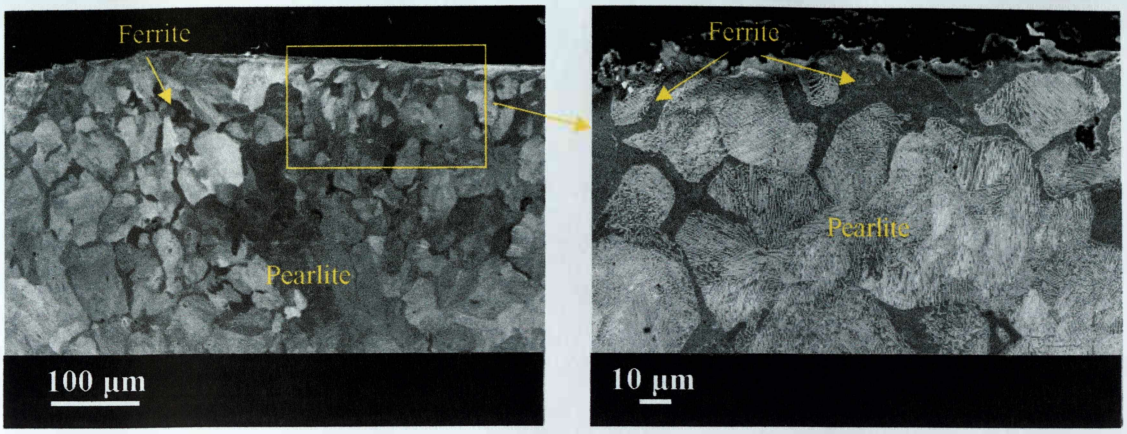

(a) (b)

Figure 5.40: SEM micrographs showing decarburisation at the surface of argon homogenised high carbon steel after one heating cycle at magnification a) x200 and b) x750. The yellow box in micrograph a) indicates the area shown at a higher magnification in micrograph b).

Unlike for the previously discussed results, a fully continuous pro-eutectoid ferrite layer has not formed for the tests using coated samples. Even though some pro-eutectoid ferrite does occur near the sample surface, its average thickness is significantly smaller, i.e. 7 µm, as opposed to 150µm, observed in the previous tests.

5.6.3 Non-Homogenised high carbon steel

Microscopy evidence has shown that no decarburised areas exist prior to testing for the unhomogenised high carbon steel samples. In figure 5.41 are displayed the impedance traces obtained for a coated unhomogenised high carbon steel sample during two heating cycles at a frequency of 2 Hz compared to the homogenised high carbon samples.

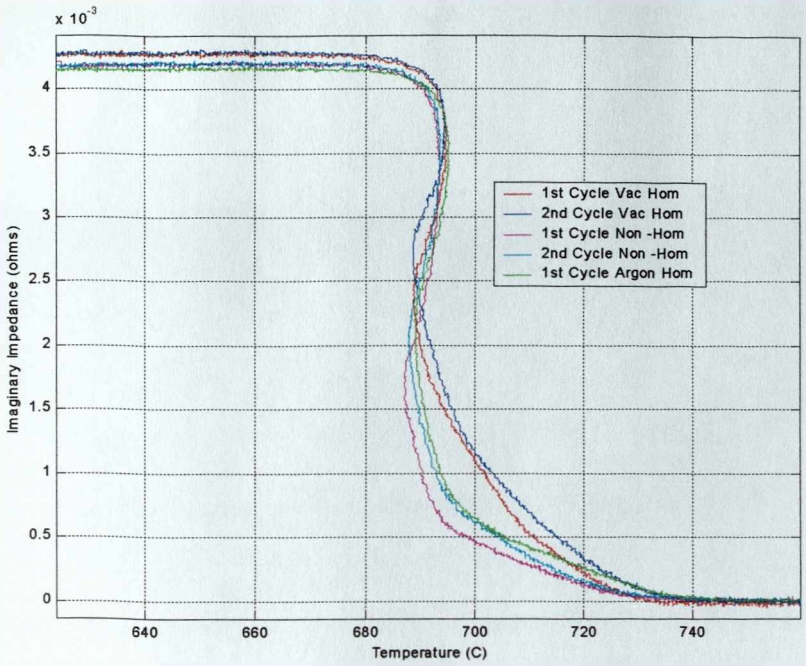

Figure 5.41: Impedance – temperature traces for the argon, vacuum and unhomogenised high carbon samples at frequency 2 Hz.

In the first cycle, the impedance starts to increase for the unhomogenised sample at 735°C with the rate of increase being slower than for the argon homogenised sample up to the eutectoid point indicating that limited decarburisation has occurred. However, the impedance – temperature trace for the second heating cycle of the unhomogenised sample has small differences if compared with the trace for the argon homogenised sample. The earlier response seen for the argon homogenised sample is due to the slightly higher amount of ferrite present due to decarburisation than in the unhomogenised sample displayed in figure 5.42. From the fact that the impedance responses for the unhomogenised and argon homogenised samples are generally similar, with the exception of the initial part of the trace which is dominated by the decarburisation factor, it can be assumed that the difference in average prior-austenite

grain size in high carbon steel has a minimal effect upon the underlying impedance response.

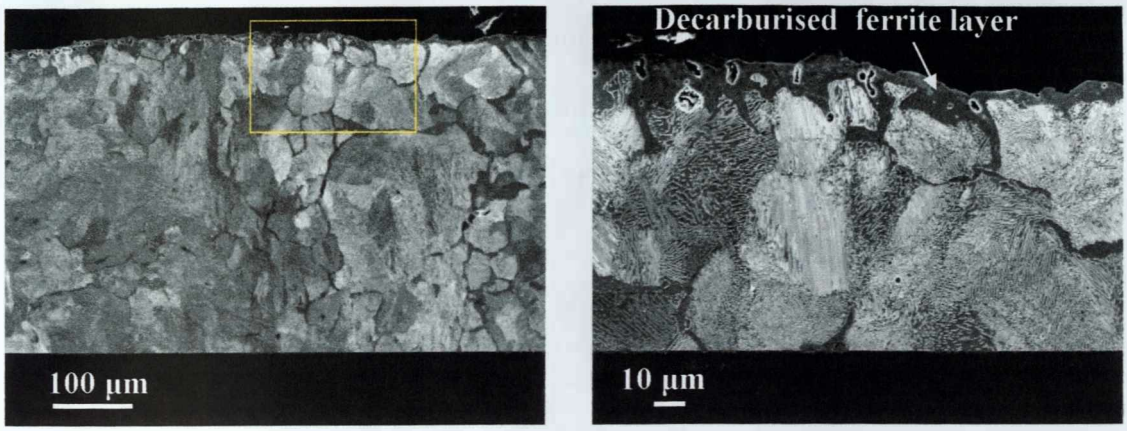

(a) (b)

Figure 5.42: SEM micrographs from the unhomogenised high carbon steel sample showing decarburisation after two thermal cycles at magnification a) x200 and b) x750.

5.6.4 Medium Carbon Steel

EM tests were conducted on coated unhomogenised and homogenised medium carbon steel samples in an effort to determine the relationship between bulk phase transformation and impedance values, particularly for the bulk pro-eutectoid ferrite formation.

5.6.5 Vacuum homogenised at 1000°C medium carbon steel

In figure 5.43 are presented the impedance – temperature traces recorded for the medium carbon steel sample in comparison with the traces obtained for the vacuum homogenised high carbon steel.

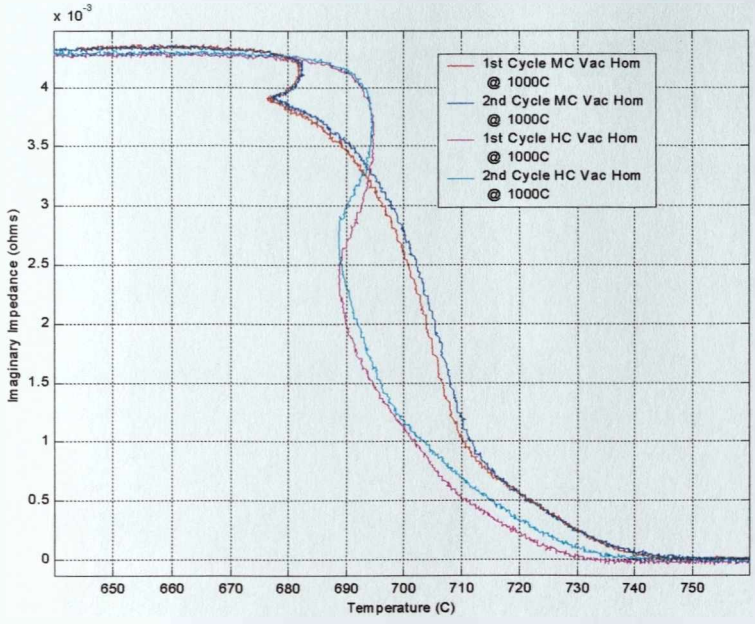

Figure 5.43: Impedance – temperature traces for high and medium vacuum homogenised carbon steels at 2 Hz.

As expected due to its composition, the initial impedance response takes place earlier (at 745°C) in the medium compared to the high carbon steel sample. The similarity between the traces for the first and second cycle shows that the ceramic coating effectively prevented any further decarburisation from occurring during the repeated tests. SEM analysis (figure 5.44) showed the presence of a small decarburised layer, approximately 10-15 μm thick, for the medium coated steel which is mostly a result of the homogenisation process.

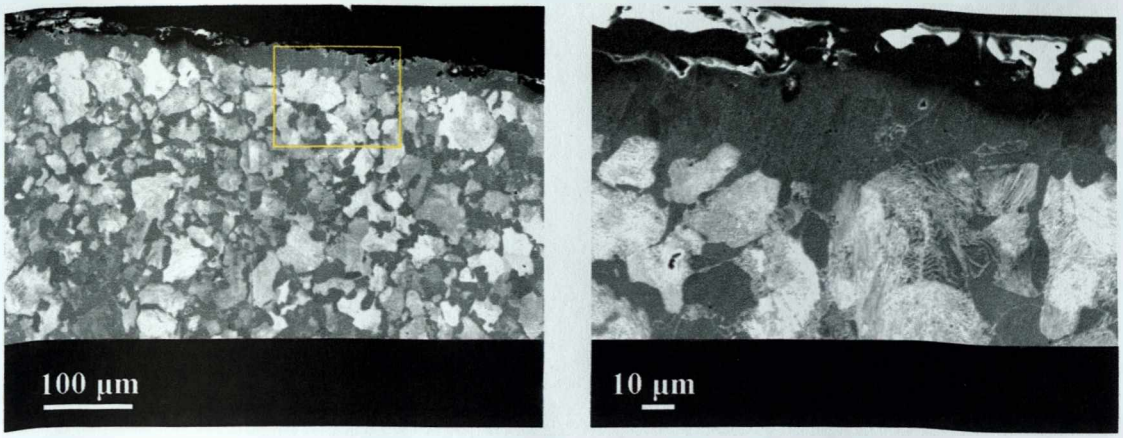

(a) (b)

Figure 5.44: SEM micrographs showing the decarburised region of vacuum homogenised at 1000°C medium carbon steel after two thermal cycles at magnification a) x200 and b) x750.

5.6.6 Vacuum homogenised at 1200°C medium carbon steel

To determine the effect of average prior austenite grain size on the impedance response, medium carbon steel samples were homogenised in vacuum at 1200°C to achieve an extremely large average prior austenite grain size. Image analysis measurements on samples before EM testing showed the average prior-austenite grain diameter to be equal to about 500 µm, figure 5.45.

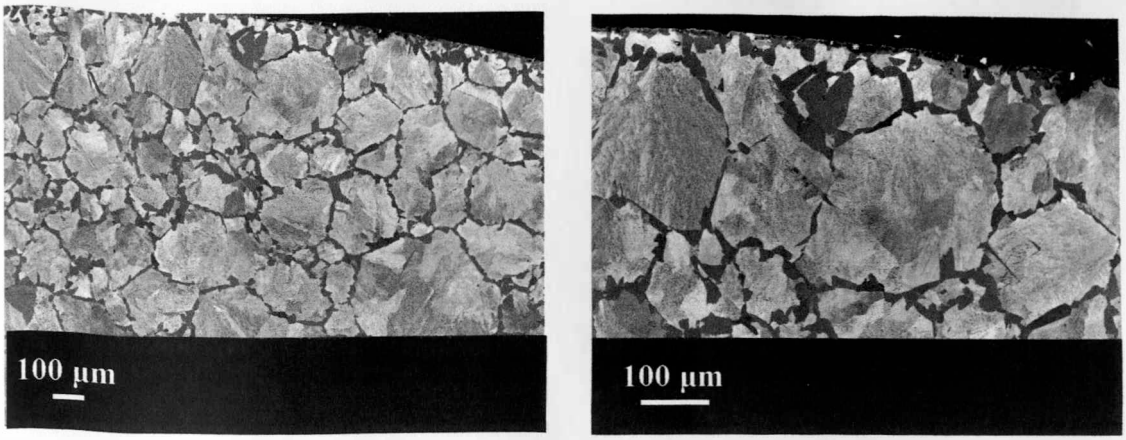

(a) (b)

Figure 5.45: SEM micrographs showing the microstructure of the vacuum homogenised at 1200°C medium carbon steel before EM testing at magnification: a) x75 and b) x150. The ferrite (dark areas) forms at the prior austenite grain boundaries allowing grain size measurement.

The homogenisation process at a higher temperature (1200°C compared to 1000°C) caused more decarburisation and thus the resulting responses were largely affected by the presence of a fully pro-eutectoid ferrite layer. Figure 5.46 presents the traces for the 1000°C and 1200°C vacuum homogenised medium carbon steel samples. A noticeable impedance increase occurs at T_C for the second sample attributable to the larger decarburised layer.

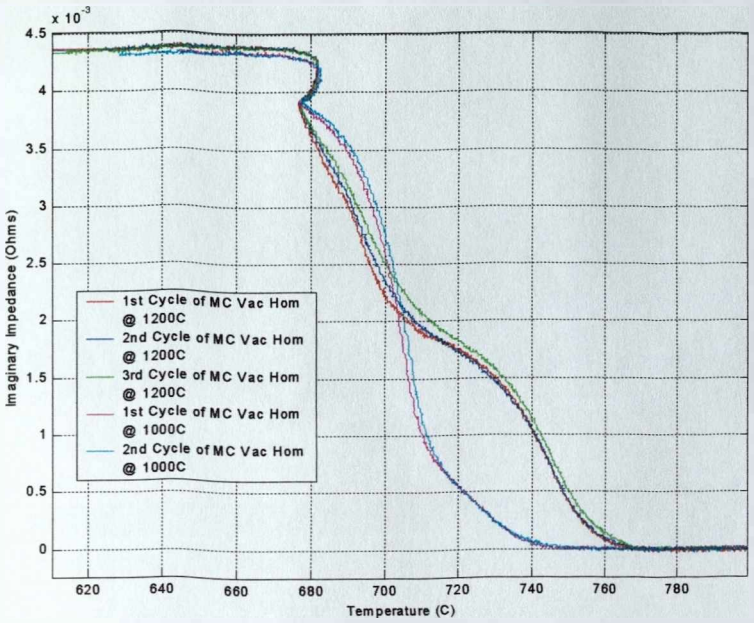

Figure 5.46: Comparison of the impedance – temperature traces for 1200°C and 1000°C vacuum homogenised medium carbon steel samples at 2 Hz after two thermal cycles.

Figure 5.46 shows similar trends to the previous results, the three traces for the 1200°C vacuum homogenised medium carbon steel sample are almost identical, indicating the prevention of further decarburisation during the EM testing by the ceramic coating. In figure 5.47 a continuous pro-eutectoid ferrite layer with average thickness 25 μm formed during vacuum homogenisation at 1200°C compared to the 5 μm decarburisation seen for the samples vacuum homogenised at 1000°C. The occurrence of greater decarburisation accounts for the increase in impedance at approximately 760°C.

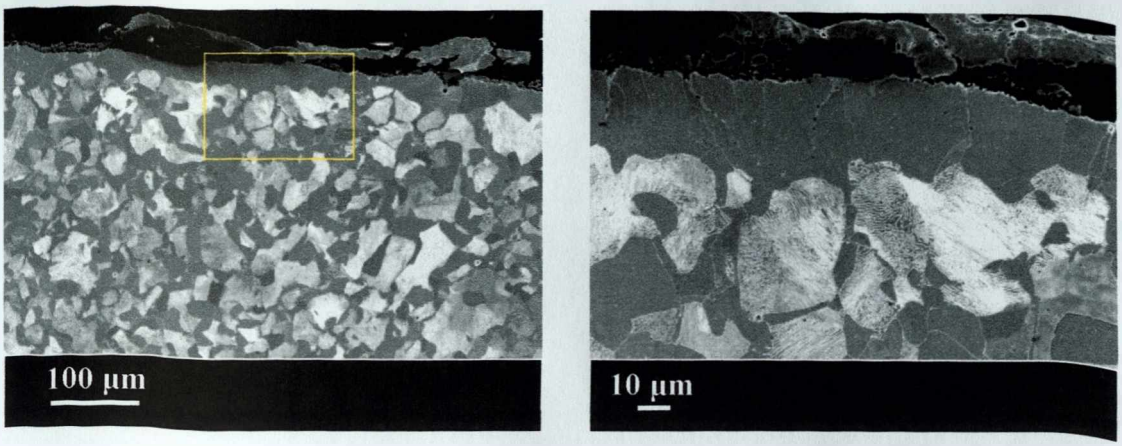

(a) (b)

Figure 5.47: SEM micrographs showing the decarburised region at the surface of vacuum homogenised at 1200°C medium carbon steel after two thermal cycles at magnification: a) x 200 and b) x750.

5.6.7 Non-Homogenised medium carbon steel

Figure 5.48 shows that EM responses for the unhomogenised medium carbon steel sample are very similar to those of the 1000°C vacuum homogenized medium carbon steel sample. Figure 5.48 also contains comparison of impedance traces for all coated medium carbon steel samples.

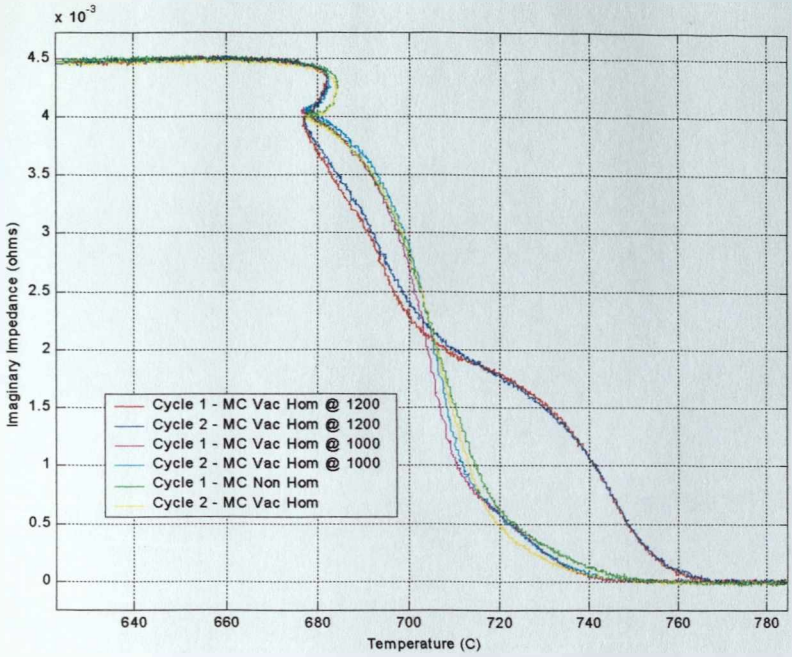

Figure 5.48: Comparison of impedance – temperature traces for unhomogenised, vacuum homogenised at 1000°C and 1200°C medium carbon steel samples at 2 Hz during two thermal cycles.

SEM analysis (figure 5.49) of the tested for two cycles unhomogenised sample showed that some decarburisation took place during EM testing despite the use of ceramic coating. The level of decarburisation is very similar to that observed for the 1000°C vacuum homogenised sample, i.e. approximately 10 μm.

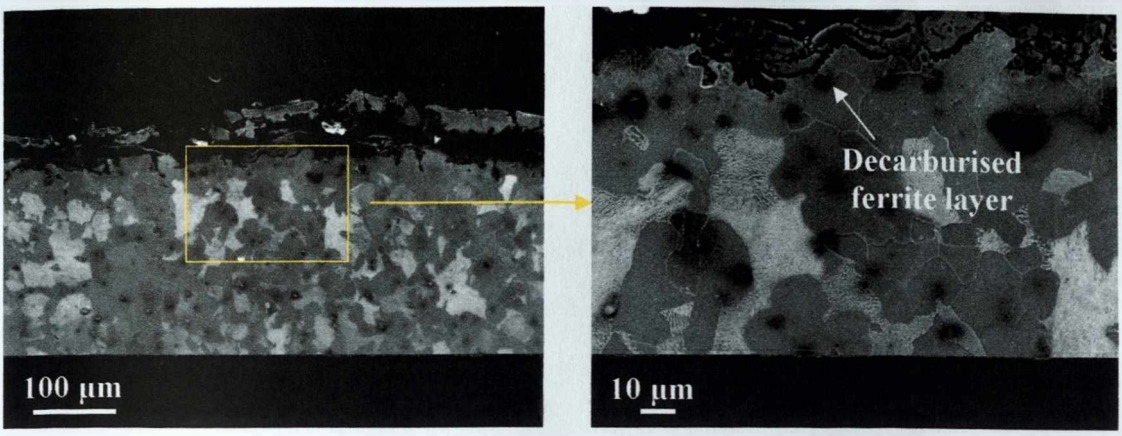

(a) (b)

Figure 5.49: SEM micrographs showing decarburisation in unhomogenised medium carbon steel after two thermal cycles at magnification: a) x200 and b) x750.

5.7 Interrupted quench tests

In order to determine the relationship between impedance value and microstructure, interrupted quench tests were performed on unhomogenised and homogenised in vacuum at 1200°C medium carbon steel samples from temperatures between 750°C and 680°C. Figure 5.50 shows the amount of pro-eutectoid ferrite present at specific points along the impedance -temperature trace for the unhomogenised medium carbon sample. From figure 5.50 it can be seen that pearlite contributes 72% of the total microstructural volume fraction, yet represents only 12% of the impedance trace. Microscopy analysis of the unhomogenised quench tested samples showed that no ferrite formation occurs in the bulk microstructure above 720°C. Nevertheless, an increase takes place in the impedance value well before any bulk ferrite has formed, at 740°C. This increase in the impedance value, as it has been shown earlier, is a result of ferrite presence at the surface of the sample due to decarburisation.

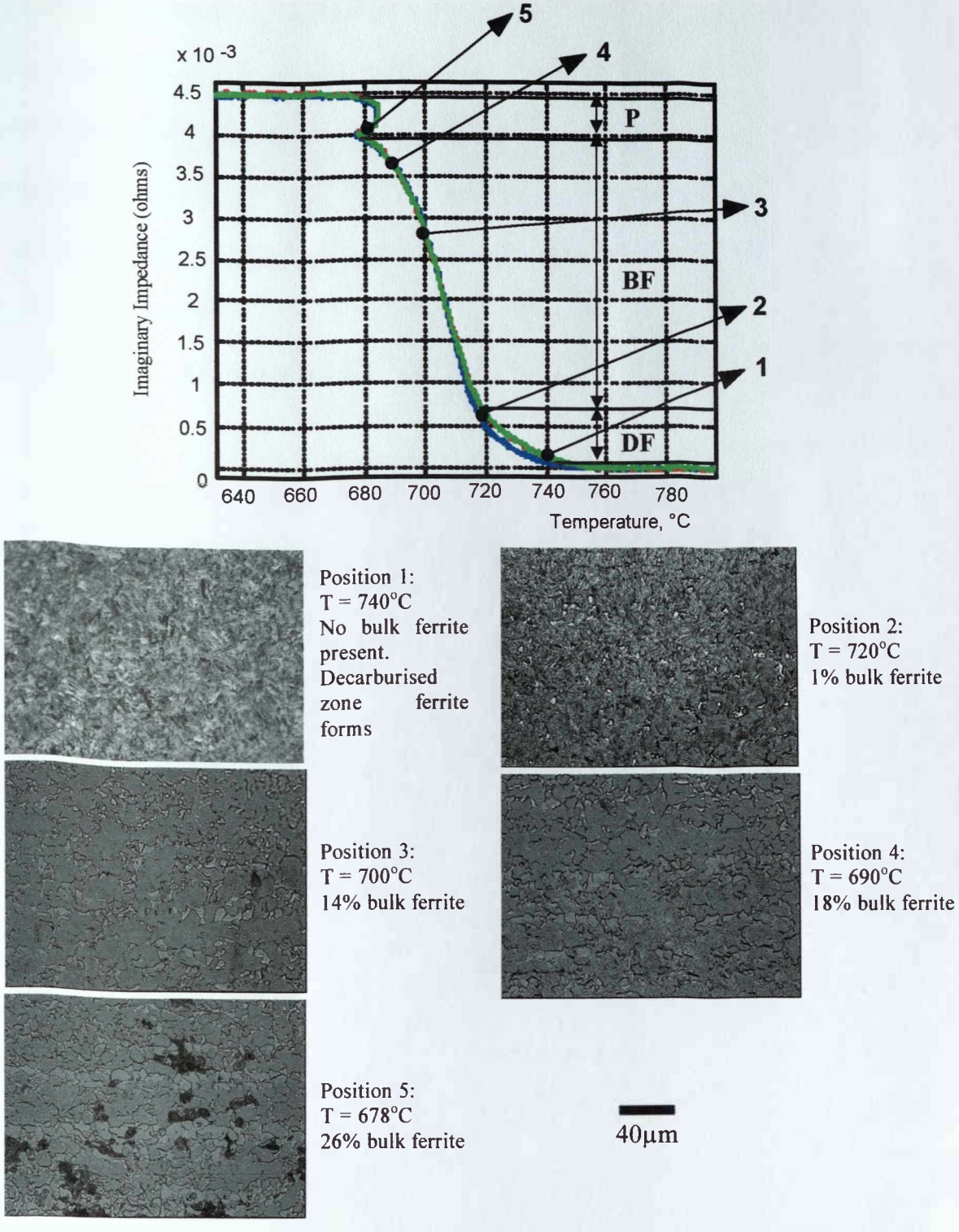

Figure 5.50: Impedance – temperature traces for the unhomogenised medium carbon steel and optical micrograph of the rolling direction obtained from the quench test samples showing the corresponding microstructure to different impedance values at 2 Hz. DF: Decarburised Ferrite, BF: Bulk Ferrite and P: Pearlite formation

In figure 5.50 the optical micrographs show the amount of ferrite formed at each temperature. Martensite in the optical micrographs represents the amount of austenite that remains to transform at each temperature point. The pearlitic reaction starts at about 678°C as shown in the corresponding micrograph for position 5. The pearlite formation is recognised straight away in the impedance – temperature trace due to the slight increase in temperature due to the exothermic nature of the pearlitic reaction. Image analysis results on homogenised samples from the interrupted quenched tests revealed that the effect of decarburisation on impedance response was much more severe than for the unhomogenised sample. In a similar manner as before figure 5.51 presents the formation of pro-eutectoid ferrite present at specific points along the impedance – temperature trace for the homogenised medium carbon steel sample.

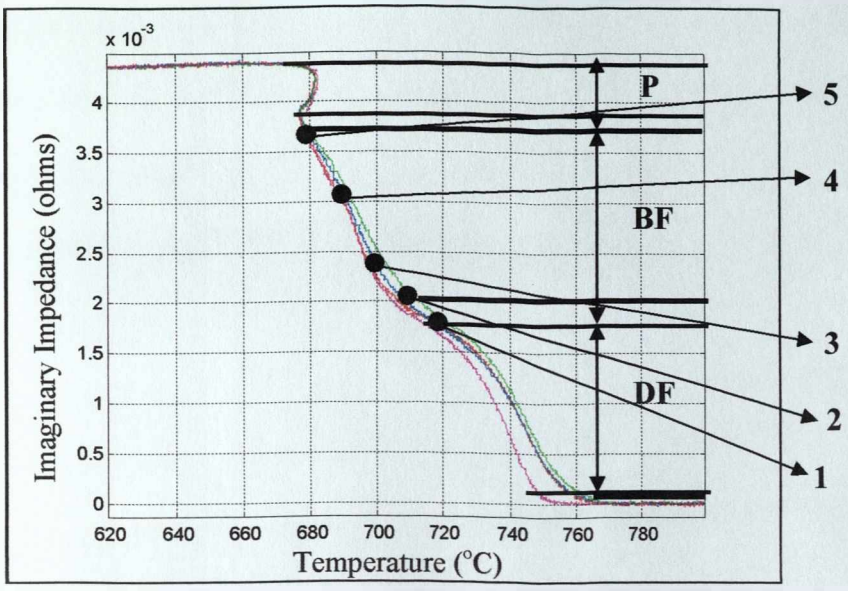

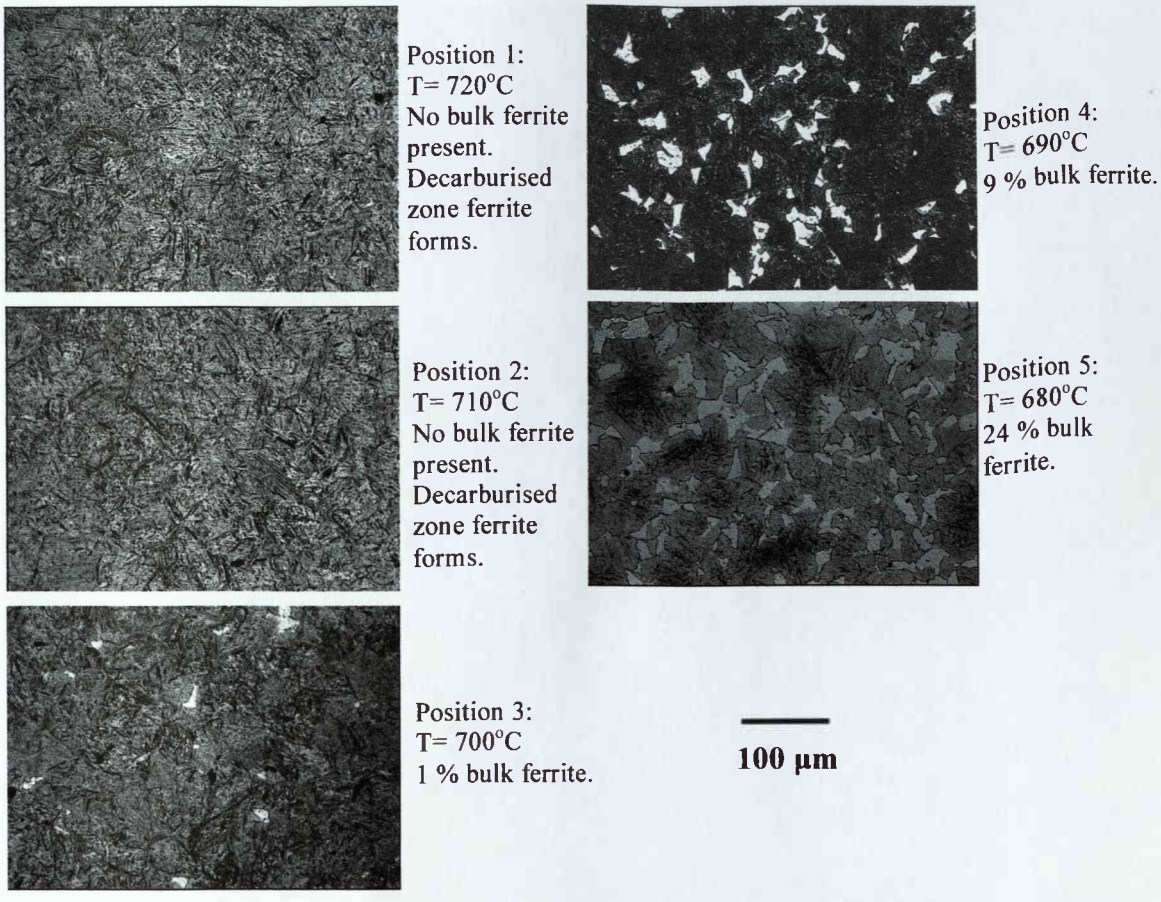

Figure 5.51: Impedance -temperature traces for the vacuum homogenised at 1200°C medium carbon steel with optical micrographs showing the amount of pro-eutectoid ferrite formed at the specified temperatures. DF: Decarburised Ferrite, BF: Bulk Ferrite and P: Pearlite formation.

Figure 5.52 summarises the results obtained with quantitative image analysis on the interrupted quench test samples for the amount of bulk ferrite formed before the pearlite reaction with respect to temperature. It can be seen that the ferrite fraction is approximately linearly related to temperature, which agrees with phase transformation theory [68].

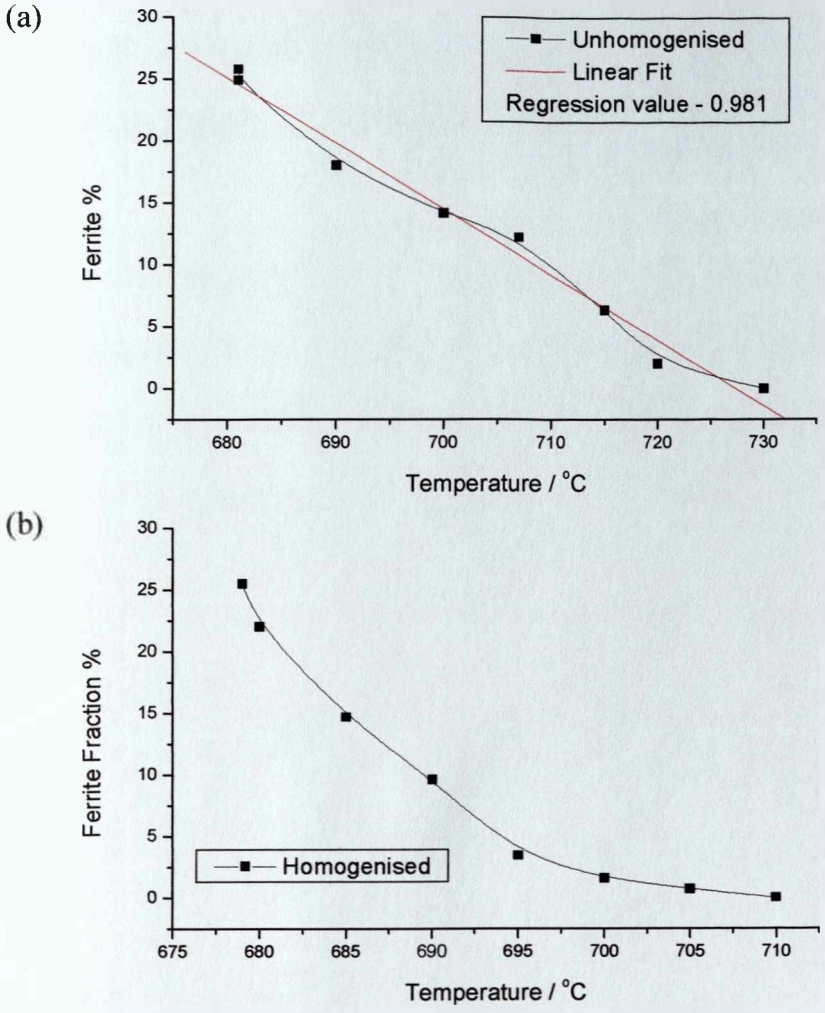

Figure 5.52: Ferrite volume fraction % - temperature diagram for the a) unhomogenised and b) homogenised samples.

In figure 5.52(b) the ferrite fraction % - temperature trace for the vacuum homogenised at 1200°C medium carbon steel shows a slow increase between 710° and 695°C which is related to the kinetics of the transformation. This is due to the very large prior-austenite grain size which results in a limited number of double and triple points where ferrite can nucleate. Thus, due to the limited number of nucleation points the transformation is suppressed to a slightly lower temperature than the one observed for the unhomogenised sample and progresses slowly until 695°C. After that transformation rate increases and ferrite formation takes place linearly [164].

If it is assumed that the magnitude of the impedance can be taken as zero when there is no bulk ferrite formed then the impedance change due to decarburisation can be disregarded. Figure 5.53 shows the impedance against temperature traces for the small and large grain samples without the influence of decarburisation.

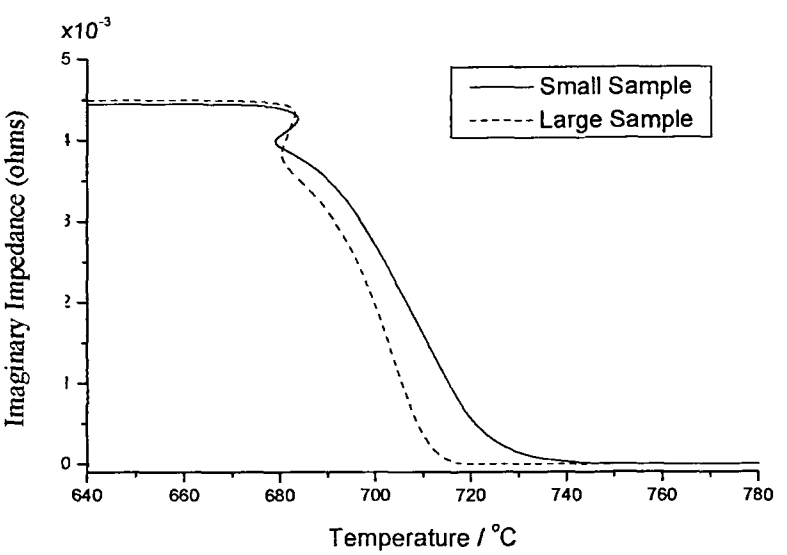

Figure 5.53: Extrapolated impedance – temperature diagram for the small and large grain samples without the influence of decarburisation.

If ferrite fraction is plotted against the impedance values (figure 5.54), it can be seen that there is no linear relationship. This is probably due to the sensitivity of impedance response to the distribution of ferrite in the microstructure as will be discussed later.

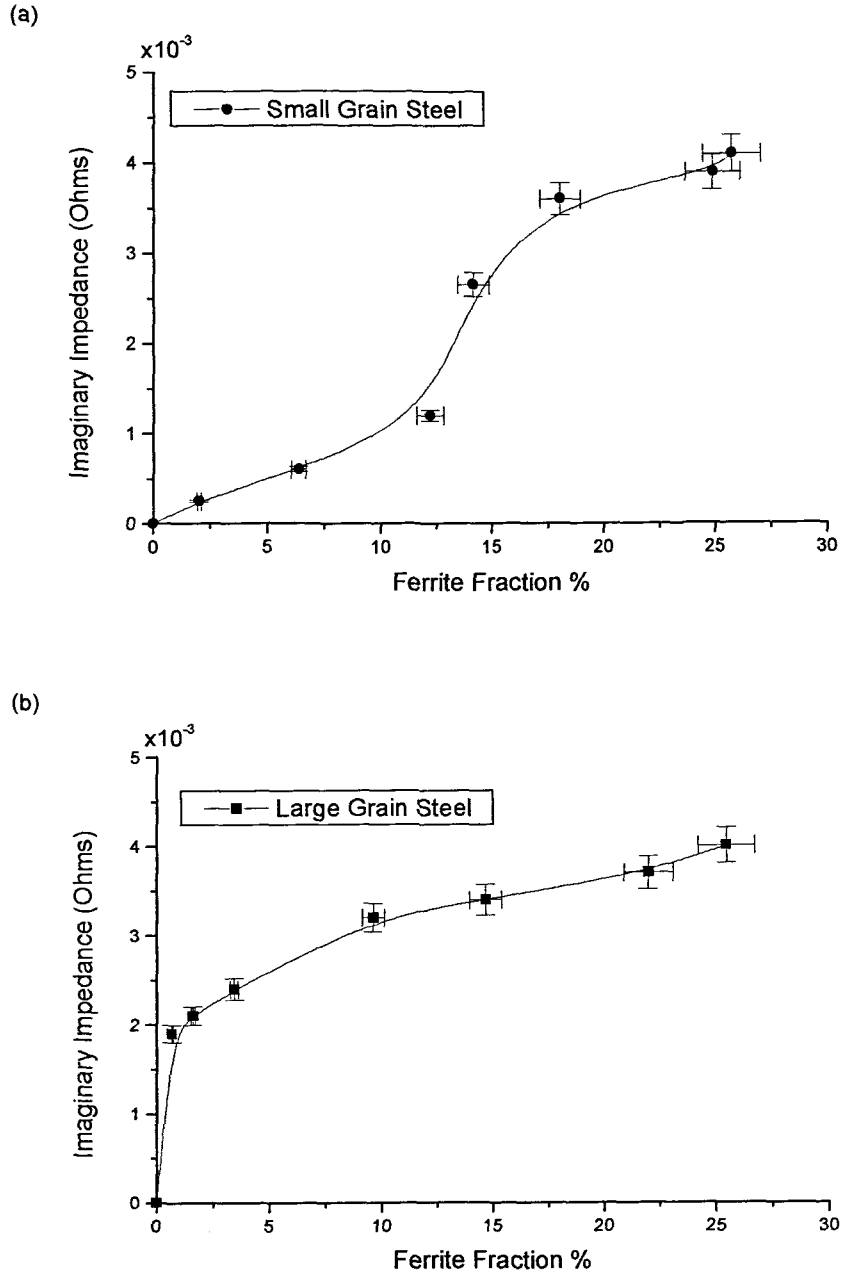

Figure 5.54: Impedance – ferrite volume fraction % for the a) small and b) large grain size medium carbon steel samples.

5.8 Ferrite Connectivity and Impedance

It has been shown that the impedance values are very sensitive to the formation of connected ferrite networks (i.e. decarburised pro-eutectoid ferrite layers) within the microstructure. This is due to there being a high permeability path for magnetic lines of flux through the connected ferromagnetic regions. Hence it might be expected that the change in impedance values with bulk ferrite formation will be affected by the connectivity, or contiguity, of the ferrite phase. Contiguity is dependent on the ferrite fraction, its distribution and the relative sizes of the ferrite and austenite regions, which is related to the prior austenite grain size.

Figure 5.55 shows the relationship between the impedance value and the contiguity of the ferrite phase for the medium carbon steel with a large and small prior austenite grain size. The results suggest that there is a slightly more linear relationship between the impedance and contiguity than between impedance and ferrite fraction, i.e. suggesting that the distribution of ferrite is also important, along with its overall volume fraction. However, it can be seen that the prior austenite grain size is not taken into account fully in the contiguity versus impedance results. Hence contiguity is not a sufficient measure of the ferrite distribution to account for the impedance variation. Part of the explanation for this effect may be that the contiguity measurements were measured in random directions on the transverse plane of the samples however the magnetic lines of flux will flow in a particular direction, i.e. along the rolling direction of the cylindrical rod samples for the EM sensor arrangement used. Therefore a measure of the connectivity of the ferrite phase along

the rolling direction would be expected to give a closer relationship to the impedance change.

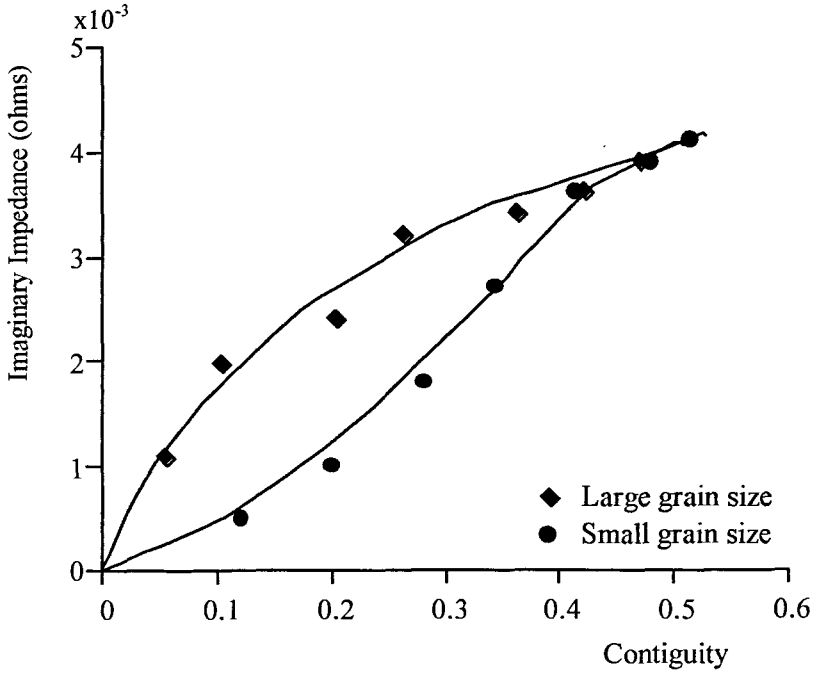

Figure 5.55: Impedance – contiguity diagram for the small and large grain medium carbon steel.

This would be of particular significance for the small grained samples, which, due to their not having received the long homogenisation heat treatment (used to produce the large prior austenite grain size), showed microstructural banding along the rolling direction (figure 5.56).

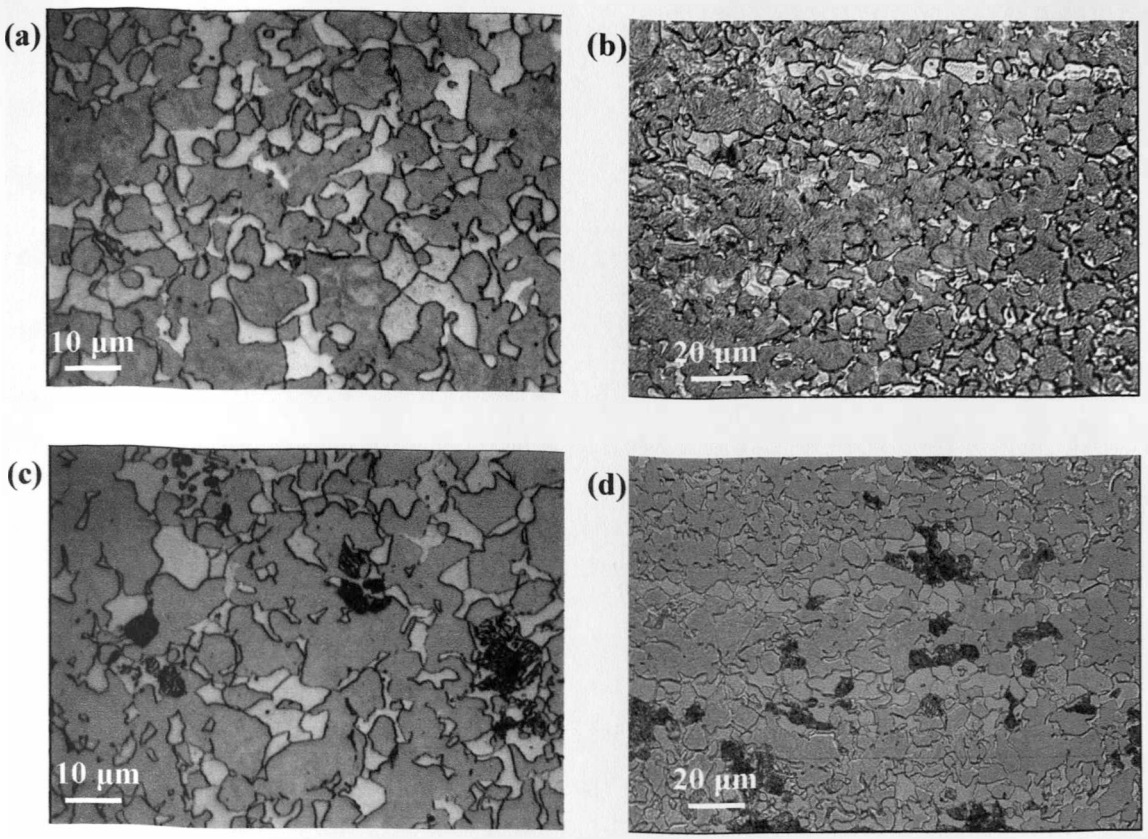

Figure 5.56: Optical micrographs of transverse (a & c) and longitudinal (b & d) cross sections of non-homogenised medium carbon steel showing distribution of ferrite at each cross-section.

In order to determine how the magnetic lines of flux, and hence impedance, are affected by the distribution of ferromagnetic phase in the material, and due to the difficulties in making appropriate experimental measurements of contiguity, a series of finite element simulations was carried out, these are discussed in chapter 6.

5.9 Summary

EM tests performed on the Gleeble revealed that the proposed a.c. EM sensor design is capable of detecting the paramagnetic to ferromagnetic transition during cooling below the T_C. It has been found that increasing the operational frequency of the

sensor causes a decrease in the sampling depth due to the eddy current effect, but it also increases the recorded impedance response by several orders of magnitude and thus reduces the EM noise effect. The carbon content of the steel has a measurable effect upon permeability, and thus impedance, as seen in the impedance responses recorded for low and high carbon steels. From the EM results obtained, the effect of thermal gradients and the limitations of the Gleeble experimental setup upon the quality of the signal was recognised. As a consequence an alternative test methodology, involving furnace heating and cooling of the sample, was employed to improve temperature control and accuracy.

Furnace tests further confirmed the capability of the EM sensor for detecting the paramagnetic to ferromagnetic transition below T_C. The effect of decarburisation and oxidation upon the impedance response was determined. The relationship between the homogenisation technique and decarburisation level was investigated and found to infuence the recorded impedance response. Furthermore, it was seen that depending on the thickness of the fully decarburised ferrite layer, a shift in the T_C was observed towards 770°C regardless of carbon content in the steel. From tests, where decarburisation was minimised by using a casting, it was possible to measure phase transformation of medium and high carbon steel samples during cooling as transformation progressed. From quench tests for the medium carbon steel it was possible to relate the ferrite fraction present with the recorded impedance value. It was found that the ferrite fraction is not linearly related to the impedance response. It was also revealed that the connectivity of ferrite grains has a significant effect on the impedance value recorded. Further investigation of the relationship between ferrite connectivity and impedance value is discussed in chapter 6.

CHAPTER 6: FINITE ELEMENT SIMULATIONS OF MAGNETIC RESPONSE DURING PHASE TRANSFORMATION OF STEEL

6.1 Introduction

Analysis of the experimental EM results presented in the previous chapter showed that the impedance response is strongly affected by decarburisation and oxidation. Quantitative image analysis, in conjunction with the experimental EM results showed that impedance is not linearly related either to the bulk ferrite fraction formed or its contiguity. Nonetheless, an influence of contiguity was observed which requires further investigation. More specifically, the presence of a contiguous fully decarburised pro-eutectoid ferrite layer at the surface of the test samples was shown to have a dominant effect on the impedance value, indicating the importance of ferrite connectivity in the microstructure.

To determine the extent of the effect of pro-eutectoid ferrite contiguity and microstructural variability on the impedance response, simulations were undertaken using Finite Element (FE) analysis. Two-dimensional finite element simulations were carried out using Maxwell 2D software to determine the influence of distribution, ferrite fraction and contiguity of the ferromagnetic phase. Simulations were split into two parts: a) simulations on user-defined patterns and b) simulations on actual microstructures.

6.2 Simulations setup

The configuration employed for the FE simulations, although two-dimensional, was designed to represent the experimental setup. The simulated EM sensor, following the experimental design of the cylindrical EM sensor, consisted of two coils; one primary or exciting and one secondary or sensing coil. The sample was represented by a 20x20 grid of equilateral hexagonal cells, as shown in figure 6.1, that were defined either as paramagnetic (i.e. representing austenite with a relative permeability of 1) or ferromagnetic (i.e. representing ferrite with a relative permeability of 1000). Each cell was defined to have a side of 20 μm and hence the total length of the sample was 400 μm. The length of the coils was defined to be 1200 μm and each consisted of one turn only. The background of the simulated setup was taken to be a vacuum with a relative permeability of one and conductivity of zero. The simulation background was chosen in such a way so as to avoid having to take into account any EM noise generated from the surroundings. Figure 6.1 shows the simulation setup.

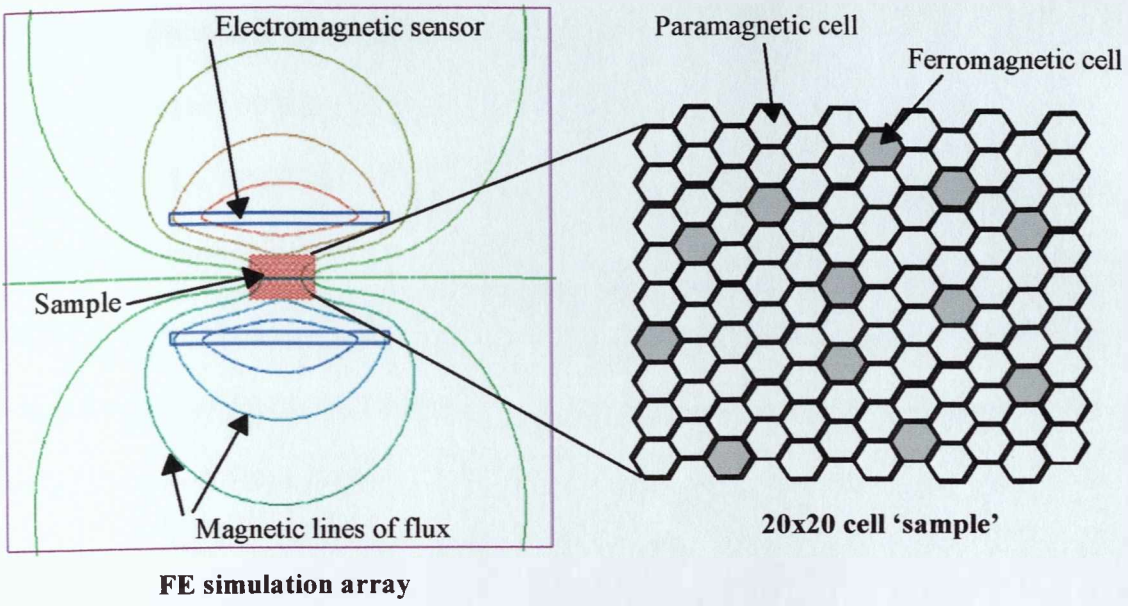

Figure 6.1: The FE simulation array and grid of cells representing the steel sample.

The conductivity of all cells was defined to be 1.1 x 10^6 Sm^{-1} and held constant at all times. The frequency used for the majority of the experimental electromagnetic tests was 2 Hz. However, for the FE trials a higher frequency of 50 Hz was chosen in order to provide a large difference in the impedance values during simulation between the fully paramagnetic and fully ferromagnetic conditions. Due to the very small size of the sample used in the simulations, full penetration of the magnetic lines of flux through the sample occurs even at a relatively high frequency, ensuring that the impedance values are comparable with the experimental results. The frequency chosen is still relatively low which ensures that any eddy current effects within a sample of this size can be ignored.

The reason for using ideal patterns in terms of the distribution of ferromagnetic cells in the sample during the FE simulations was to investigate the effect of connectivity on the impedance value. Furthermore, the influence of the ferromagnetic fraction, orientation, distribution and any microstructural artefacts such as decarburisation on impedance value was also determined. The nature of the patterns is simple and this accounts for the small-sized grid used to represent the sample. In addition, the smaller the number of components (cells) used to represent the sample, the smaller the mesh and hence the smaller the number of variables input in the problem to be solved. It is important to keep the number of variables up to a certain number in order to maintain solution times relatively low, i.e. of the order of minutes. If the number of components used was to be doubled, the number of variables would increase dramatically taking solution times in the range of several hours.

To determine the range of impedance responses, i.e. minimum and maximum values, a parametric simulation was performed. A parametric simulation defines all cells as having the same permeability and conductivity values, i.e. every part of the sample has consistent electromagnetic properties. Various permeability values ranging from 1 to 1000 are introduced and the problem is solved for each permeability value. The plot obtained through parametric simulation displays the range of impedance responses for a particular setup. Figure 6.2 shows the plot obtained through the parametric simulation.

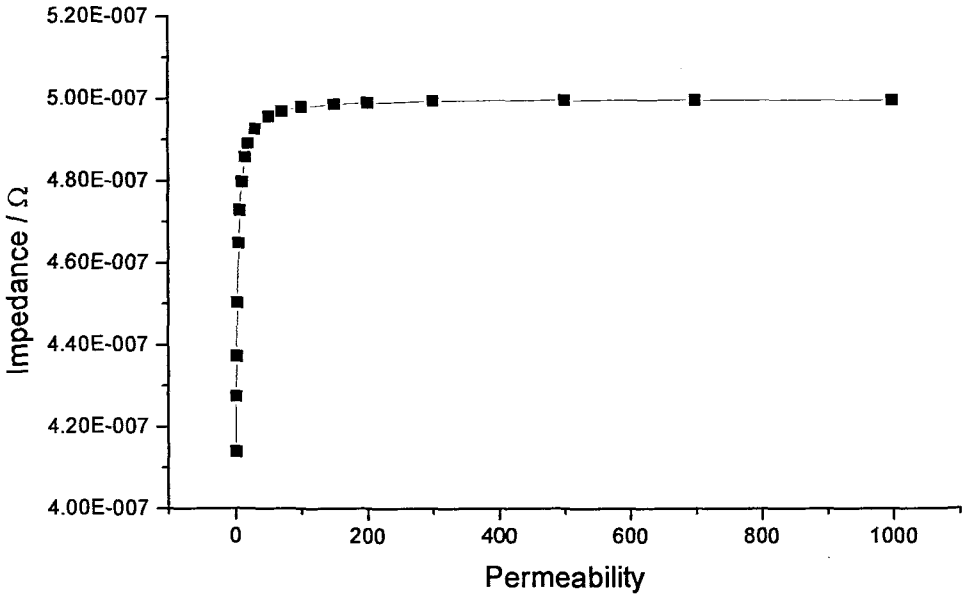

Figure 6.2: Parametric plot for the simulation setup at frequency of 50 Hz.

The impedance – permeability trace in figure 6.2 shows that the impedance value rises rapidly as permeability increases between 1 and 100. However, for permeability values between 100 and 1000 the impedance increase is negligible. This indicates that small compositional changes in the steel and hence permeability variations would not result in a dramatic variation of impedance response. The permeability values used for the parametric simulation ranged from 1 to 1000. If simulation solutions of various ferromagnetic patterns are compared with the parametric plot, it is possible to find equivalent permeability as if all cells had the same electromagnetic properties. Therefore, it is possible to relate the measured impedance at a certain frequency to the permeability of the material and hence to its carbon content.

6.3 Fully paramagnetic and ferromagnetic simulations

Initial FE simulations were performed to determine the impedance response for fully austenitic (paramagnetic) and fully ferritic (ferromagnetic) microstructures. For the simulation of the austenitic microstructure all the cells were assigned a permeability of 1, for the ferritic microstructure all the cells were assigned to have a permeability of 1000. Figure 6.3 shows the variation in the magnetic flux response for each microstructure.

a)

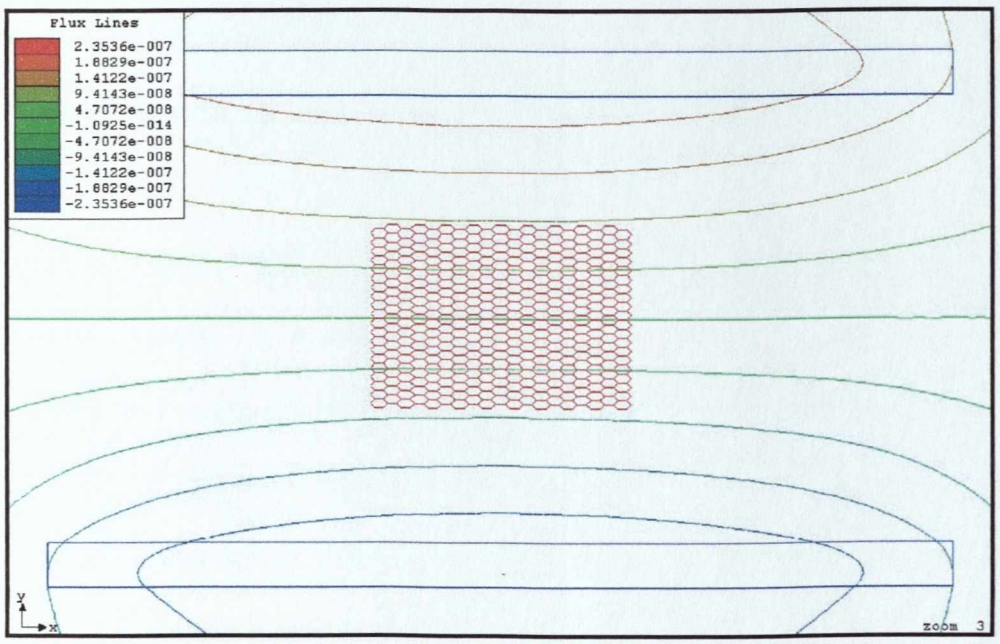

b)

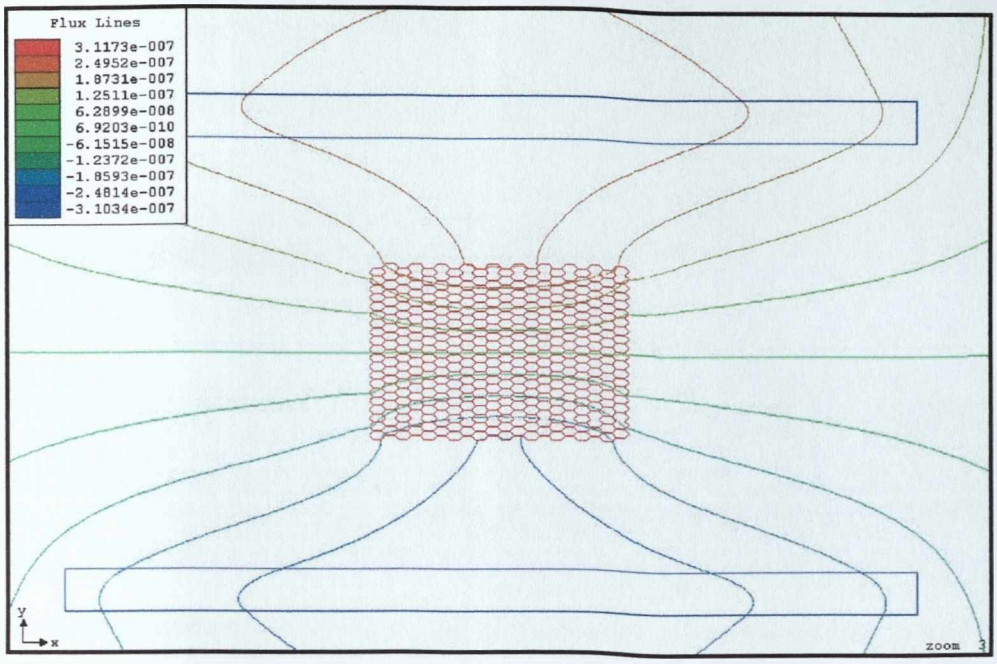

Figure 6.3: Simulations where the steel sample is a) fully paramagnetic – minimum impedance response and b) fully ferromagnetic – maximum impedance response.

As shown in figure 6.3(a), the magnetic lines of flux remain undisturbed for a paramagnetic sample, i.e. the lines of flux follow the path they would if no sample were present between the sensor. In contrast, for a fully ferromagnetic specimen the magnetic lines of flux are attracted towards the centre of the sample giving rise to a strong magnetic response as shown in figure 6.3(b). The corresponding impedance values for fully austenitic and ferritic simulations were found to be 4.138×10^{-7} Ω and 5.0689×10^{-7} Ω respectively. The magnetic responses obtained for the two configurations indicate the minimum and maximum impedance values possible for the specific simulation setup. The slight difference in the impedance values obtained through the simulations using individual permeability values and the parametric plot are due to the differences in the mesh and the number and size of elements used. In a parametric plot the mesh uses slightly larger and less elements to solve an EM

problem in order to minimise solution times. Figure 4.16 in chapter 4 shows the simulation mesh and the elements that it consists of for the paramagnetic simulation.

6.4 Connectivity Effect

In order to determine the effect of contiguity of the ferromagnetic phase in a paramagnetic matrix upon the impedance response, various configurations were used during FE simulations. Figure 6.4 shows the behaviour of the magnetic lines of flux for various distributions of 5% ferrite fraction within an austenitic matrix.

(a)

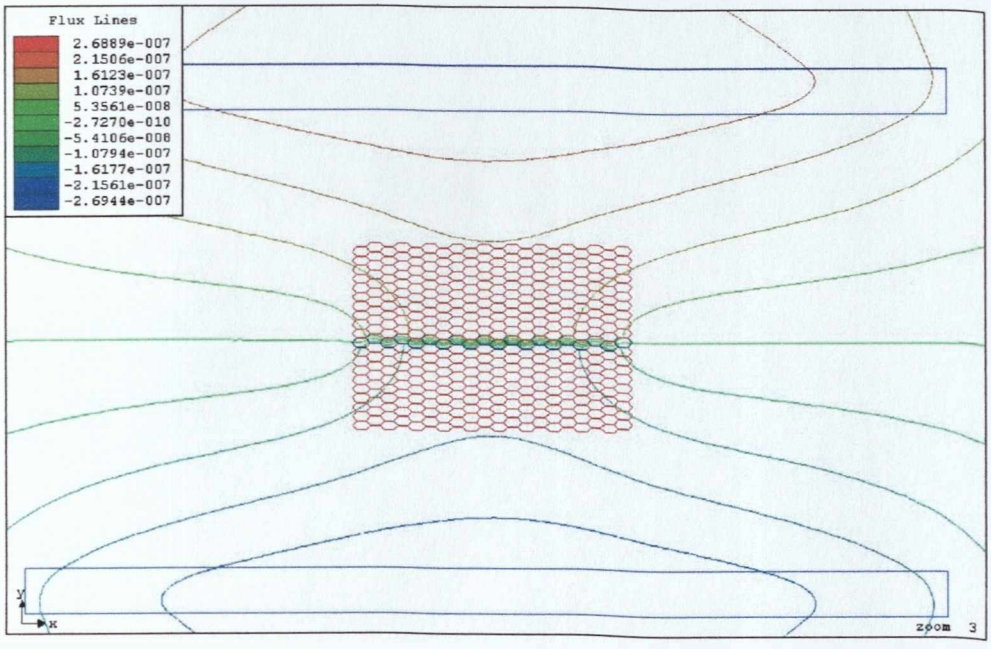

(b)

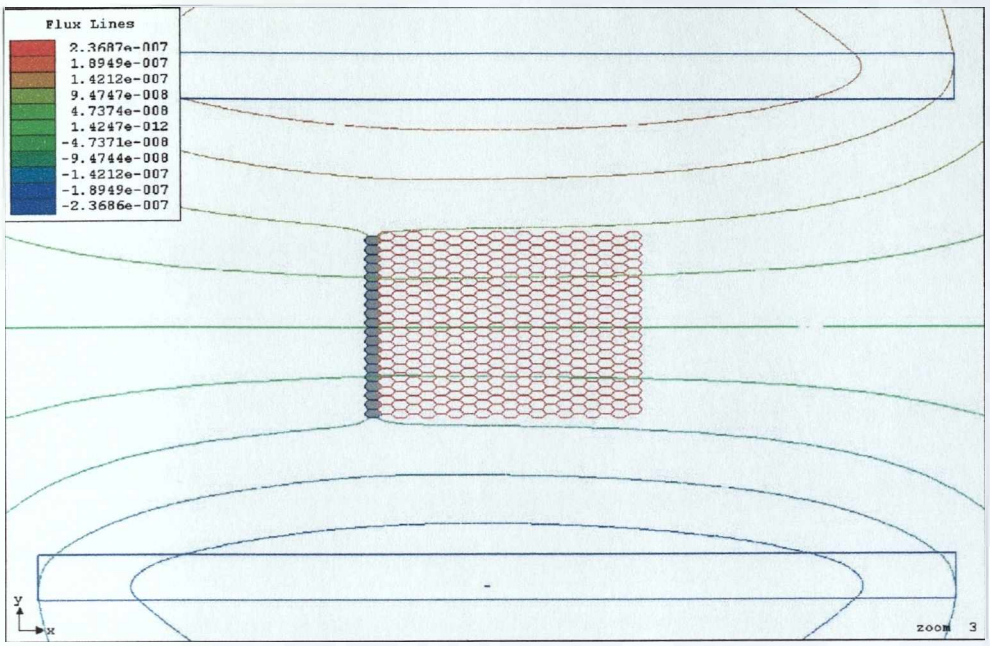

(c)

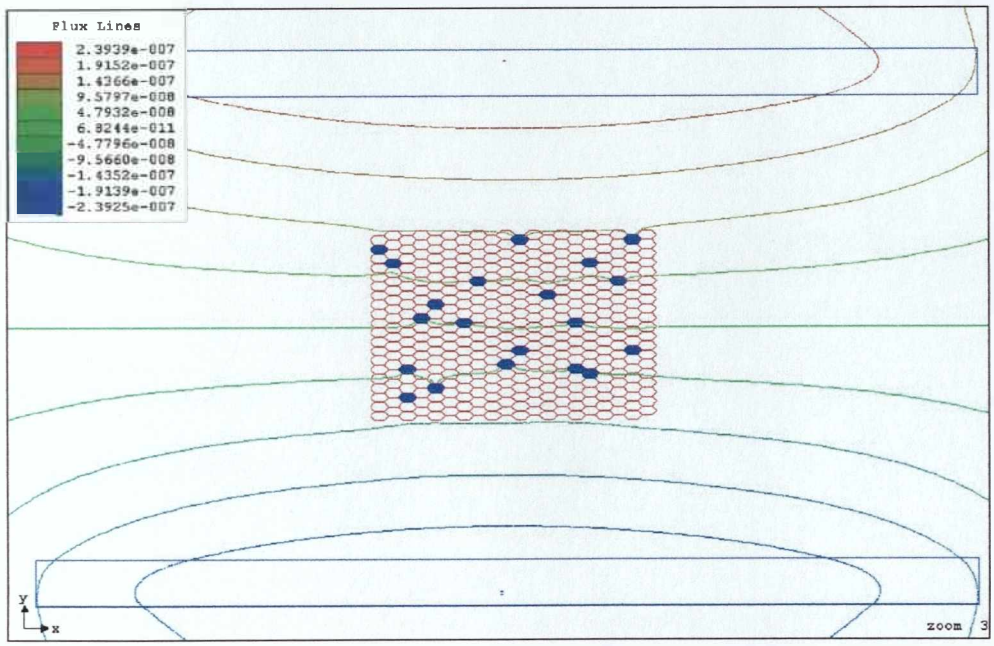

Figure 6.4: Simulations for 5% ferrite fraction distributed in a) continuous single line with orientation in the x-axis, b) continuous single line with orientation in the y-axis, c) random distribution.

From the plots in figure 6.4 it can be seen that the electromagnetic field is severely distorted in the presence of a fully connected ferromagnetic path orientated in the x-axis. The influence of a continuous ferromagnetic path orientated in the y-axis on the magnetic flux is significantly smaller and almost negligible. The orientation of the ferromagnetic phase affects magnetisation due to the shape anisotropy effect [239], which needs to be addressed during the analysis of an EM sensor response to microstructure. The importance of connectivity is displayed in the third plot, figure 6.4(c), where the ferromagnetic phase is distributed in a random manner. The distortion of the magnetic lines of flux from the path they follow in a fully paramagnetic sample is considerably less than for the x-axis orientated continuous ferromagnetic path, although some local distortion can be observed close to the ferromagnetic cells.

The difference in the impedance value exhibited for each configuration are for the x-axis orientated continuous ferromagnetic line the recorded impedance is 4.57×10^{-7} Ω, for the y-axis orientated continuous ferromagnetic line is 4.16×10^{-7} Ω and for the randomly distributed ferromagnetic phase is 4.186×10^{-7} Ω.

The resulting impedance values for the y-axis orientated continuous ferromagnetic line and the randomly distributed ferromagnetic phase are slightly higher than the impedance response obtained in the fully paramagnetic simulation. For the x-axis orientated continuous ferromagnetic line the magnetic response is almost equal to 50% of the impedance value obtained for the fully ferromagnetic simulation despite the fact that only 5% of the total area of the sample is ferromagnetic. The above results show the strong effect that connectivity has on magnetic response.

6.5 Decarburisation Simulations

The significance of decarburisation upon the magnetic response was discussed for experimental measurements in the previous chapter. FE simulations of the decarburised area were conducted in order to support the results obtained through experimental testing. Various patterns of the decarburised area were employed, i.e. fully connected or discontinuous ferromagnetic layers at the skin of the sample. Figure 6.5 presents the influence of various decarburisation patterns on the electromagnetic field.

(a)

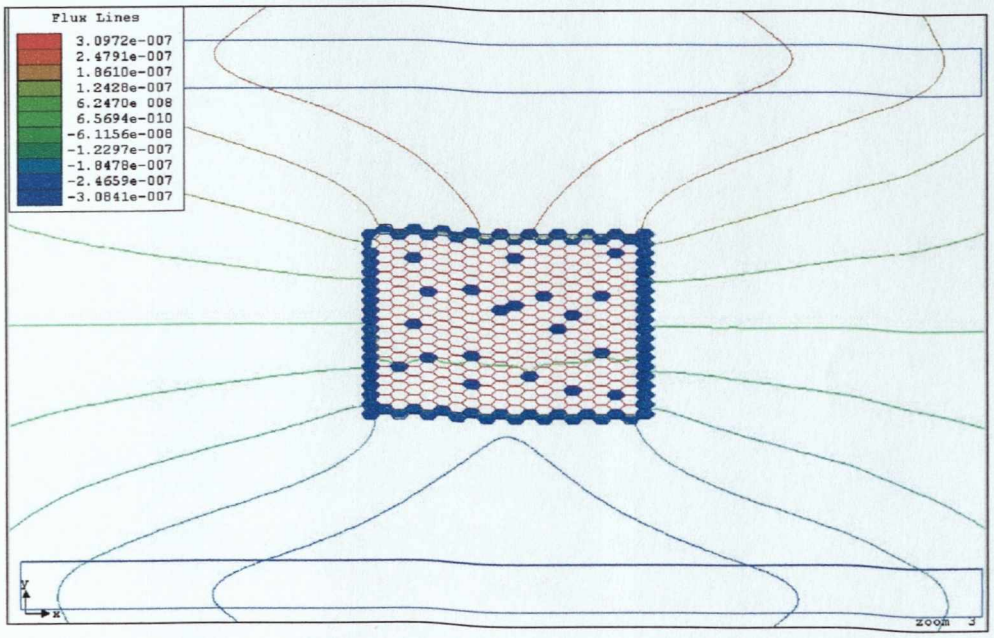

(b)

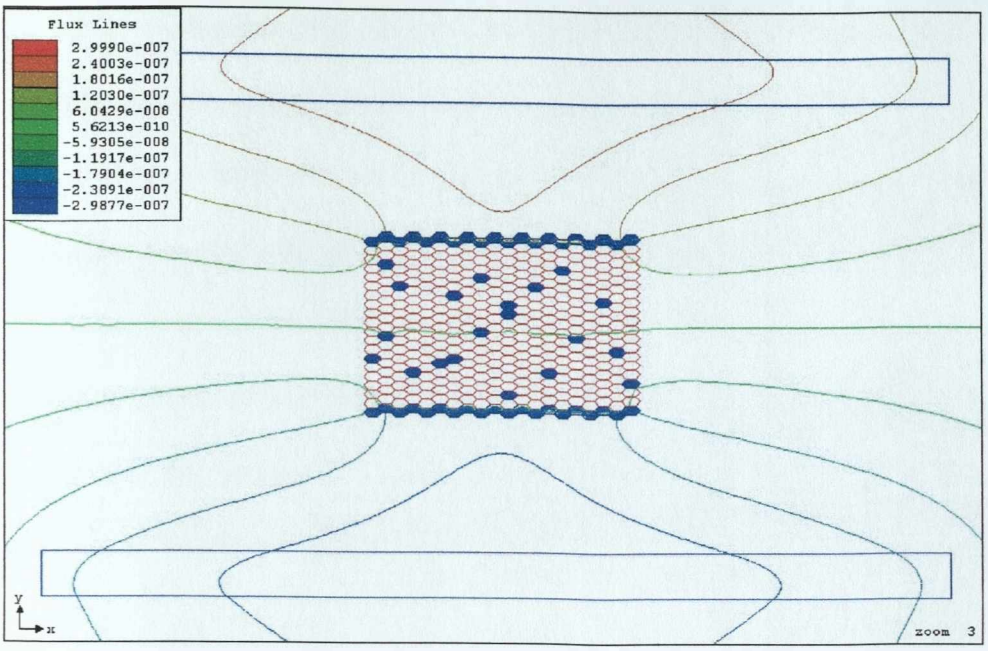

(c)

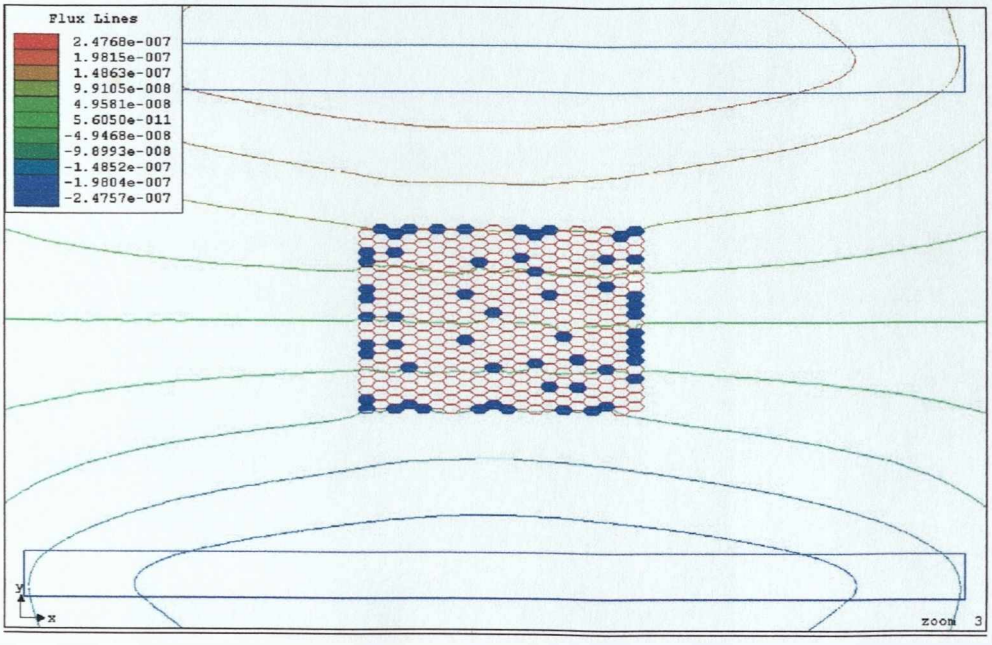

Figure 6.5: FE simulations of the influence of various decarburisation patterns on the electromagnetic field, a) fully decarburised on all surfaces, b) decarburised on two surfaces only and c) discontinuous decarburised surface region. For all simulations 5% bulk ferrite in a random array is also included.

In figure 6.5(a) is simulated the effect of a fully decarburised ferrite layer at the skin of the sample with 5% of bulk ferrite already formed. As it can be seen, the magnetic lines of flux concentrate in the x-axis oriented decarburised areas whilst the effect of y-axis oriented decarburised areas on the electromagnetic field is negligible. The effect of the presence of 5% randomly distributed bulk ferromagnetic material is also small as the magnetic flux is almost fully concentrated in the ferromagnetic layer at the surface of the sample. The obtained impedance value for the specific configuration is 5.045×10^{-7} Ω and almost equals that for the fully ferromagnetic simulation. In the second plot, figure 6.5(b), the y-axis oriented decarburised areas have been removed. Nonetheless, the magnetic response exhibited is very similar to that of the fully decarburised ferrite layer shown in figure 6.5(a). As a consequence, the recorded impedance value is also high, 4.902×10^{-7} Ω. The third plot, figure 6.5(c), examines a discontinuous decarburised layer being present along with the random 5 % ferrite in the bulk of the sample. The electromagnetic field remains largely unaffected and this is reflected in the obtained impedance response, 4.294×10^{-7} Ω. Simulation results on the effect of decarburisation agree well with the experimental data and hence, validate further the electromagnetic technique.

6.6 Random distribution of the ferromagnetic phase

In order to determine the effect of increasing the amount of the ferromagnetic phase in a random fashion, simulations were performed using increasing levels of ferromagnetic cells. The following randomly distributed ferromagnetic fractions were employed for the simulations: 2%, 5%, 10%, 15%, 20% and 25%. In figure 6.6 are shown the plots obtained for 2%, 10%, 15% and 25% ferrite respectively.

(a)

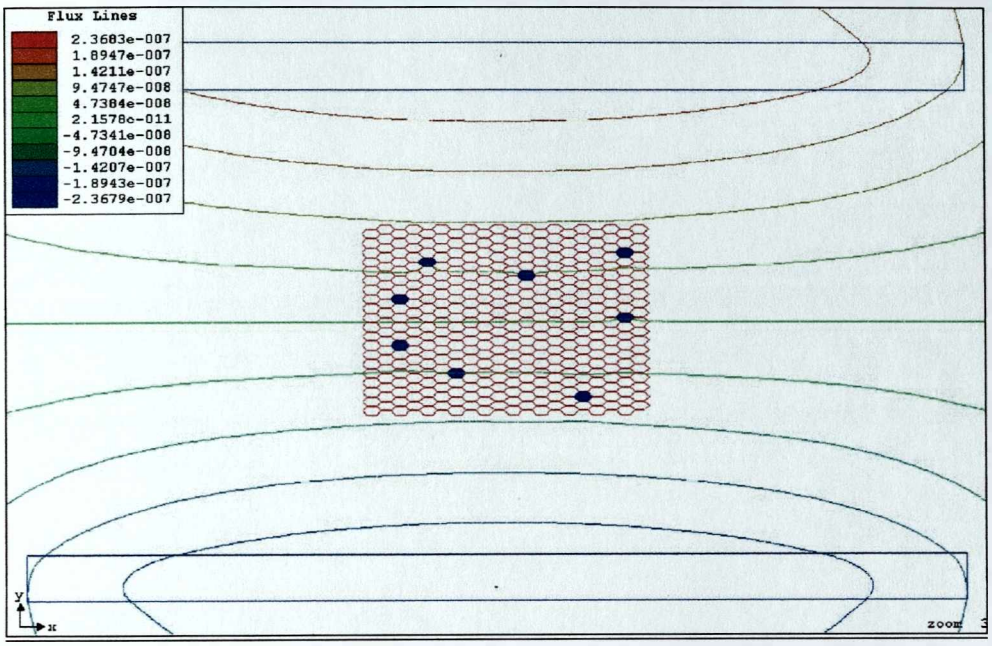
Flux Lines
2.3683e-007
1.8947e-007
1.4211e-007
9.4747e-008
4.7384e-008
2.1578e-011
-4.7341e-008
-9.4704e-008
-1.4207e-007
-1.8943e-007
-2.3679e-007
y
x
zoom 3

(b)

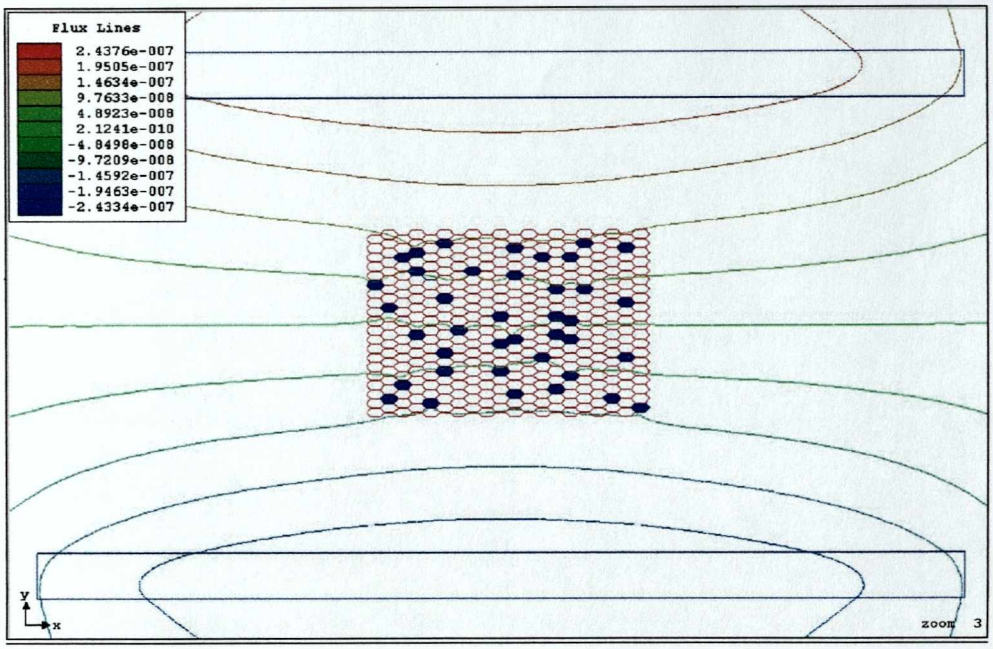
Flux Lines
2.4376e-007
1.9505e-007
1.4634e-007
9.7633e-008
4.8923e-008
2.1241e-010
-4.8498e-008
-9.7209e-008
-1.4592e-007
-1.9463e-007
-2.4334e-007
y
x
zoom 3

(c)

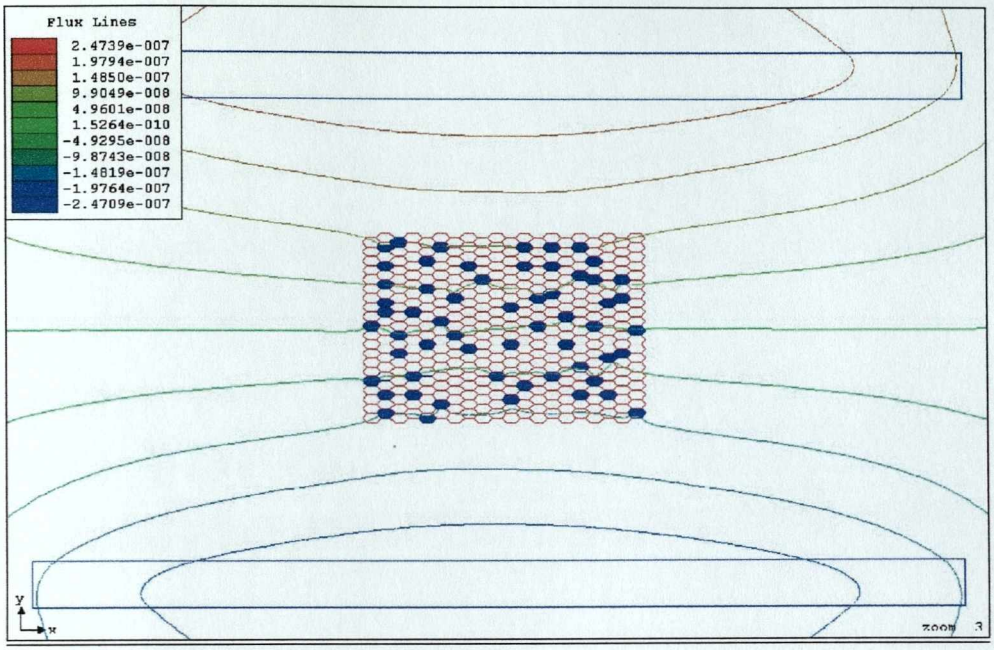

(d)

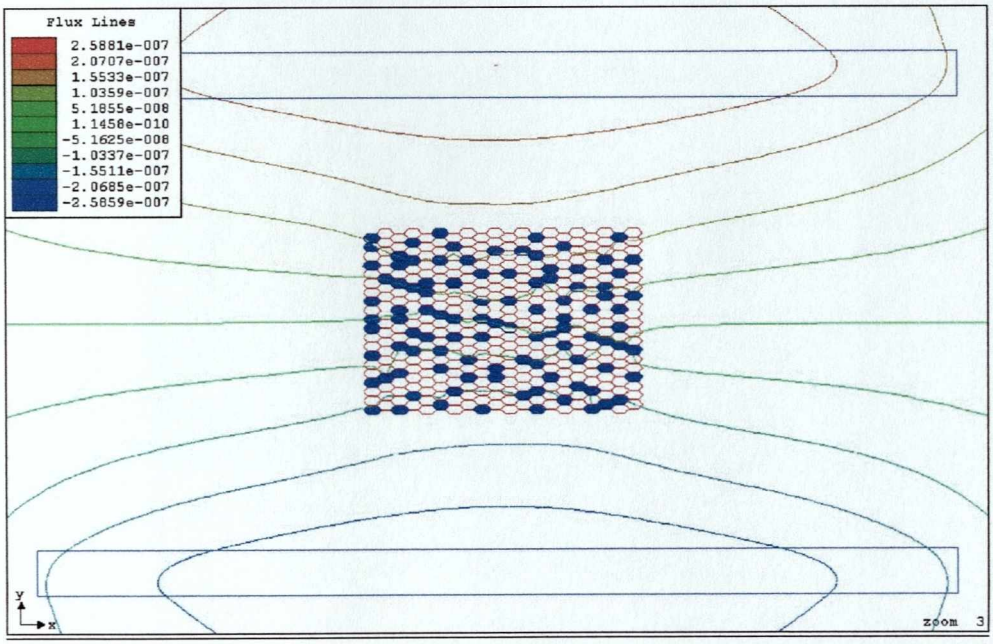

Figure 6.6: FE simulation for random distribututions of ferromagnetic phase with a) 2% ferrite, b) 10% ferrite, c) 15% ferrite, d) 25% ferrite.

From figure 6.6(a) it can be seen that for 2% ferrite present the magnetic lines of flux are effectively undisturbed. This is illustrated by the acquired impedance value, 4.157×10^{-7} Ω which is only slightly larger than the value obtained for a fully paramagnetic sample (4.138×10^{-7} Ω). As the ferromagnetic fraction increases to 10%, figure 6.6(b), a slight attraction of the magnetic lines of flux towards the centre of the sample is observed. This is signified by an increase in impedance value, 4.242×10^{-7} Ω. The impedance value increases steadily with ferromagnetic fraction and for 15% ferrite, figure 6.6(c), it reaches 4.292×10^{-7} Ω. Finally, for 25% ferrite present, figure 6.6(d) the recorded impedance is 4.437×10^{-7} Ω. The corresponding impedances obtained for each randomly distributed ferromagnetic fraction are tabulated in table 6.1.

Table 6.1: Corresponding impedance values with ferrite fraction % randomly distributed.

Ferrite Fraction	Impedance / Ω
0% (Paramagnetic)	4.138×10^{-7}
2%	4.157×10^{-7}
5%	4.186×10^{-7}
10%	4.242×10^{-7}
15%	4.292×10^{-7}
20%	4.373×10^{-7}
25%	4.437×10^{-7}

Comparison of the impedance values for randomly distributed ferrite with that for the x-axis and y-axis oriented connected ferrite lines shows that connectivity has a very strong effect on the magnetic response. This is apparent in figure 6.7.

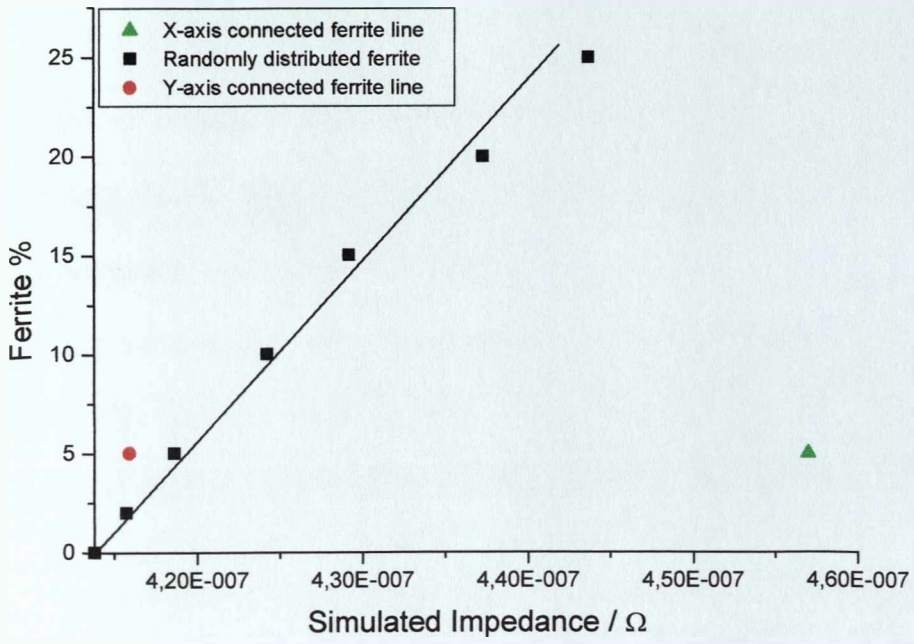

Figure 6.7: Ferrite fraction – impedance plot for randomly distributed ferrite and x-axis and y-axis connected ferrite lines.

Furthermore, from figure 6.7, it can be seen that impedance does not appear to vary linearly with increasing random ferrite fraction. Despite the initial linearity of the impedance response with ferrite fraction for random ferrite fractions of 5 – 15 % as the amount of ferrite is increased further the relationship appears to deviate from linear although further simulations are required in order to obtain an indication of the measurement error. It would appear that the simulated impedance values increase more than predicted by a linear relationship. This occurs because as the ferrite fraction increases a more connected network develops, as shown in figure 6.6(d) and the magnetic lines of flux become more strongly affected.

6.7 Random distribution and connectivity effect

The significance of contiguity of the ferromagnetic phase upon the magnetic response has been already shown. However, the relationship between a random distribution and the development of contiguity has not been fully examined. Therefore, simulation patterns were also carried out on random distribution of groups of three ferromagnetic cells with an x-axis orientation. In these simulations, both randomness and contiguity of ferrite is achieved. As before, the ferrite fractions used for these simulations were 5%, 10%, 15%, 20% and 25%.

In figure 6.8 are plotted the electromagnetic field responses for 5%, 15% and 25% ferrite. It can be seen that the attraction of the magnetic flux to the sample for each ferrite fraction is stronger when ferrite cells are grouped in sets of three forming continuous ferromagnetic paths rather than when they are just randomly positioned as shown in figure 6.8.

(a)

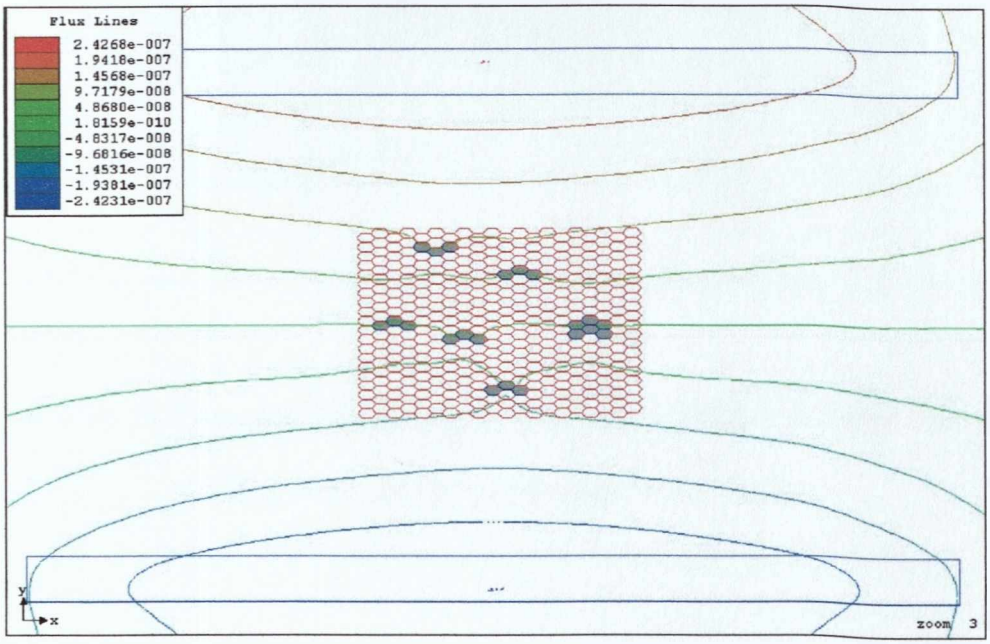

(b)

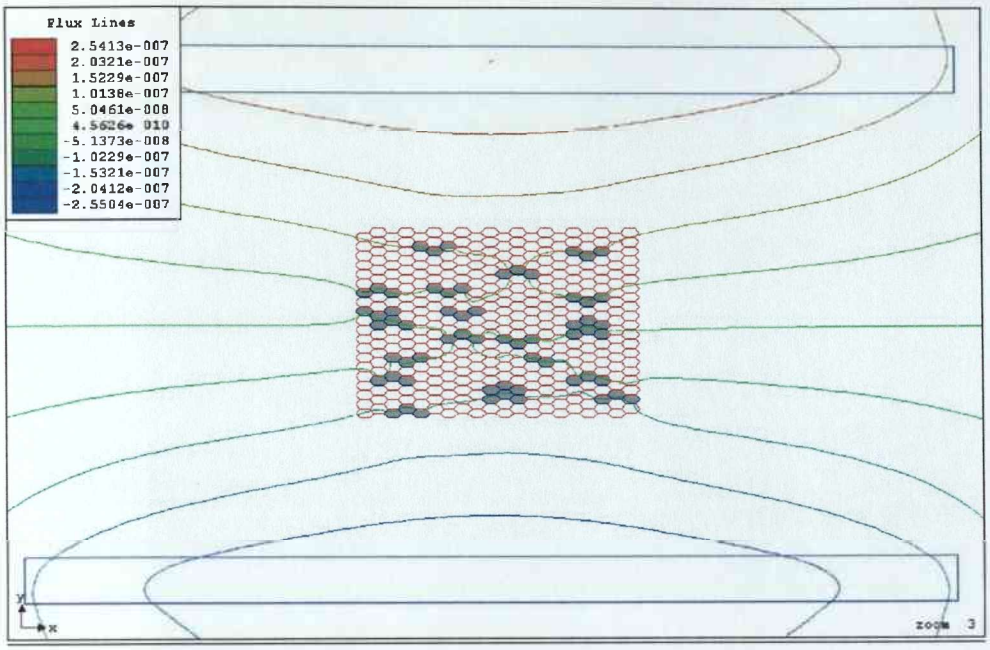

(c)

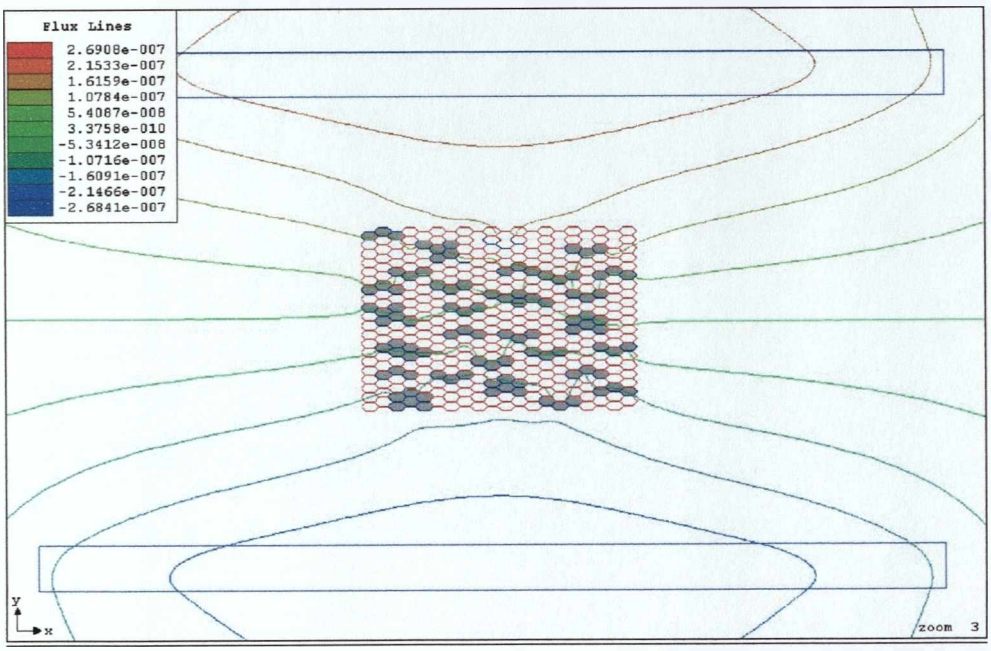

Figure 6.8: FE simulation for random distribututions of grouped ferrite cells with a) 10% ferrite, b) 15% ferrite and c) 25% ferrite.

In table 6.2 are given the corresponding impedance values for each ferrite fraction, in the form of individual cells randomly distributed and grouped cells randomly distributed.

Table 6.2: Corresponding impedance values with ferrite fraction % for individual and grouped cells randomly distributed.

Ferrite Fraction %	Random, z'' / Ω	Group Random, z'' / Ω
0	$4.138x10^{-7}$	$4.138x10^{-7}$
5	$4.186x10^{-7}$	$4.227x10^{-7}$
10	$4.242x10^{-7}$	$4.314x10^{-7}$
15	$4.292x10^{-7}$	$4.384x10^{-7}$
20	$4.373x10^{-7}$	$4.477x10^{-7}$
25	$4.437x10^{-7}$	$4.56x10^{-7}$

The corresponding impedance value with ferrite fraction % for grouped cells randomly distributed is graphically displayed in figure 6.9.

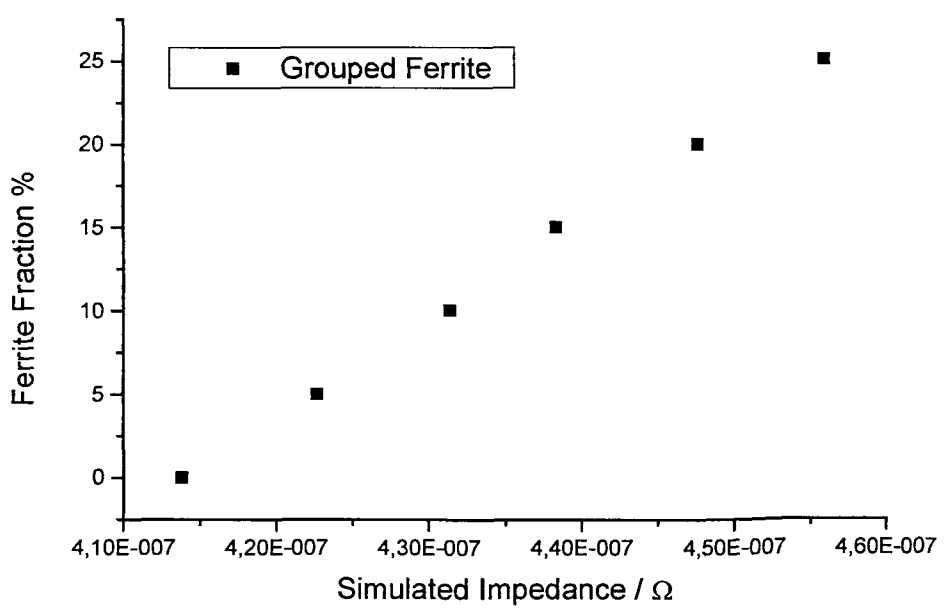

Figure 6.9: Impedance – ferrite fraction plots for randomly distributed groups of three cells.

Figure 6.9 shows that the impedance response increases linearly with ferrite fraction for randomly distributed groups of three cells. This is likely to be due to the very small change in the contiguity of ferrite with increasing ferrite fraction. Therefore, relatively small contiguity changes of ferrite could account for the linearity seen in the impedance response in this case.

6.8 FE simulations on actual microstructures

Further FE simulations were performed in order to model the actual microstructure development during cooling of the EM tested small grain 0.45 wt % carbon steel. The simple patterns used in the previous simulations could easily be carried out using a grid consisting of a small number of cells. However, in the case where the actual microstructure needed to be simulated a much larger grid was required. To do that, a 60 x 60 grid of equilateral hexagonal cells was designed with the same conditions and dimensions applying to the cells as in the previous simulations. The total length of the sample was hence increased to 1200 μm. The length of the coils was also tripled in order to maintain the proportions of the previous simulations and hence allow the previous simulation results to be used as reference. The background was set to be a vacuum and the same frequency, 50 Hz, was employed as before.

The optical micrographs used in these FE simulations were obtained from samples quenched at pre-chosen temperatures determined by the experimental EM tests that aimed to determine phase transformation, ferrite fraction and microstructure evolution during cooling.

To avoid prolonged solution times due to the large number of hexagons involved, all cells that represented the austenitic matrix were grouped as one object to cut down the number of variables. The same was done for any groups of cells that represented ferrite. By using this method, it was possible to maintain solution times in the order of minutes instead of several hours.

6.9 Fully paramagnetic and fully ferromagnetic simulations

In a similar manner as for the previous simulations the magnetic response for the fully austenitic and fully ferritic microstructures needed to be determined. The permeabilities for paramagnetic and ferromagnetic cells were assigned as 1 and 1000 respectively. The electromagnetic field is plotted for each case in figure 6.10.

(a)

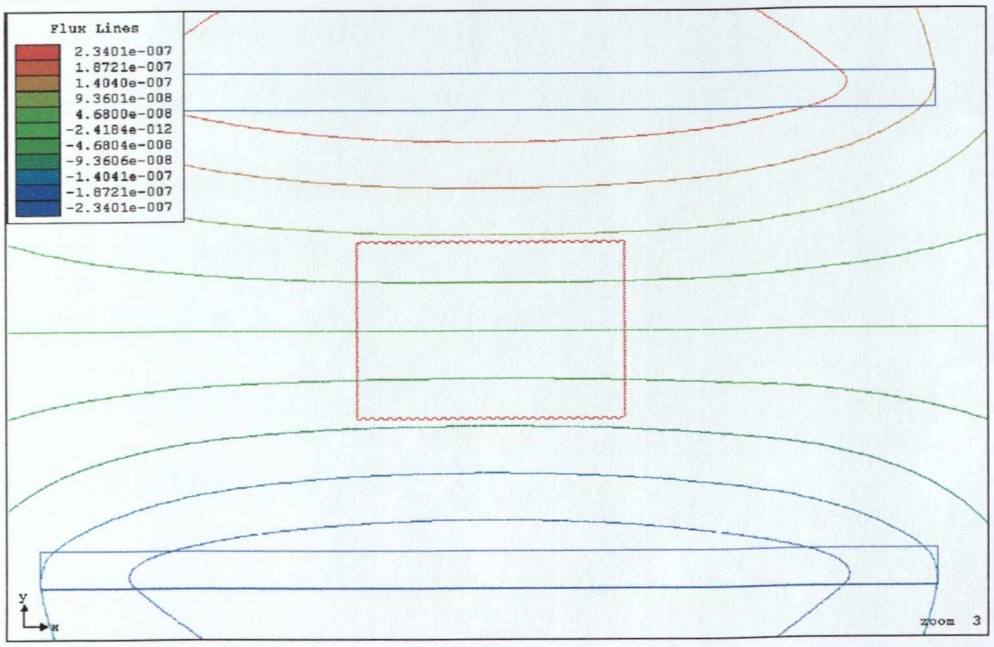

(b)

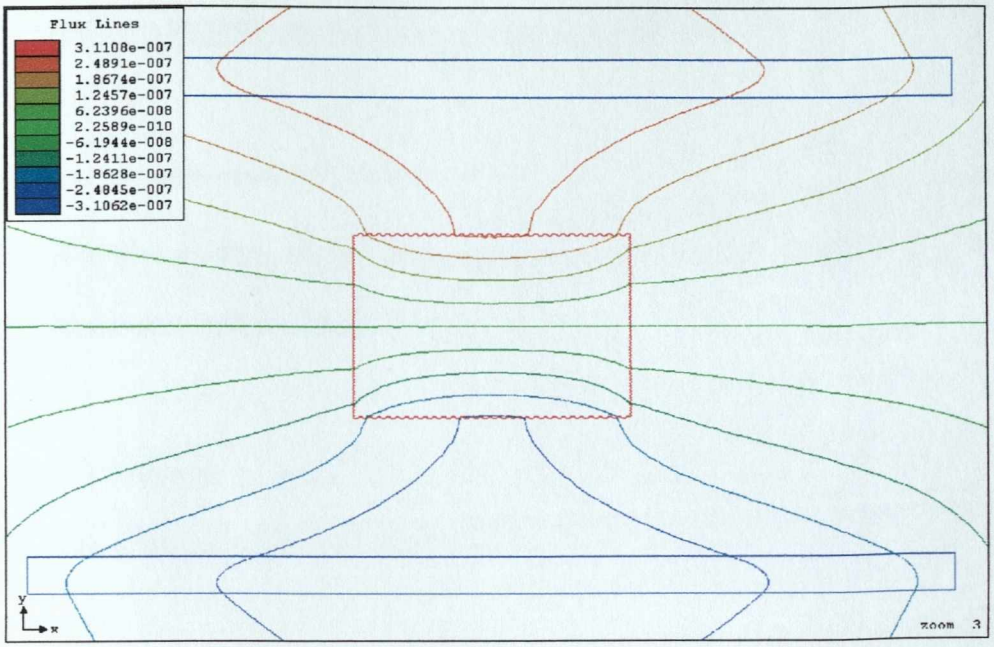

Figure 6.10: Electromagnetic field plots for: a) fully paramagnetic microstructure and b) fully ferromagnetic.

The impedance value for the fully paramagnetic sample was found to be 4.128×10^{-7} Ω while for the ferromagnetic sample equalled 5.062×10^{-7} Ω. These are the minimum and maximum impedance values for the particular simulation setup. The values obtained for these simulations are slightly different from those obtained for the 20x20 cell sample. This is due to the changes in the number and size of the elements in the simulation mesh related to the size of the configuration producing a slightly different solution for each setup.

6.10 Small grain medium carbon steel simulations

Simulations on microstructures representative of the small grain steel ignored the effect of decarburisation. Hence any impedance response rises from the presence of bulk ferrite forming within the microstructure.

In order to represent actual ferrite formation within the small steel sample microstructure, micrographs obtained from the section parallel to the rolling axis of the rod were used. Simulations were conducted for quenched samples from 720°, 715°, 707°, 700°, 690° and 681°C representing microstructures with a range of ferrite contentns (from 0 to 26 %). The sample quenched from 681°C contained some pearlite, however only the ferrite formed in the microstructure was included in the simulation.

In figure 6.11 is presented a sequence of plots of the electromagnetic field with actual ferrite formation at 715°, 700°, 690° and 681°C. The micrographs show the microstructure used as reference for each of the simulations.

(a)

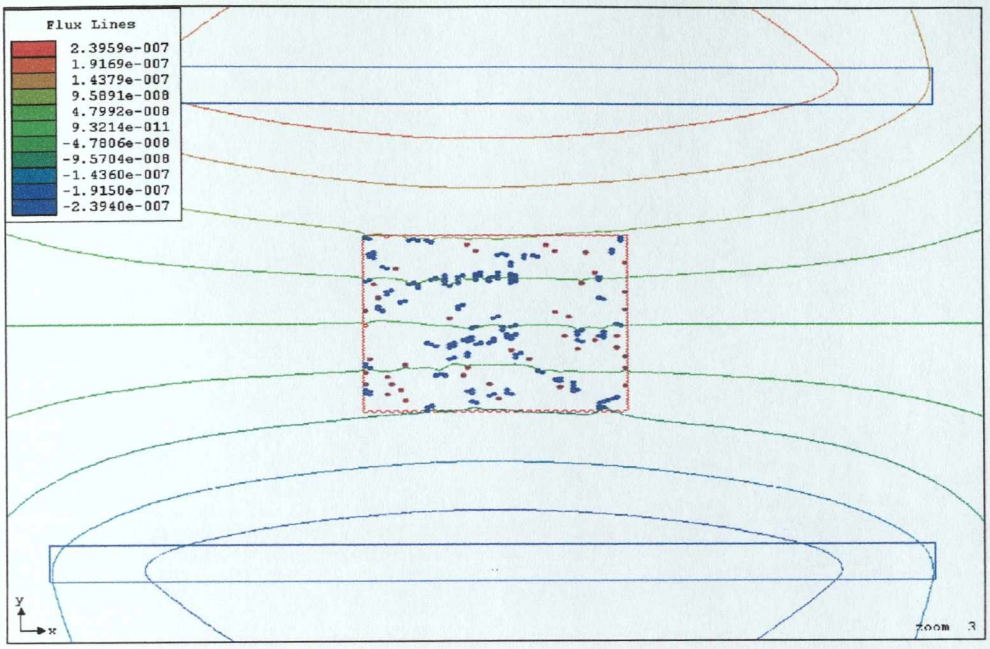
Flux Lines
2.3959e-007
1.9169e-007
1.4379e-007
9.5891e-008
4.7992e-008
9.3214e-011
-4.7806e-008
-9.5704e-008
-1.4360e-007
-1.9150e-007
-2.3940e-007
y
x
zoom 3

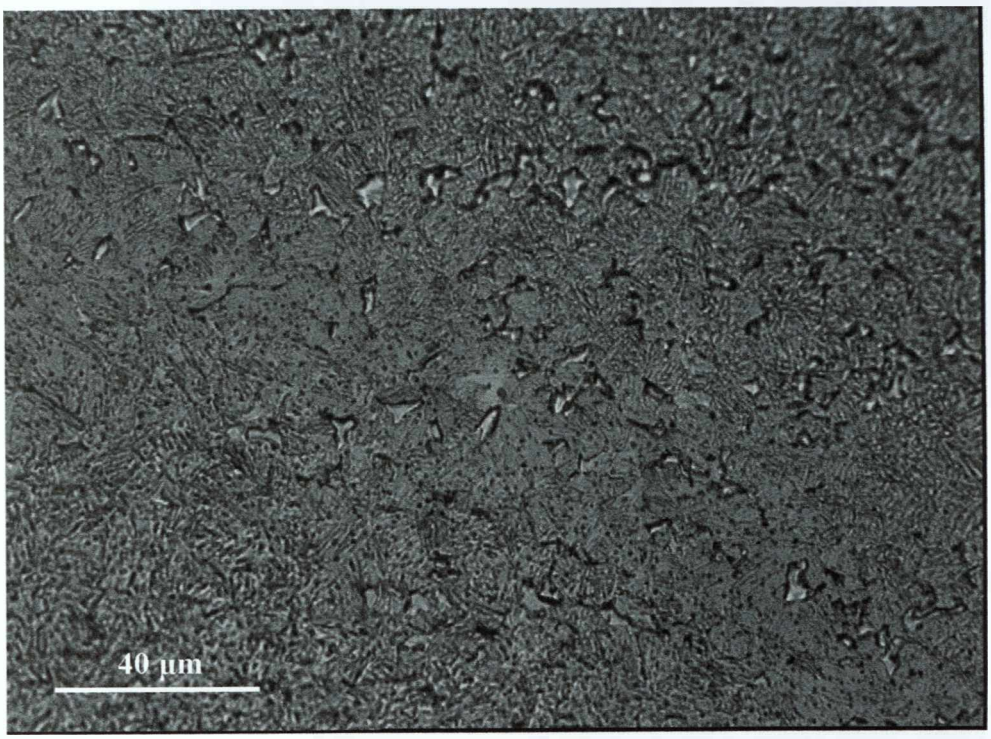
40 µm

(b)

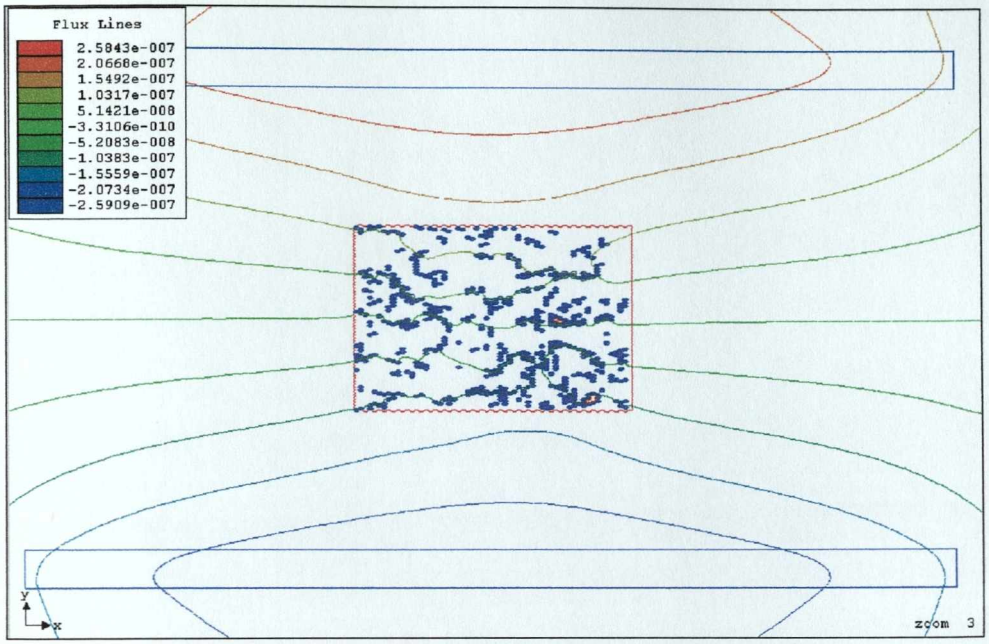
Flux Lines
2.5843e-007
2.0668e-007
1.5492e-007
1.0317e-007
5.1421e-008
-3.3106e-010
-5.2083e-008
-1.0383e-007
-1.5559e-007
-2.0734e-007
-2.5909e-007
y
x
zoom 3

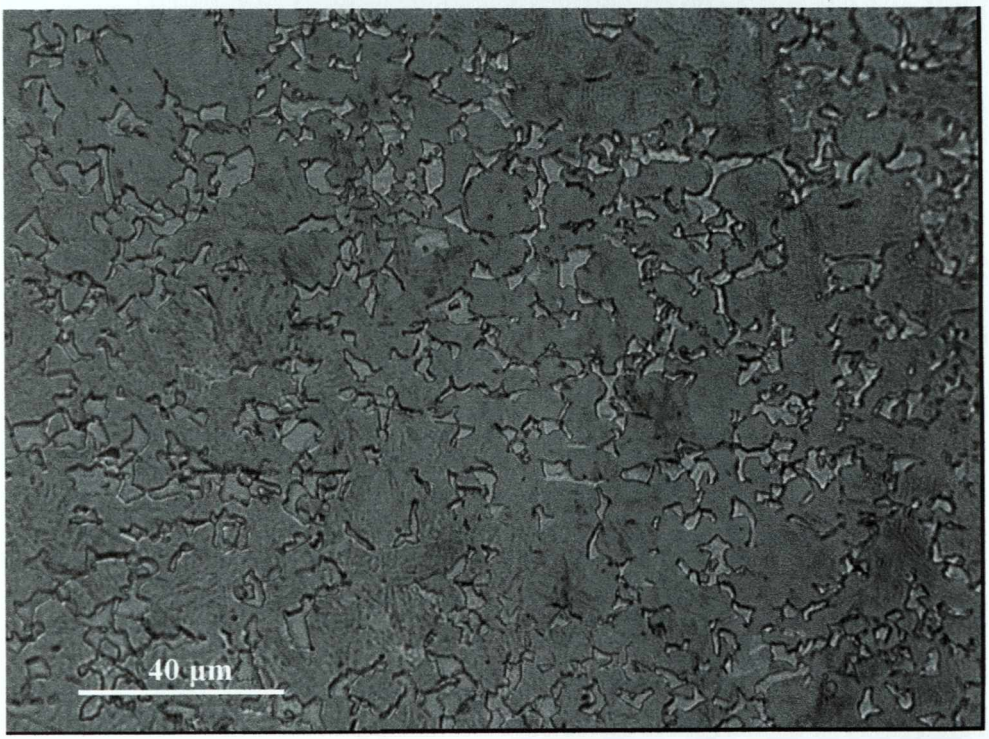
40 µm

(c)

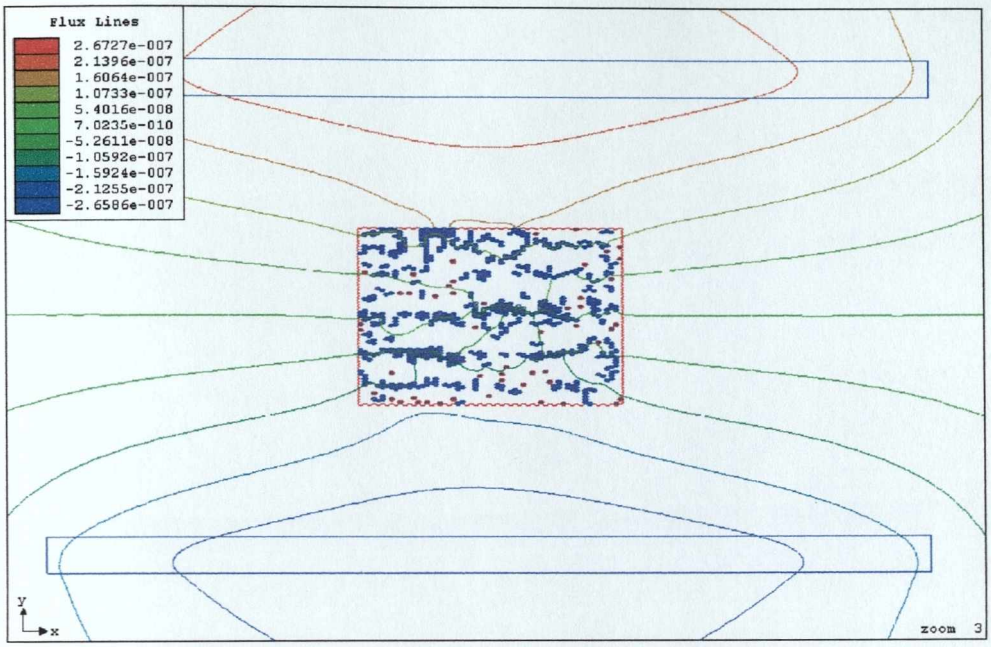
Flux Lines
2.6727e-007
2.1396e-007
1.6064e-007
1.0733e-007
5.4016e-008
7.0235e-010
-5.2611e-008
-1.0592e-007
-1.5924e-007
-2.1255e-007
-2.6586e-007
y
x
zoom 3

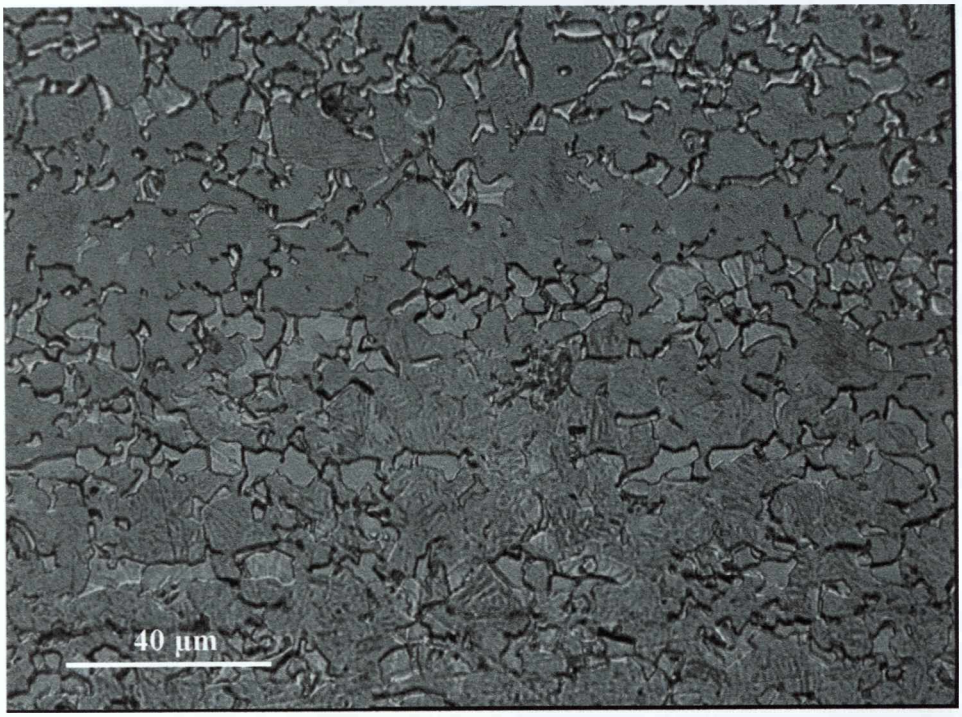
40 µm

(d)

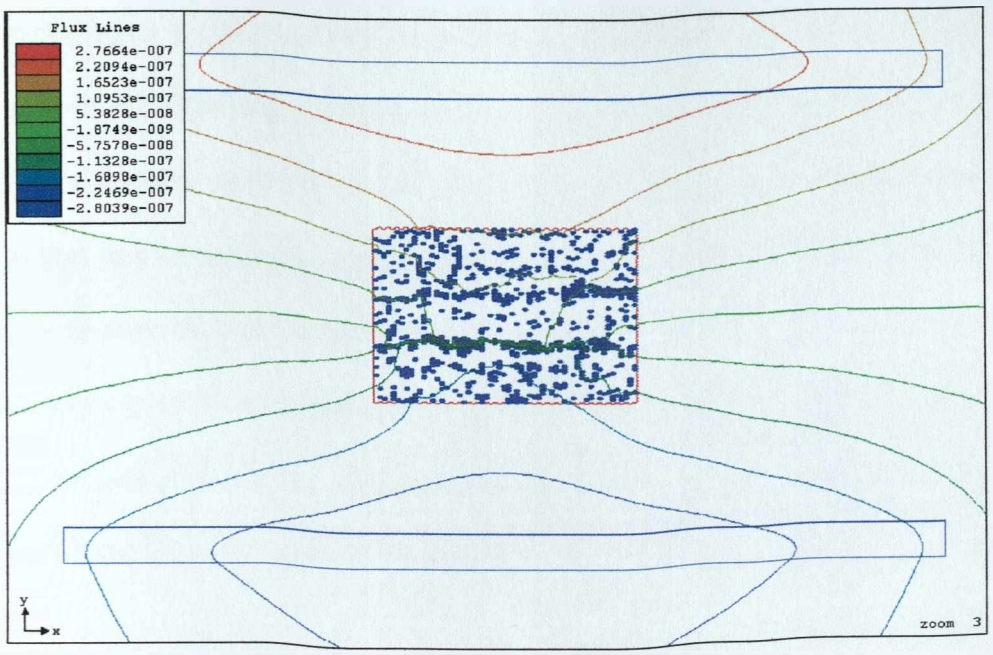

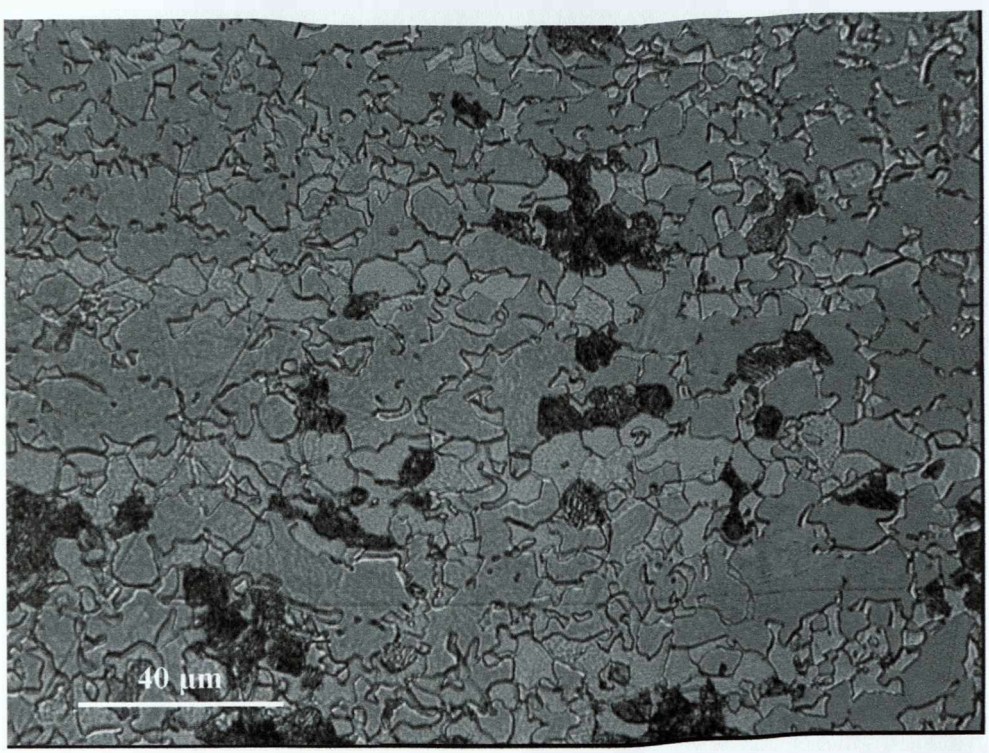

Figure 6.11: FE simulations on the actual microstructure from the small grain medium carbon steel for ferrite fraction a) 6 %, b) 14 %, c) 18 % and d) 26 %. Optical micrographs display the area of microstructure employed for representation in the simulations.

The micrographs in figure 6.11 show that in the case of the small grain steel there is a combination of randomly distributed and connected, along the rolling axis, ferrite grains. The banding of the ferrite grains observed in the microstructure is due to alloy segregation and deformation during the rolling procedure. The connected grains present a favourable path for the flux to go through. However, the formation of this ferromagnetic path is not instantaneous and it becomes more connected as the sample cools down and more ferrite forms. Figure 6.12 shows the relationship between the simulated impedance values and temperature. The resulting plot agrees well with the experimental results presented in the previous chapter, e.g. figure 5.49 for the impedance change before pearlite formation.

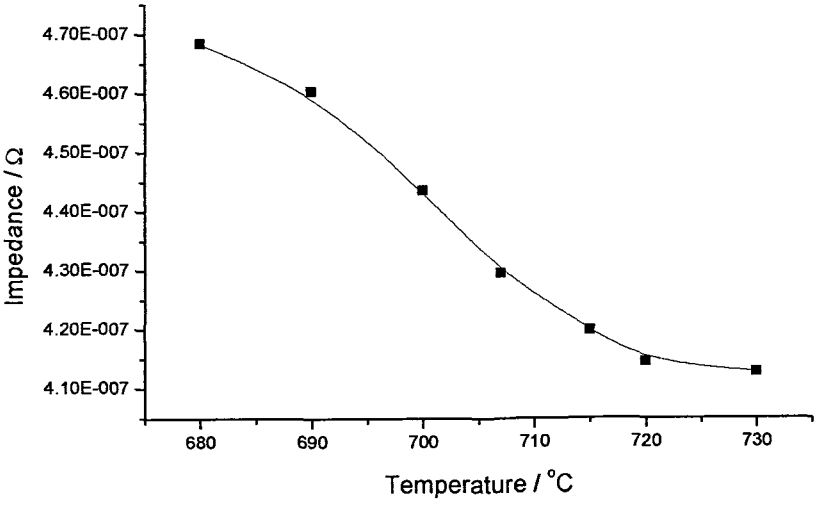

Figure 6.12: Simulated impedance versus temperature for the small grain size 0.45 wt % C steel.

Figure 6.13 shows simulated impedance relationship with ferrite fraction. It can be seen that impedance value is not related linearly with ferrite fraction but it is affected by the connectivity of ferrite. As the ferromagnetic path begins to connect, the

impedance value tends to increase at a higher rate. However, as the connectivity of the ferromagnetic path approaches its peak, i.e. fully connected high-permeability ferromagnetic pathways hence formed, the rate at which the impedance value increases becomes smaller. This is due to the fact that the flux has already concentrated in a favourable ferromagnetic path (i.e. with higher relative permeability in comparison with the surrounding microstructure due to the formation of connected ferrite grains) causing the impedance value to reach close to the impedance maximum value earlier than if the same amount of ferrite was distributed in a completely random fashion. The shape of this curve agrees very well with the experimental values as shown in figure 5.53.

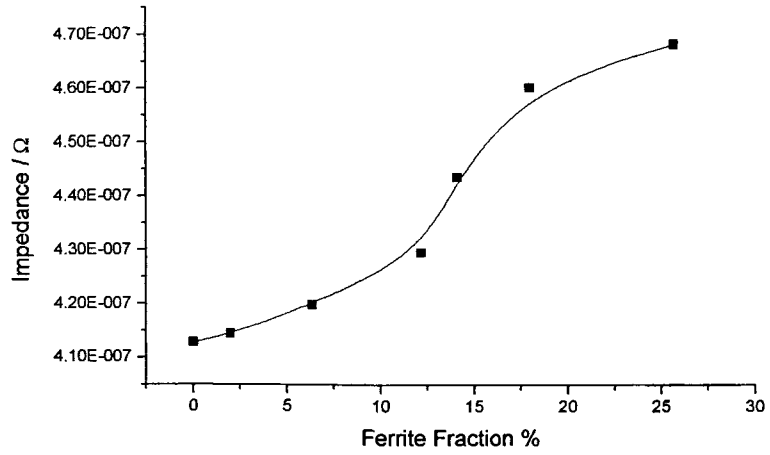

Figure 6.13: Simulated impedance versus ferrite fraction for small grain steel.

6.11 Large grain (homogenised at 1200°C) medium carbon steel simulations

Micrographs from interrupted quench test samples from the large grain sized 0.45 wt % C sample were acquired from an area parallel to the rolling axis. Due to the homogenisation process no banding of the ferrite grains occurs for the large grain

steel. As a result, the steel microstructure, and hence ferrite formation, is fully randomised although ferrite formation will occur preferentially along prior austenite grain boundaries. The samples used as a reference for the large grain steel simulations were quenched at 710°, 705°, 700°, 690° and 680°C. Figure 6.14 shows the electromagnetic field plotted against actual microstructure at 705°, 700°, 690° and 680°C.

(a)

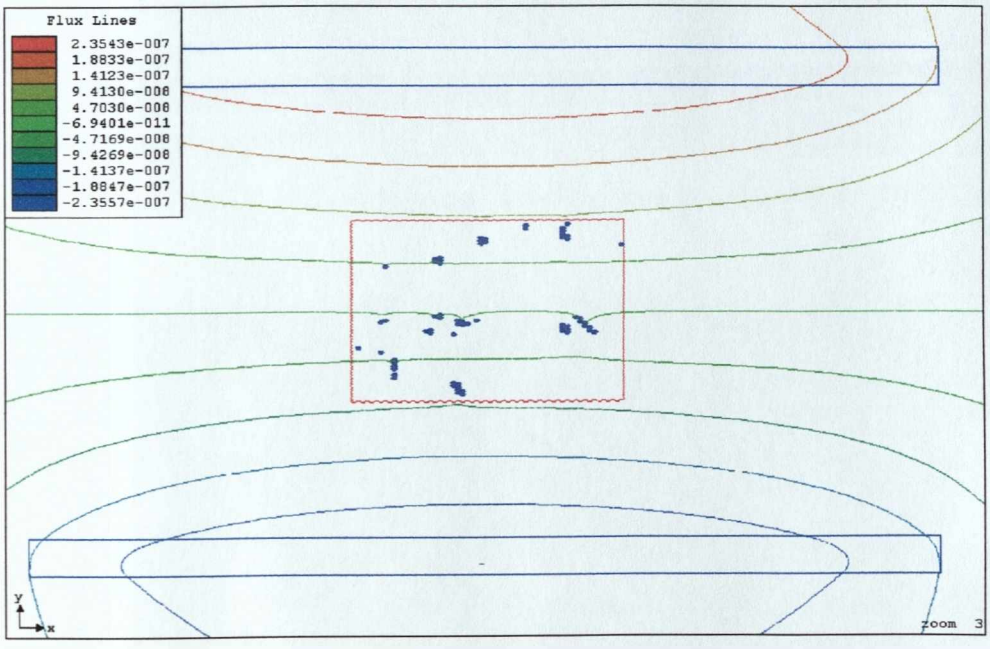

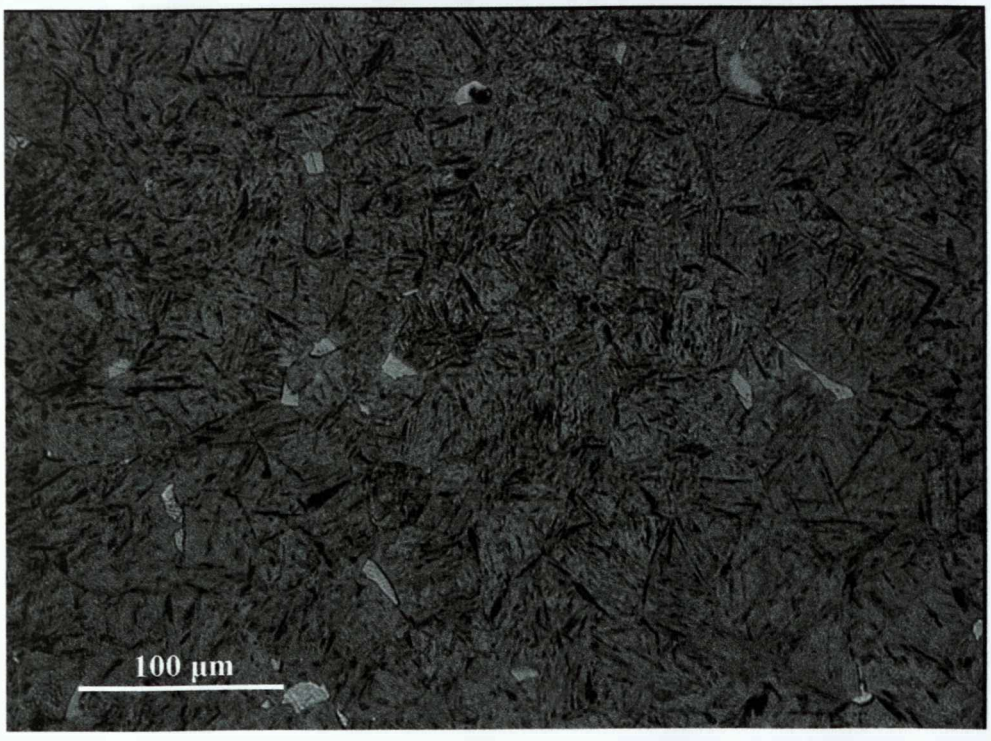

(b)

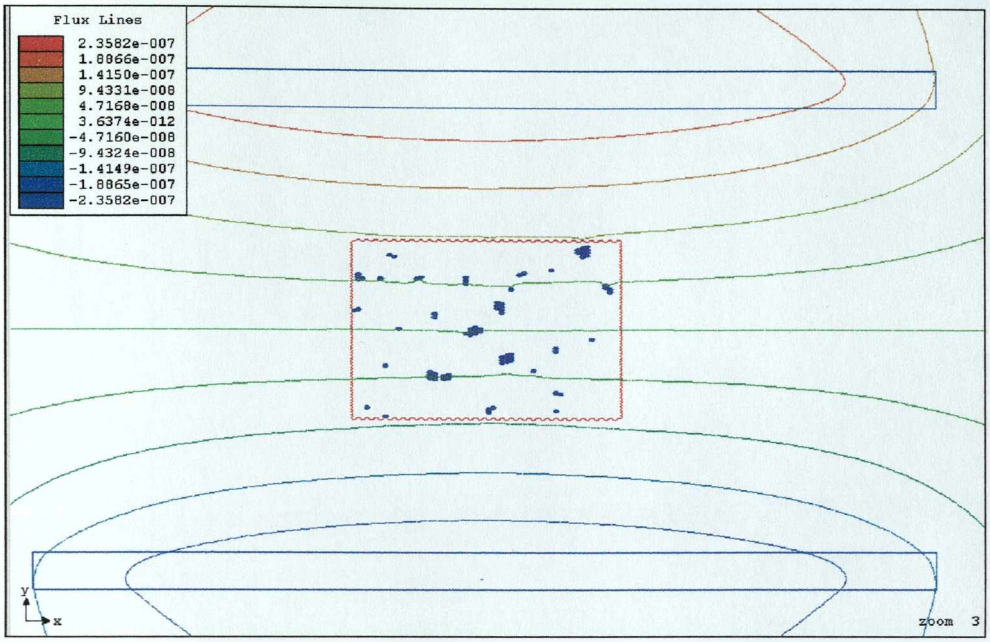
Flux Lines
2.3582e-007
1.8866e-007
1.4150e-007
9.4331e-008
4.7168e-008
3.6374e-012
-4.7160e-008
-9.4324e-008
-1.4149e-007
-1.8865e-007
-2.3582e-007
y
x
zoom 3

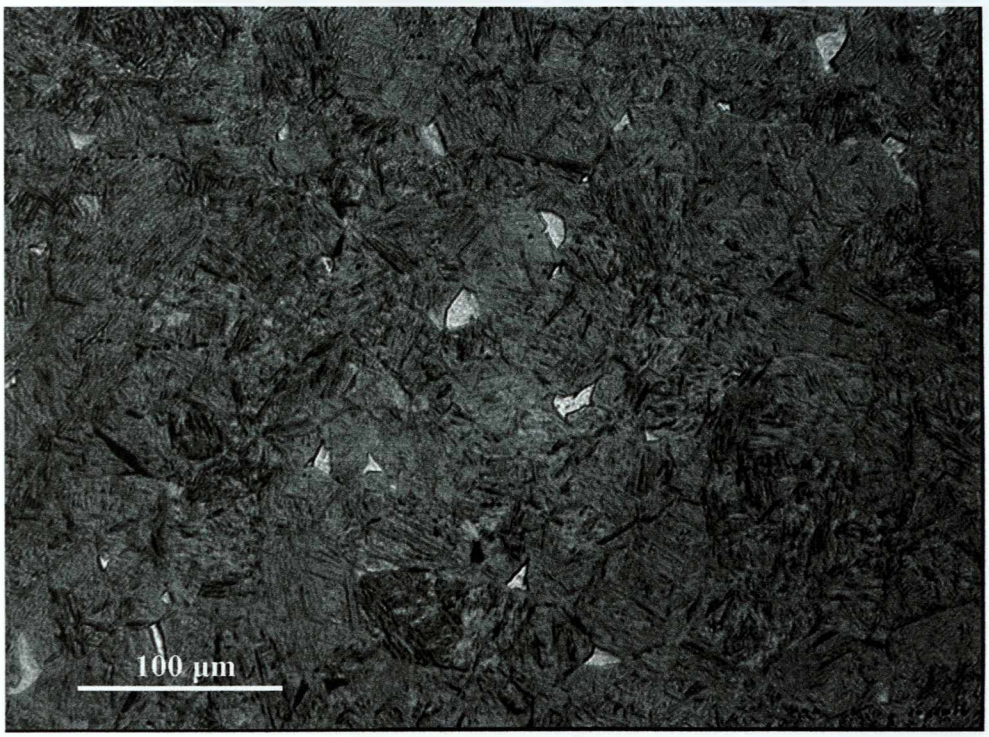
100 µm

(c)

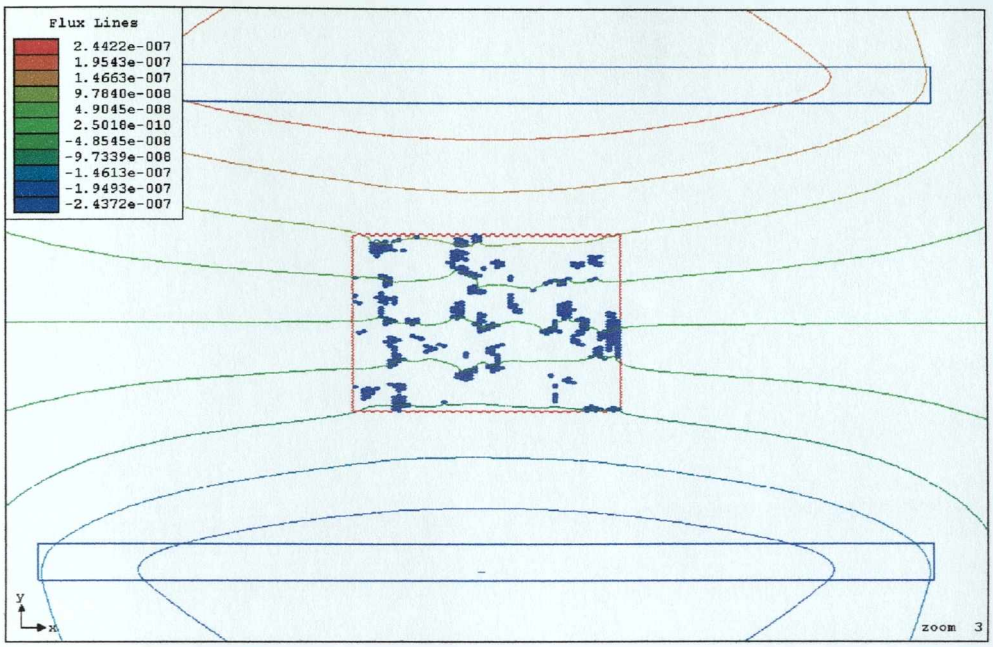
Flux Lines
2.4422e-007
1.9543e-007
1.4663e-007
9.7840e-008
4.9045e-008
2.5018e-010
-4.8545e-008
-9.7339e-008
-1.4613e-007
-1.9493e-007
-2.4372e-007
y
x
zoom 3

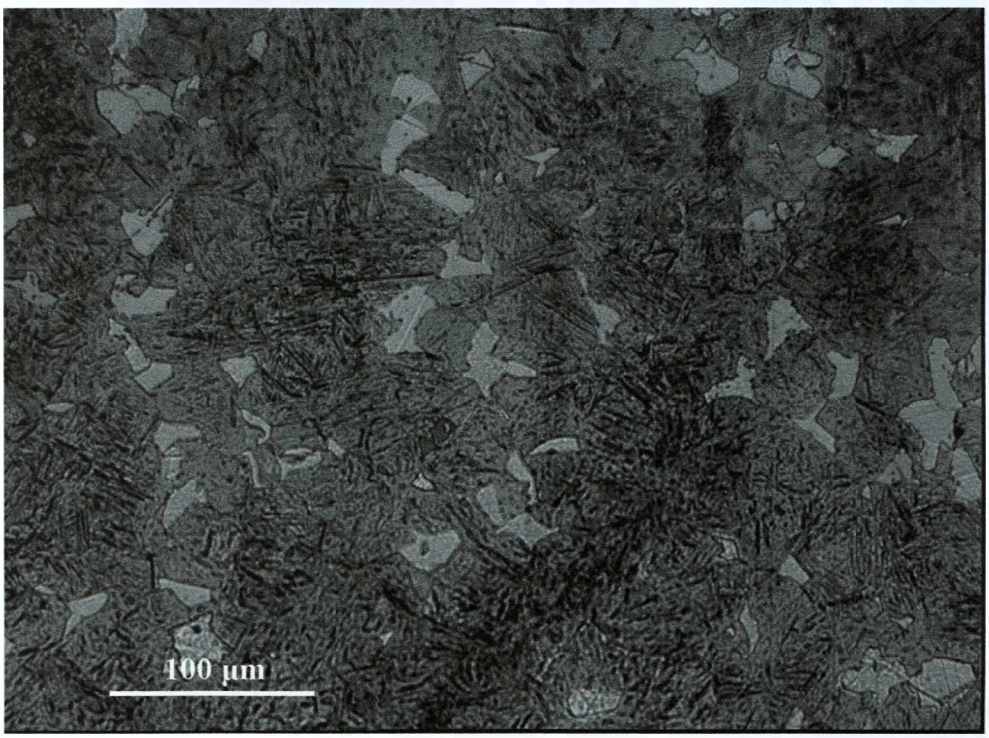
100 µm

(d)

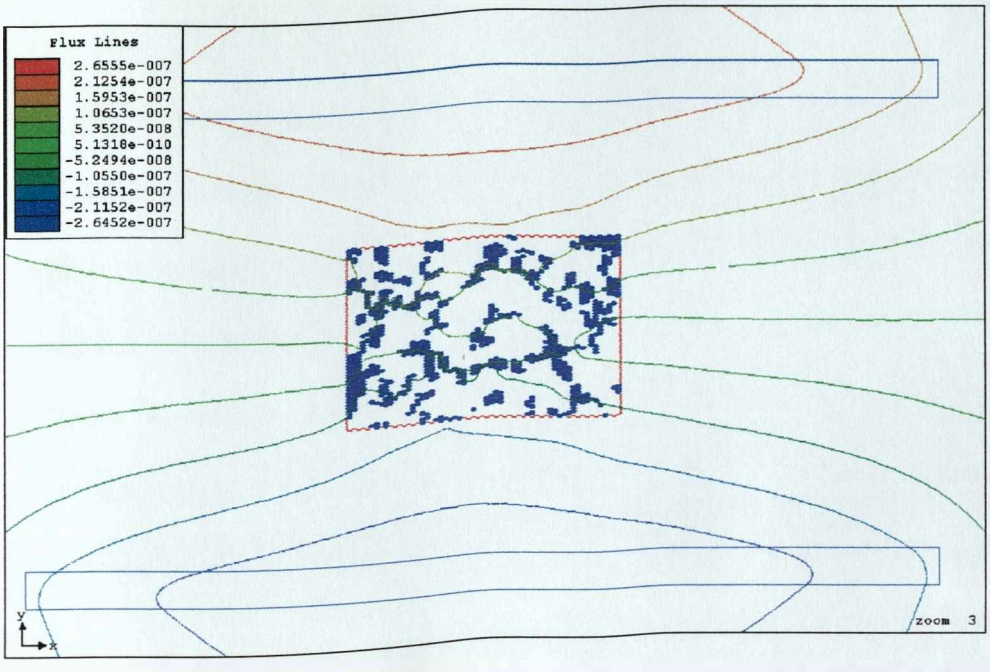

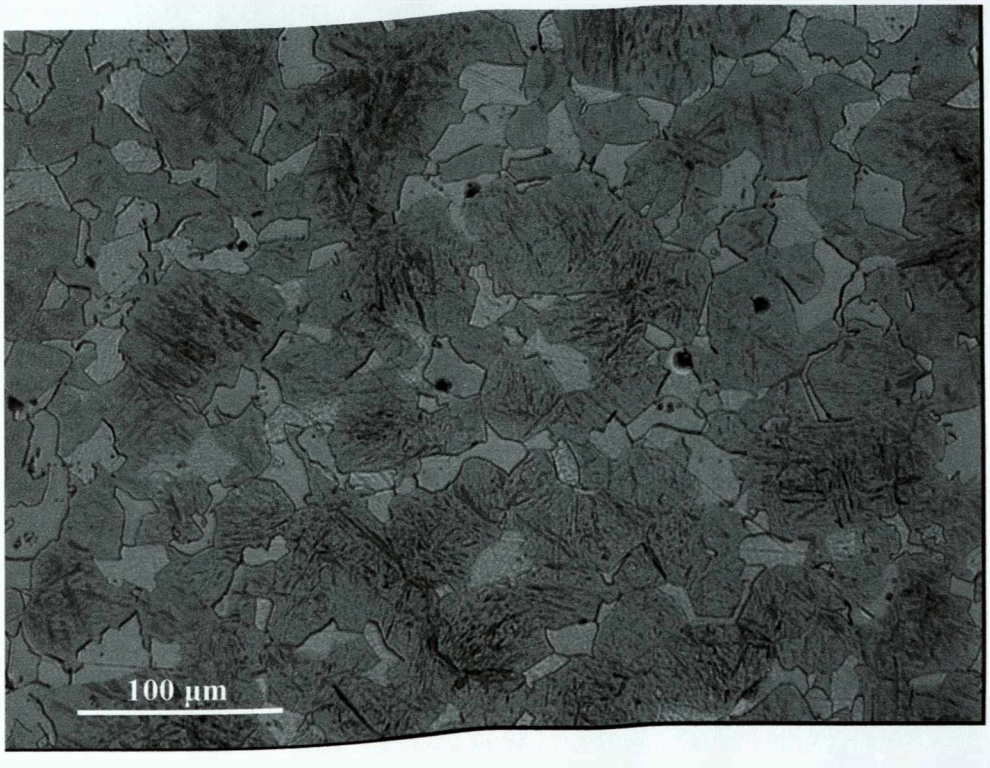

Figure 6.14: FE simulations on the actual microstructure of large grain medium carbon steel with a) 1 %, b) 2 %, c) 9 % and d) 24 % ferrite. Optical micrographs display the area of microstructure employed for representation in the simulations.

From the optical micrographs in figure 6.14, it can be seen that ferrite formation takes place around the prior austenite grain boundaries. By comparing the magnetic lines of flux plots for the small and large grain size steel, it becomes apparent that the electromagnetic field is distorted more in the case of the small grain size steel giving rise to higher impedance responses. This is mainly due to the existence of a continuous ferromagnetic path formed by the banding of ferrite small grain size steel. Figure 6.15 shows the impedance response with temperature for the large grain samples.

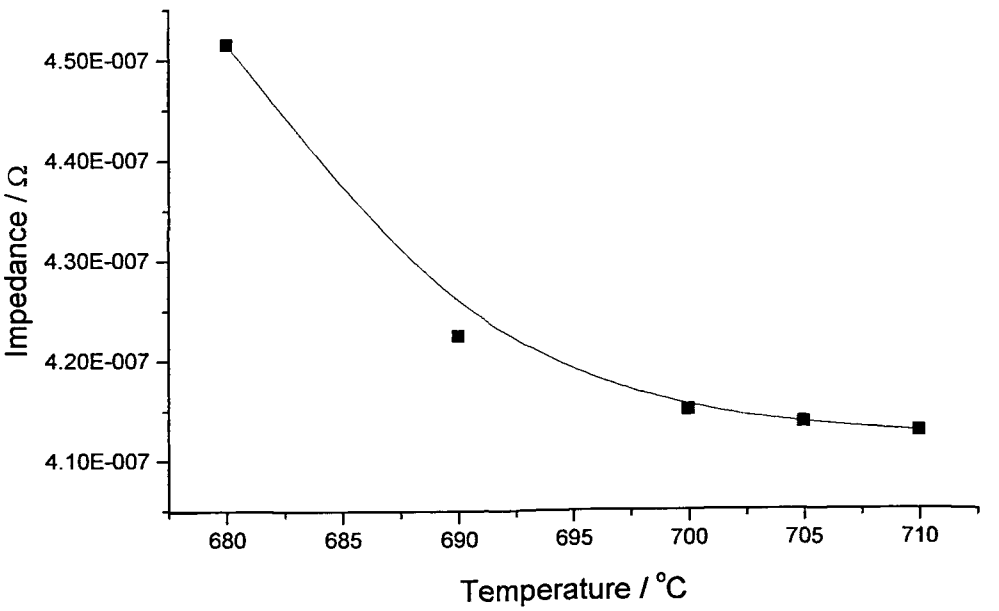

Figure 6.15: Simulated impedance – temperature diagram for the large grain size 0.45 wt % C steel.

The impedance – ferrite fraction plot in figure 6.16 shows some linearity of the magnetic response with ferrite formation. This can be attributed to the lack of ferromagnetic paths in the x-axis prior to the pearlite formation.

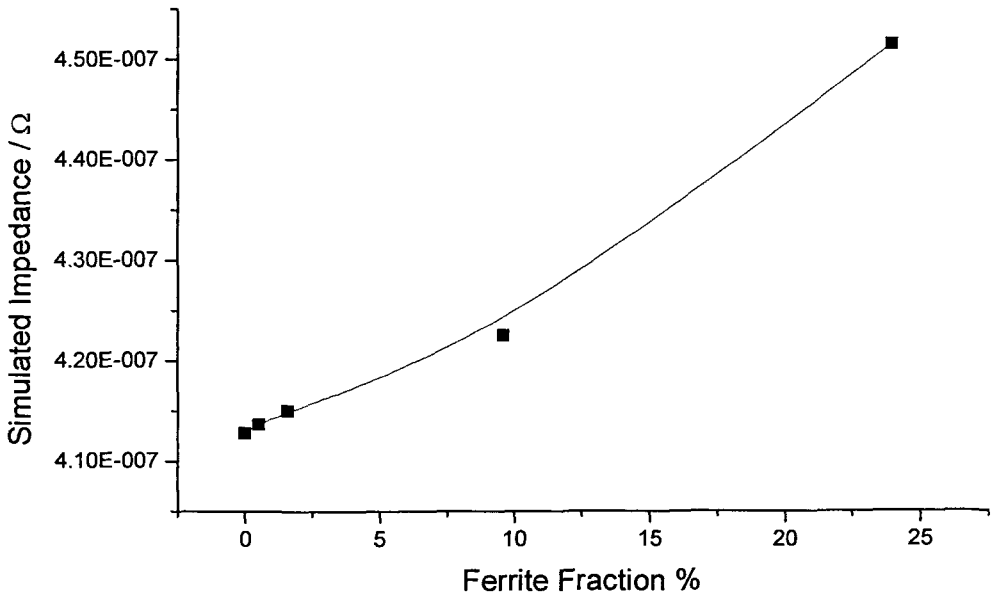

Figure 6.16: Simulated impedance – ferrite fraction diagram for the large grain size 0.45 wt % C steel.

Unfortunately the impedance – ferrite fraction plot displayed in figure 6.16 does not appear to agree well with the experimental results. The main reason for this is the extensive decarburisation that occurred in the homogenised medium carbon steel sample which contributed significantly to the recorded impedance value. Nonetheless, comparison of figure 6.16 with figure 6.7 seems to have a similarity in terms of the linearity observed in impedance increase with ferrite at low ferrite fractions and low contiguity.

It can be concluded that in order to quantitatively relate the EM sensor output with microstructure some knowledge of ferrite distribution (e.g. due to banding / prior austenite grain size) is necessary.

6.12 Summary

FE simulations were conducted in order to determine the effects of ferrite distribution, contiguity and orientation upon impedance response. The initial FE mesh consisted of a 20x20 array of cells representing the sample with cells defined as ferromagnetic or paramagnetic to represent different distributions of ferrite within an austenitic matrix. Simulations on random ferrite distributions showed that impedance response follows a linear relationship with ferrite volume fraction when it does not exceed 20% of the total volume fraction. Above that, when ferrite grains start connecting with each other, the electromagnetic field is affected more by the increased contiguity of ferrite forming a favourable ferromagnetic path which results in a higher impedance response, hence breaking the linear relationship that exists between ferrite volume fraction and impedance at the early stages of ferrite formation. The presence of a decarburised ferrite layer was found to cause an abrupt increase in the impedance response, which is affected by the contiguity and thickness of the layer. It was also found that the relative orientation of the ferrite path to the direction of the electromagnetic field is of importance to the recorded impedance response.

FE simulations were performed on actual microstructures based on microstructural data obtained from the quenching test samples. It was revealed that in the case of the small grain size steel there is a combination of randomly distributed and connected along the rolling axis ferrite grains. The connected grains present a favourable path for the flux to go through. However, the formation of this ferromagnetic path is not instantaneous and it becomes fully connected as the sample cools down. As the ferromagnetic path begins to connect, the impedance value tends to increase at a

higher rate. However, as the connectivity of the ferromagnetic path approaches its maximum the rate at which the impedance value increases reduces. This is due to the fact that the flux has already concentrated in that favourable path causing the impedance value to reach close to the impedance saturation value earlier than if the same amount of ferrite was distributed in a completely random fashion. Overall it was shown that it is possible to relate the EM sensor output of impedance to the transformed bulk ferrite fraction in the steel, however, knowledge of the distribution of ferrite is required.

CHAPTER 7: CONCLUSIONS AND FUTURE WORK

7.1 Conclusions

The present study examined the viability of the electromagnetic technique in measuring phase transformation in steels during the cooling stage. Experimental work was conducted on three different steel compositions using a cylindrical a.c. EM sensor design. The results obtained through the proposed method suggest that a.c. EM sensors are capable of detecting the paramagnetic to ferromagnetic transition and measure the phase transformation in steels as it progresses. The effects of microstructural variability upon impedance response has been evaluated via experimental work and verified through FE simulations.

The conclusions drawn from the analysis of the experimental and simulation results can be used as a springboard for the development of an EM sensor design capable of functioning in the environment of the run-out table of an industrial hot rolling mill. The main conclusions from the present thesis are the following:

- The frequency at which the EM sensor is operated is directly related to the magnitude of the recorded impedance response. Increasing operation frequency leads to an increase in the impedance response and minimises the effect of the electromagnetic noise. However, with increasing frequency the sampling depth is reduced.

- The carbon content in the steel affects the level of impedance response at a given frequency due to the effect of carbon on the permeability of steel.
- From analyses of the phase transformation - impedance response it was found that there is no linear relationship between impedance value and ferrite fraction, except at low ferrite volume fractions, i.e. less than 20 % of the total volume fraction where the ferrite is randomly distributed in the microstructure.

Work was undertaken to extend the use of an EM sensor, from simply detecting steel transformation, to the detection of steel microstructure during cooling. Practical investigations have been, to an extent, verified with FE simulations; the findings and developed methodologies are concluded below:

- Decarburisation was shown to disproportionately affect the impedance-transformation relationship, regardless of sampled depths and hence frequency.
- The effect of oxidation upon the decarburised region and impedance response has been evaluated and shown to cause a decrease in the initial EM response.
- Through EM FE simulations and SEM analysis, the influences of ferrite fraction on the impedance value were shown to be not only dependent upon quantity, but also their distribution (contiguity) and morphology. The prior austenite grain size influences the connectivity of the ferrite (e.g. due to ferrite preferentially nucleating at triple points and growing along the grain boundaries) as it forms during cooling. Thus the

impedance value was shown to be related to the prior austenite grain size and ferrite fraction for a medium carbon steel during cooling through transformation. It should be noted that the larger prior austenite grain size investigated (500 μm) is outside the grain size range typically seen in commercial steels.

- FE simulations of steel microstructures were employed to verify the actual effects of ferrite nucleation upon impedance during steel transformation.
- Image analysis conducted on quench test samples with reference to the EM results were used to relate ferrite volume fraction and temperature with the recorded impedance value.

7.2 Future work

To implement the proposed EM sensor, which is capable of accurately detecting the microstructure of steel, during processing upon the run out table the following work is required:

1. Develop a robust sensor system for use in an industrial environment, in particular Minimise the effect of electromagnetic noise to allow the full range of frequencies to be used by the EM sensor.
2. EM tests with an H-sensor arrangement to evaluate impedance response for strip steel samples.
3. Determine the mathematical relationship between ferrite volume fraction and impedance response.

4. Investigation of cooling rate influences in relation to the impedance-microstructure relationship.
5. Use of the sensor at room temperature on samples with a property gradient through thickness (e.g. coated steels, where the coating is metallic, decarburised steels, surface hardened metals, etc.) to see if the multi-frequency sensor can detect differences in the magnetic properties (e.g. due to composition and microstructure) and hence allow the sensor to be used in other applications.

CHAPTER 8: REFERENCES

[1] Lankford, W. I.; Samways, N. C.; Craven, D. F. and McGannon: The making, shaping and treating of steel, Association of Iron and Steel Engineers, New York, 1985.

[2] Budinski, K. G. and Budinski, M. K.: Engineering Materials, Properties and Selection, 7th Edition, Prentice Hall, Upper Saddle River, New Jersey, 2002.

[3] Colás, R.; de Grinberg, D. M. K. and Grinberg A.: Proc. from Materials Solutions '97 on Accelerated Cooling/Direct Quenching Steels, ASM Int., pp. 181-184, 15-18 September, Indiana, 1997.

[4] Anelli, E.; Cumino, G. and Gonzalez, J. C.: Proc. from Materials Solutions '97 on Accelerated Cooling/Direct Quenching Steels, ASM Int., pp. 67-75, 15-18 September, Indiana, 1997.

[5] Colás, R.; Garcia, C.; Morales, J. C. and Leduc L. A.: Proc. from Materials Solutions '97 on Accelerated Cooling/Direct Quenching Steels, ASM Int., pp. 141-149, 15-18 September, Indiana, 1997.

[6] Guthrie, R. I. L. and Jonas, J. J.: ASM Handbook, Vol. 1, ASM Int., USA, 1990.

[7] Suzuki, H. and McEvily, A. J.: Metall. Trans. A, p. 475, Vol. 10, 1979.

[8] Rossard, C. and Blain, P.: Rev. Mèt., p. 949, Vol. 6, 1964.

[9] Panigrahi, B. K.: Bullet. Mater. Sci., pp. 361-371, Vol. 24, 2001.

[10] Wilson, E. D. and Gladman, T.: Int. Met. Rev., p. 231, Vol. 33, 1988.

[11] Van Cauter, A.; Dilewijns, J.; Horzenberger, F.; Hubert, R. and De Cooman, B.: J. Mat. Eng. Perf., p. 131, Vol. 9, 2000.

[12] Hillert, M. : Phase Transformations. ASM, Ohio, 1970.

[13] Drury, M. D.; Perry, K. P. and Land, T.: J. Iron and Steel Inst., pp. 245-250, November, 1951.

[14] Freer, W. G.: J. of Iron and Steel Inst., p. 517, May 1967.

[15] Young, A. M. and Gruner, K. D.: Steel Times Int., pp. 36-37, November 1999.

[16] Peacock, G. R.: Proc. Soc. Photo-optical instrumentation engineers (SPIE), pp. 171-189, Vol. 3700, 1999.

[17] Dewitt, D. P.: Inferring temperature from optical radiation measurements, Thermosense VI, pp. 226-243, 1983.

[18] Salisbury, R.: Steel Times Int., September, 1997.

[19] Suehiro, M.; Oda, T.; Senuma, T. and Konishi, S.: Development of mathematical model for predicting transformation of high carbon steel during cooling on a run out table and its application to on line temperature control of hot strip, Nippon steel technical report, No. 67, 1995.

[20] Tseng, A. A.; Chang, J. G.; Raudensky, M. and Horsky, J.: J. Mat. Proc. & Man. Sci., pp. 387-408, Vol. 3, 1995.

[21] Brown, A.: Proc. of 45th SEAISI, Singapore Conference, May 2001.

[22] Loney, D.; Roberts, I. and Watson, J.: Ironmaking and Steelmaking, pp. 34-39, Vol. 24, 1997.

[23] Beale, R. and Jackson, T.: Neural Computing: an introduction, Institute of Physics Publishing, Bristol and Philadelphia, 1990.

[24] Maren, A.; Harston, C. and Pap, R.: Handbook of neural computing applications, Academic Press Inc., London, 1990.

[25] Hassoun, M. H.: Fundamentals of artificial neural networks, The MIT Press, London, 1995.

[26] Singh, S. B.; Bhadeshia, H. K. D. H.; MacKay, D. J. C.; Carey, H. and Martin, I.: Ironmaking and Steelmaking, pp. 355-365, Vol. 25, 1998.

[27] Callister, W. D. Jr.: Materials science and engineering: an introduction, 3rd Ed., John Wiley and sons, New York, 1994.

[28] Morita, M.; Hashimoto, O.; Tanaka, T.: System for on-line detecting a transformation value and/or flatness of steel or magnetic material, European Patent Application, No. 0177626, April 1986.

[29] Kitagawa, H. and Sohmura, T.: Trans. ISIJ, pp. 543-549, Vol. 23, 1985.

[30] Gullberg, R. and Lagneborg, R.: Trans. Met. Soc. AIME, p. 1482, Vol. 236, 1966.

[31] Miller, R. L.: Trans. ASM, p. 592, Vol. 61, 1968.

[32] Gaujé, P.: Rev. Met. – CIT, pp. 1145-1150, December, 1990.

[33] Non-destructive testing sub-committee: J. Iron and Steel Inst., pp. 367-369, 1951.

[34] Kopineck, H. J.; Löffel, R. and Otten, H. B.: J. NDT Eval., pp. 13-19, Vol. 12, 1993.

[35] Bunge, H. J.: Textur und anisotropie, Z. Metallkunde, pp. 411-418, Vol. 70, 1979.

[36] Bunge, H. J.: Texture Analysis in Materials Science, Butterworths Publ., London, 1982.

[37] Maurer, A., Böttcher, W. and Kopineck, H. J.: Vorzugsorientierungen Kaltgewaltzer Bänder im Verlauf des Walzprozesses, Abschlußbericht zum Forschungsvertrag Nr. 6210-GA04, August 1978.

[38] Maurer, A.: Ein Neuartiges Untersuchungsystem zur Zertörungsfreien Bestimmung von Werkstoffkennwerten an Feiblechen mittels Röntgenfeinstrukturverfahren, Dissertation, Münster, 1982.

[39] Böttcher, W. and Kopineck, H. J.: Über ein röntgentexturmeβverfahren zur zerstörungsfreien on-line-bestimmung technologischer kennwerte von kaltgewalzten stahlbändern, Stahl Eisen, pp. 509-516, Vol. 516, 1985.

[40] Kopernick, H. J. and Offen, H. B.: Textures and Microstructures, pp. 97-113, Vol. 7, 1987.

[41] Beaujard, L. and Mondot, J.: Revue Universelle des Mines, p. 462, 1962.

[42] Beaujard, L. and Mondot, J.: Rev. Mét., Vol. 63, 1966.

[43] Beaujard, L.; Dumnt-Fillon, J. and Kapluszak, M.: Proc. ICSTIS, Suppl. Trans. ISIJ, pp.720-724, vol. 11, 1971.

[44] Papadakis, E. P.; Lynnworth, L. C.; Fowler, K. A. and Carnevale, E. H.: J. Acous. Soc. Am., pp. 850-857, vol. 52, 1972.

[45] Goebbels, K.: Materials characterisation for process control and product conformity, CRC Press, Boca Raton, Florida, 1994.

[46] Scruby, C. B. and Drain, L. E.: Laser-Ultrasonics: Techniques and applications, Adam Hilger, Bristol, 1990.

[47] Monchalin, J. P; Héon, R.; Bussière. J. F.; Pascale, D. and Farahbaksh: Proc. of NDT Characterisation of Materials II, p. 717, Plenum Publ. Corp., New York, 1987.

[48] Scruby, C. B. and Moss, B. C.: NDT Int., p. 177, Vol. 26, 1993.

[49] Senkov, O. N.; Dubois, M. and Jonas, J. J.: Metall. Mater. Trans. A, p. 3963, Vol. 27A, 1996.

[50] Willems, H.: Review of progress in quantitative NDT evaluation, pp. 473-481, Vol. 6A, Plenum Press, New York, 1987.

[51] Moreau, A.; Lord, M.; Lévesque, D.;Dubois, M.;and Bussière, J.: J. All. Comp., pp. 427-431, vol. 310, 2000.

[52] Dubois, M.; Moreau, A.; Militzer, M. and Bussière, J.: Scripta Mat., pp. 735-741, vol. 39, 1998.

[53] Dubois, M.; Militzer, M.; Moreau, A. and Bussière, J.: Scripta Mat., pp. 867-874, vol. 42, 2000.

[54] Still, A.G.; Tweed, J. H. and Moss, B. C.: Proc. Measuring up to customers needs: Advances in on-line instrumentation for finishing processes in strip production, IoM, London, 2001.

[55] Jayakumar, T.; Palanichamy, P. and Raj, B.: Proc. Asia-Pacific Conf. on NDT, p. 110, Shanghai, China, 1993.

[56] Orlowicz, W.: Evaluation of mechanical properties in spheroidal graphite iron by ultrasonic method, Exercise Book No. 20, pp. 1-144, University of Technology of Rzeszów, Poland, 1990.

[57] Palanichamy, P.; Mathew, M. D.; Latha, S.; Jayakumar, T.; Bhanu, K.; Rao S.; Mannan, S. L. and Raj, B.: Scripta Mat, pp. 1025-1030, Vol. 45, 2001.

[58] Orlowicz, W. and Opiekun, Z.: Theor. App. Frac. Mech., pp. 9-16, vol. 22, 1995.

[59] Rajendran, V.; Muthu Kumaran, S.; Jayakumar, T.; Palanichamy, P. and Rak, B.: Proc. NDE 2002, National Seminar of ISNT, Chennai, India, 5 – 7th December 2002.

[60] Rajendran, V.; Palanivelu, N. and Chauduri, B.: Rev. Sci. Inst. (Submitted)

[61] He, P.: Ultrasonic Imaging, p. 275, Vol. 20, 1998.

[62] Bodin, A. and Marchal, P. D.: Steel Res., pp. 103-109, Vol. 65, 1994.

[63] Bozorth, R. M.: Ferromagnetism, Van Nostrand, 1965.

[64] Lacroix, M.; Abrigo, J. and Arnault, L.: Proc. of International Conference on Steel Rolling, p. 1286-1296. Tokyo, 1980.

[65] Bullens, D. K.: Steel and its Heat Treatment, vol. 1 - Principles, John Wiley and Sons Inc., New York, 1948.

[66] Dubé, C. A.; Aaronson, H. I.; Kinsman, K. R. and Hall, M. G.: Rev. Metal., p. 201, Vol. 55, 1958.

[67] Aaronson, H. I.: Decomposition of Austenite by Diffusional Processes, p. 387, V. F. Zackay and H. I. Arronson (Eds.), Interscience Publishers, New York, 1962.

[68] Honeycombe, R.W.K. and Bhadeshia, H.K.D.H.: Steels; microstructure and properties, Published by Edward Arnold, 2nd Edition 1995.

[69] Honeycombe, R. W. K.: Metall. Trans. A, pp. 915-936, vol. 7A, July 1976.

[70] Kurdjumov, G. V. and Sachs, G.: Z. Phys., p. 325, Vol. 64, 1930.

[71] Mehl, R. F.; Barrett, C. S. and Smith, D. W.: Trans. AIME, p. 215, Vol. 105, 1933.

[72] Liu, Y. C.; Aaronson, H. I.; Kinsman, K. R. and Hall M. G.: Metall. Trans., pp. 1318-1320, Vol. 3, May 1972.

[73] Smith, C. S.: Transactions of ASM, p. 533, Vol. 45, 1953.

[74] Christian, J. W.: Theory of Transformations in Metals and Alloys, Part I, 2nd edn. Pergamon Press, Oxford, 1975.

[75] Kinsman, K. R. and Aaronson, H. I.: Transformation and Hardenability in Steels, Climax Molybdenum Company, Ann Harbor, MI, 1962.

[76] Hillert, M.: Jernkontorets. Ann., p. 757, Vol. 141, 1957.

[77] Jones, G. J. and Trivedi, R. K.: J. appl. Phys, p. 4299, Vol. 42, 1971.

[78] Kinsman, K. R. and Aaronson, H. I.: Metall. Trans., p. 959-967, vol. 4, April 1973.

[79] Zener, C.: J. appl. Phys., p. 950, vol. 20, 1949.

[80] Bradley, J. R.; Rigsbee, J. M. and Aaronson, H. I.: Metall. Trans. A, p. 323, 8A, 1977.

[81] Kirkaldy, J. S.: Decomposition of Austenite by Diffusional Process, pp. 39-130, V. F. Zackay and H. I. Aaronson, Interscience, New York, 1962.

[82] Hultgren, A.: Trans. Am. Soc. Metals, p. 915, Vol. 39, 1947.

[83] Purdy, G. R; Weichert, D. H. and Kirkaldy, J. S.: Trans. Metall. Soc. AIME, p. 1025, Vol. 230, 1964.

[84] Gilmour, J. B.; Purdy, G. R. and Kirkaldy, J. S.: Metall. Trans., p. 3213, Vol. 3, 1972.

[85] Coates, D. E.: Metall. Trans., p. 2313, Vol. 4, 1973.

[86] Aaronson, H. I.; Domian, H. A. and Proud, G. M.: Trans. Metall. Soc. AIME, p. 768, Vol. 236, 1966.

[87] Aaronson, H. I. and Domian, H. A.: Trans. Metall. Soc. AIME, p. 781, Vol. 236, 1966.

[88] Enomoto, M. and Aaronson, H. I.: Metall. Trans. A, p. 1547, Vol. 18A, 1987.

[89] Wits, J. J.; Kop, T. A.; van Leeuwen, Y.; Seitsma, J. and van Der Zwaag, S.: Mat. Sc. Eng. A, pp. 234-241, Vol. A283, 2000.

[90] Oi, K.; Lux C. and Purdy G. R.: Acta Mater., pp. 2147-2155, Vol. 48, 2000.

[91] Capdevilla, C.; Caballero, F. G. and García de Andrés : Scripta Mat., pp. 593-600, Vol. 44, 2001.

[92] Odqvist, J.; Hillert, M. and Ågren, J: Acta Mat., pp. 3211-3225, Vol. 50, 2002.

[93] Liu, Z. and Ågren, J.: Acta Metall., pp. 3157-3163, vol. 37, No. 12, 1989.

[94] Vandermeer, R. A.: Acta Metall. Mater., p. 2461- 2470, Vol. 38, No. 12, 1990.

[95] Qiu, C.; Sietsma, J. and van der Zwaag, S.: Ironmaking and Steelmaking, pp. 200-204, Vol. 26, No. 3, 1999.

[96] Smith, Y. E. and Siebert, C. A.: Metall. Trans., p. 1711, vol. 2, 1971.

[97] Klestov, V. M.; Entin; R. I., Sokolov, K. N.; Betin, G. Y. A.; Kogan, L. I. and Mikhno V.: Fiz. Metal. Metalloved, p. 973, vol. 33, 1972.

[98] Shteinberg, M. M.; Filatov, V. I.; Shilkova, T. I.; Smirnov, M. A. and Gonshar, V. N.: Steel in the USSR, p. 872, October 1973.

[99] Walker, D. J.: Ph.D. Dissertation, University of Cambridge, 1975.

[100] Mehl, R. F. and Hagel, W. C.: The Austenite-Pearlite Reaction, in Progress in Metallurgical Physics, B. Chalmers and R. King (eds.), Vol. 6, Pergamon Press, 1956.

[101] Hillert, M.: The formation of Pearlite, in Decomposition of Austenite by Diffusional Processes, pp. 197-247, V. F. Zackay and H. I. Arronson (Eds.), Interscience Publishers, New York, 1962.

[102] Dippenaar, R. J. and Honeycombe, R. W. K.: Proc. Roy. Soc., p. 455-671, A 333, 1973.

[103] Davenport, E. S.: Trans. ASM, p. 837, vol. 27, 1939.

[104] Hawkes, M. F. and Mehl R. F.: Trans. AIME, p. 467, vol. 172, 1947.

[105] Bowen, A. W. and Leak, G. M.: Metall. Trans., p. 2767-2773, vol. 1, October 1973.

[106] Entin, R. I.: Decomposition of Austenite by Diffusional Processes, p. 295, V. F. Zackay and H. I. Arronson (Eds.), Interscience Publishers, New York, 1962.

[107] Mannerkoski, M.: Acta Polyteck. Scand., Ch. 26, 1964.

[108] Campbell, K.: Ph.D. Dissertation, University of Cambridge, 1971.

[109] Bungardt, V. K.; Kunze, E. and Korn, E.: Arch. Eisenhutten, p. 193, vol. 29, 1958.

[110] Johnson, W. A. and Mehl, R. F.: Trans. AIME, p. 416-458, vol. 135, 1939.

[111] Krauss, G.: Steels Heat Treatment and Processing Principles, ASM, Materials Park, OH, 1989.

[112] Cahn, J. W. and Hagel, W. C.: Decomposition of Austenite by Diffusional Processes, p. 39, V. F. Zackay and H. I. Arronson (Eds.), Interscience Publishers, New York, 1962.

[113] Spencer, C. W. and Mack, D. J.: Decomposition of Austenite by Diffusional Processes, p. 549, V. F. Zackay and H. I. Arronson (Eds.), Interscience Publishers, New York, 1962.

[114] Turnbull, D. and Treaftis, H. N.: Trans. AIME, p. 33, vol. 212, 1958.

[115] Puls, M. P. and Kirkaldy, J. S.: Metall. Trans., p. 2777-2795, vol. 3, November 1972.

[116] Sundqvist, B. E.: Acta Metall., p. 1413-1426, vol. 16, December 1968.

[117] Johnson, W. C. and Blakely, J. M. (eds.): Interfacial Segregation, ASM, Metals Park, Ohio, 1979.

[118] Brofman, P. J., Abell, G. S., Nichol, T. J. and Judd, G.: in Mechanical Behaviour of Metals and Alloys associated with Displacive Phase Transformations, Joint U.S.-Japan Conference, Rensselaer Polytechnic Institute, Troy, New York, June 1979.

[119] Melloy, G. F.: Austenite grain size – its control and effects, Metals Engineering Institute, ASM, Metals Park, OH, 1968.

[120] Derge, G. A. ; Kommel, R. and Mehl, R. F.: Trans. ASM, p. 153-166, vol. 23, 1938.

[121] Schane, P. Jr.: Trans. ASM, p. 1034-1035, vol. 22, 1934.

[122] Dorn, J. E. and Harder, O. E.: Trans. ASM, p. 106-133, vol. 6, 1938.

[123] Scoonover, T. M. and Krauss, G.: Met. Eng. Q, p. 41-48, vol. 12, 1972.

[124] Matsuda, S.: in New Aspects of Martensitic Transformation, p. 363-367, Japan Institute of Metals, 1976.

[125] Watanabe, S.; Ohmori, Y. and Kunitaki, T.: in New Aspects of Martensitic Transformation, p. 368-374, Japan Institute of Metals, 1976.

[126] Bain, E. C.: Functions of the alloying elements in steel, ASM, 1939.

[127] Hillert, M.: Scripta Mat., p. 447-453, vol. 46, 2002.

[128] Hilyman, P. R.: Unpublished work. Kinsman, K. R. and Aaronson, H. I., Metall. Trans., p. 959, vol. 4, 1973.

[129] Greninger, A. B. and Troiano, A. R.: Trans. ASM, p. 537-563, vol. 28, 1940.

[130] Bibby, M. J. and Parr, J. G.: J. Iron Steel Inst., p. 100-104, vol. 202, 1964.

[131] Owen, W. S. and Wilson, E. A.: in Physical Properties of Martensite and Bainite, Iron and steel Inst., p. 53-57, Special Report No. 93, London, 1965.

[132] Payson, P. and Savage, C. H.: Trans. ASM, pp. 261-275, Vol. 33, 1944.

[133] Caparella, L. A.: Met. Prog., p. 108, Vol. 46, 1944.

[134] Rowland, E. S. and Lyle, S. R.: Trans. ASM, pp. 27-47, Vol. 37, 1946.

[135] Grange, R. A. and Stewart, H. M.: Trans. AIME, pp. 467-490, Vol. 167, 1946.

[136] Nehrenberg, A. E.: Trans. AIME, pp. 494-498, Vol. 167, 1946.

[137] Steven, W. and Haynes, A. G.: JISI, pp. 349-359, Vol. 183, 1956.

[138] Andrews, K. W.: JISI, pp.721-727, Vol. 203, 1965.

[139] Krauss, G.: Martensitic Tranformation, Structure and Properties in Hardenable Steels, in Hardenability Concepts with Applications to Steel, AIME, pp. 229-248, Warrendale, PA, 1978.

[140] Kung, C. Y. and Rayment, J. J.: Met. Trans. A, pp. 328-331, Vol. 13A, 1982.

[141] Harris, W. H. and Cohen, M.: Trans. AIME, pp. 447-470, Vol. 180, 1949.

[142] Koistinen, D. P. and Marburger, R. E.: Acta Met., pp. 59-60, Vol. 7, 1959.

[143] Howard, R. T. and Cohen, M.: Trans. AIME, pp. 384-397, Vol. 28, 1940.

[144] Marder, A. R. and Krauss, G.: Trans. ASM, pp. 651-660, Vol. 60, 1967.

[145] Olsen, G. B. and Cohen, M.: Metall. Trans., pp. 1897-1923, Vol. 7A, 1976.

[146] Rohde, R. W. and Graham, R. A.: Trans. Metall. Soc. AIME, p. 2441, vol. 245, 1969.

[147] Gefen, Y.; Halwany, A. and Rosen, M.: Phil. Mag., p. 1, vol. 28, 1973.

[148] Otsuka, K.; Sakamoto, H. and Shimizu, K.: Acta Metall., p. 585, vol. 27, 1979.

[149] Patel, J. R. and Cohen, M.: Acta Metall., p. 531, vol. 1, 1953.

[150] Xie, Z. L.; Sundqvist, B.; Hannes, H. and Pietikäinen, J.: Acta Metall., p. 2283-2290, vol. 41, No. 8, 1993.

[151] Llewellyn, D. T. and Hudd, R. C.: Steel Metallurgy and Applications, Third Edition, Butterworth-Heinemann, Oxford, 1998.

[152] Aaronson, H. I.; Reynolds, Jr, W. T. ; Shiflet, G. J. and Spanos, G.: Metall. Trans. A, p. 1343, vol. 21A, 1990.

[153] Bhadeshia, H. K. D. H. and Edmonds, D. V.: Metall. Trans. A, p. 895, vol. 10A, 1979.

[154] Cuckon, F. W.: Nature, pp. 639-640, vol. 159, May, 1947.

[155] Enomoto, M.: Scripta Mater., pp. 145-149, vol. 47, 2002.

[156] Bhadeshia, H. K. D. H. and Christian, J. W.: Metall. Trans. A, p. 767, 21A, 1990.

[157] Ohmori, Y. and Maki, T.: Mater. Trans., JIM, p. 631, vol. 32, 1991.

[158] Enomoto, M.: Mater. Trans, JIM, p. 642, vol. 32, 1991.

[159] Bhadeshia, H. K. D. H.: Mater. Sci. Eng. A, p. 58-66, vol. A273-275, 1998.

[160] Christian, J. W. and Edmonds, D. V.: in Phase Transformations in Ferrous Alloys, p. 293, TMS – AIME, Warrendale, PA, 1984.

[161] Sandvik, B. P. J.: Metall. Trans. A, p. 777, vol. 13A, 1982.

[162] Swallow, E. and Bhadeshia, H. K. D. H.: Mat. Sci. Tech., p. 121, vol. 12, 1996.

[163] Crank, J.: The mathematics of Diffusion, Oxford University Press, Oxford, 1956.

[164] Porter, D. A. and Easterling, K. E.: Phase Transformations in Metals and Alloys, Second Edition, Nelson Thrones, Cheltenham, 2001.

[165] Thelning, K. E.: Steel and its Heat Treatment, Second Edition, Butterworths, London, 1984.

[166] Mallik, A. U. and Whittle, D. P.: Oxid. Met., pp. 339-353, Vol. 16, 1981.

[167] Portevin, E.; Pretet, E. and Jolivet, H.: Rev. Metall., p. 219, Vol. 31, 1934.

[168] Upthegrove, C. and Murphy, D.: Trans. Amer. Soc., Steel Treat. p. 73, Vol. 21, 1933.

[169] Siebert, C. A.: Trans. Amer. Soc. Met., p. 75, Vol. 25, 1939.

[170] McAdam, D. J. and Geil, G. W.: J. Res. Nat. Bur. Stand., p. 63, Vol.. 23, 1939.

[171] Smeltzer, W. W. and Young, D. J.: Prog. Solid State Chem., p. 17, 1975.

[172] Petch, N. J. In fracture, Proc. of the Swampscott Conference, 1959.

[173] Irvine et al.: J. Iron Steel Inst., p. 161, Vol. 205, 1967

[174] Brooks, C. R.: Principles of the austenitisation of steels, Kluwer Academic Publishers, 2001.

[175] Li, L. and Messler, R. W. Jr.: Weld. Res., pp. 78 – 84, May, 2002.

[176] Van Heuvelen, A.: Physics: A General Introduction, Second Edition, Harper Collins, US, 1986.

[177] Eddy Current Testing Manual on Eddy Current Method compiled by Eddy Current Technology Inc.

[178] ASM Handbook: Properties and Selection: Irons and Steels, Vol. 1, 9th Edition.

[179] Drury, J. C.: Insight, pp. 14-20, Vol 39, 1997.

[180] Yu, Z. and Gaydecki, P.: Meas. Sci. Tech., pp. 1571-1575, Vol. 9, 1998.

[181] Sun, Y. S., Ouang, T. and Udpa, S.: J. Mat. Eval., pp. 632-637, Vol. 54, 2001.

[182] Crangle, J.: Solid State Magnetism, Edward Arnold, 1991.

[183] Carter, G. W.: The electromagnetic field in its engineering aspects, London, 1954.

[184] Solymar, L.: Lectures on the electromagnetic theory, Oxford Science Publ., Bristol, 1986.

[185] Dekker, A. J.: Solid State Physics, MacMillan & Co. Ltd., London, 1952.

[186] Bethe, H.: Handbuck der Physic, Vol. 24/2.

[187] Barnett, S. J.: Proc. Am. Acad. Arts Sci., p. 109, vol. 75, 1944.

[188] Scott, G. G.: Phys. Rev., p. 542, vol. 82, 1951.

[189] Scott, G. G.: Phys. Rev., p. 697, vol. 87, 1952.

[190] Weiss, P.: J. Phys., p. 667, vol. 6, 1907.

[191] Sandovskii, V. A.; Kurmaeva, L. D. and Fokina E. A.: Russian J. of NDT, pp. 471-474, Vol 36, 2000.

[192] Kersten, M.: Grundlagen einer theory der ferromagnetischen hysterese und der koerzitivkraft, Hirzel, Leipzig, 1943.

[193] Néel, L.: Univ. Grenoble, p. 299, Vol. 22, 1945-1946.

[194] Williams, H. J. and Shockley, W.: Phys. Rev., p. 178, Vol. 75, 1949.

[195] Kondorskii, E. I.: Dokl. Akad. Nauk, SSSR, p. 37, Vol. 68, 1949.

[196] Dykstra, L. J.: Nonferromagnetic precipitate in a ferromagnetic matrix, in Magnetism and metallurgy, eds. A. E. Berkowitz and E. Kneller, pp. 513-522, Vol. 2, New York, 1969.

[197] Norton, S. J.; Kahn, A. H. and Mester, M. L.: Res. In NDT Eval., p. 167, Vol. 1, 1989.

[198] Moulder, J. C.. Uzal, E. and Rose, J. H.: Rev. Sci. Instrum., pp. 3455-3465, Vol. 63, 1992.

[199] Uzal, E. and Rose, J. H.: IEEE Trans. On Magnet., pp. 1869-1873, Vol. 29, 1993.

[200] Bowler, J. R.: J. Appl. Phys., pp. 8128-8137, Vol. 75, 1994.

[201] Cox, J.: Insight, pp. 822 – 823, Vol. 42, 2000.

[202] van de Bos, B.; Sahlen, B. and Andersson, J.: Insight, pp. 163-166, Vol. 43, 2001.

[203] Duijn, J.: Corus Internal Report.

[204] Johnstone, S.; Binns, R.; Peyton, A. J. and Pritchard, W. D. N.: Trans. Inst. Meas. and Contr., pp. 21-29, Vol. 23, 2001.

[205] Morita, M.; Hashiguchi, K.; Okano, S.; Hashimoto, O. and Nishida, M.: Tetsu-to-Hagané, p. 4, vol. 71, 1985.

[206] Morita, M.; Hashimoto, O. and Tanaka, T.: European Patent Application No. 0177626, 9th October, 1986.

[207] Morita, M.; Hashiguchi, K.; Hashimoto, O.; Nishida, M. and Okano, S.: In proc of The Metallurgical Society Conf., pp. 449-461, 1985.

[208] Ishibashi, N.; Morita, M.; Sakata, K.; Hashiguchi, K. and Okano, S.: Trans. ISIJ, p. B-54, Vol. 27, 1987.

[209] Yahiro, K.; Yamasaki, J.; Furukawa, M.; Arai, K.; Morita, M. and Obashi,, M.: Kawasaki Steel Technical Report, pp. 33-40, No. 24, April, 1991.

[210] Sharif, E.; Bell, C. and Peyton, A. J.: J. Electr. Imag., pp. 669- 678, Vol. 10, 2001.

[211] Binns, R.; Dickinson, S. J. and Peyton, A. J.: In proc. of Sensors and their Applications IX, Applications of Sensors, pp. 45-50, 2001.

[212] Papaelias, M. Ph.; Davis, C. L.; Strangwood, M.; Binns, R. and Peyton, A. J.: In proc, of 16th National Conference in Solid State Physics, pp. 284-287, 17-20 September 2000, Nafplion, Greece.

[213] Papaelias, M. Ph.; Davis, C. L.; Strangwood, M.; Binns, R. and Peyton, A. J.: In proc. of Materials Research Conference, Institute of Materials, London, 23 May 2001.

[214] Papaelias, M. Ph.; Davis, C. L.; Strangwood, M.; Binns, R. and Peyton, A. J.: In proc. of Progress in innovative manufacturing engineering, pp. 123-128, 20-22 June 2001, Genoa, Italy.

[215] Papaelias, M. Ph.; Davis, C. L.; Strangwood, M.; Binns, R. and Peyton, A. J.: In proc. of 17th National Conference in Solid State Physics, pp. 394-397, 6-9 September 2001, Xanthi, Greece.

[216] Binns R.; Davis, C.; Dickinson, S.; Morris, P.; Peyton, A.; Papaelias, M. Ph.; Pritchard, W. and Strangwood, M.: In proc. of Instrumentation to innovation – Applications and developments in metal production and use, 27-28th February 2002.

[217] Papaelias, M. Ph.; Davis, C. L.; Strangwood, M. and Peyton, A. J.: In proc. of 11th International Congress in Metallurgy and Materials, 5-8 June 2002, Istanbul, Turkey.

[218] Davis, C. L.; Papaelias, M. Ph.; Strangwood, M. and Peyton, A. J.: J. Ironmaking and Steelmaking, pp. 469-476, No. 6, Vol. 29, 2002.

[219] Papaelias, M. Ph.; Davis, C. L.; Strangwood, M. and Peyton, A. J.: In Proc. of Modelling the Performance of Engineering Structural Materials III, TMS Fall Meeting 2002, pp. 311-320, Columbus, OH, U.S., 6-10th October 2002.

[220] Papaelias, M. Ph.; Strangwood M; Peyton, A. J. and Davis C. L.: J. of Metall. Trans. A, Accepted for publication.

[221] Papaelias, M. Ph.; Davis, C. L.; Strangwood, M. and Peyton, A. J.: In proc. of 2nd Materials Research Conference, Institute of Materials, London, 17-18th February 2003.

[222] Omega temperature measurement catalogue.

[223] Fan, Z.; Miodownik, P. and Tsakiropoulos, P.: Mat. Sci. Tech., pp. 1094-1100, Vol. 9, 1993.

[224] Gustaffson, P.: C-Fe, Scan. J. Metall., pp. 259-267, Vol. 14, 1985.

[225] Dinsdale, A.: SGTE data for pure elements, NPL Report, DMA (A) 195, September 1989.

[226] Huang, W.: C-Fe-Mn, Metall. Trans., pp. 2115-2123, Vol. 21A, 1990.

[227] Shim, J. -H., Chung, H. –J and Lee, D. N.: Fe-C-P, Metallukunde, 1999.

[228] Lacaze, J. and Sundman. B.: Fe-Si and Fe-Si-C, Metall. and Mater. Trans., pp. 2211-2223, Vol. 22A, 1991.

[229] Huang, W.: Fe-Mn, Calphad, pp. 243-252, Vol. 13, 1989.

[230] Shim, J. -H., Oh, C. –S and Lee, D. N.: Fe-P, J. Korean Inst. Met. Mater., pp. 1385-1393, Vol. 34, 1996.

[231] Tibballs, J. E.: Fe-Si, SI Norway, Report 890221-5, 1991.

[232] Miettinen, J. and Hallstedt, B.: Fe-Si and Fe-Si-C, Calphad, pp. 231-256, Vol. 22, 1998.

[233] Forsberg, A. and Agren, J.: Fe-Mn-Si, J. Phase Equil., pp. 354-363, Vol. 14, 1993.

[234] Binns, R., Ph.D. Thesis, Lancaster University, 2002.

[235] Binns, R. and Peyton, A. J.: In proc. of Regional Symposium on Quality and Automation, pp. 155-162, 2000.

[236] Ajersch F: In proc. of 34th mechanical working and steel processing conference, pp. 419-437, Vol. 30, 1993.

[237] Senkevich, J. J.; Jones, D. A. and Chatterjee I.: Corro. Sci., pp. 201-210, Vol. 42, 2000.

[238] Wood, G. C. and Scott, F. H.: J. Mat. Sci. Tech., pp. 519-530, Vol. 3, 1987.

[239] Spalding, N.: Magnetic Materials, Fundamentals and Device Applications, Pub. Cambridge University Press, 2003.